8-2017

Development and Characterization of a Plate Fuel Hotspot Model in COMSOL

Michael Joseph Richards
University of Tennessee, Knoxville, mricha44@vols.utk.edu

To the Graduate Council:

I am submitting herewith a dissertation written by Michael Joseph Richards entitled "Development and Characterization of a Plate Fuel Hotspot Model in COMSOL." I have examined the final electronic copy of this dissertation for form and content and recommend that it be accepted in partial fulfillment of the requirements for the degree of Doctor of Philosophy, with a major in Energy Science and Engineering.

<div align="right">Arthur E. Ruggles, Major Professor</div>

We have read this dissertation and recommend its acceptance:

G. Ivan Maldonado, Kivanc Ekici, Kwai L. Wong

<div align="right">Accepted for the Council:
<u>Dixie L. Thompson</u></div>

<div align="right">Vice Provost and Dean of the Graduate School</div>

(Original signatures are on file with official student records.)

Development and Characterization of a Plate Fuel Hotspot Model in COMSOL

A Dissertation Presented for the
Doctor of Philosophy
Degree
The University of Tennessee, Knoxville

Michael Joseph Richards
August 2017

Acknowledgements

I would like to thank the many different people who have aided me throughout this process: Dr. Arthur E. Ruggles, Dr. Kivanc Ekici, Dr. Ivan Maldonado, Dr. Kwai Wong, Dr. James D. Freels, Dr. David H. Cook, Dr. Prashant Jain, and Dr. Leo Riedinger.

Abstract

Aluminum clad plate fuel is common to many high performance water cooled research reactors, including the High Flux Isotope Reactor (HFIR) at ORNL. Fuel manufacturing defects associated with fuel segregation and incomplete bonding of the cladding to the fuel material currently limit the performance of HFIR. A high resolution multi-physics (HRMP) simulation of concurrent fuel segregation and incomplete bonding of fuel cladding is developed in this dissertation. The simulation development begins with a review of legacy modeling of the fuel segregation and cladding non-bond, and then proceeds to identify improvements possible in the HRMP framework. A contact conductance model is selected for the incomplete bonding of cladding to fuel, advancing previous models. A verification of the COMSOL simulation platform used to construct the evaluation model is performed using the method of manufactured solutions, including assessments of the solid conduction modeling domain, the fluid coolant channel domain, and coupled fuel to coolant channel domains. Solution verification is performed with the least squares, grid convergence index approach, and indirect validation of the evaluation model is performed using data generated to establish thermal performance limits for the Advanced Neutron Source reactor. The verification and validation efforts are also extensions to previous work using COMSOL for HRMP modeling of HFIR, and establish numerical and modeling uncertainties. The evaluation model is then employed in a sensitivity assessment of 18 parameters in the evaluation model using Latin Hypercube sampling methods to establish a ranking of parameter importance in predicting four quantities of interest.

Preface

This work reports on advancements made in modeling local areas of increased temperature, known as hotspots, in nuclear research reactor fuel plates through the development and characterization of an improved hotspot model. The first 6 chapters offer a background on research reactors and fuel manufacture. A review of past hotspot modeling is also offered to position this work within the body of literature. Chapters 7 through 11 describe the new efforts made in understanding hotspots. A sensitivity assessment is developed that showcases the modeling utility. Chapter 12 concludes the report. Eight appendices provide more detailed information about various topics.

Plate fueled research reactors develop high continuous neutron fluxes and are useful to materials research and other scientific studies. Many of these reactors were initially fueled with high enriched uranium. Plans to convert the High Flux Isotope Reactor (HFIR) at ORNL to low enriched uranium motivate this study. The HFIR operating characteristics include one of the highest neutron fluxes in the world, and this high flux is attendant with very high thermal power density in the core. Core cooling is accomplished using forced flow of water at near 15 m/s. The fuel cladding is aluminum to offer high conductivity and low neutron cross-section. Fuel plates are 1.27 mm thick to minimize the conduction distance between fuel centerline and coolant, facilitating the high power density. While average parameters are often used to characterize the HFIR performance, such as the 85 MW of thermal power generated in the core, the parameters that limit the performance are local due to spatial variation in power density deliberately engineered into the core design, and due to potential manufacturing tolerances and defects in the fuel.

Non-bonds are defects resulting in areas of incomplete bonding within the fuel plate and are the focus of Chapter 4. Previous works on the topic are examined, and a new approach, thermal contact conductance (TCC) is considered. The theory and approaches of TCC are reviewed and applicability to fuel plate non-bonds is established. Another fuel manufacturing defect is a fuel segregation which provide a local increase in fission power. This dissertation examines a fuel segregation located under a cladding non-bond, as the worst case fuel defect that can pass manufacturing quality inspection measurements. These defects are local and small in scale, and require high resolution multiphysics assessment. The combination of fuel segregation and non-bond models in the fuel are connected to a fluid domain model of the fuel cooling channel to form a hotspot model in the COMSOL code suite. COMSOL is a high resolution multiphysics (HRMP) finite element analysis (FEA) code which consists of a main program and physics-specific modules. The nature of the hotspot dictates the use of the heat transfer module and the computational fluid dynamics module. COMSOL offers two features to model small entities without the need to use extremely fine meshes typical of FEA modeling of a system of this type. These two approaches were identified as possible options for modeling non-bonds, and the

overall performance of these features were assessed through comparison with conventional fine mesh approaches. Several discoveries were made regarding artifacts these approaches introduce, however, the COMSOL features were found to be adequate for the hotspot thermal model development.

Earlier hotspot and fuel plate models are discussed as each domain of the new hotspot model is developed. Initial testing of the new model includes the use of 5 turbulence models and 9 mesh densities, and compares predicted pressure drop, temperature, velocity, energy and mass balances, and run times for each of the simulations. These assessments informed the modeling features used later in the research.

A systematic approach to quantifying the uncertainty in the hotspot model is developed using the tools of verification and validation. This rigorous approach to uncertainty quantification is emerging in CFD and mechanics simulations, and is not mature for multiphysics simulations typical of this hotspot work. Chapter 9 explains the purposes of and processes for code and solution verification. The relevant portions of COMSOL are subject to these processes which required invention of several manufactured solutions, and application of the method of manufactured solutions across computational domains. This effort results in an estimate of the numerical uncertainty of the hotspot simulation results. A validation is also performed using legacy experimental data developed for research reactor design, and the resulting modeling error plus uncertainty is estimated from that process. This is the most advanced assessment of combined numerical model and solution uncertainty performed for a multiphysics simulation of fuel plate hotspots available in the literature.

Finally, a sensitivity analysis of the hotspot model is performed in which 18 model parameters are examined. Surrogate models are developed and the relative importance of the parameters to three quantities of interest are identified. A grid refinement study indicates that the ranking of the parameters is independent of the mesh used.

Several software utilities were developed to support this research that have enduring value and are archived in appendices. These include the MATLAB code that implements the least squares grid convergence index algorithm for estimating numerical uncertainty. A set of instructions for repeating the sensitivity analysis which integrated COMSOL with DAKOTA. Adaptations made to the hotspot model to facilitate the sensitivity analysis which includes remeshing of the model for geometric parameter variations. An example method for visualizing the multi-variate surface of the surrogate model developed during the sensitivity assessment is also offered.

Table of Contents

List of Tables

List of Figures

xiii

xviii

Chapter 1   Research Reactors

Nuclear reactors come in a wide variety and are often distinguished by their use. The most familiar of nuclear reactors are those used in the power industry for electricity generation. Another category of reactors are those used to power marine or naval vessels. Both of these categories describe reactors that are in systems whose primary purpose is the conversion of thermal energy to mechanical and electrical energy. A third category of reactor, research reactors, is not focused on using the thermal energy from fission, but rather is primarily focused on using the neutrons produced by the reactor [1].

Neutrons have proven to be extremely valuable. Almost every field of science has benefitted from their use in research [2]. They are used in commercial applications for production, testing, and treating of various products [3]. Additionally, research reactors are used for the manufacture of radioisotopes for both medicine and industry [1]. Section 1.1 discusses a number of different uses in more detail.

Because the purposes of research and power production reactors differ, the designs also differ. While power production reactors can operate in the gigawatt range, the power level of research reactors ranges from zero power, known as critical assemblies, to hundreds of megawatts [4]. The majority, however, are below 1 megawatt [5]. Additionally, while the majority of power reactors generally (and broadly) fall into a few categories, such as pressurized water reactors or boiling water reactors, research reactors vary widely in design and operation. Section 1.2 discusses how research reactors can be categorized and provides examples of common categories.

Other differences between power and research reactors include fuel, configuration, and operation. Research reactors often produce very high neutron fluxes, and to maintain such high fluxes, fuels for research reactors are typically enriched in ^{235}U much higher than fuels for power reactors. Typical enrichments are just below 20% (in order to stay within the low enriched uranium (LEU) threshold), though a very few reactors continue to make use of high enriched uranium (HEU) with enrichment levels of almost 94% [1, 4]. Efforts are underway to convert these reactors to using LEU [1]. Section 3.3 discusses these efforts. Besides fuel enrichment, fuel configuration differs within research reactors and can be found, for example, as rods, plates, or dissolved salts. Both research reactors and power reactors utilize moderators such as water, heavy water, and graphite, and require cooling [1]. Also, like power reactors, some research reactors use reflectors to reduce neutron losses [4]. However, unlike power reactors, research reactors are often located in large, open pools of water where natural circulation provides all of the needed cooling, and the pool itself provides sufficient reflection and shielding that operators can safely walk around and over the pool. Finally, while power reactors generally operate best as baseload providers (with little change in power level during operation), many research reactors

are designed to operate in a pulsed mode, rapidly rising from zero or low power to extremely high power and then returning to low power in fractions of a second [4].

Where a power reactor might use a number of tons of fuel, research reactors may only require on the order of kilograms of fuel. They operate at lower temperatures (typically below 100°C) and frequently under atmospheric pressure, but their power density can be significantly higher (perhaps 17 kW/cc) than is found in power reactors (about 5 kW/cc) [1].

In September 2015, the International Atomic Energy Agency showed 247 active research reactors with 6 under construction, and 12 planned. These reactors were in 56 countries throughout the world [5]. Over 70% of these reactors are more than 30 years old, and 50% are over 40 years old [4]. For many of these reactors, financial support from governments is declining and the need for security and maintenance is raising operational costs. As such there is a great deal of interest in generating income with these reactors through engagement with private sector customers [3]. The following section discusses some of the ways in which research reactors can be used.

1.1   Uses of Research Reactors

A wide variety of fields have found uses for the products, frequently neutrons, that research reactors provide. These uses can be categorized broadly as investigating matter and changing matter. The following two sections cover each of these categories.

Depending on the details of the specific research reactor, experiments (or other uses) are typically performed by exposing some material to the radiation (neutrons, gamma rays, etc.) for some application. This exposure can be accomplished through access ports that reach within the core or by "channeling" the radiation down beam tubes to the intended target [2].

1.1.1   Investigating Matter with Research Reactors

The first broad category of activities that are commonly performed with research reactors is investigating matter. Neutrons have relatively short wavelengths, are electrically neutral, carry a magnetic spin, and are relatively massive. Each of these properties proves beneficial in certain investigative activities. Research reactor neutrons are used in neutron scattering, neutron radiography, and neutron activation analysis.

Neutron scattering describes a number of different techniques used to characterize materials. Among these are small angle scattering, reflectometry, triple-axis spectrometry, time-of-flight scattering, backscattering, and spin echo [6]. In each technique, the material being investigated is subjected to a beam of neutrons. The interaction of the beam with the material is measured and converted into information about the characteristics of the material. "Neutron scattering is an important tool in experiments dealing with superconductors, polymers, metals, and proteins.

Researchers can analyze molecular structure, surfaces and interfaces, measure electronic and magnetic properties, stress and strain conditions, and gauge other characteristics" [2].

Neutron radiography, often used generically to describe all neutron based imaging procedures, is comparable to medical x-rays in concept. An object is subject to a beam of neutrons. Some sort of recording material (film or otherwise) placed behind the object responds to the neutrons (or some other energetic source that is generated by the neutrons) and an image of the interior of the object is obtained. Neutrons are relatively heavy and have higher penetrating power than x-rays. They also interact more with lighter elements than x-rays. Figure 1 shows a plant imaged through neutron radiography. When used together x-rays and neutrons can develop a more complete image of the interior of objects [4]. These techniques are used in manufacturing for non-destructive inspection of internal components such as glues and welded or brazed joints.

A third way in which neutrons are used falls into both categories of investigating matter and changing matter, but is grouped with investigating matter because characterizing the material, not changing it, is the goal. This technique is referred to as neutron activation analysis. Its objective is to detect small amounts of specific materials. This is accomplished by subjecting a sample to a large number of neutrons and then watching for decay products that indicate the presence of the sought-after material. If the material is present, it will absorb neutrons and enter into an unstable state, a process called activation. From that unstable state, it will decay releasing characteristic radiation that will enable the material's identification. This process can be used to identify the presence of minute quantities of pollutants, toxins, or special nuclear material [2].

1.1.2 Changing Matter with Research Reactors
In addition to investigating matter, neutrons from research reactors are used to change matter. The changes that neutrons induce vary widely. In the case of materials research, sometimes the
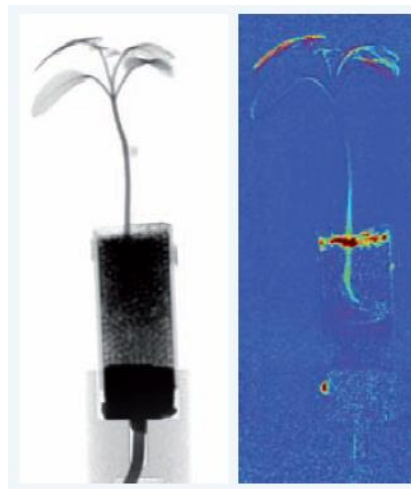
Figure 1 A plant imaged through neutron radiography [4]

only purpose of the change is to observe how materials change when exposed to neutrons. In other cases, the change actually increases the value of the material, including gem stone coloration, medical isotope production, and semiconductor doping.

Materials testing reactors are used, among other things, to help determine how exposure to intense or long term radiation affects materials. Most of the nuclear reactors in the world were built decades ago. Many have since extended their operating licenses. The structural materials within these reactors have been exposed to high levels of radiation for long periods of time. Confidence in the continued safe operation of these reactors requires understanding of how the structural materials within the reactor have changed because of exposure to radiation [1]. Similar questions about new materials proposed for use in nuclear environments are answered in materials testing reactors and are relevant to operation and licensing of reactors [2].

A more commercial application of research reactors is in the coloration of gem stones. The value of stone can be increased up to 30 times by inducing specific colors through exposure to radiation. This increase in value can make the process profitable for research reactors. The process, however, is not simple, and the details involved are not generally shared by those who have mastered the practice. A few known details include the necessity of fast neutrons and control of the temperature during the process. Additionally, it is not exclusively neutrons that lead to the color change, but a combination of neutrons, photons and electrons [3].

While also very commercial, but perhaps more in line with the higher ideals of humanity, research reactors participate in a wide range of medical activities. These include production of radio-isotopes such as yttrium-90 microspheres which are used to treat liver cancer, technetium-99m which is the most common medical diagnostic radio-isotope, and many other radio isotopes used for both diagnostics and therapies [1, 2, 3]. Over 10,000 hospitals use radio isotopes, with over 70,000 procedures per day, utilizing more than 200 radio-isotopes [4]. Related, but slightly separate, cobalt-60 is also used in both the medical and food industry for sterilizing equipment and certain packaged foods [4].

The electronics industry and radiation detection industry also make use of research reactors. By placing a single-crystal silicon ingot inside a reactor reflector vessel, a small portion of the silicon is transmuted into phosphorus, effectively doping the semi-conductor [2]. Finally, radiation detectors and other instruments can be developed, tested, calibrated, and qualified with the aid of research reactors [4].

1.2 Categorization

Like power reactors, research reactors lend themselves to a number of different categorization schemes. They can be categorized by their power level (zero power, sub kilowatt, kilowatt, megawatt, etc.), neutron spectrum (thermal, epithermal, fast), moderator and coolant type (water, heavy water, polyethylene, graphite, gas), fuel type (rod, plate, salts, LEU, HEU, plutonium,

etc.), physical configuration (critical assembly, pool, tank), specific use (materials testing, isotope production, training, etc.), origin, manufacturer, location, etc. [1, 2, 7].

A wide variety of fuel types and configurations is currently in use in research reactors. Three notable types of reactors are Training, Research, Isotopes, General Atomic (TRIGA) Reactors, Aqueous Homogenous Reactors, and Pool Type Reactors. Each of these is discussed in the following sections.

1.2.1   TRIGA Reactors

TRIGA reactors are very common with approximately 35 currently in operation. This makes them the most common non-power reactor in world. TRIGA reactors are popular largely because of the inherent safety in the fuel they use: Uranium Zirconium Hydride [7]. This fuel has a very large negative temperature coefficient of reactivity, which means that as the temperature increases, the likelihood of fission taking place within the fuel decreases. This enables the reactors to be pulsed to powers as high as 25 GW without any adverse effects [4].

The fuel comes in cylindrical rods, about 36 mm in diameter with aluminum cladding [1]. The UZrH is chemically stable, and can retain 99% of fission products at 650°C without any cladding. It can be safely quenched in water at temperatures as high as 1200°C [7].

1.2.2   Aqueous Homogenous Reactors

Aqueous homogenous reactors (AHR) consist of a fuel solution in the form of uranium salts dissolved into light or heavy water held within a vessel. By mixing the fuel directly with the moderator, a relatively homogenous distribution of fissile nuclear material and moderator can be achieved. This design was one of the earliest forms of nuclear reactors, first appearing under the direction of Enrico Fermi in May 1944 at Los Alamos [9]. While they were popular in the early days of nuclear reactors, there are few in current operation [1]. There have, however, been some efforts to argue for a return to popularity due to their expected superiority in medical isotope production [8].

AHRs offer a number of advantages over other reactor designs. They require very little fuel to reach criticality. They have inherent passive safety in the form of a large negative coefficient of reactivity due to a large negative density coefficient from both the thermal expansion of the solution and the creation of gas bubbles from radiolysis in the solution. They operate at around 80°C and at slightly below atmospheric pressure providing thermodynamic stability and allowing for versatile reactor vessel geometry and designs. All of these features make them relatively inexpensive to produce and to operate [8].

While AHRs offer a number of advantages over other research reactors, especially for the production of medical isotopes, they are not without their drawbacks. The primary drawbacks is

that the fuel solution with fission products mixed in tends to corrode the exposed metal components of the reactor vessel [8].

1.2.3   Pool Type and Tank Reactors

While there are numerous other categories of reactors, the final forms discussed here are pool type and tank reactors. These are combined because of the overlap in categories—there are tank-in-pool reactors. Pool type reactors represent a large category made up of reactors where fuel elements positioned within a pool of water compose a core [1]. The fuel elements may be aluminum clad plates or cylindrical rods held within an open container including open channels for experiments and control rods. Moderation is provided by the water and cooling is provided by the natural circulation in the pool. Since the pools are open, the "cooling system" is under atmospheric pressure [4]. The water in the pool is typically 20 to 30 feet deep and provides all the shielding required. These features make the reactor components easily accessible with ports and beam tubes in the sides of the pool [2].

At higher power levels, it is common to use forced convection rather than natural circulation to cool the reactors. Controlling the coolant flow is easier when the fuel element clusters are enclosed within a tank or pressure vessel. For this reason, tank-in-pool reactors are sometimes used. Additionally, higher power reactors often add concrete shielding to the shielding provided by the pool water. Not all tank type research reactors are held within pools [2].

Chapter 2   The High Flux Isotope Reactor

The High Flux Isotope Reactor (HFIR), located at the Oak Ridge National Laboratory (ORNL), in Oak Ridge, Tennessee is one of the world's most powerful research reactors, offering one of the highest thermal neutron fluxes. Of the various kinds of research reactors described in section 1.2, HFIR most closely aligns with the tank-in-pool type. It is composed of a core of highly enriched uranium (HEU) fuel plates within a pressure vessel that sits in a pool of water. The purpose of this chapter is to provide technical details, the history, and the current operating characteristics of HFIR. This section also discusses the Global Threat Reduction Initiative (GTRI), its predecessors, and how they have been driving US research reactors towards conversion from HEU to low enriched uranium (LEU) fuel.

2.1   HFIR Technical Specifications

HFIR is a light-water cooled and moderated research reactor. It fits the tank-in-pool category description of containing a core of fuel elements in a pressure vessel held within a pool of water. It is also described as a flux-trap type reactor for reasons described below. It utilizes a beryllium reflector, and currently uses HEU plate fuel [10]. Figure 2 shows a cut-away view of the reactor in the pool [11].

The core of the reactor consists of 2 concentric annular fuel elements measuring approximately 2 ft [0.61 m] tall. The inner element is composed of 171 fuel plates; the outer element is composed
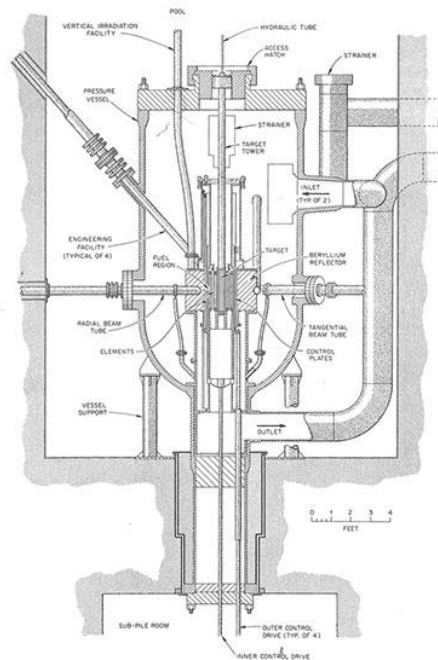
Figure 2 Cut-away view of the HFIR in the pool [11]
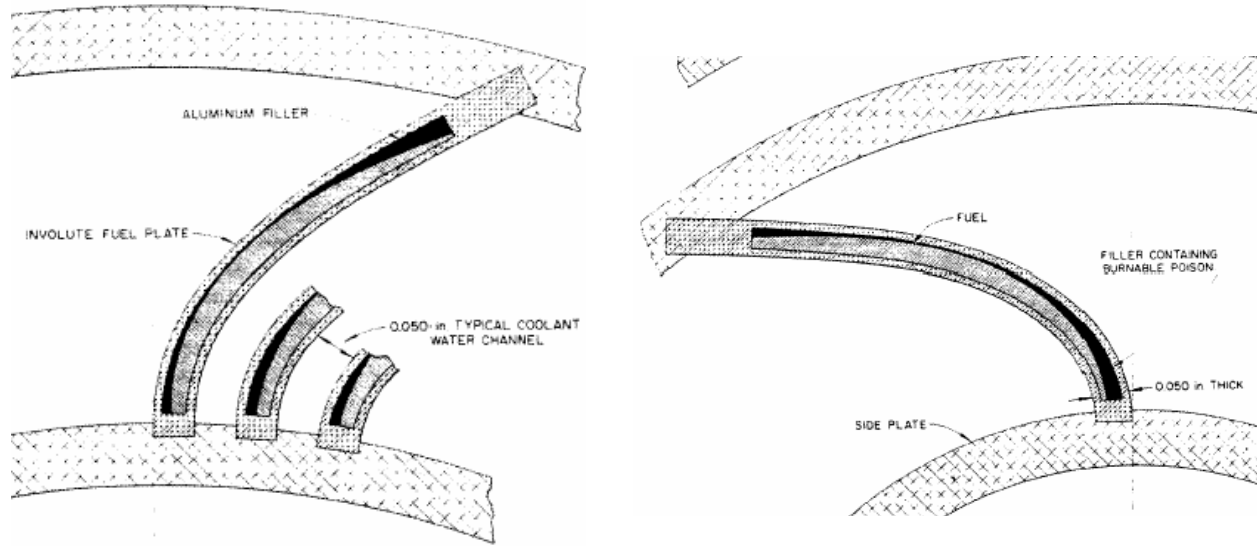
Figure 3 Arrangement of fuel plates within the outer (left) and inner (right) fuel elements [13]

of 369 fuel plates [12]. Each plate is 0.050 in [1.27 mm] thick, shaped in an involute and positioned within 2 concentric aluminum cylinders such that a constant gap of 0.050 in [1.27 mm] is maintained between the surfaces of adjacent plates to allow coolant to flow [13]. Figure 3 shows the arrangement of these plates within the cylinders. Figure 4 provides the dimensions and configuration of the fuel elements.

This arrangement of fuel is the source of the term "flux-trap". The open "hole" in the center of the core, 5 in [12.7 cm] in diameter, provides a space where neutrons that leak from the fuel can be moderated by the water present and are "trapped" [12]. This trap provides space for irradiating materials at fluxes on the order of 2.5×10^{15} neutrons/m^2 [13]. This represents the highest flux of neutrons in any research reactor in the US and among the highest in the world. Figure 5 provides a typical flux profile across the core at various times in the cycle.

Figure 6 is a photograph looking down at the top of the fuel elements and shows the target bundle, consisting of 37 experimental stations, used to hold targets for irradiation within the flux-trap. Typically isotopes such as curium-244 and other transuranic isotopes are placed within the target bundle [12].

The fuel plates are composed of U_3O_8-Al cermet and clad in aluminum 6061 [12]. The uranium is enriched to 93.75%. The fuel is distributed in the plate non-uniformly to help reduce the peak-to-average power radially across the core. Each inner element plate contains 15.18 g ± 1% ^{235}U as well as 2.8 g of a burnable poison (^{10}B), for a total inner fuel element loading of 2.60 kg ^{235}U.

8
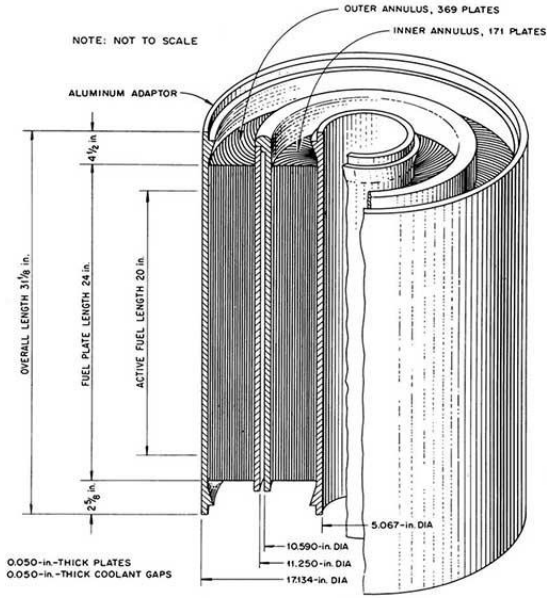
Figure 4 Fuel element dimensions and configuration [14]
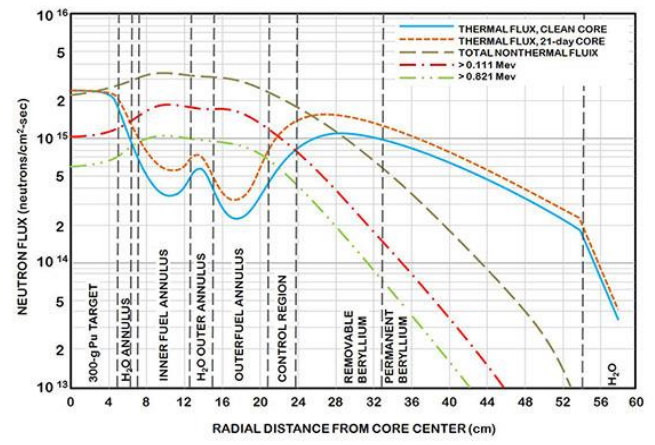
Figure 5 Flux profile across the core and reflector at various stages in the cycle [12]

Each outer plate contains 18.44 g ± 1% ^{235}U and no burnable poisons, for a total outer fuel element loading of 6.83 kg ^{235}U [13]. More details about the plate fuel are provided in Chapter 3.

The reactor is controlled by curved control plates that surround the outer fuel element. Just outside of the control plates is a beryllium reflector composed of 3 distinct regions. One portion can be removed, another portion is considered semi-permanent, and the third portion is permanent. Figure 7 is a photograph of the removable portion of the reflector [13]. The reflector is approximately 1 ft [30 cm] thick [12]. It has numerous access ports where experiments can be placed, and through which radiation is channeled to other experimental stations. Figure 9 shows the fuel elements and reflector with the various test stations and beam tubes labeled.

Surrounding the reflector is pressurized water held within an 8 ft [2.44 m] diameter pressure vessel. The vessel sits 17 ft [5.18 m] below the surface of a pool of water. This amount of water essentially acts as an infinite reflector for the neutrons [12]. Water enters the pressure vessel from the side and exits through the bottom at a rate of 16,500 gallons per minute [14]. Figure 8 shows how the flow is divided within the pressure vessel.

2.2 HFIR History

HFIR was originally conceived of in the late 1950's as the need for transuranic isotopes grew. Authorized in 1959, with construction beginning in 1961, it was completed and reached criticality in 1965. That year and the following year saw a program of tests at 20, 50, 70, and 90

Figure 6 Top of the inner and outer fuel elements as well as the target bundle [13]
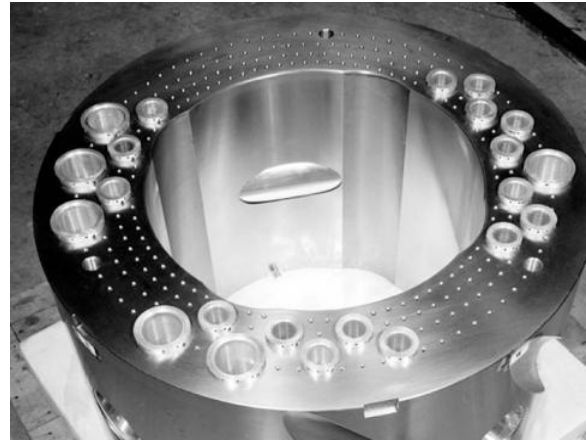
Figure 7 Removable portion of the beryllium reflector [3]

MW before HFIR finally reached full power of 100 MW in September of 1966. The total cost for construction, including the cooling tower, was $14.7 Million (about $112M in 2017 dollars) and its first year operating budget was $2.3 million. It ran from then until late 1986 with little interruption to normal operation, a record for US reactors [15].

In November of 1986 HFIR was shut down following an effort to review ORNL reactors amid safety concerns [14]. This review was partly in response to the incidents at Three Mile Island and Chernobyl and growing public concern about nuclear reactors [15]. A primary concern was embrittlement of the reactor vessel [14]. In the following months the requirements to get HFIR operational again were identified and a plan was developed to meet those requirements. In following with that plan, the reactor was restarted in January 1990 and has had continual operation since [15].

HFIR has had an illustrious career and has participated in numerous ground breaking research projects as well as notable non-research related activities. Included among these widely varied activities are participation in the investigation into who killed John F. Kennedy, and more recently the production of the Berkelium used for the first ever synthesis of Tennessine, element 117 [17]. HFIR is the world's largest manufacturer of elements heavier than plutonium [16]. In 2014, HFIR was named a National Nuclear Landmark by the American Nuclear Society, joining the Graphite Reactor, Tower Shielding Reactor, Oak Ridge Electron Linear Accelerator, the Molten Salt Reactor, and the Radiochemical Processing Plant [17].

2.3 Present Day Operating Characteristics

While designed to run at 100 MW with an operating pressure of 1000 psi [6.88 MPa] in the tank, today HFIR runs at 85 MW at 482.7 psi [3.33 MPa]. The decision to downgrade power and
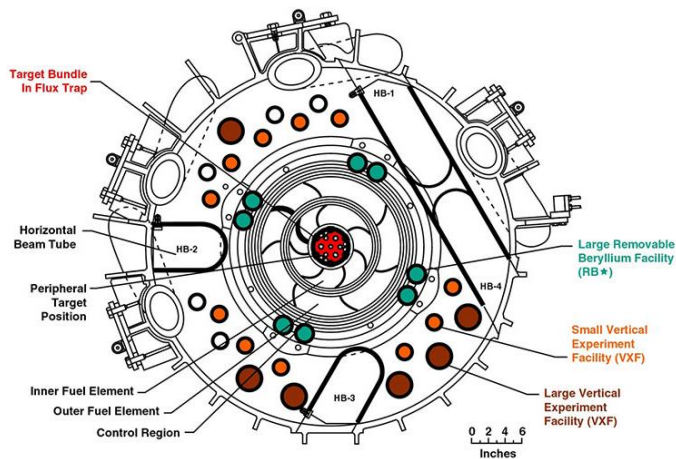
Figure 9 Top view of the fuel elements and reflector showing the experimental facilities and beam tubes [11]
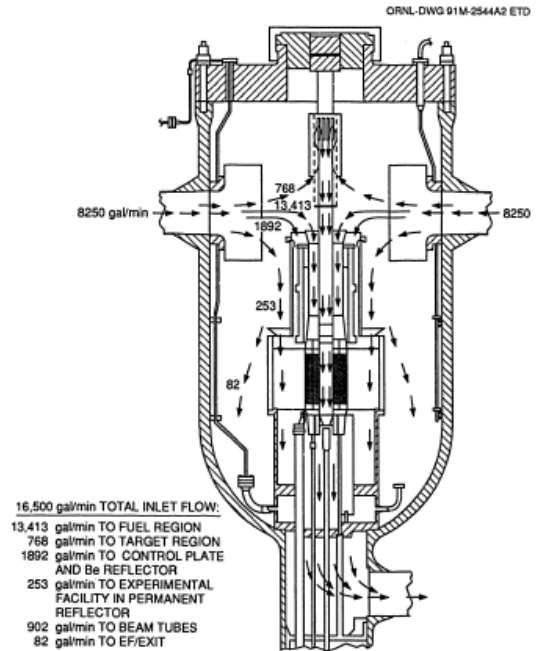
Figure 8 Cut-away of the pressure vessel detailing the flow path of the coolant [14]

pressure came as a result of the safety reviews of the late 1980's and pressure vessel integrity reduction due to neutron embrittlement [14].

In any given year, hundreds of researchers (423 in 2014) make use of HFIR for the study of physics, chemistry, material science, engineering and biology [16]. Additionally, HFIR produces isotopes for medical, industrial and research use [10]. A number of upgrades in the past several years have increased HFIR's utility including state-of-the-art neutron scattering instruments [18].

In its current operations profile, HFIR has a typical fuel cycle of 21 to 23 days. The actual duration depends on the experiments and targets in the reactor during a given cycle [12]. The contributions to heat generation and reactivity of the experiments and targets must be determined prior to the start of a new cycle to ensure safe operation. In earlier years of operation, these determinations were made by experiment and through expert opinion. More recently, MCNP has been used, allowing for more accurate predictions of the behavior of the reactor [13]. Experiments are typically only loaded and unloaded during the outage for refueling. Most maintenance activities are performed during these outages as well [12].

The reactor power level is controlled by a number of control plates which comprise two thin cylinders situated between the outer fuel element and the reflector. Their various positions during operation are show in Figure 10. As can be seen in the figure, the inner and outer cylinders of

control plates move in opposite directions. The inner cylinder is used for power regulation, but does not have a designated safety function. The outer cylinder consists of 4 plates which are used for both power regulation and safety. Any one of those plates has the ability to shut down the reactor [12].

85 MW of power are produced primarily in the fuel elements, but, as can be seen in Table 1, a portion also comes from other components of the reactor [14]. In order to remove that energy, approximately 16,500 gallons per min (gpm) of water flows into the reactor vessel through two 16-in [40.64 cm] diameter pipes. Of that flow, approximately 13,000 gpm passes through the fuel region. While passing through the pressure vessel, the flow experiences a drop in pressure of about 110 psi [7.58 x 10^5 Pa] and an increase in temperature of about 36°F [20°C] [12]. As mentioned above the fuel elements start with a gap of about 0.050 in [1.27 mm] between each plate through which the cooling water can flow. However, as the cycle proceeds, oxide begins to accumulate on the surface of the plates, the plates deflect due to thermal expansion, irradiation, and fluid-structure interactions, and by the end of cycle, the gap may be reduced to as little as 0.035 in [0.889 mm] [14].

2.4 Change to LEU

In the early 2000's, it was determined that HFIR would run until at least 2035. With that decision and the motivation to maximize the usage of the reactor, the past decade has seen a number of upgrades both in facilities and in analysis methods [13, 18].

One of the most significant challenges that HFIR currently faces is converting to a low enriched uranium (LEU) fuel. This effort at HFIR is part of a larger, long term effort by the US government in coordination with many other national governments to reduce the amount of HEU
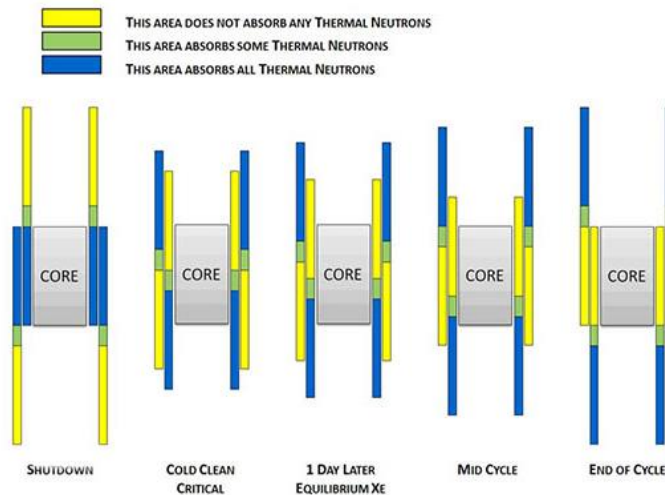
Figure 10 Control plate positions based on location in fuel cycle [12]

Table 1 HFIR core heat loads at nominal 85-MW power level [14]

Region	Heat Load (MW)
Fuel	80.7
Target	0.888
Control cylinders	1.71
Removable beryllium reflector	0.327
Semi-permanent beryllium reflector	1.21
Permanent beryllium reflector	1.08
Total	85.9

used in research reactors throughout the world. This section provides a brief history on this effort.

The Atoms for Peace project, started in 1953, was an effort to assist countries in developing peaceful use of atomic energy [19]. Part of that effort saw widespread distribution of research reactors. Initially these reactors were fueled only with LEU, but by the mid 1960's new, more powerful research reactors as well as upgraded existing reactors required higher levels of enrichment. It was not long until a large portion of research reactors around the world used HEU.

Following the unexpected nuclear detonation in India in 1974 and accompanied by the growing threat of international terrorism, the proliferation of HEU that could be diverted to weapons usage began to be seen as a serious problem. A 1977 review, the International Nuclear Fuel Cycle Evaluation, while primarily focused on plutonium proliferation, recommended the curtailment of HEU usage in research reactors [20]. These circumstances led to the development of the Reduced Enrichment for Research and Test Reactors (RERTR) program in 1978 [21].

The US began converting reactors to LEU in the early 1980's, though that initial effort has been described as lukewarm [20]. The benefit of converting domestic reactors to LEU was seen as only marginal—the threat of domestic terrorism was small. Proponents of RERTR argued that the US leading the way would motivate other countries that were less secure to convert to LEU. However, this argument did not persuade leaders in the US to take greater action.

Adding to the slow implementation of the program, responsibility for RERTR was disputed, and different agencies had different approaches. In 1986 the Nuclear Regulatory Commission (NRC) instituted a policy requiring all of the reactors it oversaw to convert to LEU where technically feasible; the Department of Energy (DOE), however, did not follow suit. In 1988, following a DOE statement that the majority of the research efforts required to convert to LEU were accomplished, responsibility for RERTR was given to the Arms Control and Disarmament Agency (ACDA). Because of budgetary problems, ACDA determined to phase out RERTR in

1991, and DOE decided to again take responsibility for the program. Besides the political issues with RERTR, military use of HEU had a negative impact on HEU usage reduction [20].

The discovery of Iraq's nuclear weapon program spurred RERTR efforts both domestically and internationally, and despite domestic issues, the progress of RERTR and international efforts continued [21]. In 1993 the US and Russia agreed to work together towards the development of LEU fuel for high power research reactors.

Through most of the 1990's, progress was halting. Steps forward, such as conversion of a number of reactors to LEU would be countered with steps backward, such as plans to convert weapon-material production reactors to HEU fuels [22]. With the terrorist attacks in 2001, a new emphasis was placed on RERTR efforts [23]. In 2002 the RERTR put out a goal to convert all reactors to LEU by 2012. But, 2004 failures of high density fuels required to support LEU conversion in both Russia and France made that goal unlikely. That same year, the Global Threat Reduction Initiative (GTRI) was formed with the purpose of consolidating the HEU reduction programs under a single entity [20].

In 2005 the US agreed with Canada and Mexico to convert all civilian reactors by 2011 with the formation of the Security and Prosperity Partnership of North America. This agreement, however, had the caveat of applying only to those reactors for which LEU would work [24].

Today there are still 5 research reactors in the United States that use HEU [25]. The past decade has seen a great deal of effort put into LEU fuel development for the remaining HEU reactors, though a forecast of when the conversions will be complete has been elusive. Through a series of international and programmatic obligations, the US is still committed to converting the 5 remaining reactors to LEU. This research effort on hotspot modeling represents one part in that endeavor.

Chapter 3   Plate Fuel

This chapter examines research reactor plate fuel in general, discusses the details of manufacturing HFIR fuel elements, and briefly discusses efforts to convert to LEU.

3.1   Introduction to Plate Fuel

While there are many different kinds of plate fuel, they all have a number of features in common. The typical arrangement is with the fissile material sandwiched between a top and bottom cover, typically made of aluminum. The common manufacturing technique is known as the "picture-frame technique". This consists of placing a fissile briquette within a "frame" of aluminum—an aluminum plate with a rectangular hole punched out of it. The fissile briquettes are manufactured using powder metallurgy techniques and are typically ceramic or metallic composites with aluminum powder as the matrix material [26]. Before the efforts of RERTR to replace HEU fuels with LEU, most fuel plates were manufactured with 18 wt% HEU [26]. The frame and briquette are placed between a top and bottom cover and the assembly is then hot and cold rolled to final dimensions [26]. Figure 11 shows a typical fuel plate post rolling.

After rolling the fuel plates are shaped to fit within the structural components of a fuel element. Figure 12 shows a number of different fuel element configurations. The HFIR fuel elements are most similar to the ring-shaped category of those shown in Figure 12. The plates within the cylindrical support structures are involute in shape.

3.2   HFIR Fuel Assembly

The fuel assembly used in the HFIR consists of an inner and an outer fuel element. Each element contains a number of fuel plates. The fuel plates contain a fuel meat section consisting of 40 wt% of triuranium octaoxide (U_3O_8) enriched to 93.75% [26]. The inner plates contain 15.18 g of ^{235}U
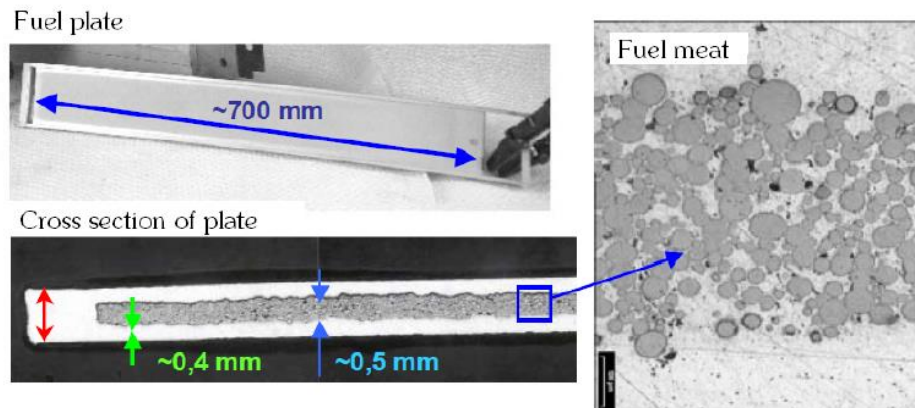
Figure 11 A typical fuel plate post rolling including a detail view of the fuel meat dispersions among the aluminum matrix [27]

15
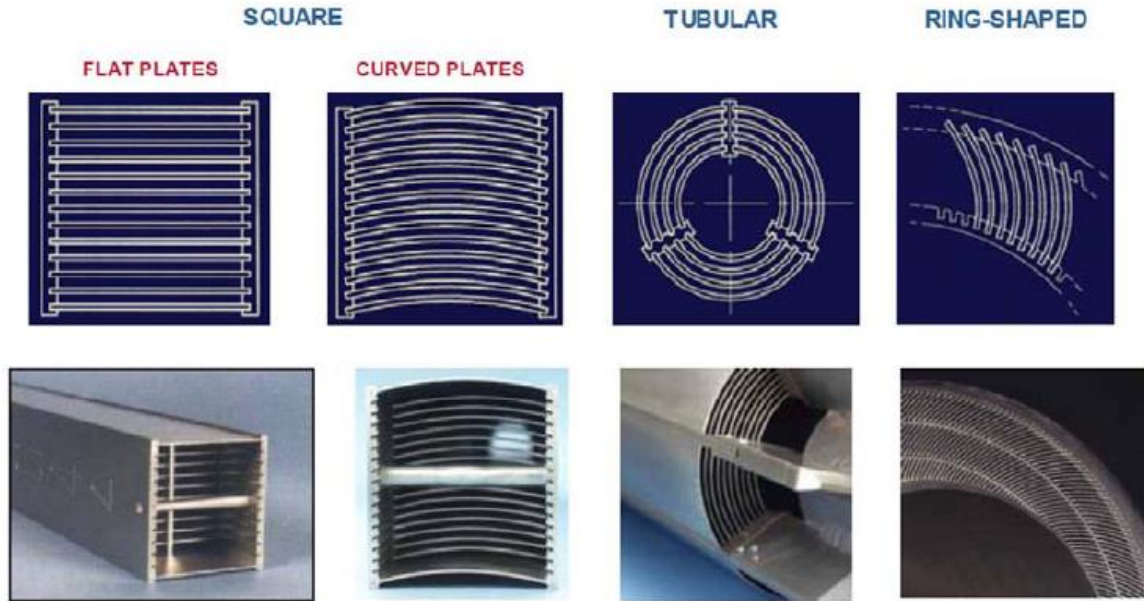
Figure 12 Different shaped fuel elements [27]

while the outer plates contain 18.44 g [28].

Fuel plates must meet tight dimensional and quality specifications to meet performance requirements and provide adequate margins of safety [28]. The manufacturing process conforms to these specifications and ensures that parts are handled appropriately to reduce quality rejections due to human error. Small pits and inclusions are a major source of rejections. A number of actions help reduce the overall rejection rate. For example, cotton gloves are worn by workers handling the fuel plates, work tables are covered with formica and cleaned frequently, or covered with mats that have rubber fingers to allow deburring chips to fall harmlessly between the rubber fingers [28].

The following three sections will cover the manufacture of fuel plates and fuel elements as well as inspections for the HFIR fuel assembly.

3.2.1 Plate Manufacture

This section discusses the process used to manufacture the fuel plates as described by [28]. Unless otherwise noted, all information comes from this reference.

The fabrication process, shown in Figure 13, consists of a series of steps involving different aspects of the plates. One series focuses on the preparation of the fuel meat. This process includes preparing the U_3O_8, aluminum and boron carbide (B_4C) powders, mixing them, and constructing the fuel meat.

Fuel Core Preparation | Fuel Plate Fabrication

B₄C Powder   Aluminum Powder   U₃O₈ Powder

Vacuum Anneal   Blend

Screen

Filter Section   Fuel Section

Weigh (Al, B₄C*)   Weigh (Al, U₃O₈)

Blend*   Blend

Contouring   Contouring

Press

Vacuum Anneal

Inspect

Q.C. Release

Aluminum Components

Frames   Covers

Inspect   Inspect

Shear   Shear

Cold Roll to Gage   Cold Roll to Gage

Shear Blanks   Inspect

Blank Cavities   Degrease

Degrease   Anneal

Anneal   Inspect

Inspect

*Inner Fuel Plates Only

Clean Frames and Covers

Etch Frames and Covers

Assemble

Weld

Hot Roll Bond

Degrease

Anneal

Inspect for Blisters

Cold Roll to Gage

Degrease

Final Anneal

Inspect for Blisters

Inspect - Hump Orientation

Fluoroscope - Punch

Blank Plates

Deburr

Machine Radius

Inspect

—— Fluoroscope/Radiograph

—— X-Ray Scan

—— Ultrasonic

—— Alpha Count

—— Dimensional and Surface

Section
—— Cladding Thickness

Q.C. Release —— Core Thickness

Form (Involute) —— Bond

Inspect —— Boron Analysis

—— Surface

—— Contour

Figure 13 Plate fuel manufacturing process

17

The aluminum powder is Alcoa-type 101 or equivalent. It is held in a vacuum furnace at 500°C ± 10°C to remove any moisture within the powder. The temperature must be controlled tightly to ensure that it is high enough for the powder to be sufficiently dehydrated, but low enough to prevent the aluminum powder from sintering. The aluminum powder is then stored in a low pressure environment to maintain the low moisture content.

The U_3O_8 is supplied by ORNL. Special care is taken in the issuing, handling, and usage of the U_3O_8 to ensure precise accountability is maintained. The U_3O_8 and aluminum are weighed out to appropriate proportions for the fuel meat and blended. For the inner fuel plates, boron carbide, with particle sizes smaller than 4 µg, is also blended with the aluminum and U_3O_8.

This fuel meat powder blend is then poured into a die which has a profile to provide the right shape for the fuel meat section of the fuel compact. Care is taken to contour the powder blend to match the die without compacting or leaving tool marks in the powder. The profiles for inner and outer plates are shown in Figure 14 [29]. The radial fuel curvature helps flatten the flux profile in the reactor. Another die, with a bottom surface that complements the first die is placed on top of the first die. Filler material, aluminum powder, is added on top of the meat powder to fill in the top die, creating a uniform thickness fuel briquette.

The filler powder is then leveled, again ensuring no tool marks or compaction. The powder is then pressed within the dies at 2600 psi to form a solid compact. This process is unique in that it produces a curved interface between the fuel section and the filler in a single cold pressing process. The compacts are vacuumed and annealed to remove moisture and entrapped lubricant from the press.

The solid aluminum components of the fuel plates go through a number of steps prior to assembly. The aluminum 6061 sheet is supplied to the manufacturing facility in a slightly thicker grade than is required and is cold rolled upon arrival. This is done to ensure better control over the thickness of the material than is available from the manufacturer. Cleaning, heat treating, and inspection are used throughout the manufacturing process to ensure required material properties and acceptable surface characteristics. After being cold rolled, 2 blanks are sheared from the frame plate to accommodate 2 fuel compacts. Aluminum components are cleaned, etched, rinsed, soaked in nitric acid, rinsed again (etching and nitric acid are repeated if necessary), rinsed with hot water, and swung to dry.

Fuel plates are assembled with a bottom cover and top cover sandwiching the frame with fuel compacts inserted into the opening between them. The frame provides the required dimensional control to the fuel compacts as the plates are rolled to the final dimensions. Additionally, the frame provides material for the top and bottom cover to seal the fuel within aluminum. The edges of the assembly are welded except along the corners to allow venting during the rolling process.
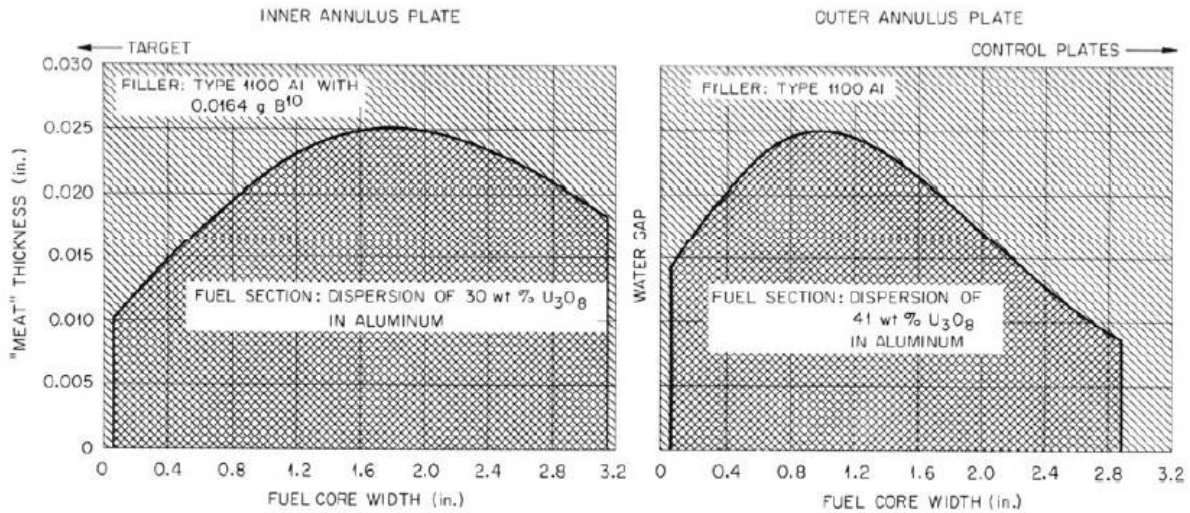
Figure 14 Profiles of inner and outer fuel plate fuel sections [29]

The welded plates are rolled to bond together and to achieve the required final dimension. Prior to rolling, the assemblies are preheated to 482°C. If this temperature is not attained, non-bonds will form. If it is exceeded, less stable control of fuel width will result. 11 hot rolling passes are required to reach a thickness of 0.0635 – 0.064 inches. The plates are annealed after hot rolling, and are then subject to 28 cold roll passes. The final thickness achieved is 0.0505 inches.

At this thickness, the plates are relatively delicate and special handling is required to prevent damage from occurring. Following the rolling procedures, the plates are washed, annealed and flattened. Individual plates are cut from the larger two- plate assembly and machined to shape. Those plates that pass a series of inspections (detailed in section 3.2.3) are formed to the final involute shape, ensuring that the fuel side (as opposed to the filler side) is on the correct side of the involute.

3.2.2   Element Manufacture

Once the fuel plates are complete, the fuel element can be assembled. Both the inner and outer fuel elements consist of an inner and outer side plate. The term "plate" used here can be confusing, because, as an assembly, the plate is actually a cylinder [30]. Possibly, the use of the term "plate" arose from reduced-dimension analysis where the small segment of the cylinder in a single coolant channel was modeled as a plate. Another possibility is that the term is a carry-over from design and analysis of earlier reactors.

A basic description of the assembly is that the completed fuel plates are inserted into slots in the side plates and welded in place. End adapters are attached to each end of the assembly as support and to help position the assembly in the reactor [30]. The details of this process follow, and, as with the fuel plates, unless otherwise noted, this description comes from [28].

The inner and outer side plates are received as extruded 6061 aluminum tubing. They are machined to the correct size, and slots for the fuel plates and weld grooves are added. Following each of the steps in the machining process, the side plates are cleaned and inspected. Once the machining is completed on the side plates, they are ready to receive the fuel plates. Each plate is slid into corresponding slots in the inner and outer side wall. Plates that do not fit easily into the machined slots are discarded. Because the dimensional requirements are so strict, special care is used during assembly. To help in this process, isopropyl alcohol is used as a lubricant. Teflon spacers are placed between the fuel plates as the elements are assembled to help stabilize them and to keep them in place during welding. The plates are welded in place by metal inert gas welding. The alcohol draws water from the air, so after assembly, the fuel elements are baked in a modified pizza oven to ensure no residual moisture is retained. The majority of the element manufacturing process is conducted in a room maintained at 20°C.

3.2.3 Inspections

Unlike other research reactors, the HFIR core assembly only consists of two fuel elements. Within those elements, however, are a relatively large number of fuel plates [28]. Because of this arrangement, extreme care is taken throughout the manufacturing process to ensure that unacceptable components are identified and rejected. Rejection of a completed assembly represents the loss of a substantial investment. To help ensure this does not happen, inspections are conducted frequently throughout the manufacturing process. With only a few exceptions, when components are found to fall outside of the specifications, they are rejected. Repairs are occasionally permitted, but in most cases, attempts to repair components risk making things worse. The manufacturing techniques described above were selected primarily for reliability [28].

The fuel plates go through a number of inspections throughout the production process. The fuel meat compacts are inspected for dimensional accuracy and weight [28]. Upon receipt and after most of the operations, aluminum fuel plate components are inspected for cleanliness and surface contamination, inclusions, and blisters. Dimensional inspections are performed to ensure each step achieves its purpose, but even with all of the dimensional inspections, the formed plates are trial fit within fuel elements because "… the involute inspection does not measure the shape of the plate edges" [28].

In addition to dimensional and surface inspections, fuel plates are subject to nondestructive internal inspections prior to being formed into the final involute shape. The process used for producing the plates "…results in small random variations in local fuel density throughout each fuel plate. This in turn causes local deviations from the nominal core thermal hydraulic conditions such as subchannel coolant temperature and local heat flux" [30]. X-ray transmission is used to establish that acceptable fuel homogeneity exists within the fuel meat. Ultrasonic inspections are performed to identify the presence of non-bonds. Alpha count inspections ensure

that no uranium has migrated (due to excess heat in production or from contamination) to the surface of the plate [28].

Two destructive inspections are performed. One plate of each set of plates that make up an element is subject to destructive inspection of cladding dimensions and bonding. A boron homogeneity inspection is also performed [28].

The rejection rate for the fuel plates was approximately 7% in 1999 [28]. No current, published data for fuel plate rejection rates was available. Approximately half of the fuel compact rejections are a result of thickness violations, though the causes of these violations are varied [28]. Plate rejections result from surface defects (often caused by the harder, jagged edges of the welds), bond defects (usually between the compact and the cover plate), fuel location issues (such as fuel in the ends of the plates where no fuel should be), homogeneity violations (which are evenly divided between average and local violations), and dimensional issues (most of which are violations of the involute shape) [28].

Fuel elements are inspected for dimensional violations. The primary violation is an out-of-roundness condition. Additional violations include thin-wall violations, concentricity, and miscellaneous dimensional rejections. These rejections are rare [28]. Additionally, coolant channel dimensions are inspected within the fuel elements. "The average coolant channel thickness for any individual cross section is specified at 0.050 in. (1.27 mm) $\pm$ 0.006 in. ($\pm$ 0.15 mm). Each individual or spot coolant channel measurement is specified at 0.050 in. (1.27 mm) $\pm$ 0.010 in. ($\pm$0.25 mm) when measured at any point." Violations in coolant channels represent one of the few violations that is easily corrected. By drawing an oversized Teflon coated wand through the channel, it can be deformed to an acceptable configuration. [28]

Drawings in [27] and specifications in [31] provide details required for performing the inspections mentioned in this report.

A report for each fuel element is prepared containing the following, "

1. certification statement
2. ^{235}U and ^{10}B fuel element loadings,
3. minimum and maximum cross section average channel thickness and minimum and maximum spot channel thickness for each coolant channel, overall average fuel element channel thickness,
4. inner and outer side-plate wall thicknesses at 30° increments around the circumference, inner and outer side plate minimum wall thickness and location,
5. measured values of fuel element dimensions 1, 21, 41, 42, 63, and 64 called for by drawing 8-7213 and 1,22, 43, 44, 63, and 64 called for by drawing 8-7214 …,
6. acceptance-rejection summary of pre- and post-weld circular weld-test specimens – visual inspection, metallographic attributes, and measured values of weld tensile strength,

7. inspection data for control fuel plates from fuel-plate lots represented in the fuel element:
   a. fuel core location
   b. ^{235}U surface contamination
   c. flat-plate dimensions
   d. flat-plate thickness,
8. involute data for fuel plate lots represented in the fuel element, and
9. summary of cladding thickness data and analytical results of boron samples (inner element only) from fuel plates sectioned to represent fuel-plate lots used in the fuel element." [28]

3.3   LEU Conversion Efforts

A great deal of effort has been made with the RERTR and related programs to convert all research reactors from HEU to LEU. A brief discussion of those efforts as they relate specifically to fuel plates follows, with focus on the HFIR.

As discussed in section 2.4, not long after research reactors became common, it also became common to use HEU to fuel those reactors. The efforts associated with RERTR required the development of LEU fuels that could provide the same performance as the HEU fuels. The first attempt was to increase the concentration of uranium and reduce the portion of aluminum in the fuel. A practical limit was achieved of 2.3 gU/cm^3 for UAlx-Al and 3.2 gU/cm^3 for U_3O_8-Al [26]. This limit was the result of the fragility and propensity for fuel segregation in these fuels at higher concentrations. While this limit was sufficient for some reactors, many others needed higher densities of uranium for a feasible LEU fuel. This requirement led to the development of other fuel options. Focus was turned to the use of intermetallics with higher concentrations of uranium, "…such as U_3Si, U_3SiAl and U_6Fe as fissile material in the form of dispersions in aluminum" [26]. These fuels show unacceptable dimensional instability under irradiation, and attention was turned to U_3Si_2-Al dispersions. This fuel was qualified by the USNRC in 1988 for use with up to 4.8 gU/cm^3 [27]. It is currently the most widely used fuel in research reactors [26].

A number of high performance reactors, including the HFIR, require uranium densities of 8-10 gU/cm^3. With a practical upper limit of 55% fuel to matrix volume ratio, the fuel would need to have a density of greater than 14.5 g/cm^3 [27]. Currently, there is no acceptable fuel that provides such high densities. Other fuels have been and continue to be studied "…including dispersions based on U-Mo, U_3SiCu, $U_3Si_{1.5}$, $U_3Si_{1.6}$, $U_{75}Ga_{15}Ge_{10}$, $U_{75}Ga_{10}Si_{15}$ and uranium nitrides" [26]. Manufacturing techniques besides power metallurgy are also being investigated, including "…hot isostatic compaction … or increasing the volume fraction of U_3Si_2 beyond 50% (the limit currently accepted for this technology is 45%) or using wires of U_3Si and/or $U_{75}Ga_{10}Si_{15}$ and/or $U_{75}Ga_{15}Ge_{10}$ metallurgically bonded with aluminum…." [26].

3.3.1 HFIR LEU Conversion

For the HFIR, the change to LEU involves numerous considerations besides thermal hydraulics, including neutronics, and changes in fuel element handling protocols, and operations—transportation and storage, regulations involving plutonium inventory at ORNL, the source and funding for LEU, etc. [29].

A primary constraint is for essentially the same performance from HFIR with any new fuel. As with other research reactors, in order to maintain the same level of performance with LEU fuel as currently experienced with HEU fuel, the number density of ^{235}U needs to be the same. To make this happen, the overall density of the fuel needs to be increased, or the ratio of fuel to matrix needs to be increased [27]. Additionally, limitations to the budget for conversion of HFIR essentially require that the configuration and construction of the reactor components—pressure vessel, reflector, etc.—remain unchanged. This means the dimensions of the fuel elements must not be changed. This requirement and that of a higher density fuel means that additional engineering effort will be necessary to ensure that the added mass of the fuel elements will not surpass the load bearing capability of the reactor or the spent fuel storage area [29].

Chapter 4   Heat Transfer through Non-bonds

The fuel plate manufacturing process can result in non-bonds and fuel segregation defects that are of concern for power limitations as a result of their effects on heat transfer. This section will address non-bonds. A non-bond is an area within the finished fuel plate where the cladding fails to bond to the fuel meat or where the filler and the fuel meat fail to bond. The lack of a complete bond results in poor heat transfer characteristics across the non-bond. This leads to a greater heat flux through and higher temperature at the surface of the fuel plate opposite from the non-bond.

This section will cover past efforts in determining the effects of non-bonds in HFIR fuel plates and contact conductance theory with its potential applicability to fuel plate non-bonds.

4.1   Previous Non-bond Analyses

Non-bonds were recognized as an important fuel defect in the early design stages of the HFIR. Since that time there have been a number of efforts to determine or estimate their influence on the thermal hydraulic performance of the HFIR. Each of the major efforts will be reviewed and discussed.

4.1.1   Hilvety and Chapman [32]

The first significant effort in estimating the effects of non-bonds on the thermal hydraulics of the HFIR were performed by Hilvety and Chapman in 1967. Their paper reports on an effort to capture the entire thermal analysis performed on HFIR. The resulting work, in their own description, had outgrown their original intentions, but functioned adequately.

Their focus was on limiting the conservatism in their calculations without eliminating it entirely [32]. As such, they sought to simulate all conditions detrimental to heat transfer as coincident and simultaneous and took the result to be the worst possible case. This practice led to modeling hotspots that resulted from both non-bonds and coincident fuel segregations, without performing an independent analysis of the non-bonds. The model, including the dimensions, material properties, and assumptions they used is shown in Figure 15.

The purpose of their analysis was to determine whether the thermal hydraulic conditions of the HFIR could support the proposed 100 MW power level. They determined that, as far as the hotspots were involved, the primary limiting phenomenon would be burn out, but also recognized that a lack of a good model for heated, very-narrow channel fluid flow with hotspot conditions made it difficult to determine at what heat flux burn out would occur. Instead, they opted to use incipient boiling as the limiting phenomenon and ran their analysis to identify at what power level incipient boiling would occur. They further argued that based on available data, burn out would likely occur at a flux and temperature very near incipient boiling, further justifying their selection of incipient boiling as the limiting phenomenon.

In addition to the assumptions already mentioned (coincident non-bond and fuel segregation, limiting condition of incipient boiling), they also assumed no mixing across the width of the coolant channel, no heat transfer between fuel and side plates, no heat transfer parallel to the fuel plate surface except in the immediate vicinity of the hot spot, and a maximum non-bond size limited by the inspection process and the drawings. While they did provide reasoning for most of the assumptions they made, and some explanation for most of the choices they made, the descriptions were at times incomplete [33]. These facts make it difficult for future investigators to exactly reproduce their results. Despite this drawback, their work did provide a great deal of material with which future analysis could begin.

While the fuel segregation receives attention in their analysis, the challenges associated with heat transfer through the non-bond are conservatively discarded by assuming the non-bond to be an adiabatic disk separating either cladding from fuel meat or filler from meat.

4.1.2 McClain [34]

Not long after Hilvety and Chapman finished their work, McClain was tasked with disassembling their multifaceted work and reassembling it in a more robust and streamlined analysis program. This effort was developed into a computer model and came to be known as the

Figure 15 Hotspot Model used by Hilvety and Chapman

25

HFIR steady state heat transfer code (SSHTC) and is still in use today. While McClain made changes in some areas, he left the analysis of hot spots (non-bonds and fuel segregations) largely as [32] had initially formulated it, including the decision to assume the non-bond is adiabatic.

4.1.3 Kirkpatrick [33]

As part of the HFIR shut down in the late 1980's, Kirkpatrick was tasked with reviewing the hotspot model within the SSHTC and ensuring that it continued to provide conservative estimates for HFIR running at an 85 MW power level. In order to do so, he reexamined the works of [32] and [34], and attempted to tease out the reasoning for some of the unexplained assumptions and actions. He was largely successful in doing so as attested to by his ability to reproduce most of the results from those earlier studies.

Kirkpatrick observed that non-bonds and fuel segregations are independent phenomena, and unlike previous studies, analyzed non-bonds and fuel segregations both separately and together. He also included radiative heat transfer in one calculation of the heat transfer across a non-bond. Estimating a surface emissivity of 0.05 (that of polished aluminum foil), he found that the contribution to heat transfer was sufficiently small to justify treating the non-bond as adiabatic. In his report, he states, without citing any reference, that "There is some evidence that the presence of a fuel segregation defect raises the probability of having a nonbonding defect", and then proceeds to analyze all scenarios with a non-bond coincident with a fuel segregation.

Kirkpatrick was also the first to mention having considered the influence of the mesh used during the calculations on the solution obtained. For a single case among the many he ran, he doubled the number of nodes in the radial direction and repeated the calculation. He states, "None of the fluxes in this test case changed by as much as 0.005 compared with the 71F case, which leads me to believe that the results of my calculations will not be sensitive to radial mesh spacing." He does not, however, explain whether the 0.005 is a ratio, as in 0.5% difference or if it is the difference in values. The fluxes for the 71F case were given as 1.26×10^6 BTU/h-ft^2 and 0.34×10^6 BTU/h-ft^2.

4.1.4 Giles [35]

[35]'s focus was on an analysis technique for fuel defects in the proposed fuel for the Advanced Neutron Source Reactor (ANSR), but was applicable to other plate fuels, as well. He used a new technique for analyzing fuel plates that yielded accurate results with reduced margins which were still conservative. The two main differences in his approach were first that he examined the actual (or estimated) conditions at various locations on the fuel plate. Previous studies had assumed a standard configuration (as seen in Figure 15) and varied the thickness of the combined filler and clad, "t" in the figure, to approximate the various locations while holding all other conditions constant. Secondly, he replaced individual aspects of the heat transfer calculation, such as the convective heat transfer coefficient, the power density, the conductivity of fuel meat,

filler, and clad, the oxide growth, etc. with calculated values for each location on the fuel plate, rather than values that were conservative for *any* location.

As far as the non-bond is concerned, he recognized that, "The heat transfer across a non-bond depends on many parameters, such as contact pressure and gas composition between the surfaces of the non-bond, fuel composition at the surfaces, hardness, yield strength, fuel swelling, local burnup, and surface emissivities." Like the others, he decided that because of a lack of information, he would treat the non-bond as adiabatic.

4.1.5   Bodey [36]

As part of his work on turbulent heat transfer within the HIFR fuel core coolant channels, [36] included an analysis of the hotspots. Unlike previous efforts, which all used the HEATING heat transfer analysis code, Bodey used COMSOL Multiphysics to perform his analysis. Additionally, like Kirkpatrick, Bodey analyzed both the non-bond and the fuel segregation separately before examining them together. Like the others, he treated the non-bond as an adiabatic disk.

4.2   Thermal Contact Conductance

Previous studies have assumed that no conduction takes place across a non-bond. The lack of a complete bond certainly reduces conduction, but if the two surfaces are in contact or the gap is filled with gas, conduction still takes place. In determining whether or not assuming an adiabatic disk is the best choice for heat transfer across the non-bond, approaching the opportunity from the perspective of thermal contact conductance (TCC) may provide the necessary information. Knowing the value of this approach is difficult as TCC depends on factors which are unknown for fuel plate non-bonds, such as contact pressure between the cladding and the fuel meat, surface roughness of the two surfaces, and mechanical properties of both the cladding and the fuel meat after manufacturing. A straightforward approach is to consider a reasonable range for each of these parameters and then determine the highest TCC given those parameters. If that TCC proves to be insignificant, then assumption of an adiabatic non-bond is further justified. However, if that TCC proves to be significant, then the results may provide justification for further examination of non-bonds to better quantify the parameters that were simply estimated in the first place. With this approach in mind, a brief review of the relevant aspects of TCC, following the monograph by Madhusudana [37], and how plate fuels fit within the existing TCC models is offered.

4.3   An introduction to TCC

TCC has been studied for many years in many different industries. Figure 16 lays out the various industries and applications that have motivated research in the field since the 1930s [38]. As shown in Figure 17, when heat is transferred across two adjoining, imperfect surfaces, there is a temperature drop [39]. This temperature drop can be accounted for in heat transfer calculations by the introduction of a contact resistance, *R*, given by

$$R = \frac{A\Delta T}{Q}$$

where A is the nominal cross-sectional area of the interface, Q is the heat flux, and ΔT is the temperature difference across the contact. Frequently, the reciprocal of contact resistance, contact conductance, is discussed.

$$h = \frac{1}{R} = \frac{Q}{A\Delta T}$$

This decrease in conduction is explained by the fact that, at a microscopic level, the actual contact area is only a limited portion of the nominal contact area between two adjacent surfaces. Figure 18 shows an example of how this is visualized [39]. Under these conditions heat transfer must take place by conduction through the limited, actual contact area, by conduction through any interstitial material (fluids or otherwise) in the gaps, and by radiation from the non-contacting surfaces. The limit imposed on heat transfer by the relatively small actual contact area is referred to as a constriction. The number of contact points and the total area of contact are functions of the roughness of the adjoining surfaces as well as the contact pressure between the surfaces. Additionally, these quantities depend on the mechanical properties of the materials. At a slightly larger scale than the microscopic constriction, there is a macroscopic constriction which results from the "waviness" of surfaces that are not perfectly flat. This waviness further reduces the actual contact area, relative to the apparent contact area, between the two surfaces.

4.3.1   Microscopic Constriction
Constriction resistance describes the increased temperature difference required to maintain the same heat transfer in a constriction as would take place without the presence of the constriction, and is given by
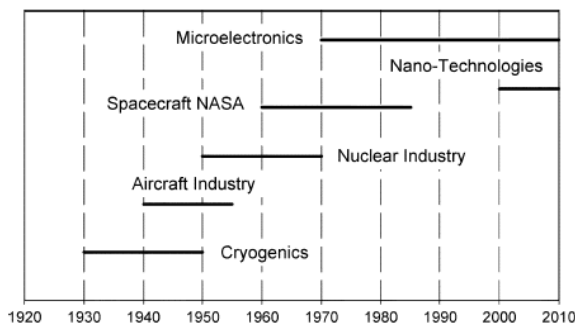
Figure 16 Ranges of different fields interested in TCC [38]
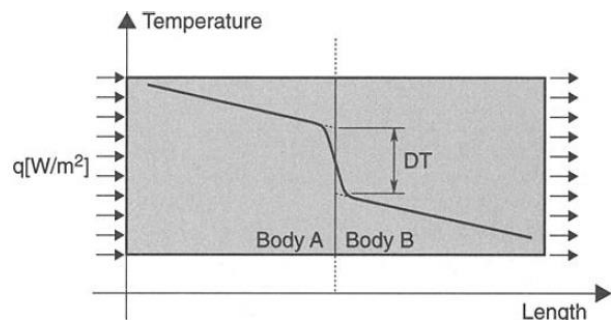
Figure 17 Temperature drop across an imperfect interface [38]

28
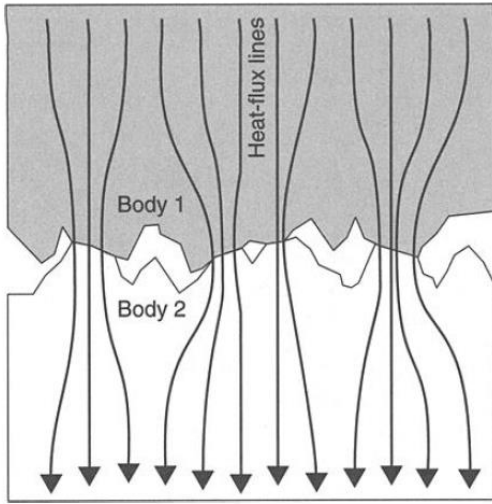
Figure 18 Exaggerated illustration of contact surfaces showing microscopic constriction [39]
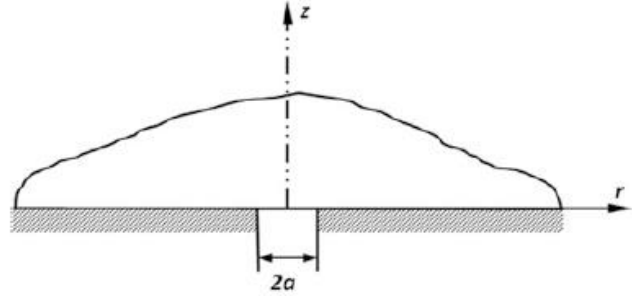
Figure 19 Half space representation of a thermal constriction [37]

$$R_c = \frac{T - T_0}{Q}$$

where T is the temperature difference required with the constriction and T_0 is the temperature difference without the constriction [37].

A theoretical approach to determining R_c begins by considering a circular constriction in half space as shown in Figure 19. The constriction is described by imposing a boundary condition where heat is only transferred into the half space through a circle of radius a, or

$$\frac{dT}{dz}\bigg|_{z=0} = 0, \qquad r > a.$$

This scenario can be solved for a uniform temperature at the conducting interface or a constant heat flux [37]. When the temperature is constant, the constriction resistance is given as

$$R_{c,uT} = \frac{1}{4ka}.$$

When the heat flux is constant, the constriction resistance is given as

$$R_{c,cQ} = \frac{0.27}{ka}.$$

29

This description of constriction resistance accounts for only a single area of true contact in an infinite half space, and must be extended to account for the multiple contact spots in actual, finite interfaces. These additional contact spots act to reduce, or alleviate, the resistance caused by a single spot. By assuming that each constriction, with radius a_i, in the interface is fed by a relatively large cylinder, with radius b_i, and that A_r, the real or true contact area is given by

$$A_r = \sum \pi a_i^2$$

and the apparent, or nominal contact area, A_n, is given by

$$A_n = \sum \pi b_i^2$$

a quantity called the "constriction alleviation factor", F_a, given as a function of a/b can be determined. [37] This factor modifies the constriction resistance as

$$R_c = R_{c,uT} F_a \left(\frac{a}{b} \right).$$

 Table 2 presents a comparison of constriction alleviation factors from a number of authors [37].

4.3.2   Surface and Deformation Analysis
The analysis thus far has only considered the constriction resistance associated with one side of an interface. When both sides are considered, the total resistance for a single contact spot is

$$R_c = \frac{F_{a1}}{4ak_1} + \frac{F_{a2}}{4ak_2}.$$

By using the harmonic mean of the thermal conductivities,

$$k = \frac{2k_1 k_2}{k_1 + k_2},$$

Table 2 Comparison of constriction alleviation factors [37]

a/b	Roess	Mikic	Gibson	N-Y
0.1	0.8549	0.8584	0.8594	0.8594
0.2	0.7205	0.7202	0.7209	0.7208
0.3	0.5853	0.5851	0.5865	0.5865
0.4	0.4558	0.4557	0.4586	0.4586
0.5	0.3340	0.3341	0.3398	0.3395
0.6	0.2230	0.2231	0.2328	0.2318

the thermal contact conductance for a single spot can be written as

$$h = \frac{2ak}{F_a}.$$

In a real joint with multiple contact points, the total conductance is the sum of all of the individual spots' conductance, or

$$h_s = 2k\Sigma\left(\frac{a_i}{F_{ai}}\right).$$

Accurately predicting TCC depends on accurately determining the real contact area and the distribution of microcontacts. Following is one approach to determining these quantities. Other approaches, including deterministic, statistical, fractal and multiscale methods have been used [40]. Some of these are discussed in section 4.3.4.

By assuming n contact spots, a mean contact spot radius can be determined

$$a_m = \frac{\Sigma a_i}{n}.$$

This value, along with some appropriately weighted value for F_a can be used to produce [37]

$$h_s = \frac{2ka_mn}{F_a}. \tag{1}$$

Determining a_m and n requires surface and deformation analysis. Given a surface topology in the form of $z = f(x, y)$ for a rough surface with $z = 0$ at the mean height of the profile, the number per unit area, n_a, and average size, s, of the spots can be shown to be

$$n_a = \frac{1}{4g_s}\frac{A_n}{A_r}\left(w(\epsilon_\sigma)\right)^2 \int_{-\infty}^{\infty}|z_x|w(z_x)dz_x \int_{-\infty}^{\infty}|z_y|w(z_y)dz_y \tag{2}$$

and

$$s = \frac{A_r}{A_nn_a} \tag{3}$$

where

- g_s is a shape factor defined by the spot area divided by the product of the mean lengths in the x- and y-directions ($g=1$ for a square, $4/\pi$ for an ellipse)
- A_n is the nominal or apparent contact area
- A_r is the real or true contact area
- $w()$ is the probability density function
- ϵ_σ is the distance between the mean height of the rough surface and the contacting surface

31

    –   the x and y subscripts indicate derivatives in those directions.

To calculate these values, a probability density function that describes the surface is required as well as the contact area ratio [37]. These equations come from examining a rough surface coming into contact with a smooth surface, but can be used for 2 rough surfaces by calculating equivalents as

$$z_e = z_1 + z_2$$

$$z_{x,e} = z_{x,1} + z_{x,2}$$

$$z_{y,e} = z_{y,1} + z_{y,2}$$

and treating them as a single rough surface coming into contact with a flat surface as in Figure 20.

If a Gaussian distribution of heights and slopes is used, then

$$\epsilon_\sigma = \sqrt{2}\, erfc^{-1}\left(\frac{2A_r}{A_n}\right),$$

and eq. (2) becomes

$$n_a = \frac{1}{4\pi^2 g_s} \frac{\sigma_{mx}\sigma_{my}}{\sigma_d^2} \frac{A_n}{A_r} e^{-2\left(erfc^{-1}\left(\frac{2A_r}{A_n}\right)\right)^2} \tag{4}$$

where σ_d is the standard deviation of the profile heights, or the root mean square roughness measured on a surface [37].

σ_{mx} and σ_{my} are the standard deviations of the slopes in their respective directions. The slope are determined from the surface profile data by

$$m_x = \frac{1}{L} \int_0^L \frac{dz(x, y_0)}{dx}\, dx$$

$$m_y = \frac{1}{L} \int_0^L \frac{dz(x_0, y)}{dy}\, dy$$

where L is the trace length used in obtaining the roughness data, and the 0 subscripts indicate the trace happens only in the x or y direction [38]. It is recommended that the length of L be comparable to the length of the nominal contact area [41].

32

Assuming circular contact spots the area of a mean spot, s, is

$$s = \pi a_m^2$$

so

$$a_m = \sqrt{\frac{s}{\pi}}.$$

Substituting (4) from the previous page into (3) and then that modified (3) in for *s* above yields

$$a_m = \sqrt{\frac{A_r}{A} \frac{1}{\pi} \left[\frac{1}{4\pi^2 g_s} \frac{\sigma_{mx}\sigma_{my}}{\sigma^2} \frac{A_n}{A_r} e^{-2\left(erfc^{-1}\left(\frac{2A_r}{A}\right)\right)^2} \right]^{-1}}$$

$$= \sqrt{\left(\frac{A_r}{A_n}\right)^2 \frac{1}{\pi} e^{2\left(erfc^{-1}\left(\frac{2A_r}{A_n}\right)\right)^2} 4\pi^2 g_s \frac{\sigma^2}{\sigma_{mx}\sigma_{my}}}$$

$$= 2\sqrt{\pi g_s} \frac{\sigma}{\sqrt{\sigma_{mx}\sigma_{my}}} \frac{A_r}{A_n} e^{\left(erfc^{-1}\left(\frac{2A_r}{A_n}\right)\right)^2}.$$

As stated previously, for a circle, $g_s = 4/\pi$. Additionally, we can define
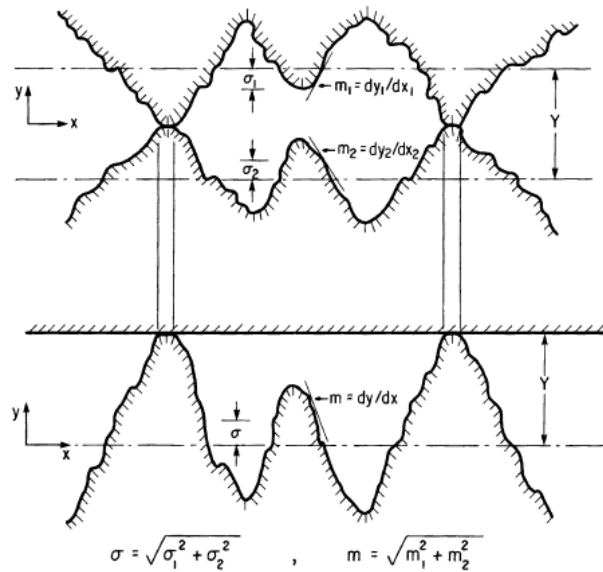
Figure 20 Equivalent surface for use with two rough surfaces [38]

33

$$\tan(\theta) = \sqrt{\sigma_{mx}\sigma_{my}}.$$

Substituting these in, we find

$$a_m = \frac{4\sigma}{\tan(\theta)}\frac{A_r}{A_n}e^{\left(erfc^{-1}\left(\frac{2A_r}{A}\right)\right)^2}. \tag{5}$$

Similarly, substituting these into (4) we obtain

$$n_a = \frac{1}{16\pi}\left(\frac{\tan(\theta)}{\sigma}\right)^2\frac{A_n}{A_r}e^{-2\left(erfc^{-1}\left(\frac{2A_r}{A_n}\right)\right)^2} \tag{6}$$

We can now substitute a_m and n_a from (5) and (6)into (1) to get an equation for TCC

$$h_s = \frac{1}{2\pi}\frac{k\tan(\theta)}{\sigma}\frac{1}{F_a}e^{-\left(erfc^{-1}\left(\frac{2A_r}{A_n}\right)\right)^2}. \tag{7}$$

This equation depends on the ratio of real to apparent contact area and on properties of the contact surfaces, the standard deviation of the peak distributions ($\sigma \cong 1.25$ CLA roughness, or RMS roughness for example) and the standard deviation of the slopes that can be obtained by suitable measurement techniques, as well as an appropriate value for F_a [37].

A number of models predict the contact ratio as a function of applied pressure, P, and the microhardness, H_m, of the softer of the contacting surfaces when the contact results in plastic deformation. A simple force balance shows that, in equilibrium, the applied force, F_{ap} must be

$$F_{ap} = PA_n = A_r H_m$$

which can be rearranged to show that

$$\frac{A_r}{A_n} = \frac{P}{H_m}.$$

This analysis ignores the plastic deformation of the surfaces, (it essentially assumes the material disappears as it deforms) but can be used for low contact pressures without significant errors. For larger contact pressures, however

$$\frac{A_r}{A_n} = \frac{P}{H_m + P}$$

should be used.

In cases where elastic deformation is expected, the following can be used:

34

$$\frac{A_r}{A_n} = \frac{P\sqrt{2}}{E'\tan(\theta)}$$

where E' is the reduced modulus for the two materials in contact and $\tan(\theta)$ is the mean absolute slope given by $\tan(\theta) = \sqrt{m_x^2 + m_y^2}$ [42]. E' is given by

$$\frac{1}{E'} = \frac{1 - v_1^2}{E_1} + \frac{1 - v_2^2}{E_2}$$

where v is Poisson's ratio for the materials.

4.3.3 Macroscopic Constriction

When modeling surfaces in contact, a number of different situations can take place. First, two perfectly smooth, perfectly flat surfaces brought into contact will have a real contact area equal to the apparent contact area. Such ideal surfaces suffer from no contact resistance. Second, if one of the surfaces is not perfectly flat but both are still smooth, there will be a single point of contact for every convex feature of the non-flat surface. Third, if one of the surfaces is rough and one of the surfaces is non-flat, numerous micro-contacts will exist in every convex feature. Fourth, if both surfaces are flat, but at least one is rough, micro-contacts will exist across the entire apparent contact area. Figure 21 shows the latter three cases. The two previous sections, 4.3.1 and 4.3.2, discussed the last case which is known as conforming contact, and this section will discuss the second to last case. The lack of flatness is generally not limited to a single convex feature on one of the surfaces, but instead is often characterized by multiple features on both surfaces. This situation is often referred to as "waviness". When wavy surfaces are brought into contact with each other, the regions that touch are referred to as contour areas. An illustration of this phenomenon is shown in Figure 22, where the small ellipses represent individual contact spots within the larger contour area.

The concept already developed for microscopic constriction extends to macroscopic constriction, as well. The macroscopic constriction can be visualized as being fed by a cylinder of constant heat flux. The flow is first constricted by the waviness and then by the microscopic contact spots. Mathematically, this is represented by

$$R_t = R_L + R_s$$

$$= \frac{F_L}{2a_L k} + \frac{F_s}{2a_s k}$$

where the subscripts L and s indicate the larger (macroscopic) and smaller (microscopic) constrictions. [37]

4.3.4 Models for TCC

Numerous theoretical and empirical models have been produced for predicting TCC. The theoretical models are frequently divided into plastic and elastic deformation. By nondimensionalizing TCC and contact pressure, [43] was able to compare many of the theoretical models for nominally flat, rough surfaces with data collected from various experiments. The results are reproduced in Figure 23 for both elastic and plastic deformation models. As is apparent, of the models examined, the plastic deformation models were more accurate than the elastic deformation models, with the elastic models often under predicting the experimentally measured conductance.

4.3.4.1 *Yovanovich TCC Model [38]*

A commonly used semi-empirical, plastic model by [38] is given by

$$h_c = \frac{1}{R_c} = 1.25 \, k \frac{m}{\sigma} \left(\frac{P}{H_m}\right)^{0.95}$$

where all properties are in metric units. Some difficulties arise with the use of microhardness because the value obtained depends on the method of measurement [40]. An example of a correlation for microhardness is given by [44]:
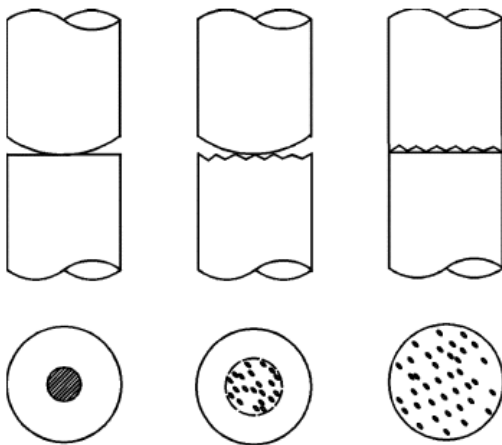
Figure 21 Different ways of modeling contact, left smooth, non-flat surface, center rough non-flat surface, right rough, flat surface [38]
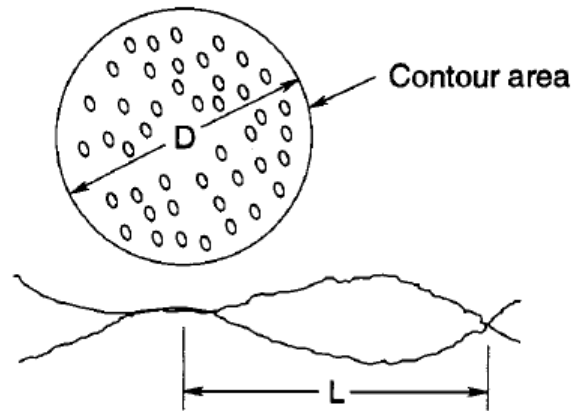
Figure 22 Illustration of macroscopic constriction due to waviness. The small ellipses indicate areas of microscopic contact [39]
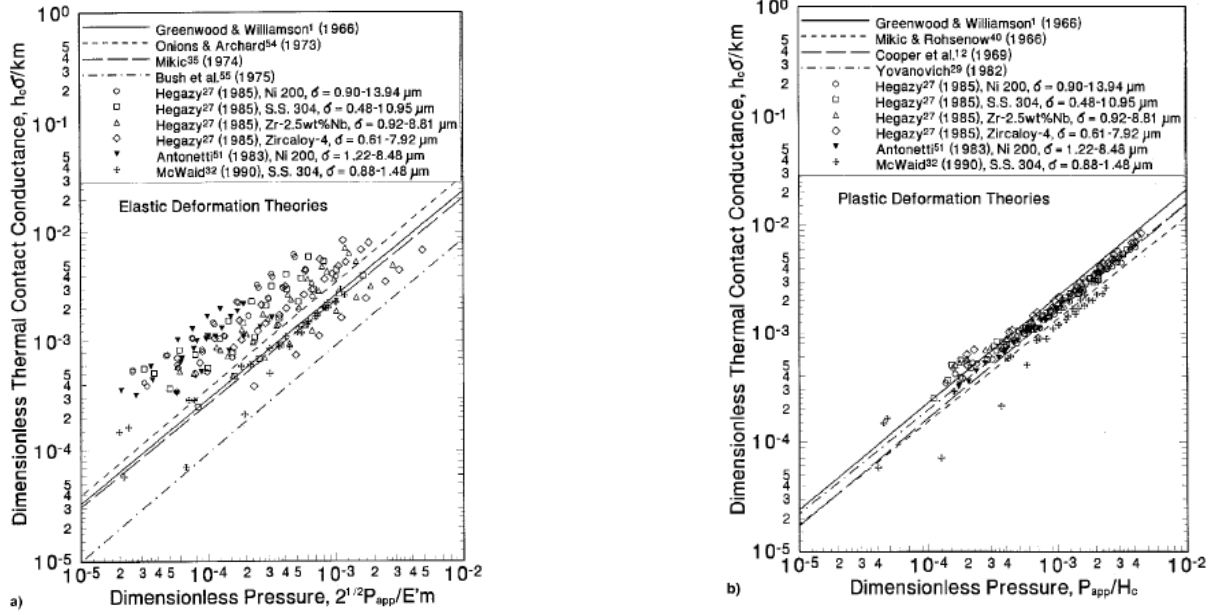
Figure 23 Comparison of 4 theoretical elastic (left) and plastic (right) TCC models with experimental data [43]

$$\frac{P}{H_m} = \left[\frac{P}{H \left(1.62 \times 10^{12} \, \frac{\sigma}{m} \right)^{c_0}} \right]^{\frac{1}{1+0.071c_0}}$$

where H is the bulk hardness and c_0 is -0.26.

4.3.4.2   Bahrami TCC Model [45]

[45] follows the procedure of dividing the nature of contact into a small scale, where microscopic contact is the predominant factor for determining contact area, and a large scale, where the radii of curvature of the contacting bodies is the predominant factor. Between these two extremes exists a transition region where each factor affects the total contact area, and thus, the TCC. This relationship, as shown earlier, is

$$R_j = R_L + R_s$$

where j indicates the total for the joint, L the macroscopic (or large) scale and s the microscopic (or small) scale. [45] focuses on the ratio of σ/m (surface roughness over surface slope) as the primary factor that describes the nature of the rough surface profile, and uses superposition to combine the large and small scale components of resistance. The small component is given by

37

$$R_s = \frac{0.565 H^* \left(\frac{\sigma}{m}\right)}{k_s F_{ap}}$$

where as seen earlier σ, the RMS roughness, is a measure of the mean asperity height, m is the mean slope of the surface profile, k_s is the geometric mean of the thermal conductivities, F_{ap} is the applied load, and H^* is a correlation for determining microhardness and is given below.

$$H^* = c_{v,1} \left(\frac{\sigma}{m\sigma_0}\right)^{c_{v,2}}$$

where σ_0 is 1 μm, and the c_v's are Vickers hardness testing coefficients which are given by

$$c_1 = H_{BGM}(4.0 - 5.77\kappa + 4.0\kappa^2 - 0.61\kappa^3)$$

$$c_2 = -0.57 + 0.82\kappa - 0.41\kappa^2 + 0.06\kappa^3$$

where $H_{BGM} = 3.178$ GPa, H_B is the Brinell hardness of the bulk material, and $\kappa = \frac{H_B}{H_{BGM}}$. This correlation is valid for $1.3 \leq H_B \leq 7.6$ GPa. Based on the tabulated results, these correlations do not appear to have been used in the calculations of [45], and direct measurements of the coefficients to determine H^* may have been used instead.

The macroscopic component of resistance is given by

$$R_L = \frac{\left(1 - \frac{a_L}{b_L}\right)^{1.5}}{2k_s a_L}$$

where a_L is the radius of the macroscopic contact area, b_L is the size of the contacting bodies. a_L is given by

$$a_L = 1.80 a_H \frac{\sqrt{\alpha_1 + 0.31\tau^{0.056}}}{\tau^{0.028}}$$

where $\alpha_1 = \frac{\sigma \rho_c}{a_H^2}$, $\tau = \frac{\rho_c}{a_H}$, with ρ_c being the radius of curvature of the equivalent contacting surface, as determined below, and a_H is the Herzian contact radius, also given below.

$$a_H = \left(\frac{3F\rho_c}{4E'}\right)^{\frac{1}{3}}$$

$$\rho_c = \frac{b_L^2}{2\delta_f}$$
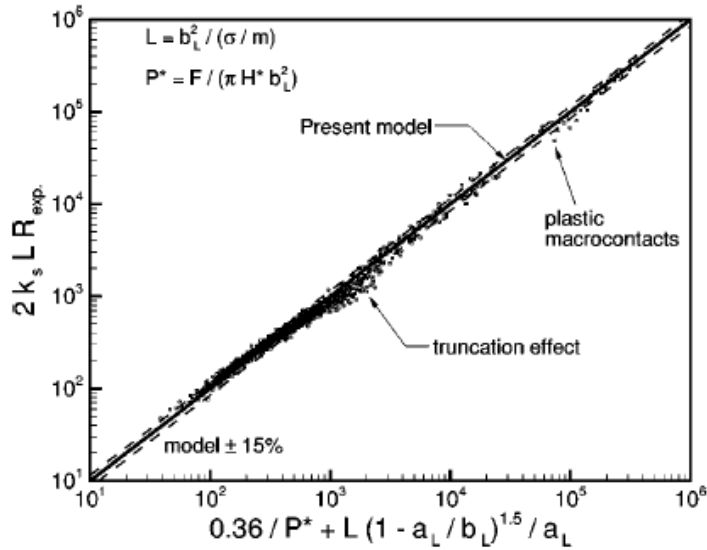
Figure 24 Comparison of general model from [45] with experimental results

where δ_f is the maximum out-of-flatness of the surface.

By using these correlations and the general formula, [45] was able to show that 730 out of 880 data points from 17 studies, involving similar and dissimilar metals in contact were contained within 15% of the model as described. These results are displayed graphically in Figure 24. This model is applicable for contact which experiences plastic deformation.

The models discussed thus far generally assume a flat, rough surface. Those that have included waviness view the two, waviness and roughness, as distinct features of a surface. More recently a number of studies have examined roughness and waviness as a continuum of the same phenomenon. These studies have a used what they term a "scale" approach. They have also noted that many of the earlier works on TCC used an unsound assumption of a constant hardness during deformation [41].

4.3.4.3 Jackson TCC Modeling Approach

In a series of papers, [40, 41, 46, 47] developed a scale approach that uses fast Fourier transform of the surface profile to characterize the nature of the roughness and determine TCC, essentially "…converting the surface profile data into a series of stacked sinusoids", see Figure 25 [40]

Shifting from the general description of waviness and returning to an early concept of "protuberance on protuberance", they developed an iterative approach to determining the true contact area utilizing the idea that collections of smaller asperities reside on an asperity at a given scale [41]. By treating the contact area of a larger scale as the apparent contact area, and by using any of a number of contact models, they calculate the ratio of apparent to real contact area.

The process is then iterated at the next smaller scale, assigning the real contact area of the larger scale to the apparent contact area of the smaller scale, until all scales of interest are included. This process is shown in a flow chart in Figure 26.

The value η_i, the asperity areal density, is calculated from the Fourier series as follows

$$\eta_i = 2f_i^2$$

where f_i is the frequency.

[40] further developed a closed form model, replacing the iterative model, and converting from spherical contacts to the sinusoidal surface mentioned above. By examining a number of different cases of surface topology, [47] demonstrated that focusing on B_{max}, the maximum ratio of amplitude over wavelength, instead of iterating through the entire spectrum of wavelengths, provides a real contact area that shows only minor errors relative to the full iterative approach. Applying this method for contact area prediction to TCC, [40] provides the following equations for TCC. For elastic-plastic deformation

$$k_c^{-1} = R_c = \frac{\pi^{\frac{3}{2}} E' \Delta_{max}}{2k F_{ap}} \left[\frac{11}{\frac{12\pi E' B_{max}}{\sqrt{2} S_y e^{\frac{2}{3}v}} + 7} \right]^{\frac{3}{5}} \tag{8}$$
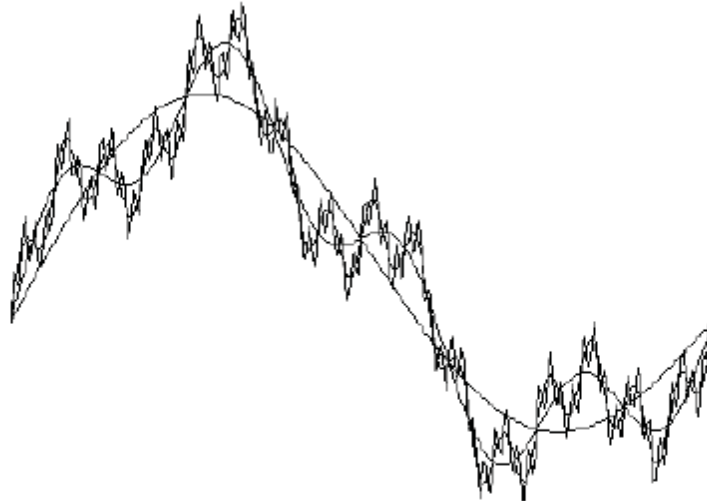
Figure 25 "Schematic depicting the decomposition of a surface into superimposed sine waves. Each line represents a different scale of roughness" [40]
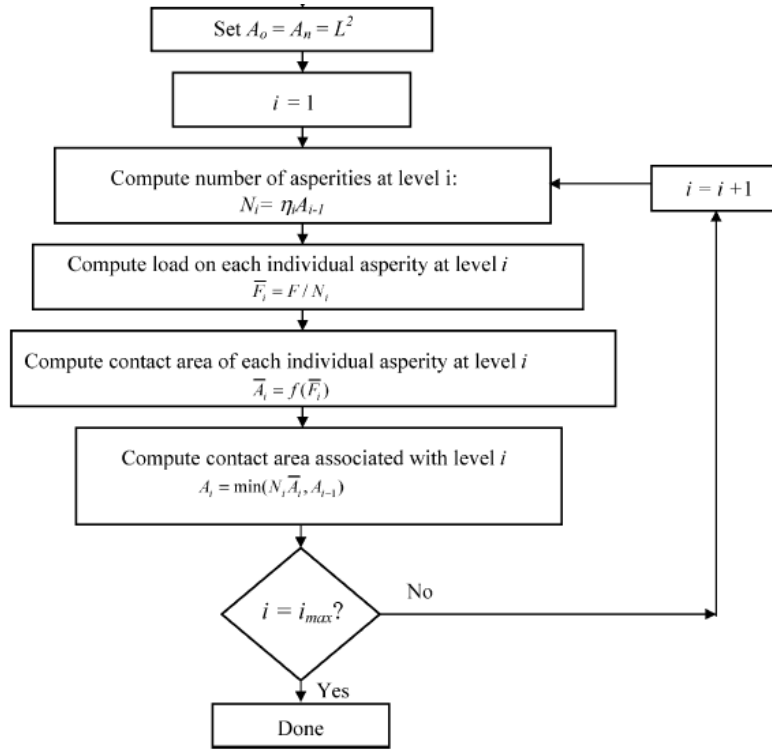
Figure 26 Flow chart for determination of real contact area [46]

where

- F_{ap} is the applied force at the joint or area of contact
- Δ_{max} is the amplitude of the wavelength that is identified in B_{max}
- S_y is the scale dependent yield strength
- v is Poisson's ratio
- B_{max} is the maximum ratio of amplitude over wavelength, Δ/λ, from the Fourier series.

S_y must be solved for from the following equation

$$S_y = (S_y)_0 \sqrt{1 + \frac{h^*}{\Delta_{max}} \left[1 - \left(\frac{11}{\frac{12\pi E' B_{max}}{\sqrt{2} S_y e^{\frac{2}{3} v}} + 7} \right)^{\frac{3}{5}} \right]^{-1}} \tag{9}$$

where $(S_y)_0$ is the bulk yield strength and h^* is a material dependent length scale. [48] gives the following theoretical equation for h*, when a Berkovich type indenter is used for determining hardness,

$$h^* = \frac{81}{2} b_v \alpha_1^2 \tan^2 \theta \left(\frac{\mu_\tau}{H_O}\right)^2$$

where b_v is the Burgers vector, α_1 is a constant (taken to be 0.5), θ is the angle the indenter tip makes with the surface being indented, and μ_τ is the shear modulus of the material. H_O is given by

$$H_O = 3\sqrt{3}\alpha_1 \mu b_v \sqrt{\rho_s}$$

where ρ_s is the density of statistically stored dislocations—the dislocations associated with homogenous strain on a material (as opposed to geometrically required dislocations that arise from curvature of crystal lattices). No method is provided for determining ρ_s. Instead, it is recommended that the square of the hardness measured during the indentation be plotted against the inverse of the depth of indentation. The resulting intercept (hardness measured at an "infinitely" deep penetration) will then be H_O (H at the origin) and the slope of the line will be h^*. This is suggested by the relation

$$\frac{H}{H_O} = \sqrt{1 + \frac{h^*}{h_p}}$$

where h_p is the depth of penetration during the indentation. As an example, Figure 27 shows a plot of the hardness ratio squared vs the reciprocal of depth of penetration for cold worked polycrystalline copper.

The method, then, for determining the TCC using this approach is to first determine the length scale, h^* by performing nano-indentation to create a plot similar to Figure 27 and extracting the slope. Use that slope in equation (9) and solve for the scale dependent yield strength, S_y. Substitute that value into equation (8). At the same time, take a roughness measurement of the surfaces and perform an FFT on the resulting profiles. Determine the maximum B value and associated Δ. Substitute these into equation (8) as well and solve for R_c. Again, this procedure is for determining TCC for the case of elastic-plastic deformation.

For purely elastic deformation, [40] gives the following equation

$$R_c = \frac{\pi^{\frac{3}{2}} E' \Delta_{max}}{2kF} \tag{10}$$

In support of this model, [40] provides a comparison of a set of experimental results and the commonly used TCC models by Yovanovich and Greenwood and Williamson, Figure 28.

4.3.5　Scale Dependent TCC

Many material properties and physical phenomena exhibit scale dependence. As already mentioned with some of the models, microhardness, which differs from macroscopic material hardness, must be used for more accurate TCC predictions. In addition to microhardness, consideration has been given to the manner in which radiative heat transfer varies with the size of the gap between surfaces and how thermal conduction resistance varies with contact scale. It is argued that both of these have negligible impacts on the overall TCC.

[49] points out that the majority of TCC cases involve contact that is separated by μm sized gaps and thus is sufficiently large that nanoscale effects can be neglected. These effects include those on radiation heat transfer. [41] observed that asperities smaller than 1 μm tend to flatten out during contact when plastic deformation is expected and any variation in physics due to nanosized effects could be ignored. [41] also investigated the effect small scales have on the governing equation for TCC. Citing [50], instead of using the standard microscopic constriction resistance relationship,

$$R_c = \frac{1}{2ka}$$

[41] used a scale dependent

$$R_c = \frac{3\pi + 8K}{6\pi ak}$$
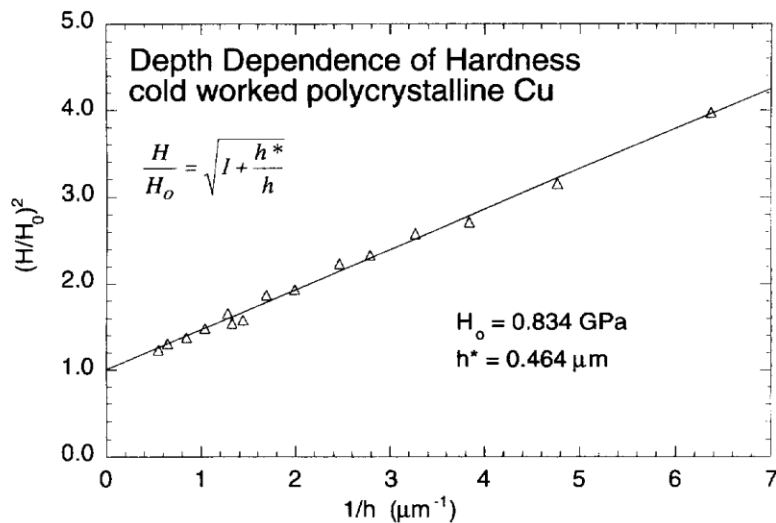
Figure 27 Plot showing the determination of h* and H$_O$ for cold worked polycrystalline Cu [48]

43
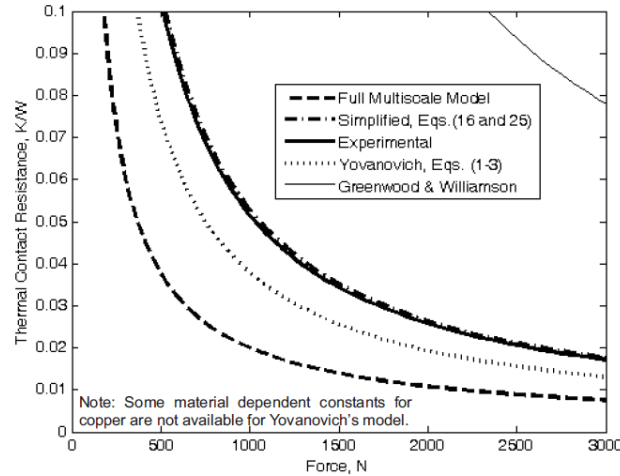
Figure 28 Comparison of experimental results with [40] simplified and [41] full multiscale and common Yovanovich and Greenwood and Williamson models

where K is the Knudsen number given by

$$K = \frac{\lambda_p}{a}$$

with λ_p as the phonon free mean path given by

$$\lambda_p = \frac{2k}{\rho v_s C}$$

where ρ is the density, v_s is the speed of sound, and C is the heat capacity.

[41]'s efforts indicated that the effect from the scale dependent contact resistance was small. To answer questions of how the choice for λ might have affected the results (it has been suggested that the equation used under-predicts the true value of λ), [41] multiplied that calculated value of λ by 10 and observed an increase in resistance of about 16%.

4.3.6 Loading Cycle Effect on TCC

Thermal contact conductance is dependent on loading cycle and exhibits contact pressure hysteresis. [49, 51, 52, 53] each investigated this hysteresis and loading cycle dependency, but drew different conclusions from their observations. All agree, however that there is contact pressure hysteresis for the first loading and unloading cycle, and that the subsequent loadings produce higher conductivity than is produced by the initial loading.

[51] measured the hysteresis during the initial loading and unloading of two joints. In both cases the unloading TCC was higher than the loading TCC, but the nature of the difference was not

44
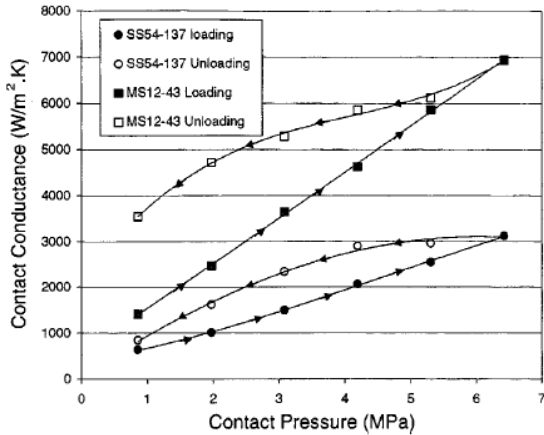
Figure 29 Hysteresis effect on TCC of loading and unloading 2 joints [51]
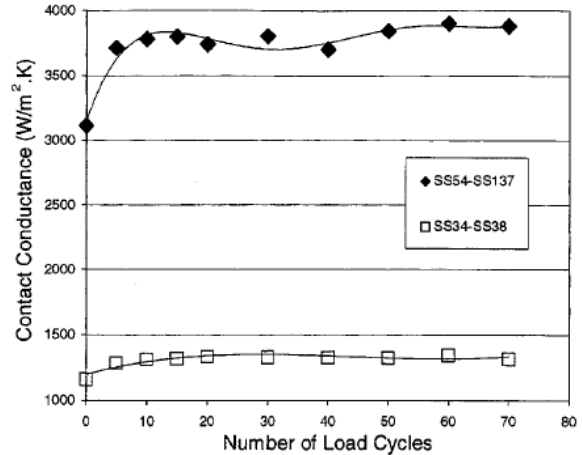
Figure 30 TCC vs loading cycle number for two joints [51]

consistent, see Figure 29. Upon continued loading and unloading, they observed a dramatic increase in TCC during the first 5 cycles followed by a fairly low increase during the next 25 cycles after which the TCC appeared to remain constant, as shown in Figure 30.

[52] repeated the work of [51] and provided an estimated uncertainty in the TCC measurements of 10.8%. [52] determined that the majority of the benefit of repeated loading was obtained in the first loading cycle. By taking into account the temperature dependent thermal conductivity of the measurement apparatus, [53] suggested that, aside from the increase after the first loading and unloading cycle, all apparent further increases in previous studies (which did not take into account the temperature dependence of thermal conductivity) fall within the uncertainty of the experiment. [49] examined the hysteresis at low contact pressures (>1 MPa), observing that the plastic models frequently under-predict the TCC at low contact pressures, but do fairly well at higher pressures.

[51] and [52] both demonstrated that overloading—or subjecting the joint to higher pressure than the in-service contact pressure—increases the TCC. That this might be a result of improving the conformity of the two surfaces or reducing the relative roughness of the surfaces is mentioned, but no report is made of any post-test surface profile measurements. Figure 31 shows [51]'s results from overloading. After subjecting the joint to the higher pressure, the joint was returned to the lower, "operating" pressure to measure TCC. Figure 32 compares the results from [51] and [52].

4.3.7 The Effect of Interstitial Material

Interstitial material affects TCC by providing a parallel conduction pathway. When contact pressure is low or the interstitial material is a good conductor, this effect can be significant. The

45
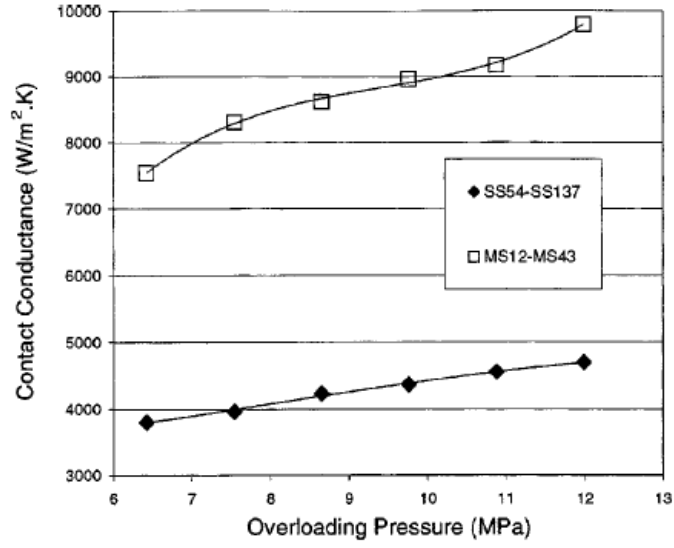
Figure 31 TCC vs overloading pressure. TCC was measured back at operational pressure (6.25 MPa) after experiencing the overloading indicated [41]
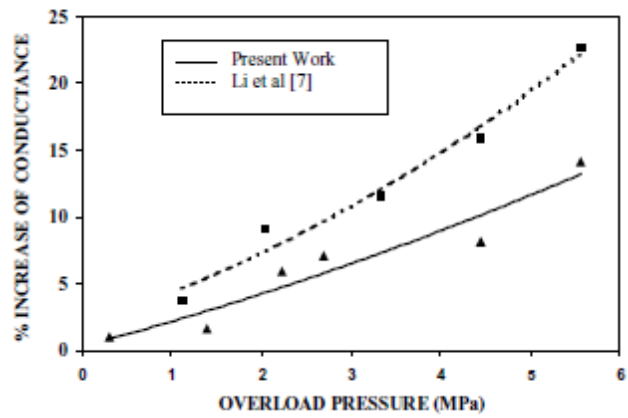
Figure 32 Comparison of [51] and [52]'s results from overloading experiments

added conduction depends on the average surface roughness, the portion of the nominal contact area that is not real contact area, that is, $A_{Interstial} = A_n - A_r$, and the thermal conductivity of the interstitial material. Convection is negligible when the gaps are filled with fluid because the gaps are small.

Depending on the conditions at the interface, the mean free path for gas molecules may be close to the width of the gaps. If this is the case, a phenomenon known as a "temperature jump" may become important, Figure 33. This phenomenon results from the inefficiencies of conducting energy from a solid surface to a gas and essentially acts to elongate the distance over which the thermal conductivity of the gas is influential.

The thermal conductivity of the gas gap may then be expressed as

$$h_g = \frac{k_g}{\delta_g + g_1 + g_2}$$

where, k_g is the thermal conductivity of the gas, and the g's are the temperature jump distances which depend on the gas in the gap, the material type and the nature of the surface. Whether or not this equation is necessary can be determined by calculating the Knudsen number,

$$K_g = \frac{\lambda}{\delta_g}$$

where λ is the mean free path for the molecules in the gap. If $K_g \ll 1$, Fourier's law applies; if $0.01 < K_g < 10$, temperature jump is relevant; if $K_g > 10$, then

$$h_g = \frac{k_g}{g_1 + g_2}$$

and the conductivity is independent of the gap thickness [37]. The value of g depends on a number of factors. It can be given by

$$g = \frac{2 - \alpha_t}{\alpha_t} \frac{2\gamma}{\gamma + 1} \frac{1}{Pr} \lambda$$

where α_t is the thermal accommodation coefficient, γ is the ratio of specific heats for the gas, and Pr is the Prandtl Number. When mixtures of gasses are present, the following may be used to determine the temperature jump distances:

$$g_m = \frac{\Sigma\left(\dfrac{x_i g_i}{M_i^{0.5}}\right)}{\Sigma\left(\dfrac{x_i}{M_i^{0.5}}\right)}$$

where x is the mass fraction and M is the molecular mass of the gas.

Determining the accommodation coefficient is challenging. It essentially describes how much each gas molecule is accommodated towards the energy of the wall after each collision. Currently, the only way to determine it is to measure it for the specific combination of gas and surface. [37] makes the following statements about accommodation coefficients:

"- Accommodation coefficients usually range in values from 0.01 to 1.0, although values higher than 1 are possible.

- In general, lighter monatomic gases have low accommodation coefficients.

- Clean surfaces have lower accommodation coefficients compared with contaminated surfaces.

- For unclean surfaces, the accommodation coefficient decreases as the temperature increases.

- The accommodation coefficient appears to be inversely proportional to the thermal conductivity of the gas.

- The accommodation coefficient is independent of the gas pressure as it is mainly dependent on the relative molecular masses of the gas and the solid."

[37] also provides Table 3 as an example of the different accommodation coefficients'
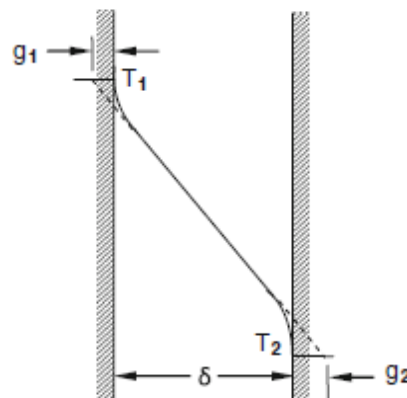
Figure 33 Illustration of the temperature jump distances on either side of a gap [37]

dependence on gas type and surface type and finish.

Experiments have demonstrated that as gas pressure between a gap decreases from an initially high pressure, the TCC remains largely unchanged until some "threshold pressure", when $\lambda \cong \delta$, is obtained, at which point the TCC decreases as a fairly strong function of pressure until approximately 1 mm Hg at which point the TCC due to the gas is essentially 0 [37]. This behavior is seen in Figure 34 where the gas conductance makes up a large part of the TCC. When the pressure drops below the threshold, the contact resistance goes up to the level provided by the solid contact alone.

4.3.8 TCC Considerations for Treating Fuel Plate Non-bonds

Fuel plate non-bonds can be considered as a TCC opportunity. However, reasonable estimates for contact pressure, roughness, waviness, and material properties for the rolled cladding and fuel meat are needed to use the models discussed above.

Of particular challenge in the case of fuel plates is that many, if not all of these properties change with burnup. The non-bond condition of the fuel plate as manufactured in isothermal conditions may be altered when placed in service and the thermal stress field is added. Fuel swelling and gas production and migration may significantly alter the non-bond thermal performance. This is a multiphysics assessment that could be addressed using COMSOL in a future, more advanced simulation to further identify appropriate treatment of the fuel thermal performance. For the current effort, the study is focused on initial operating conditions.

In consideration of the foregoing material regarding TCC, a number of points can be made about fuel plate non-bonds and where they fit into the landscape of TCC:

1. Non-bonds are subject only to elastic deformation, not plastic, while in operation. In essence, the manufacturing procedure (rolling, see section 3.2.1) subjects the non-bond to extreme

Table 3 Accommodation factors for a number of gasses and solids [37]

Material		He	Ne	Ar	H2	O2	N2	CO2
Platinum		0.38	0.75	0.8	0.24	0.62	0.86	0.52
	bright	0.44			0.32			
	blackened	0.91			0.72			
	uncleaned	0.446	0.816	1.01			0.975	1
Tungsten						0.54		
	fresh	0.06						
	uncleaned	0.393	0.796	1			0.975	1
UO2		0.55		0.75				
Nickel		0.457	0.831	1.02			0.978	1.02
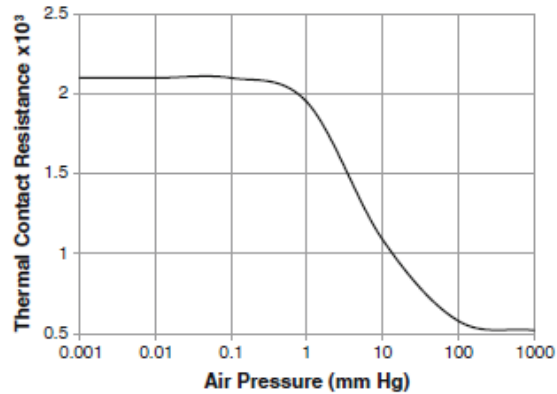
Figure 34 Thermal contact resistance as a function of air pressure [37]

overloading. Following the rolling process, residual stresses are relieved through annealing, and the plate is then formed into the involute shape. This suggests that the operating pressure the non-bonds are subject to will not cause further plastic deformation and means that elastic relationships ought to be used for calculating TCC.

2. The joint is conforming—any waviness exhibited by the cladding will be similarly found in the fuel meat. This means that any radius of curvature or out-of-flatness within a model can be eliminated.

3. At least initially, interstitial material can be ignored. The manufacturing process of venting from the corners during hot rolling excludes all free gas from the non-bonds. During irradiation, fission gasses will accumulate and may aggregate within the non-bond. As already stated, this potential and the effect on non-bond heat transfer may need to be examined in future, more advanced simulations.

4. The contact pressure or contact force the non-bonds are subject to is at least equivalent to the operating pressure of the reactor. In the case of HFIR this is 468 psi at the inlet, dropping 110 psi across the core. As the fission gasses accumulate, this contact pressure may be reduced.

Chapter 5   Conjugate Heat Transfer

The rate at which heat is transferred between a solid and a fluid at different temperatures is dependent on a large number of factors. The earliest efforts at quantifying this heat transfer simplified the analysis by considering an average heat transfer coefficient. This analysis, in its simplest form, assumes a constant temperature for both the solid body and the incoming or approaching fluid. Newton observed that the amount of heat transferred between a solid and a moving fluid was proportional to this temperature difference, as in

$$\vec{q}'' = h_h \Delta T$$

where $\vec{q}''$ is the heat transfer rate per unit area normal to the surface, h_h is the proportionality constant known as the convective heat transfer coefficient, and ΔT is the difference in temperature between the incoming fluid and the surface. The simplicity of this expression is obtained by wrapping all of the influential parameters into h. Within h we find the influence of the solid and fluid material properties (thermal conductivity, k, heat capacity, c, density, ρ, viscosity, μ) and the flow characteristics (relative velocity between the fluid and the solid, $\vec{v}$, the resulting laminar or turbulent flow regime, the geometry, etc.).

In this approach h can be difficult to determine analytically, especially in complicated engineering assessments. Because of this difficulty, engineers frequently use empirically determined values of h. However, in many cases experimental data are not available for determining a satisfactory value of h. Additionally, because h is generally an average value across the interface between solid and fluid, specific details about local heat fluxes and temperature fields in the solid and fluid cannot be obtained through this simple relationship. These difficulties make it sometimes preferable to determine the temperature field and the resulting heat transfer directly from the coupled physics of conduction in the solid and energy transport in the fluid. This coupled analysis is known as conjugate heat transfer. The remainder of this chapter will cover the processes of heat conduction within solids, energy transport within fluids, and the process of coupling these two phenomena. Additionally, this section will review how previous investigators have addressed conjugate heat transfer in hot spot models and what should be done in the development of an improved hotspot model.

5.1   Heat Conduction in Solids

Heat transfer within solids takes place at the atomic level. In metallic solids, the energy is carried primarily through free electrons. In non-metallic crystalline solids, the energy is carried primarily through phonon interactions. Semiconductors experience energy transfer through both phonons and electrons. Phonons are fundamental units of vibrational energy. Regardless of the energy carrier, heat conduction is a diffusive process [54].

The law used to describe the heat transfer process depends on the scale at which the heat transfer is being analyzed. This scale is best described in terms of the Knudsen number

$$\mathrm{Kn} = \frac{\lambda}{l}$$

where λ is the mean free path of the energy carrier in the medium and l is a characteristic length of interest. At very small scales, when $\mathrm{Kn} > 0.1$, energy transport in solids is best described by the Boltzmann Transport equation. At large scales, that is, when $\mathrm{Kn} < 0.1$, the rate of heat conduction is described by Fourier's law,

$$\vec{q}'' = k\nabla T.$$

By performing an energy balance on an element within a stationary solid, one can produce the heat equation,

$$\rho c \frac{\partial T}{\partial t} = \nabla \cdot (k\nabla T) + g$$

where g represents a volumetric generation term. This equation can be understood, from left to right as stating that the time rate of change of energy within a differential element is equal to the net rate of energy entering the differential element plus volumetric energy generation within the element.

The heat equation is general—that is, it can be used in solids (or still fluids) where the Knudsen number is sufficiently large as described. Depending on the situation being analyzed, however, it can be simplified through a number of assumptions including constant material properties, steady state, reduced dimensionality, and no generation. For example, constant property, one dimensional, steady state conduction with no generation is described by

$$\frac{\partial^2 T}{\partial x^2} = 0.$$

Boundary and initial conditions are required, in addition to these equations, to fully characterize a given scenario. Of particular concern for conjugate heat transfer is the boundary between a solid and a fluid. This topic will be addressed in section 5.3.

5.2   Energy Transport in Fluids

Energy transport in fluids is more complicated than heat conduction in solids because in fluids energy is not only transferred through diffusion but also by convection of the fluid. This convective motion must be determined in order to solve the temperature field. This section will discuss the equations necessary to describe energy transport in fluids. The importance of fluid behavior near the interface between solid and fluid boundaries, known as the boundary layer,

will be discussed. The turbulent flow regime will be described and a sample of methods available for treating it will be identified.

5.2.1 Transport Equations

By examining a stationary differential control volume within a flow, the equations of motion and energy can be determined. Each of the equations is developed from conservation laws. The first is from conservation of mass.

$$\frac{\partial \rho}{\partial t} + \nabla \cdot \rho \vec{V} = 0$$

where $\vec{V}$ is the velocity field of the fluid. This equation states that the change of mass per unit volume within the differential element plus the net flow of mass per unit volume into the element is equal to zero. This equation can be simplified, depending on the situation being analyzed. In the case of incompressible flow, the density is not a function of time or position. This leaves

$$\nabla \cdot \vec{V} = 0.$$

The second equation is determined from conservation of momentum. Because momentum is a vector quantity, three equations are required, one for each spatial direction, in 3 dimensional flow. Using indicial notation, these equations can be written with a single expression

$$\rho \frac{D\vec{V}}{Dt} = \vec{B_f} - \nabla p + \frac{\partial}{\partial x_j} \left[\mu \left(\frac{\partial v_i}{\partial x_j} + \frac{\partial v_j}{\partial x_i} \right) + \delta_{ij} \lambda_b \nabla \cdot \vec{V} \right]$$

where the material derivative operator, $\frac{D}{Dt} = \frac{\partial}{\partial t} + (\vec{V} \cdot \nabla)$, is used. Additionally, B_f is used for body forces, such as gravity. δ_{ij} is the Kronecker delta function. In this equation the fluid has been assumed to be Newtonian.

The terms in this expression describe, from left to right, that the total change of momentum within the differential element is equal to the change provided by body forces, the pressure gradient, molecular viscosity, μ, and bulk viscosity, λ_b. Note here the differential element is arbitrarily small, such that turbulence would be directly simulated. Additional modeling approaches to accommodate turbulence when larger fluid elements are used in simulation will be introduced in section 5.2.3.

The combination of these equations with the continuity equation constitutes what are known as the Navier-Stokes (NS) equations. No general solution for these equations exists. Even with simplifications, only a limited number of analytical solutions exist. For incompressible flows without changes in elevation, and assuming constant viscosity, the equations reduce to

53

$$\rho \frac{D\vec{V}}{Dt} = -\nabla p + \mu \nabla^2 \vec{V}$$

A final transport equation is determined by analyzing a differential element with respect to conservation of energy.

$$\rho c_p \frac{DT}{Dt} = \nabla \cdot k\nabla T + \beta T \frac{Dp}{Dt} + \mu \Phi$$

where c_p is the specific heat at constant pressure, β is the coefficient of thermal expansion, and Φ is a dissipation function. Kinetic energy and pump work terms are assumed small and have been neglected. This equation states that the time rate of change of thermal energy within the differential element is equal to the net heat that diffuses into the element plus the work done on the element plus the kinetic energy converted to thermal energy through frictional interactions.

With the assumption of incompressible fluid, and constant thermal conductivity, the equation becomes

$$\rho c \frac{DT}{Dt} = k\nabla^2 T + \mu \Phi \,.$$

Having established the equations that describe the interior of fluid domains, it is appropriate to now consider the behavior of fluids along a solid-fluid boundary.

5.2.2   Boundary Layer on a Flat Plate

When considering flow over a solid surface, the viscous terms in the NS equations are only important in a small region near the interface surface between the fluid and the solid. This region is known as the viscid boundary layer. Outside of this boundary layer, the fluid can be treated as inviscid, and the equations simplify significantly.

The boundary layer comes into existence because of the tendency of a fluid to "stick" to a surface. That is, the fluid in contact with a surface tends to remain in the same location even as fluid further away from the surface flows past. This phenomenon is known as the no-slip condition. A consequence of the no slip condition is that a gradient in the velocity of the fluid, normal to the surface, exists. In flow over a flat plate, the velocity goes from 0 at the surface of the solid object to the free stream velocity, V_∞, at some distance from the surface of the solid object, as shown in Figure 35 [55]. This region, where the velocity changes, is known as the boundary layer. The edge of this boundary layer is typically defined as the distance, δ, at which the fluid velocity reaches 99% of V_∞.
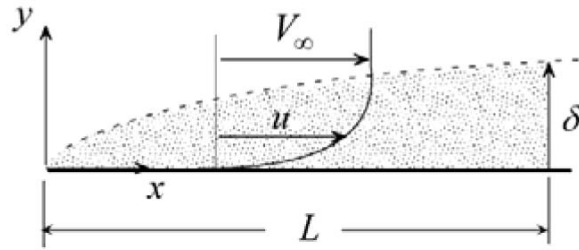
Figure 35 A boundary layer along a flat plat [55]

Within the boundary layer, a number of simplifying assumptions can be made through scale analysis. Focusing only on 2 dimensions, the first assumption, confirmed by experimental observation for most cases of interest is that

$$\frac{\delta}{L} \ll 1$$

where L is, again, some characteristic length along the flat plate. Similarly, if it is assumed that the following are of corresponding scale,

$$u \sim V_\infty$$

$$x \sim L$$

$$y \sim \delta$$

where u is the velocity in the x-direction along the plate, the relative sizes of the terms in the NS equations can be compared and those terms that are significantly smaller can be eliminated. From these terms, and continuity, an estimate for the scale of the velocity in the y-direction can be determined as

$$\frac{\partial v}{\partial y} = -\frac{\partial u}{\partial x}$$

$$v \sim V_\infty \frac{\delta}{L}.$$

Each term in the momentum equations can now be compared using the above relationships. Doing so, for example indicates that $u\frac{\partial u}{\partial x}$ is of the same order as $\frac{\partial v}{\partial y}$, but that $\frac{\partial^2 u}{\partial x^2} \ll \frac{\partial^2 v}{\partial y^2}$. This latter relationship suggests that the first term can be neglected without significantly affecting the solution of the equations. Continuing this process through each term of the momentum equation, and after a number of simplifying assumptions the following equations can be obtained,
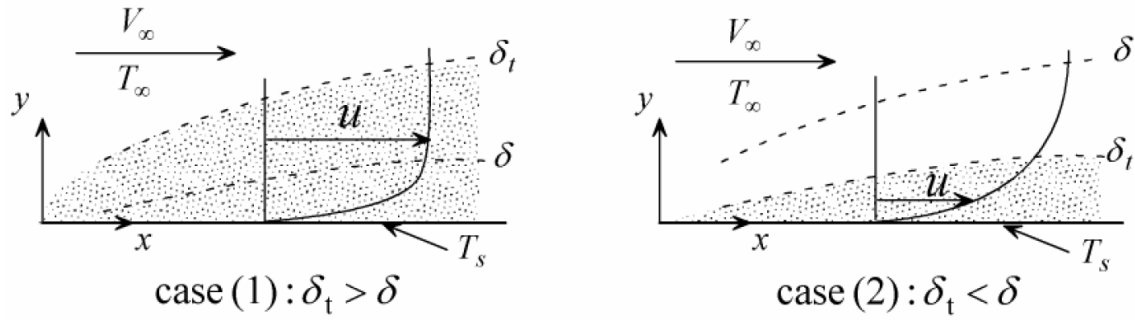
Figure 36 The thermal boundary layer for two cases [55]

$$u\frac{\partial u}{\partial x} + v\frac{\partial v}{\partial y} = -\frac{1}{\rho}\frac{dp_\infty}{dx} + v\frac{\partial^2 u}{\partial y^2}.$$

Following a similar procedure making use of a thermal boundary layer, δ_t, which contains the temperature gradient between the solid and the flowing fluid, as in Figure 36, it can be shown that the energy equation within the boundary layer reduces to

$$u\frac{\partial T}{\partial x} + v\frac{\partial T}{\partial y} = \alpha\frac{\partial^2 T}{\partial y^2}.$$

where α is the thermal diffusivity. The assumptions used in the generation of these equations are as follows: "(1) Continuum, (2) Newtonian fluid, (3) two-dimensional process, (4) negligible changes in kinetic and potential energy and (5) constant properties…: (6) slender surface, (7) high Reynolds number (Re > 100), and (8) high Peclet number (Pe > 100). (9) steady state, (10) laminar flow, (11) no dissipation, (12) no gravity, and (13) no energy generation" [55].

5.2.3 Turbulent Flows

Within the list of the previous assumptions, number 10 requires that the flow be laminar. Flowing fluids can generally be described as falling into one of two regimes: laminar or turbulent (with a transition region between the two). Laminar flow is characterized by a smooth predictable flow pattern and is observed in low velocity flow and high viscosity fluids, specifically in flows where the viscous forces dominate the inertial forces. Turbulence appears when the forces associated with the momentum of the flowing fluid overcome the frictional forces associated with the fluid viscosity. The Reynolds number is a non-dimensional ratio of inertial forces to viscous forces, and thus can be used to predict the presence of turbulence [56].

"Turbulent flows are characterized mainly by unsteadiness, vorticity, three dimensionality, dissipation, wide spectrum of scales, and large mixing rates" [57]. This chaotic nature makes deterministic approaches difficult and explains why turbulence is usually modeled with statistical

tools. "But within this chaotic motion is a localized identifiable structure: regions of intermittent, swirling patches of fluid called eddies" [55].

Eddy formation and character description can be viewed in different ways. For example,

"A common view of eddy formation is depicted in [Figure 37]. An eddy begins as a disturbance near the wall – perhaps a small fluctuation in velocity – that begins rotating a fluid element. A small vortex filament forms that rolls along the wall and in a line normal to the flow. The vortex filament does not stay straight for long: because of its rotation within the surrounding flow, there is a tendency for the filament to lift up from the wall, like a rotating cylinder in a flowing fluid. Eventually some part of the filament begins to lift, where it is now exposed to a higher velocity flow. The lifted region of the vortex filament is now dragged further down the flow, and in doing so it gets stretched into a shape referred to as a horseshoe or hairpin vortex. Vortex stretching increases the kinetic energy of the vortex, and is thought to be a major mechanism for the main flow to transfer energy to the turbulence. Weaker, secondary vortices may form next to the hairpin vortex as well. Eventually the vortex becomes unstable, and breaks up from its
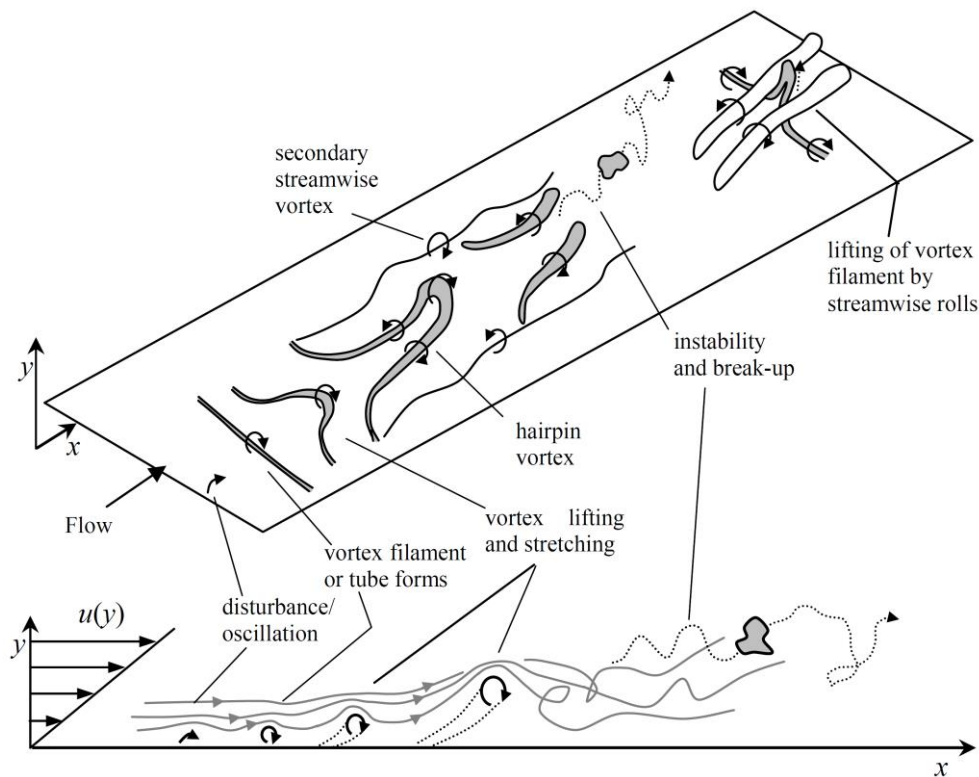
Figure 37 Formation and propagation of turbulent eddies [55]

own oscillations or by interaction with some other eddy. Streamwise rolls, which may be the remnants of prior hairpin vortices, may also be responsible for lifting vortex filaments from the wall." [55]

Turbulent eddies can also be thought of as parcels of fluid that have properties (temperature, velocity, etc.) distinct from the fluid that surrounds them. The distance such a parcel can travel while retaining its distinct identity can be considered a characteristic length, l_c. The velocity at which the eddy travels can also be considered a characteristic velocity, u_c. These two, along with the kinematic viscosity, v_v, can be used to determine a turbulent Reynolds number,

$$Re_t = \frac{l_c u_c}{v_v}.$$

Dividing the characteristic length by the characteristic velocity will produce a time that is called the eddy turnover time, which represents the lifespan of the eddy [55].

Eddies within a flow exist in a wide range of sizes, from the size of the characteristic length of the entire flow, down to the smallest scales within a flow. The larger eddies contain most of the kinetic energy. Inertial forces break up these larger eddies into smaller eddies. The process repeats with the smaller eddies in a cascade of continually decomposing eddies. The smallest eddies have relatively little kinetic energy, but carry the majority of the vorticity. The cascade continues until the eddies reach the point where the turbulent Reynolds number is about 1. At this point, the high vorticity corresponds to a great deal of shear stress, and the viscous effects of the fluid surpass the inertial effects. The eddies dissipate and their energy is converted to heat [55]. Figure 38 illustrates this process.

The previous description establishes the challenge of quantitatively characterizing turbulence. The most useful descriptions in the literature utilize a statistical approach. The next section will discuss the Reynolds averaged NS (RANS) equations. Later sections will make use of these equations. Additionally, as described above, turbulent flow is distinct from laminar flow. This distinctiveness is not limited to the bulk flow, but also affects the fluid behavior in the boundary layer, as is discussed in section 5.2.3.2.

5.2.3.1 *Modeling Turbulent Flow*
Osbourne Reynolds suggested modeling turbulence as a perturbation of an average property, illustrated in Figure 39, as in

$$c = \bar{c} + c'$$

where the bar indicates the average and the prime indicates the fluctuations about the average.
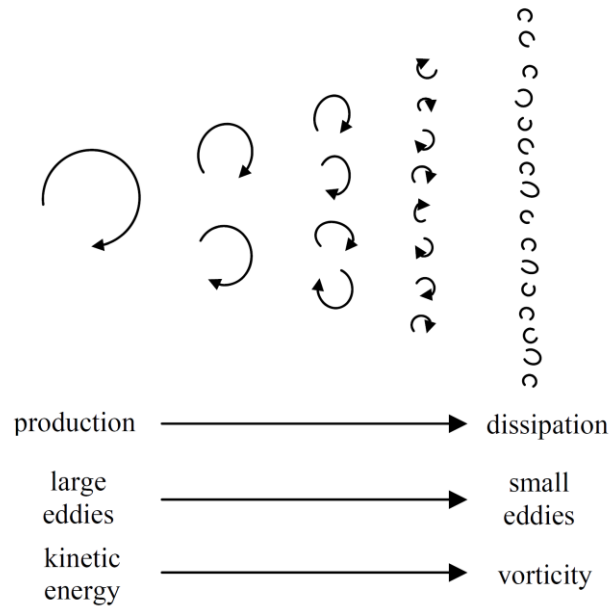
Figure 38 An illustration of the turbulent eddy cascade [55]

a. velocity profiles

b. fluctuating component
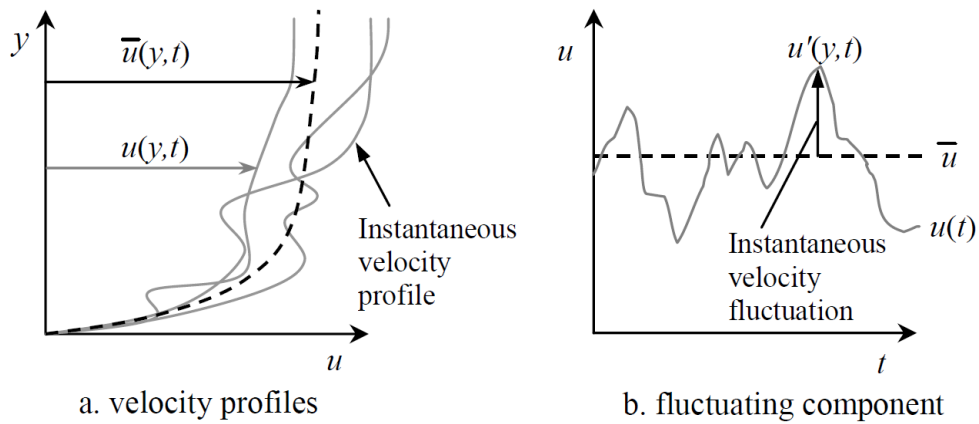
Figure 39 Turbulence as the sum of an average value and a fluctuation [55]

The average is given by

$$\bar{c} = \lim_{t \to \infty} \frac{1}{t} \int_{t_0}^{t_0+t} c \, dt' \,.$$

By substituting these perturbations into the fluid transport equations for incompressible, constant property flows, the following equations in indicial notation can be produced

$$\frac{\partial \bar{v}_j}{\partial x_j} = 0$$

$$\rho \frac{\partial \bar{v}_i}{\partial t} + \rho \frac{\partial (\bar{v}_i \bar{v}_j)}{\partial x_j} = -\frac{\partial \bar{P}}{\partial x_i} + \frac{\partial}{\partial x_j} \left[\mu \left(\frac{\partial \bar{v}_i}{\partial x_j} + \frac{\partial \bar{v}_j}{\partial x_i} \right) - \rho \overline{v_i' v_j'} \right]$$

$$\rho c \frac{\partial \bar{T}}{\partial t} + \rho c \frac{\partial (\bar{v}_i \bar{T})}{\partial x_i} = \frac{\partial}{\partial x_i} \left(k \frac{\partial \bar{T}}{\partial x_i} - \rho c \overline{v_i' T'} \right)$$

These equations are known as the Reynolds averaged Navier-Stokes (RANS) equations plus the energy equation with Reynolds decomposition less the kinetic energy terms. They are almost identical to the equations established earlier, except for the presence of $\rho \overline{v_i' v_j'}$ in the momentum equation and $\rho c \frac{\partial}{\partial x_i} \overline{v_i' T'}$ in the energy equation. The first term is known as the Reynolds stress (or turbulent shear stress) because it appears to act as an additional stress like that caused by the shear stress terms, while the second term is known as the Reynolds heat flux (or turbulent heat flux) because it acts as a turbulence induced heat flux [55].

The new terms that result from Reynolds decomposition represent new unknowns to the transport equations without providing additional equations to help solve them. This situation is known as the closure problem. It can be solved by either modeling the terms or writing transport equations for these unknowns themselves, though additional transport equations may introduce additional unknowns as well [56].

A first step in many of the closure models seeks to simplify the Reynolds stress and heat flux. Because of how these terms appear in the equations, it is common to assume that the Reynolds stress can be modeled as proportional to the mean strain rate,

$$-\rho \overline{v_i' v_j'} = \epsilon_m \left(\frac{\partial \bar{v}_i}{\partial x_j} + \frac{\partial \bar{v}_j}{\partial x_i} \right)$$

and the Reynolds heat flux as proportional to the temperature gradient,

$$-\rho c \overline{v_i' T'} = \rho c \epsilon_h \frac{\partial \overline{T}}{\partial x_i}$$

where ϵ_m and ϵ_h ,the momentum eddy diffusivity (or eddy viscosity) and the thermal eddy diffusivity, are proportionality constants and are properties of the flow, not material properties of the fluid. This is known as the Boussinesq approximation. Before examining the details of the remaining steps in a sample of methods developed for addressing the closure problem, the boundary layer equations developed earlier will be updated to account for turbulence.

5.2.3.2 Turbulent Boundary Layer

In laminar flow, viscous diffusion is the mechanism by which the boundary layer develops. In turbulent flow, the advection carried out by the random motion of turbulent eddies also contributes to development of the boundary layer [55]. Through turbulence, those eddies with higher velocity, which are further from the surface, move closer to the surface where their higher momentum tends to speed up the flow. Similarly, near the edge of the boundary layer, turbulence carries eddies below the bulk velocity into the main flow, slowing it and essentially pushing the edge of the boundary layer further from the surface. The effect of these interactions is shown in Figure 40 which compares a turbulent and a laminar boundary layer. Two primary observations are that the velocity gradient near the surface is much greater for turbulent flow, and the size of the boundary layer is also greater in turbulent flow [55].

The steeper velocity gradient at the wall suggests that the wall friction is greater in turbulent flow. This essentially indicates that the turbulent eddies act to transfer more momentum to the surface. Similar observations are made with regard to the temperature boundary layer, where it can be observed that the turbulent eddies also enhance heat transfer [55].

Using the Reynolds averaged transport equations, and following the same procedure for scale analysis used in section 5.2.2, the following turbulent boundary layer equations for 2
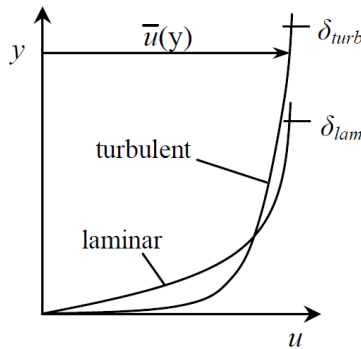
Figure 40 A comparison of a turbulent and a laminar boundary layer [55]

dimensional, incompressible, steady state flow can be written,

$$\frac{\partial \bar{u}}{\partial x} + \frac{\partial \bar{v}}{\partial y} = 0$$

$$\rho \left(\bar{u} \frac{\partial \bar{u}}{\partial x} + \bar{v} \frac{\partial \bar{u}}{\partial y} \right) = -\frac{d\bar{p}}{dx} + \frac{\partial}{\partial y} \left(\mu \frac{\partial \bar{u}}{\partial y} - \rho \overline{u'v'} \right)$$

$$\rho c \left(\bar{u} \frac{\partial \bar{T}}{\partial x} + \bar{v} \frac{\partial \bar{T}}{\partial y} \right) = \frac{\partial}{\partial y} \left(k \frac{\partial \bar{T}}{\partial y} - \rho c \overline{v'T'} \right).$$

Using the eddy viscosity and thermal eddy diffusivity and dividing by density and heat capacity, the last two equations can be rewritten as

$$\bar{u} \frac{\partial \bar{u}}{\partial x} + \bar{v} \frac{\partial \bar{u}}{\partial y} = -\frac{1}{\rho} \frac{d\bar{p}}{dx} + \frac{\partial}{\partial y} \left[(v_v + \epsilon_m) \frac{\partial \bar{u}}{\partial y} \right]$$

and

$$\bar{u} \frac{\partial \bar{T}}{\partial x} + \bar{v} \frac{\partial \bar{T}}{\partial y} = \frac{\partial}{\partial y} \left[(\alpha + \epsilon_h) \frac{\partial \bar{T}}{\partial y} \right].$$

The boundary layer in turbulent flow exhibits a universal velocity profile. It can be divided into an inner and an outer region. The inner region, which takes up between 10 to 20% of the boundary layer, can be further divided up into different regions where either molecular or eddy viscosity dominate as well as the area where they are of similar magnitude [57]. Molecular viscosity dominates close to the wall because the boundary imposed by the wall blocks momentum transfer of turbulent eddies there, making eddy viscosity approximately 0. This region is called the viscous or laminar sublayer.

To describe the mean velocity at different locations within the boundary layer, dimensional analysis is again used. It is also assumed that the mean velocity depends only on a few parameters: distance from the wall, density, dynamic viscosity, and the shear stress at the wall, τ_w. The mean velocity is nondimensionalized by dividing by a quantity known as the friction velocity,

$$v_\tau \equiv \sqrt{\frac{\tau_w}{\rho}},$$

and is written as

$$v^+ \equiv \frac{\bar{v}}{v_\tau}.$$

This value, along with wall coordinates given by

$$y^+ \equiv \frac{y\rho v_\tau}{\mu},$$

are used to write the law of the wall

$$v^+ = f(y^+)$$

where f indicates an unknown function. Analysis of this relation shows that close to the wall, within the linear sublayer,

$$v^+ = y^+$$

while further away from the wall,

$$v^+ = \frac{1}{\kappa}\ln(y^+) + C$$

Experimentation has provided the constants as well as the regions of applicability for these equations.

$$v^+ = y^+, \qquad y^+ \in (0, 5-7)$$

$$v^+ = 2.44\ln(y^+) + 5.0, \qquad y^+ \geq 50$$

Between the regions where these two equations apply is a buffer layer where the behavior transitions from linear to logarithmic. Figure 41 shows these relationships plotted against a number of experimental data sets.

There are several models which describe the whole boundary layer with a single equation. These include those by Van Driest [59], Spalding [60], Reichardt [61 cited in 55], Cole [62], and Whitfield [63].

The outer portion of the boundary layer in a turbulent flow accounts for between 80 and 90% of the boundary layer. In flow constrained on only one side by a solid surface, the edge of the boundary layer is irregular. That is, any specific location towards the edge of the boundary layer will experience intermittent burst of turbulence. For flows within a pipe or channel, generally, once the flow is fully developed, the boundary layer extends to the center of the pipe or channel [58]. In section 6.2.2.8 "wall functions" used by some of the computational models to simulate the velocity profile near the wall are discussed. These wall functions extend to $y^+ = 11.06$ and
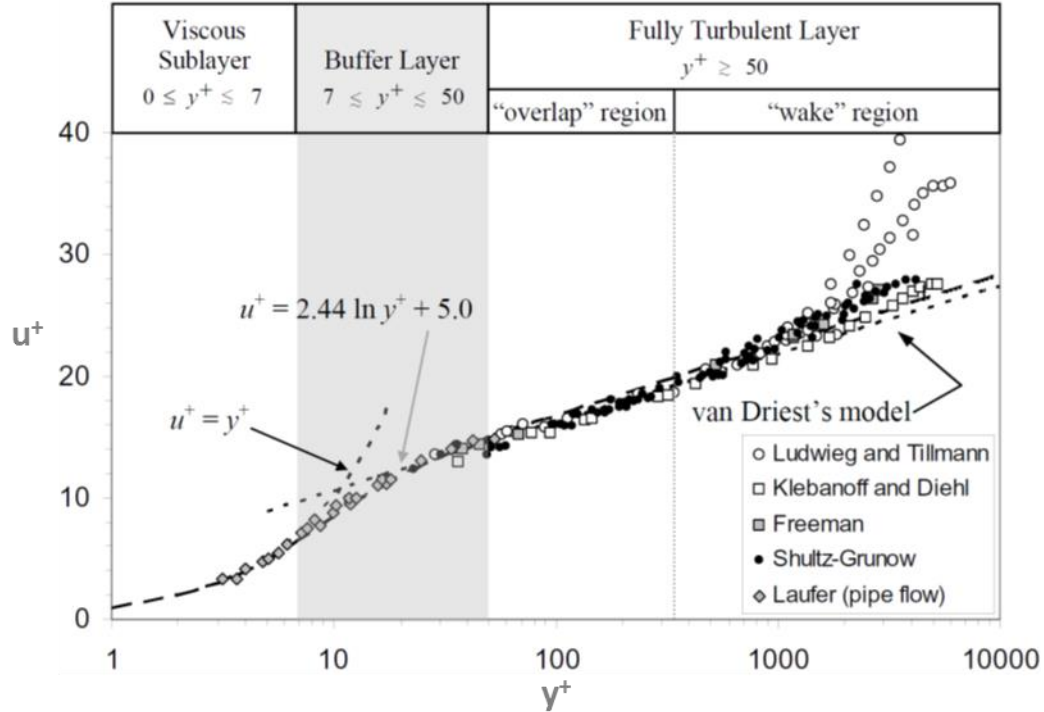
Figure 41 The universal velocity profile for turbulent boundary layers [57]

have a form similar to the universal velocity profile discussed in this section. This approach to handling the near-wall behavior was introduced by Prandtl over a century ago.

5.2.3.3   The Closure Problem: Specific Turbulence Models

Returning to the closure problem of having more unknowns than equations, several different solutions have been proposed. These solutions are generally categorized by the number of additional differential equations used. This section will identify a number of these different solutions including mixing length or algebraic models, one and two equation models, and will end with a brief description of two approaches that do not depend on Reynolds averaging.

5.2.3.3.1   Mixing Length Models

The simplest of the closure models are known by many names, including mixing length models, algebraic models, eddy viscosity models, or zero equation models. These models are unique in that they do not introduce additional differential equations while solving the closure problem.

The basic approach of these models is to assume that the eddy viscosity can be written as a product of a velocity scale, u, and a length scale, l_{mix}. This assumption can be seen by examining the dimensions of a viscosity term, and is written as

$$\nu_t \sim u \times l_{mix}.$$

Also, by assuming a time scale such that

$$\frac{u}{l_{mix}} \sim \frac{\partial \bar{v}}{\partial y},$$

then

$$v_t = l_{mix}^2 \left| \frac{\partial \bar{v}}{\partial y} \right|.$$

Making use of Boussinesq's approximation produces,

$$-\rho \overline{v'u'} = l_{mix}^2 \left| \frac{\partial \bar{v}}{\partial y} \right|^2$$

which was the goal of the effort.

This approach was first introduced by Prandtl. It gives rise to the aforementioned logarithmic form of the boundary layer velocity function by assuming $l_{mix} = \kappa y$ and that the shear stress is constant near the wall. The approach has also been used to generate other formulations of mixing length models including those by Cebeci and Smith [64], Michael et al [65 cited in 58], Johnson and King [66] and Johnson and Coakley [67], Cebeci and Chang [68], Baldwin and Lomax [69].

While this approach is fairly easy, [57] identifies the following drawbacks:

"a. These do not directly account for the flow history effects, as the eddy viscosity is related to local mean flow properties.

b. Eddy viscosity reduces to zero when the mean strain rate equals zero, but this condition may not be valid in all cases.

c. These models cannot be directly applied to three-dimensional flows without any modification.

d. These are incomplete models because the mixing length needs to be specified. In addition, a prescription of the mixing length is not unique and depends on a particular flow configuration being studied.

e. The formulation of the model becomes difficult if there is a sudden change in the flow conditions. For example, the above mentioned prescription of the eddy viscosity for wall bounded flows can be used up to the trailing edge of an airfoil and subsequently the flow has the characteristics of separated flow and it is difficult to prescribe the mixing length for the separated region."

5.2.3.3.2   One Equation Models

One equation models are those that make use of one additional transport equation for one of the unknowns, or a related variable. Two example of variables used include the turbulence kinetic energy and the eddy viscosity itself. Turbulent kinetic energy is defined as

$$k_t = \frac{1}{2}(v_i v_i)^{1/2}.$$

The Spalart and Allmaras (SA) model is a well-known one equation model based on a semi-empirical transport equation for eddy viscosity itself. It offers an advantage over mixing length models in that it performs well under adverse pressure gradients, such as those found in aerospace applications and turbomachinery [57].

With the exception of SA, one equation models are less popular than two equation models [58]. In cases where more information about the turbulence is required, two equation models are more commonly used.

5.2.3.3.3   Two Equation Models

A large number of two equation models exist. In these models two properties or variables are modeled directly with transport equations. Turbulence kinetic energy, k_t, and its dissipation rate, ϵ^h, are modeled in the eponymous k-ϵ model. The standard k-ϵ model is the foundation for many other models. It is "…widely used in industrial turbulent flow and heat transfer computations mainly due to its robustness, computational economy, and reasonable accuracy for a wide variety of turbulent flows" [57]. It depends on $u \sim \sqrt{k_t}$ for a velocity scale, and uses the dissipation rate to calculate a length scale [56].

In this model, the Reynolds stress is provided as

$$\epsilon_m \equiv C_\mu \frac{k_t^2}{\epsilon^h}$$

where C_μ is a constant, and k_t and ϵ^h are determined by solving their respective transport equations. The exact transport equations cannot be solved, but instead require certain terms to be modeled. The turbulence kinetic energy equation, for example, requires 2 of the 7 final terms to be modeled. The dissipation equation requires 7 of 10 terms to be modeled [57]. This necessity makes these equations semi-empirical. By way of comparison, in a one equation model that uses k_t, the ϵ^h is modeled with an algebraic equation. In these two equation models, a transport equation for ϵ^h is solved after some specific terms within that transport equation are modeled.

A number of observations can be made about the standard k-ϵ model.

"1. It is a high turbulence Reynolds number, $Re_t = \frac{k_t^2}{\epsilon_m}$, model. Therefore it cannot be applied without suitable modifications in the regions with low Re_t, for example, in the vicinity of a solid wall, in laminar to turbulent transition, etc.

2. In this model the solution of two separate transport equations for k_t and ϵ^h allows the turbulent velocity and length scales to be independently determined. It is one of the simplest complete models of turbulence.

3. Each term of the modeled transport equation for k_t almost accurately represents the corresponding term in the exact equation. However, the gross effect of several terms in the exact dissipation equation is modeled by few terms, or in other words, there is no one to one correspondence between different terms in the modeled and exact transport equations for dissipation" [57].

As mentioned above, walls are a challenge to the standard k-ε model because of the no slip condition and the resulting high gradients near the wall. These issues can be handled with semi-empirical wall functions to obtain the required information near the walls rather than solving the differential equations. This approach does not place the first node against the wall, but instead at some distance from the wall, thus avoiding the no-slip condition. This method also simplifies the effort required by avoiding resolving the region right against the wall. The wall functions may use the wall co-ordinates and universal law of the wall introduced in section 5.2.3.2 to simplify the expressions for properties near the wall. Many different wall functions exist for different conditions [57].

While wall functions are easier, and require fewer grid points (and thus less computational effort), another, though more challenging, approach to accurate results near walls is the use of low-Re models. These models include a damping feature in the turbulence kinetic energy term of the k-ε model, and an additional term in the dissipation equation to ensure that dissipation remains large at solid surfaces [56].

Several variants of the k-ε model have been developed. These include the Renormalization group (RNG) k-ε, which attempts to satisfy physical constraints that exist in reality but are not satisfied in the standard k-ε model [70]. While this approach brings the model closer to reality, in experience it has little effect on the actual results in simulations [56]. Another variant is the Realizable k-ε [71]. This model presents a new formulation for turbulent viscosity as well as a new transport equation for ε. The model ensures that the quantity $\overline{v_i v_i} \geq 0$ which other models fail to do.

Another two equation model that can be considered a variant of the k-ε model, even though it was first proposed several decades before the k-ε model, is the k-ω model [72 and 73 cited in 56]. This model uses a transport equation for the specific dissipation rate, ω_t, which can be considered as

$$\omega_t \sim \frac{\epsilon^h}{k_t}.$$

This model accurately handles low Re situations and thus is appropriate for wall bounded flows [57]. A somewhat hybrid model of the k-ω and k-ε models is found in the shear stress transport (SST) k-ω model [74]. While the actual machinery is more complicated, in essence, this model utilizes the accurate wall behavior of the k-ω model and transitions to the k-ε model further from the wall.

Other modifications have been made to these standard models to more accurately account for various phenomena. These include modifications to account for intermittency in dissipation [75], intermittency of boundary layers [76], and streamline curvature [77], among others.

5.2.3.3.4   DNS and LES
Direct numerical simulation (DNS), as the name implies, involves numerically solving the "…governing partial differential equations for instantaneous, three-dimensional turbulent flow…" without modeling [57]. In order to accurately solve these equations, the grid and time step spacing must be small enough to capture the smallest spatial scales of turbulence where dissipation occurs and the shortest times scales which correspond to the lifetimes of the smallest eddies. As such it is a computationally intense approach, though it offers the possibility of more accurate results than those based on averaging. By making use of molecular kinematic viscosity and dissipation, the length, (η_L), time, (τ), and velocity (v_{sc}) scales of DNS can be determined [57]

$$\eta_L = \left(\frac{v_v}{\epsilon^h}\right)^{\frac{1}{4}}, \qquad \tau = \left(\frac{v_v}{\epsilon^h}\right)^{\frac{1}{2}}, \qquad v_{sc} = (v_v\epsilon^h)^{\frac{1}{4}}.$$

Also, using an integral length scale, L_f, which is related to the lengths of the boundary conditions and peak energy in the system, a Reynolds number can be calculated as

$$\mathrm{Re}_{L_f} \equiv \frac{u'L_f}{v}$$

which can be related to the required number of degrees of freedom (n_{dof}), [56]

$$n_{dof} \propto \mathrm{Re}_{L_f}^{\frac{9}{4}}.$$

68
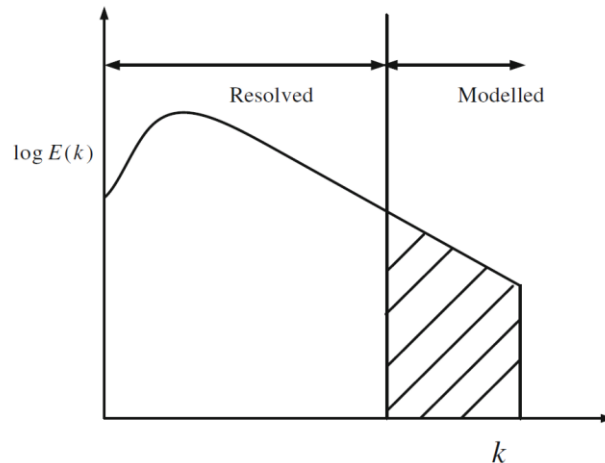
Figure 42 Filtering effect of LES [57]

This relationship shows why high Re DNS simulations are relatively rare—they quickly become too computationally demanding.

Large eddy simulation (LES) is similar to DNS, but has lower computational requirements because in LES a spatial filter is applied to the mass, momentum, and energy equations, thus reducing the grid resolution required [56]. Figure 42 provides a typical energy spectrum with the log of the kinetic energy (E) as a function of the wavenumber (k) from an LES simulation that shows the results of this filtering process. The filtered information is called the subgrid component, and is modeled with a subgrid scale model (SGS model) [57]. A number of SGS models exist including Smagorinsky [78], Dynamic [79], and Scale Similarity [80].

While still modeling certain effects, filtering is considered an accurate approach because the larger eddies are affected by boundary conditions, however, the small eddies are generally homogenous and isotropic, and are essentially independent of the flow geometry [57]. In addition to a coarser spatial grid, LES can also use larger time steps because the smaller time steps required in DNS are associated with smaller spatial scales.

Both LES and DNS need accurate initial conditions because the initial conditions affect the results for several eddy turnover times. It is typical to start a run with randomly generated initial turbulence, run a few eddy turnovers and then use those results as the starting point for the actual calculations.

In addition to the actual computations required, DNS and LES generate enormous amounts of data because of the fine grid resolution and the small time steps. Storing and manipulating this data also represent a challenge [57]. In general, DNS is not used for design efforts because of its computational intensity; rather "DNS can provide comprehensive views of turbulence dynamics

69

and enables the assessment of numerous quantities which cannot be found experimentally such as correlations involving pressure" [56].

5.3   Coupling Solid and Fluid Energy Transport

The previous descriptions of conduction and fluid transport only lightly touched on the important feature of boundary conditions. When conduction through a solid and heat transfer from that solid into a fluid are modeled, the coupling takes place at the boundary or interface surface between the two domains. This is referred to as conjugate (or coupled or adjoint) heat transfer. Mathematically, this is signified by a general boundary condition at the interface boundary on each domain. At that boundary the temperature on either side, assuming a completely wetted surface, is equal, and the heat flux on either side is equal. Mathematically,

$$T_{solid}(x_{interface}, t) = T_{liquid}(x_{interface}, t)$$

where $x_{interface}$ is a general variable that indicates the position along the interface. This relationship does not require that the temperature be constant along the interface. Similarly,

$$q_{solid}(x_{interface}, t) = q_{liquid}(x_{interface}, t)$$

This leaves a large set of equations (the heat equation, mass, momentum, and energy equations along with all of the required boundary conditions) to be solved simultaneously. Fortunately, in cases when the density can be assumed constant, the mass and momentum equations can be solved independent of the energy equation, thus reducing the severity of the coupling—that is, the results of the mass and momentum solution still feed into the energy equation, but information does not flow from the energy equation to mass and momentum [56].

Methods have been developed for addressing this large set of equations. One approach is to treat the unknown temperature interface boundary condition as a modified constant temperature boundary condition, and solve for the heat transfer as

$$q = h_* \times f\left(\frac{\partial T}{\partial x}, \frac{\partial^2 T}{\partial x^2}, \ldots \frac{\partial^n T}{\partial x^n}\right)$$

where h_* is the isothermal convective heat transfer coefficient [81 and 82].

To avoid the mathematical complexity (and often impossibility) of determining an analytical solution to these conjugate heat transfer problems, the more common approach is a numerical solution. Because of the separate domains which the equations (the heat equation and the fluid transport equations) describe, a numerical approach solves the equations independently, while coupling the two at the physical interface. A number of methods exist for performing this coupling. A direct approach includes all of the equations in a single system and solves them simultaneously while a segregated approach solves each domain separately and uses the results

70

from one solution as input to the other. A typical approach is referred to as Picard coupling, which uses the following algorithm to solve sets of couple equations, ϕ_1 and ϕ_2,

Guess x_1 and x_2.

For iteration k:

Solve $\phi_1\left(x_1^k, y_2\left(x_2^{k-1}\right)\right) = 0$ for x_1^k

Solve $\phi_2\left(y_1\left(x_1^k\right), x_2^k\right) = 0$ for x_2^k

Iterate until converged. In these equations y represents a transfer function that is dependent on x.

5.4   Remarks Relevant to Hot Spot Model

Keeping in mind the purpose of this review, attention is now turned to the hotspot model. This section will cover the approaches for dealing with conjugate heat transfer in hotspot models in the past and what this review suggests about current approach options.

5.4.1   Previous Treatments

In most of the previous work modeling hotspots, the conjugate heat transfer over the hotspots was modeled as a convective heat transfer boundary condition with a constant value for h. Hilvety and Chapman [32], McClain [34], and Kirkpatrick [33] all used an h of 15,000 [Btu/hr-ft^2-°F]. McClain mentions use of a modified Hausen relationship for determining the heat transfer coefficient within the coolant flow channels. [31] gives the relationship as

$$\text{Nu} = 0.116 \left(\text{Re}^{\frac{2}{3}} - 125\right)\text{Pr}^{\frac{1}{3}} + \frac{1}{3}\frac{D_e^{\frac{2}{3}}}{z}\frac{\mu}{\mu_s}^{0.14}$$

where D_e is the equivalent diameter in feet, z is the length along the fuel element in inches, and μ_s is the viscosity along the surface of the wall as recommended by [83]. This recommendation is interesting because during the examination of friction factor the viscous thinning term, $\frac{\mu}{\mu_s}^{0.14}$, was found to move the friction factor model further from the data [88]. However, in making the recommendation for the heat transfer correlation, the approach was to use an already existing correlation and not develop a new one, so, it appears, the term was left in the equation.

Giles [35] improved the process when evaluating fuel plates for the ANSR. His work modeled the conjugate heat transfer over fuel defects by recalculating a local convective heat transfer coefficient based on the conditions at each location in the fuel plate where the defects were modeled. Bodey [36] modeled hotspots using COMSOL. In place of a constant convective heat transfer value, the flow over the defect was simulated. Turbulence was modeled using a k-ω

model. Tschaepe [84] similarly modeled hotspots using COMSOL, and used a k-ϵ model, with a wall function to address k-ϵ models difficulty with low Re_t numbers.

5.4.2 Current Approach Options

Applying this information to the hotspot model, a number of items need to be considered. First, which conduction heat transfer domain does this situation fall in given the small dimensions in the fuel plates? Second, is the flow through the coolant channels turbulent, and if so, which approach to turbulence is best suited for this application? Finally, does this problem best lend itself to an analytical solution through conjugate heat transfer methods or a numerical solution?

The Knudsen number is the most direct method for determining into which heat transfer domain a given situation fits. To determine the characteristic length, the dimensions of the fuel plate must be examined. The thinnest dimension is the thin end of the fuel within the fuel meat in the outer annulus. It is approximately 0.008 inches [0.203 mm] thick. Satisfying the requirement of Kn < 0.1 requires a mean free path of less than 0.02 mm for the energy carrier. While the actual mean free path is unknown, for comparison, at room temperature, the mean free path in aluminum is around 10-40 nm and in diamond is 100-460 nm [54]. Choosing a large value of 500 nm, we find that this is about 400 times smaller than is required. This result suggests the use of Fourier's law for conduction.

Under steady state and standard operating conditions within the HFIR, the Re in the coolant channels is about 71,000 [36]. This is well above that required for fully turbulent flow. Addressing which approach to turbulence to use is a more challenging question. A fuel plate coolant channel experiences a flow that has a favorable pressure gradient, no chance for flow separation (within the channel) or concern for reattachment, and very little curvature in flow. These conditions suggest that a mixing length model would likely provide sufficient accuracy. Of course, given sufficient resources LES or DNS would likely provide more accurate and better resolution solutions. Between these extremes, the one and two equation models are also available. Since this is a wall bounded flow, the standard k-ϵ model would not work without a low Re or wall function option. k-ω and SST would work well and may represent the best option because of their ability to model right up to a solid boundary.

Finally, for a number of reasons, a numerical approach to conjugate heat transfer for hotspots, rather than an analytical approach is the better option. The complicated nature of the heat generation within the fuel plate will be very difficult to handle analytically. The decision to contend with turbulence also necessitates a numerical approach.

Final decisions on the details of the approach to take depend, to some extent, on the options available within the tools that must be used. With that in mind, the next section will examine the different options available within COMSOL Multiphysics.

Chapter 6   COMSOL

6.1   COMSOL Multiphysics

COMSOL Multiphysics is a finite element modeling software program designed specifically for modeling coupled physical phenomena. It is structured modularly, consisting of a main program as well as a number of physics and software linking modules that add capabilities. This section discusses features of the main program and two modules, the computational fluid dynamics (CFD) module and the heat transfer module, which are relevant to modeling hotspots in plate fuel. The primary sources for this chapter are the user's manuals for each of those three components. All references in Section 6.1 referring to the COMSOL Multiphysics Reference Manual [85] will only give the page number, as in [p. 33]. References to other sources will not include the "p.", as in [X].

The main program contains an integrated model builder, materials library, physics interfaces (for identifying which physical phenomena are modeled), a number of solvers, including conditioners, as well as post processing and display tools. Each of these features is controlled through the addition of a node to the simulation. COMSOL carries out simulations by evaluating each node in sequence—building the geometry, applying the physics, running the solver, and performing the post processing. By adding multiple nodes of any feature (different meshes to the geometry or different portions of the physics to be modeled, for example), and controlling the sequence in which COMSOL evaluates the nodes, multiple studies can be performed [p. 199].

6.1.1   Simulation Development

The model builder allows the construction of model geometries and meshing. Model geometries can be generated with shape primitives, such as rectangles, spheres, cylinders, etc. By adding or subtracting these shapes, complicated geometries can be developed. Additionally, COMSOL allows import of complete models from other modeling software. Once a model is available, a number of options for generating meshes can be used. These include fully automated mesh generation, physics aware mesh generation, user directed mesh generation, and combinations of these.

Materials are assigned to components of a model as the model is being built or upon completion. The main COMSOL program comes with a material data base, and each module has module specific materials as well. When a material is assigned to a domain, the properties of that material are associated with the domain. These properties include functions for property dependence (such as on temperature or pressure). An optional data base containing over 2,500 materials and 20,000 functions is available [p. 557].

The physics to be solved are similarly assigned to the model. By assigning physics to each domain, default boundary conditions (BC) and initial conditions (IC), where appropriate, are also

assigned. These default BCs and ICs can be overridden by adding other boundary conditions. When two or more physics interfaces are added to a model, a multiphysics (coupling) node is automatically added to allow the user to specify the coupling that should take place between the physics interfaces. Each of the physics interfaces and multiphysics nodes can be disabled or enabled during the solution depending on the purpose of the study.

6.1.2   Solving

COMSOL has a number of different solvers and solving options from which it automatically selects based on the model size and the physics being used [p. 890]. Small models, and those with single physics interfaces are solved with a direct solver that fully couples all of the equations for the various physics [p. 158]. This approach is memory intensive, scaling with $N^{1.5}$ to N^2, where N is the number of degrees of freedom. As models become larger or include more physics, this approach becomes challenging due to memory constraints. For these simulations, COMSOL automatically selects a segregated approach and uses iterative solvers, which scale with N in memory usage [86]. The segregated solver approach solves each physics separately and then passes the results to the other physics through whatever coupling is taking place, as in the Picard iteration shown in section 5.3. This passing back and forth of solutions is repeated until convergence for the whole system is achieved [p. 160]. Different settings within the solvers, such as the tolerance for error within each of the segregated steps, can be controlled by the user to aid in obtaining a solution [p. 887].

The solution process uses a "…Newton type iterative method…" which means convergence may depend on a good initial starting value [p. 153]. Also because of this method, a segregated solver approach may fail to converge where a direct solver, given sufficient memory, would converge [86]. The guidance provided for running large, multiphysics simulations is to first solve the individual physics uncoupled, and then use those solutions as initial guesses in a coupled, segregated solution. This same procedure, solving less complicated portions of a model, is recommended for situations where one type of modeling is more computationally intense than another, for example solving with a k-ω turbulence model then using that solution as an initial guess for an SST model solution [p. 153, p. 892, p. 903]. Besides reducing computational time for the final, more complicated solution, this procedure also allows the user to do quality control, such as checking that domain and boundary settings are performing as expected. Finally, when possible, there may be value in using the solutions of a coupled, segregated approach as the initial guess for a direct, fully coupled solver to get tighter convergence.

Modeling turbulent flows will be discussed in detail in section 6.2.2, but a comment relevant to solving them will be included here. The use of a turbulence model automatically engages a segregated solution approach: NS equations in one group and the turbulence transport equations in another. To ensure that the non-linear terms in the transport equations are appropriately

74

handled, the turbulence group typically undergoes two or three iterations for each iteration of the NS group [86].

6.2 Fluid Flow Modeling

The CFD Module provides a number of capabilities including many not present in the main COMSOL program. These capabilities include "laminar and turbulent flow, Newtonian and non-Newtonian flow, isothermal and non-isothermal flow, multiphase flow, … flow in porous media… flows that occur in thin-films or in bounded regions, and in stationary and rotating domains… heat transfer, and transport and reactions of chemical species" [86]. The majority of these capabilities will not be used in this research, but this section will focus on those that will. As in the previous section, all references will be to the COMSOL CFD User's Guide [86] and will only include the page number unless otherwise noted.

Where in the previous section, the general recommendation to start with a simplified model and then build in complexity as the model is developed was suggested without specific guidance, a number of specific recommendations for model development within the CFD module are provided [p. 30]. Of the recommendations made, those relevant to this work include starting the model with constant density and viscosity and, then, after the model works, adding in dependencies for these properties [p. 31], using a simplified 2d version of the model before 3d [p. 31], and using less complicated turbulence models before more complicated [p. 32].

The remainder of this section will focus on the equations COMSOL solves for fluid flow and the turbulence models that COMSOL provides.

6.2.1 Fluid Flow Equations

A number of different physics interfaces are available within the CFD module. The most relevant to the hotspot model is the conjugate heat transfer interface. This interface includes models for non-isothermal flow as well as heat transfer within solids. The latter portion will be dealt with in section 6.3, the former is described below.

The non-isothermal flow interface uses the following form of the continuity, momentum, and energy equations

$$\frac{\partial \rho}{\partial t} + \nabla \cdot (\rho \vec{u}) = 0$$

$$\rho \frac{\partial \vec{u}}{\partial t} + \rho \vec{u} \cdot \nabla \vec{u} = -\nabla p + \nabla \cdot \left(\mu (\nabla \vec{u} + (\nabla \vec{u})^T) - \frac{2}{3} \mu (\nabla \cdot \vec{u}) \vec{I} \right) + \vec{B_f}$$

$$\rho C_p \left(\frac{\partial T}{\partial t} + (\vec{u} \cdot \nabla) T \right) = -(\nabla \cdot \vec{q}) + \vec{\tau} : \vec{S} - \frac{T}{\rho} \frac{\partial \rho}{\partial T} \bigg|_p \left(\frac{\partial \rho}{\partial t} + (\vec{u} \cdot \nabla) p \right) + \vec{Q}$$

where B_f is the body force vector, the strain rate tensor, $\vec{S} = \frac{1}{2}(\nabla\vec{u} + (\nabla\vec{u})^T)$, and Q is the heat source term for sources other than viscous heating [p. 190]. Since these equations contain terms to account for compressibility, the application of Reynold's decomposition, as was used in discussing turbulence models previously, introduces additional terms in the form of

$$\overline{\rho'u'}.$$

To avoid this complexity, Favre averaging, a density based average, is used in addition to Reynolds averaging [p. 141].

6.2.2 Turbulence Models

The CFD Module offers a number of turbulence models along with features to aid in utilizing those models. Each of the turbulence models use these Favre averaged RANS equations. These models include [p. 49]

- Algebraic yPlus
- L-VEL
- k-ϵ
- k-ω
- SST
- Low Re k-ϵ
- Spalart-Allmaras.

COMSOL's implementation of each of these models is reviewed in the following subsections.

6.2.2.1 Algebraic yPlus

The Algebraic yPlus model is an algebraic turbulence model that uses an "enhanced viscosity model based on the scaled wall distance" to account for turbulence effects [p. 54]. The model is based on Prandtl's mixing-length theory, and utilizes wall coordinates and the law of the wall [p. 142]. "It is less mesh sensitive than transport-equation models like Spalart-Allmaras or the k-ε model" [p. 142].

In this model the effective, molecular plus turbulent, nondimensionalized viscosity, v+ is given by

$$v^+ = \begin{cases} 1, & y^+ \leq y^* \\ \dfrac{1 + \chi_y}{2}, & y^+ > y^* \end{cases}$$

with $y^* = B - \frac{1}{\kappa}(\log(4\kappa) - 1)$, and $\chi_y = \sqrt{1 + 4\kappa^2(y^+ - y^*)^2}$. Using Re to get the local value of y+ by

$$
\mathrm{Re} = \begin{cases} y^{+2}, & y^+ \leq y^* \\ y^+ \left(y^* + \dfrac{1 - \chi_y}{2\kappa^2(y^+ - y^*)} + \dfrac{1}{\kappa}\log\left(\chi_y + 2\kappa(y^+ - y^*)\right) \right), & y^+ > y^* \end{cases}
$$

v+ can be calculated with values for the parameters κ and B, which by default are optimized for turbulent pipe flow [p. 54, p. 144]. This Re is determined from the local velocity and distance to the nearest wall.

6.2.2.2 L-VEL

The Length-Velocity (L-VEL) model is another algebraic turbulence model. Like Algebraic yPlus, it is less mesh sensitive than the one and two equation models. It is based on "…an extension of the logarithmic law of the wall which applies all the way down to the wall" [p. 145].

In this model, the effective viscosity is determined through

$$
v^+ = 1 + \frac{\kappa}{E}\left(e^{\kappa u^+} - 1 - \kappa u^+ - \frac{(\kappa u^+)^2}{2} - \frac{(\kappa u^+)^3}{6} \right)
$$

with the local u^+ determined through

$$
\mathrm{Re} = u^+ \left(u^+ + \frac{1}{E}\left(e^{\kappa u^+} - 1 - \kappa u^+ - \frac{(\kappa u^+)^2}{2} - \frac{(\kappa u^+)^3}{6} - \frac{(\kappa u^+)^4}{24} \right) \right)
$$

and the local Re from the local velocity and the distance to the wall. The parameters E and κ come defaulted to values optimized for internal flows.

6.2.2.3 k-ε

The k-ε model uses the "…standard two-equation k-ε with realizability constraints" [p. 56]. The realizability constraints in each of the two-equation models ensures the diagonal of the stress tensor, the $\overline{\rho u' u'}$ terms, take positive values. Turbulent kinetic energy, k, and turbulent dissipation rate, ϵ are modeled with the following equations:

$$
\rho \frac{\partial k}{\partial t} + \rho \vec{u} \cdot \nabla k = \nabla \cdot \left(\left(\mu + \frac{\mu_T}{\sigma_k} \right) \nabla k \right) + P_k - \rho\epsilon
$$

$$
\rho \frac{\partial \epsilon}{\partial t} + \rho \vec{u} \cdot \nabla \epsilon = \nabla \cdot \left(\left(\mu + \frac{\mu_T}{\sigma_\epsilon} \right) \nabla \epsilon \right) + C_{\epsilon 1} \frac{\epsilon}{k} P_k - C_{\epsilon 2} \frac{\epsilon^2}{k}.
$$

The production term is given by

$$
P_k = \mu_T \left(\nabla \vec{u} : (\nabla \vec{u} + (\nabla \vec{u})^T) - \frac{2}{3}(\nabla \cdot \vec{u})^2 \right) - \frac{2}{3}\rho k \nabla \cdot \vec{u}.
$$
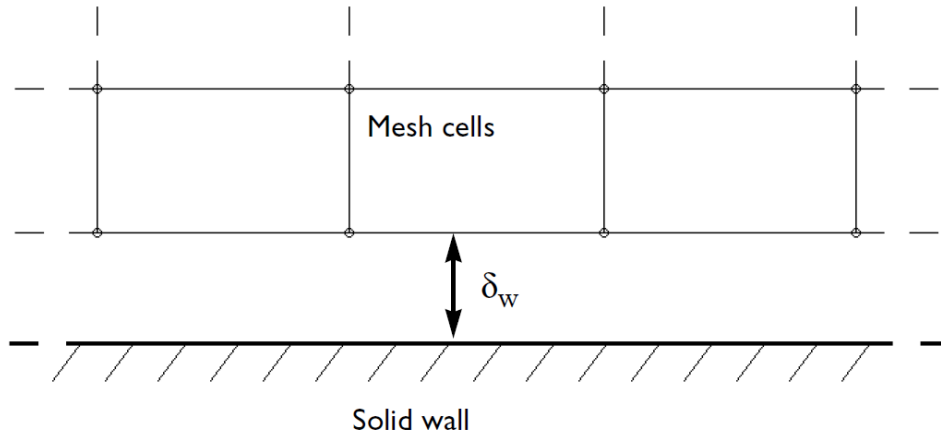
Finally, the turbulent viscosity is modeled as

$$\mu_T = \rho C_\mu \frac{k^2}{\epsilon}.$$

$C_{\epsilon 1}, C_{\epsilon 2}, \sigma_k, \sigma_\epsilon$, and C_μ are all model constants that have been "…optimized to fit as many flow types as possible" [p. 56].

Because the standard k-ϵ model is not a low-Re model, a wall function is required to describe flow near the wall [p. 149]. This wall function depends on an assumption that the computational grid is some distance, δ_w, from the wall surface, as shown in Figure 43. This distance is assumed to be located where the logarithmic layer would meet the viscous sublayer if there were no buffer layer. It is determined by

$$\delta_w^+ = \frac{\rho u_\tau \delta_w}{\mu} = 11.06,$$

where $u_\tau = C_\mu^{\frac{1}{4}}\sqrt{k}$.

6.2.2.4   k-ω
This model uses the Wilcox revised k-ω model with realizability constraints [p. 58, p. 154]. To model turbulent kinetic energy, k, and the specific dissipation, ω, the following equations are used,

$$\rho \frac{\partial k}{\partial t} + \rho \vec{u} \cdot \nabla k = P_k - \rho \beta^* k \omega + \nabla \cdot \left((\mu + \sigma^* \mu_T) \nabla k \right)$$

78

$$\rho \frac{\partial \omega}{\partial t} + \rho \vec{u} \cdot \nabla \omega = \alpha_2 \frac{\omega}{k} P_k - \rho \beta_1 \omega^2 + \nabla \cdot \left((\mu + \sigma_t \mu_T) \nabla \omega \right)$$

and

$$\mu_T = \rho \frac{k}{\omega}.$$

A number of constants and relationships are given for these equations as

$$\alpha_2 = \frac{13}{25}, \qquad \beta_1 = \beta_0 f_\beta, \qquad \beta^* = \beta_0^* f_{\beta^*}, \qquad \sigma_t = \frac{1}{2}, \qquad \sigma^* = \frac{1}{2}$$

$$\beta_o = \frac{13}{125}, \qquad f_\beta = \frac{1 + 70\chi_\omega}{1 + 80\chi_\omega}, \qquad \chi_\omega = \left| \frac{\Omega_{ij}\Omega_{jk}S_{ki}}{(\beta_0^*\omega)^3} \right|$$

$$\beta_0^* = \frac{9}{100}, \qquad f_{\beta^*} = \begin{cases} 1, & \chi_k \le 0 \\ \dfrac{1 + 680\chi_k^2}{1 + 400\chi_k^2}, & \chi_k > 0^* \end{cases}, \qquad \chi_k = \frac{1}{\omega^3}(\nabla k \cdot \nabla \omega)$$

Where Ω_{ij} is the mean rotation-rate tensor and S_{ki} is the mean strain-rate tensor. P_k is the same as in k-ϵ [p. 155]. These parameters "…are optimized to fit as many flow types as possible" [p. 58].

As implemented in the CFD module, k-ω still uses a wall function, as k-ϵ does. The wall function is treated just as in k-ϵ with β_0^* replacing $C\mu$ in determining δ_w^+ [p. 155].

6.2.2.5 *Shear Stress Transport*

Mentor's shear stress transport (SST) model of 2003 with realizability constraints is the basis for the SST model in the CFD module [p. 59]. The model essentially combines k-ω, for near wall calculations, and k-ϵ for high Re calculations with an interpolation scheme between the two [p. 156]. While in the previous subsection it was noted that k-ω as implemented within the CFD module uses a wall function, SST does not use a wall function because the k-ω portion of SST is a low-Reynolds number model [p. 59]. As such, SST resolves the flow all the way to the wall if adequate mesh refinement is provided. Additionally, "The version of the SST model in the CFD Module includes a few well-tested modifications, such as production limiters for both k and ω, the use of S instead of Ω in the limiter for μ_T, and a sharper cut-off for the cross-diffusion term" [p. 156].

The transport equations solved for this model are given by

$$\rho \frac{\partial k}{\partial t} + \rho \vec{u} \cdot \nabla k = P - \rho \beta_0^* k\omega + \nabla \cdot \left((\mu + \sigma_k \mu_T)\nabla k \right)$$

$$\rho \frac{\partial \omega}{\partial t} + \rho \vec{u} \cdot \nabla \omega = \frac{\rho \gamma_t}{\mu_T} P - \rho \beta_1 \omega^2 + \nabla \cdot \left((\mu + \sigma_\omega \mu_T) \nabla \omega \right) + 2(1 - f_{v1}) \frac{\rho \sigma_{\omega 2}}{\omega} \nabla \omega \cdot \nabla k$$

with

$$P = \min(P_k, 10 \rho \beta_0^* k \omega)$$

and

$$\mu_T = \frac{\rho a_1 k}{\max(a_1 \omega, S f_{v2})}$$

where $S = \sqrt{2 S_{ij} S_{ij}}$.

The model constants are determined by interpolation,

$$\phi = f_{v1} \phi_1 + (1 - f_{v1}) \phi_2 \quad \text{for} \quad \phi = \beta_1, \gamma_t, \sigma_k, \sigma_\omega$$

where

$$f_{v1} = \tanh(\theta_1^4)$$

$$\theta_1 = \min \left[max \left(\frac{\sqrt{k}}{\beta_0^* \omega l_w}, \frac{500 \mu}{\rho \omega l_w^2} \right), \frac{4 \rho \sigma_{\omega 2} k}{C D_{k\omega} l_w^2} \right]$$

$$C D_{k\omega} = \max \left(\frac{2 \rho \sigma_{\omega 2}}{\omega} \nabla \omega \cdot k, 10^{-10} \right)$$

and

$$f_{v2} = \tanh(\theta_2^2)$$

$$\theta_2 = \max \left(\frac{2 \sqrt{k}}{\beta_0^* \omega l_w}, \frac{500 \mu}{\rho \omega l_w^2} \right).$$

As with both k-ϵ and k-ω, the SST, "… parameters are optimized to fit as many flow types as possible" [p. 59].

6.2.2.6 Low-Re k-ϵ

The CFD Module offers a low-Re k-ϵ model in the form of the AKN k-ϵ model. As a low-Re model, it resolves the flow all the way to the wall and does not require a wall function [p. 60]. This is accomplished through the inclusion of damping functions in the transport equations [p. 159],

$$\rho \frac{\partial k}{\partial t} + \rho \vec{u} \cdot \nabla k = \nabla \cdot \left(\left(\mu + \frac{\mu_T}{\sigma_k} \right) \nabla k \right) + P_k - \rho \epsilon$$

$$\rho \frac{\partial \epsilon}{\partial t} + \rho \vec{u} \cdot \nabla \epsilon = \nabla \cdot \left(\left(\mu + \frac{\mu_T}{\sigma_\epsilon} \right) \nabla \epsilon \right) + C_{\epsilon 1} \frac{\epsilon}{k} P_k - f_\epsilon C_{\epsilon 2} \frac{\epsilon^2}{k}$$

where the production term is the same as in standard k-ϵ and the turbulent viscosity has been modified to include a damping term

$$\mu_T = \rho f_\mu C_\mu \frac{k^2}{\epsilon}.$$

Here

$$f_\epsilon = \left(1 - e^{-\frac{l^*}{3.1}} \right)^2 \cdot \left(1 - 0.3 e^{-\left(\frac{R_t}{6.5} \right)^2} \right)$$

and

$$f_\mu = \left(1 - e^{-\frac{l^*}{14}} \right)^2 \cdot \left(1 + \frac{5}{R_t^{\frac{3}{4}}} e^{-\left(\frac{R_t}{200} \right)^2} \right)$$

where

$$l^* = \frac{\rho u_\epsilon l_w}{\mu}, \qquad R_t = \frac{\rho k^2}{\mu \epsilon}, \qquad u_\epsilon = \left(\frac{\mu \epsilon}{\rho} \right)^{\frac{1}{4}}.$$

Again, the "…parameters are optimized to fit as many flow types as possible" [p. 160].

6.2.2.7   Spalart-Allmaras

The Spalart-Allmaras turbulence model is also included in the CFD module, but it is used primarily for aerodynamic applications and has been tuned for airfoil and compressor blade simulations [p. 162]. It is not applicable to modeling this flow.

6.2.2.8   Auxiliary Model Features

The proper functioning of the turbulence models depends on additional functions and features within COMSOL. This section will discuss a few of those including wall functions as boundary conditions, turbulence initialization and inlet values.

As mentioned in their respective sections, the k-ε and k-ω models each make use of wall functions, restricting the computational grid to a distance, δ_w, from the actual boundary. The wall functions then provide the boundary conditions for the fluid state from the wall to δ_w. Those conditions are specified as follows: for velocity, a no-penetration condition at the surface

$$\vec{u} \cdot \vec{n} = 0$$

for shear stress

$$\vec{n} \cdot \vec{\sigma} - (\vec{n} \cdot \vec{\sigma} \cdot \vec{n})\vec{n} = \rho u_\tau \frac{\vec{u}}{|\vec{u}|} \max\left(C_\mu^{\frac{1}{4}} \sqrt{k}, u_\tau \right)$$

where

$$\vec{\sigma} = \mu(\nabla\vec{u} + (\nabla\vec{u})^T)$$

and

$$u_\tau = \frac{|\vec{u}|}{\frac{1}{\kappa_v}\ln(\delta_w^+) + B}$$

with $\kappa_v = 0.41$, the von Karman constant, and $B = 5.2$.

The turbulent kinetic energy BC is

$$\vec{n} \cdot \nabla k = 0,$$

and dissipation is

$$\epsilon = \frac{C_\mu^{\frac{3}{4}} k^{\frac{3}{2}}}{\kappa_v \delta_w}$$

or

$$\omega_w = \frac{\rho k}{\kappa \delta_w^+ \mu}$$

for k-ε or k-ω respectively [p. 149, p. 155].

These boundary conditions for k-ε and k-ω, as well as the transport equations for other models require the distance to the wall from each computational element. This distance is determined by using the wall distance initialization [85].

The two equation models require an initialization of the turbulent kinetic energy and dissipation. These are initialized by default to the following conditions

$$\vec{u} = 0, \quad p = 0, \quad k = \left(\frac{10\mu}{\rho\left(0.1 l_{mix}^{lim}\right)}\right)^2, \quad \epsilon = \frac{C_\mu k_{init}^{\frac{3}{2}}}{0.1 l_{mix}^{lim}}, \quad \omega = \frac{\sqrt{k_{init}}}{0.1 l_{mix}^{lim}}$$

where the mixing length limit, l_{mix}^{lim} is defaulted to the smallest dimension within the flow and can be adjusted by the user [p. 153, p. 155].

When turbulent conditions of the inlet are unknown, the following approximations can be used

$$k = \frac{3}{2}\left(|\vec{U}| I_T\right)^2, \quad \epsilon = C_\mu^{\frac{3}{4}} \frac{k^{\frac{3}{2}}}{L_T}, \quad \omega = \frac{\sqrt{k}}{(\beta_0^*)^{\frac{1}{4}} L_T}$$

where I_T is the turbulence intensity and ranges from 0.05% (for good wind tunnels) to 5% to 10% for fully turbulent flows, and L_T is the turbulence length scale and corresponds to 0.07 hydraulic diameters for fully developed channel flow [p. 164].

6.2.2.9 Energy Equation

By using the non-isothermal flow or conjugate heat transfer physics interface, the energy equation is included in the fluid flow equations. This equation makes use of Favre averaging and defines the Favre average of temperature as

$$\tilde{T} = \frac{\overline{\rho T}}{\bar{\rho}}$$

where the bars indicate the usual Reynolds average, and

$$T = \tilde{T} + T''$$

where T'' is the temperature fluctuation due to turbulence [p. 192]. With this definition, the energy equation, neglecting kinetic energy terms, can be written as

$$\bar{\rho} C_p \left(\frac{\partial \tilde{T}}{\partial t} + \tilde{u}_j \frac{\partial \tilde{T}}{\partial x_j}\right) = \frac{\partial}{\partial x_j}\left((\lambda + \lambda_T)\frac{\partial \tilde{T}}{\partial x_j}\right) + \tilde{\tau}_{ij}\tilde{S}_{ij} - \frac{\tilde{T}}{\bar{\rho}}\frac{\partial \bar{\rho}}{\partial \tilde{T}}\bigg|_{\bar{p}} \left(\frac{\partial \bar{p}}{\partial t} + \tilde{u}_j \frac{\partial \bar{p}}{\partial x_j}\right)$$

where λ has been used for thermal conductivity to prevent confusion with the turbulent kinetic energy [p. 195]. Also,

$$\tau_{ij} = 2\mu S_i - \frac{2}{3}\mu \frac{\partial u_k}{\partial x_k}\delta_{ij}.$$

83

Finally, the Kays-Crawford model

$$Pr_T = \left(\frac{1}{2Pr_{T\infty}} + \frac{0.3}{\sqrt{Pr_{T\infty}}}\frac{C_p\mu_T}{\lambda} - \left(0.3\frac{C_p\mu_T}{\lambda}\right)^2 \left(1 - e^{-\lambda\frac{1}{0.3C_p\mu_T\sqrt{Pr_{T\infty}}}}\right)\right.$$

is used for the turbulent conductivity with Pr_T at infinity set to 0.85 [p. 195].

Temperature wall functions are also provided [p.196]. Assuming a fluid temperature, T_f, in the computational cell nearest a segment of wall at temperature T_w, the heat flux between the two is

$$q_{wf} = \frac{\rho C_p C_\mu^{\frac{1}{4}} k^{\frac{1}{2}}(T_w - T_f)}{T^+}$$

where

$$T^+ = \begin{cases} Pr\delta_w^+, & \delta_w^+ < \delta_{w1}^+ \\ \left(15Pr^{\frac{2}{3}} - \frac{500}{\delta_w^{+2}}\right), & \delta_{w1}^+ \le \delta_w^+ < \delta_{w2}^+ \\ \frac{Pr_T}{\kappa}\ln(\delta_w^+) + \beta, & \delta_{w2}^+ \le \delta_w^+ \end{cases}$$

and

$$\delta_w^+ = \delta_w \rho \frac{\sqrt{C_\mu^{\frac{1}{2}} k}}{\mu}, \qquad \delta_{w1}^+ = \frac{10}{Pr^{\frac{1}{3}}}, \qquad \delta_{w2}^+ = 10\sqrt{10\frac{\kappa}{Pr_T}}, \qquad Pr = \frac{C_p\mu}{\lambda}$$

$$\beta = 15Pr^{\frac{2}{3}} - \frac{Pr_T}{2\kappa}\left(1 + \ln\left(1000\frac{\kappa}{Pr_T}\right)\right).$$

For clarity, in the preceding relationships, k is the turbulent kinetic energy, κ is the von Karman constant, and λ is the thermal conductivity.

6.3 Heat Transfer

The Heat Transfer Module extends the capabilities of the main COMSOL program into many areas of heat transfer. These areas include bioheat transfer, heat transfer in porous media, with phase change, lumped isothermal domain, thin structures, surface-to-surface radiation, radiation in participating media, thermal contact, moist air fluid, out-of-plane heat transfer, and temperature dependence of surface tension [87]. This section will focus on the areas of the heat transfer module relevant to this project including heat transfer in solids, the thin layer

approximation, and thermal contact. As with the previous 2 sections, all references to the COMSOL Heat Transfer Module User's Guide[87] will only include the page number.

6.3.1 Heat Transfer in Solids

The heat transfer in solids interface allows for the deformation of the solid, and as such solves the following energy equation

$$\rho C_p \left(\frac{\partial T}{\partial t} + \vec{u}_{trans} \cdot \nabla T \right) + \nabla \cdot (\vec{q} + \vec{q}_r) = -\beta T {:} \frac{DS}{Dt} + Q$$

where $\vec{u}_{trans}$ accounts for translational motion of the solid, $\vec{q}$ is the heat flux by conduction and $\vec{q}_r$ by radiation. The first term on the right accounts for thermoelastic effects in the solid, where S is the second Piola-Kirchhoff stress tensor, β is the coefficient of thermal expansion and D/Dt indicates the material derivative. Q captures all additional heat sources.

6.3.2 Thin layer Approximation

The Heat Transfer Module contains a method for dealing with thin structures without generating an extremely fine mesh around and within the structure. In essence, the thin structure is treated as a boundary rather than a domain, and a different set of equations are used to describe heat transport across the boundary [p. 117]. Figure 44 shows the reduction in nodes that can be accomplished using the thin layer approximation by comparing a copper wire modeled as a domain and the same wire represented as a thin layer.

Three options are provided for designating a boundary as a thin layer: conductive, resistive, or general. A conductive thin layer boundary condition is an appropriate selection when the layer is thin relative to areas of interest in the model and the material in the thin layer is a good thermal conductor relative to the adjacent material. When these conditions are met, the heat equation

Copper wire modeled
with a mesh

Copper wire represented
as a conductive layer
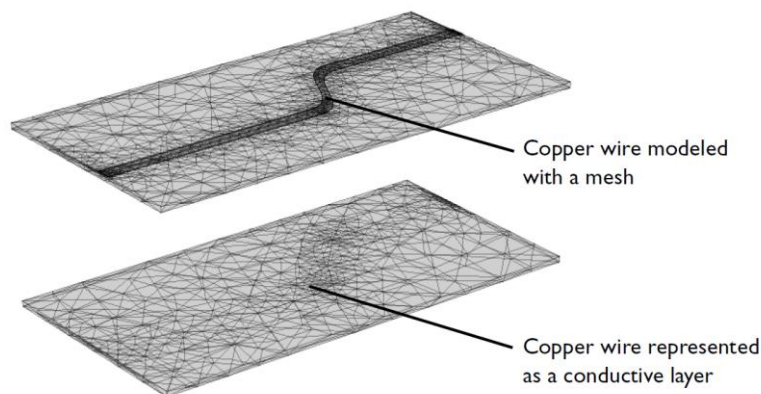
Figure 44 Illustration of the reduction of mesh requirements when using a thin layer approximation instead of modeling a wire [p.118]

85

reduces to

$$d_s\rho C_p \frac{\partial T}{\partial t} + \nabla_t \cdot \vec{q}_s = d_s Q + q_0$$

where d_s is the thickness of the layer, Q is a density distributed heat source within the layer, and q_0 is the received out-of-plane heat source, with

$$\vec{q}_s = -d_s k \nabla_t T$$

where ∇_t is the tangential gradient and is defined by

$$\nabla_t = \nabla T - (\nabla T \cdot \vec{n})\vec{n}$$

where $\vec{n}$ is the normal vector for the thin layer [p. 199]. This set of equations essentially assumes that $\nabla T \cdot \vec{n} = 0$, that is, there is no temperature variation in the normal direction within the layer [p.118].

The documentation relevant for the resistive thin layer boundary only discusses heat transfer across the boundary. It is assumed that the appropriate conditions for this feature are similar but opposite to the conduction thin layer—that the layer is thin and that the thermal conductivity is low compared with adjacent material. Since no mention of heat transfer along the layer is mentioned, it seems likely that the resistive layer limits heat transfer to the direction normal to the layer. Given Figure 45 as a reference, the following equations are provided [p. 120]

$$-\vec{n}_d \cdot \vec{q}_d = -k_s \frac{T_u - T_d}{d_s}$$
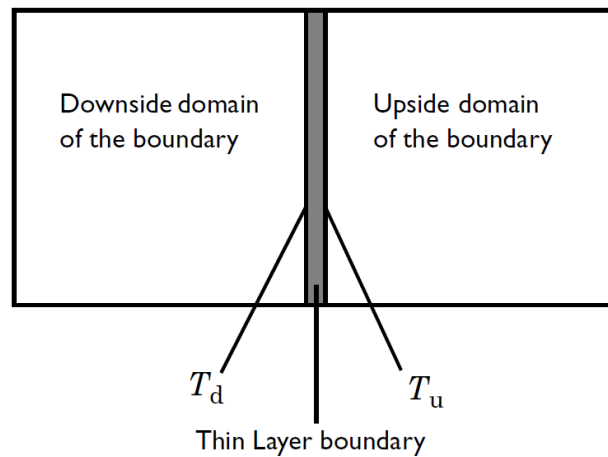
Figure 45 Conceptual illustration of the resistive thin layer boundary [p. 120]

86

$$-\vec{n}_u \cdot \vec{q}_u = -k_s \frac{T_d - T_s}{d_s}$$

where the u and d represent the "up" and "down" surfaces. No mathematical description of the "general" thin layer is provided in the documentation.

6.3.3 Thermal Contact

Heat transfer across two surfaces in thermal contact can be modeled with a thermal contact boundary condition in the Heat Transfer Module. The flux across the boundary is determined through

$$-\vec{n}_d \cdot \vec{q}_d = -h(T_u - T_d) + rQ_b$$

$$-\vec{n}_u \cdot \vec{q}_u = -h(T_d - T_u) + (1 - r_p)Q_b$$

where r_p is the heat partition coefficient, and Q_b is a general heat source [p. 353, p. 355].

Two methods for determining h are provided: Cooper-Mikic-Yovanovich (CMY) correlation for plastic contact and Mikic correlation for elastic contact.

CMY is determined as follows

$$h_c = 1.25 k_{contact} \frac{m_{asp}}{\sigma_{asp}} \left(\frac{p}{H_c} \right)^{0.95}$$

with

$$k_{contact} = \frac{2k_u k_d}{k_u + k_d}, \qquad \theta_{asp} = \sqrt{\theta_{u,asp}^2 + \theta_{d,asp}^2}, \qquad \text{for } \theta = m_{asp}, \sigma_{asp}$$

where m_{asp} is the mean slope of the surface and σ_{asp} is the mean surface asperity height. The ratio of pressure to microhardness, $\left(\frac{p}{H_c} \right)$ is determined as follows

$$\frac{p}{H_c} = \left(\frac{p}{c_1 \left(1.62 \frac{\sigma_{asp}}{\sigma_0} m_{asp} \right)^{c_2}} \right)^{\frac{1}{1+0.071c_2}}$$

with $\sigma_0 = 1$ μm, and

$$\frac{c_1}{H_0} = 4.0 - 5.77 \frac{H_B}{H_0} + 4.0 \left(\frac{H_B}{H_0} \right)^2 - 0.61 \left(\frac{H_B}{H_0} \right)^3$$

$$c_2 = -0.37 + 0.442 \frac{H_B}{c1}$$

where H_B is the Brinell hardness and H_0 is 3.178 GPa [p. 169].

The Mikic correlation is provided as

$$h_c = 1.54 k_{contact} \frac{m_{asp}}{\sigma_{asp}} \left(\frac{\sqrt{2}p}{m_{asp}E'} \right)^{0.94}$$

where E' is the reduced modulus.

6.4 Application to the Hotspot Modeling

Based on the information presented thus far, a basic approach is outlined for the development of the model. First, the general guidance of simple to complicated model development and testing is followed. A 2d representation of a flat fuel plate and coolant channels is developed. A series of simulations, each adding more physics than the last, is performed with that model and a sensitivity analysis is performed once all of the relevant physics is in place.

In order to follow this outline, additional pieces of information are required. The first is to how to best model the non-bond. Two options have been identified: the thin layer approximation and thermal contact. From the description provided here and in the user's manuals, it is presumed that the thermal contact feature and the thin layer feature could be used to model a non-bond. The next section, Chapter 7, presents a study designed to provide this information.

The second deals with which turbulence model is most appropriate for this simulation. This can be addressed by performing simulations using the various turbulence models and comparing the results. Mass and Energy balances, pressure drops, velocity fields, and numerical uncertainty with the different turbulence models are compared in sections 8.4 and 9.2.3.2.

Chapter 7   Comparison of Thin Layer and Thermal Contact Models

As discussed in section 6.3, COMSOL offers two features that may be useful in modeling non-bonds: the thin layer feature and the thermal contact feature. The stated benefit of using these features is that they eliminate the need to generate an extremely fine mesh around small features of a model by incorporating the features into a boundary.

An analysis was performed to compare these options. The analysis consisted of comparing models of a fuel plate (a heat source within aluminum cladding) with (1) no special boundary, (2) the thin layer boundary, and (3) the thermal contact boundary. These models were run without a non-bond, with a non-bond (in the form of an adiabatic disc for the thin layer and base model and a representative non-bond for the thermal contact), and with a fuel segregation both with and without a non-bond. The model without a special boundary was used as a control to which the other models were compared.

7.1   Models

The model was created to mimic, to some extent, the legacy hotspot model, Figure 15. However, instead of using a 2d axis symmetric geometry, a 2d plane geometry was used. Additionally, to see the edge effects of the thin layer and thermal contact boundaries, the fuel did not extend the entire length of the model. The model is illustrated in Figure 46. Note that the vertical scale is significantly enlarged. In this model the rectangle in the center is the fuel meat, the larger rectangle is the cladding, and the red line beneath the fuel is the boundary where the non-bonds are located. The base model cladding is 38.1 mm [1.5 in] long and 1.27 mm [0.05 in] thick. The
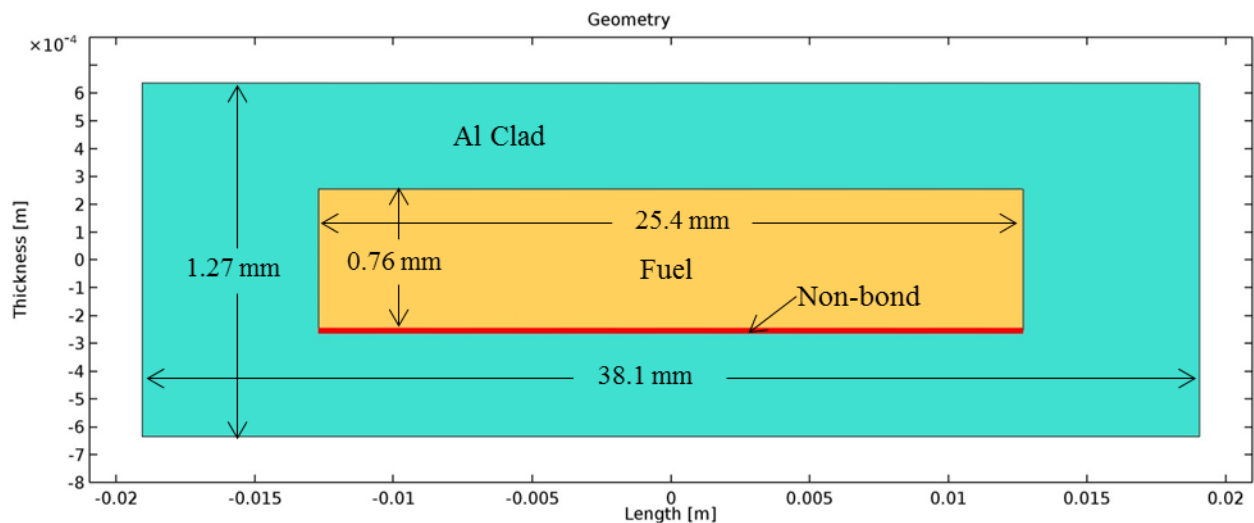
Figure 46 Geometry of hotspot model where the tan center represents the fuel, the cyan rectangle represents the cladding, and the red line indicates the boundary where the non-bond is placed (Note: thickness is exaggerated)
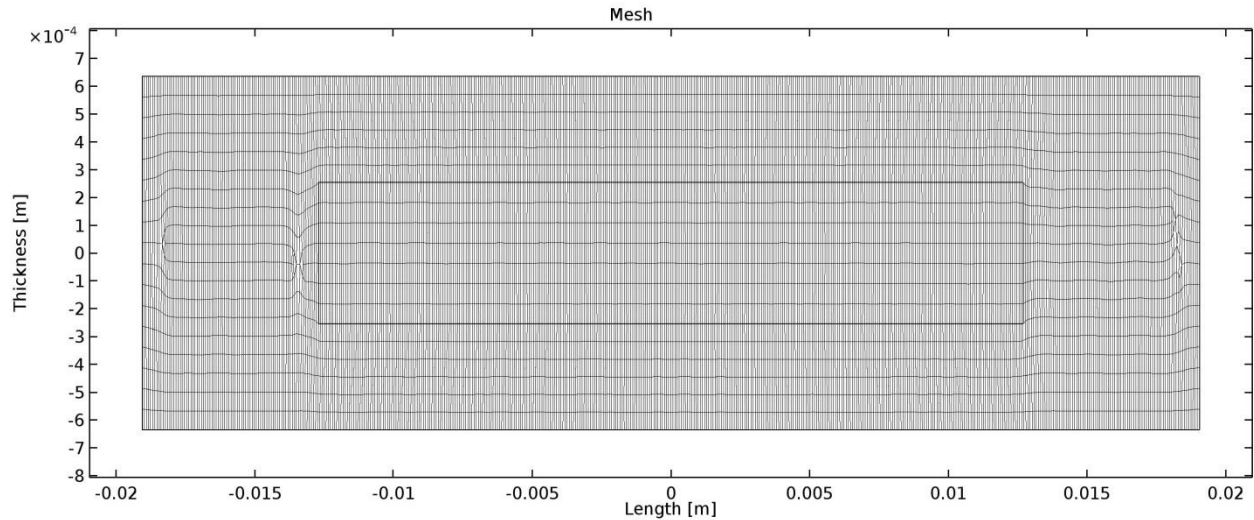
Figure 47 "Finer" mesh used for the majority of images and data produced (Note: thickness is exaggerated)

fuel is centered within the cladding and is 25.4 mm [1 in] long and 0.76 mm [0.03 in] thick.

Figure 47 shows the mesh used for the majority of the images and data. This mesh was generated using the "semiconductor" settings, "Finer" for the grid size, with free quadrilaterals. The mesh includes 9455 quadrilateral elements, a minimum element quality of 0.5306, and an average of 0.97. Additional meshes were used for comparison. Using the "Fine" setting generated a coarser mesh with 750 elements, while using the "Extra Fine" setting generated a mesh with 36,759 elements.

The built-in material properties for aluminum were used for both cladding and fuel. Heat generation rates and the convective heat transfer rate from the legacy model were used for both fuel and cladding. The fluid temperature was set to 322 K [120°F] for the convective boundary condition. The left and right edges of the model were insulated, though this boundary condition has negligible effect on the heat transfer within the model. This is referred to as the base model.

7.1.1 Thin Layer (TL)

For the thin layer and thermal contact models, the bottom of the fuel portion, the red line in Figure 46, was used as the altered boundary. The goal was to have the models with an altered boundary (either thin layer or thermal contact) be identical to the base model, with the unaltered boundary, except when a non-bond was present. Approaching this goal required that the heat flux through the altered boundary be as close to the unaltered boundary as possible.

The thin layer is mathematically modeled as

90

$$-\vec{n}_d \cdot \vec{q}_d = -k_s \frac{T_u - T_d}{d_s}$$

where the d and u subscripts indicate the "up" and "down" side of the boundary, k_s is the thermal conductivity of the layer, and d_s is the thickness of the boundary. The up and down side of the boundary represent the same location, physically, and operate as coincident nodes between two domains. When the boundary is between two materials with different thermal conductivities the geometric mean of the two conductivities is used. Within COMSOL the options available are to use the material properties of the two surfaces to determine the conductivity or to provide a user defined thermal conductivity. The built-in material properties were used, and a thin layer thickness of 1 μm was used.

7.1.2 Thermal Contact (TC)

COMSOL offers two models for thermal contact conductance, CMY for plastic contact and Mikic for elastic contact. As discussed in section 4.3.8, the non-bond contact is elastic and this analysis used the Mikic elastic contact model, which is repeated here as

$$-\vec{n}_d \cdot \vec{q}_d = -h_c(T_u - T_d) + rQ_b \tag{11}$$

with

$$h_c = 1.54 k_{contact} \frac{m_{asp}}{\sigma_{asp}} \left(\frac{\sqrt{2}p}{m_{asp}E'} \right)^{0.94}$$

where m_{asp} is the average slope of the surface topology, σ_{asp} is the average asperity height, or surface roughness, E' is the reduced modulus of the two materials, $k_{contact}$ is the geometric mean of the thermal conductivity of the two materials, and p is the contact pressure between the two surfaces. To reduce the impact of the altered boundary on the temperature field, the heat transfer through this thermal contact boundary should equal that through the unaltered boundary. The following steps were taken to achieve this result. By rearranging the conductance relationship, h_c becomes

$$h_c = \left[1.54 \, m_{asp}^{0.06} \left(\frac{\sqrt{2}p}{E'} \right)^{0.94} \right] \frac{k_{contact}}{\sigma_{asp}}.$$

Substituting this into (11) produces

$$-\vec{n}_d \cdot \vec{q}_d = \left[1.54 \, m_{asp}^{0.06} \left(\frac{\sqrt{2}p}{E'} \right)^{0.94} \right] \frac{k_{contact}}{\sigma_{asp}} (T_u - T_d) + rQ_b.$$

By assuming heat transfer can only occur normal to the contact and that there is no heat generation within the boundary, this can be rewritten as

$$-q_{tc} = \left[1.54 \, m_{asp}^{0.06} \left(\frac{\sqrt{2}p}{E'}\right)^{0.94}\right] \frac{k_{contact}}{\sigma_{asp}} (T_u - T_d).$$

By letting

$$C_{tc} = 1.54 \, m_{asp}^{0.06} \left(\frac{\sqrt{2}p}{E'}\right)^{0.94}$$

This becomes

$$-q_{tc} = C_{tc} \, k_{contact} \frac{T_u - T_d}{\sigma_{asp}}.$$

Recognizing that σ_{asp}, the mean asperity height of the surfaces in contact, is the length separating the up and down temperature, it can be seen that this is essentially Fourier's law with an added coefficient, C_{tc}. This coefficient can be thought of as the modification to heat transfer due to the constrictions imposed by the contacting surfaces. In order to make this heat transfer equal to what would take place if there were complete thermal contact, this coefficient must equal 1.

Due to the lack of surface data available for the non-bond, values for m_{asp} and σ_{asp} were unknown. As such, a wide range of values for these terms was considered. Table 4 provides

Table 4 Values of p/E' as a function of slope to set C_{tr} equal to 1

Slope	p/E'
1	0.4467
0.5	0.4669
0.2	0.4950
0.1	0.5174
0.05	0.5408
0.01	0.5993
0.001	0.6942
0.00001	0.9314
0.000001	1.0789
0.00000001	1.4475
0.000000001	1.6767
1E-10	1.9422

values for $\frac{p}{E'}$ based on the slope used, to set C_{tc} to 1. The slope, m, has a relatively weak influence on heat transfer. Except where noted, values of 1 μm [39 μin] for the asperity height, a slope of 0.2 and the corresponding $\frac{p}{E'}$ of 0.4950 for the parameters are used for the thermal contact layer.

7.1.3   Modeling Non-bonds

The purpose of examining the thin layer and thermal contact models was to evaluate their ability to simulate a non-bond between the fuel and cladding. To this end, an adiabatic disk was introduced as a model for a non-bond in the thin layer model. This mimics how non-bonds have been modeled in the past. The adiabatic disc was produced by using a function to provide the user-defined thermal conductivity. The center 1.59 mm [0.0625 in] of the function was set to 0 while the remainder of the length was set to the built-in thermal conductivity. A 0.254 mm [0.01 inch] transition, an arbitrarily chosen length, was included to soften the otherwise discontinuous thermal conductivities. Use of a smaller transition, 0.0254 mm [0.001 in] produced an increase in the numerical distortion in flux around the simulated non-bond. This transition maintained a continuous second derivative. That function, conductivity for adiabatic disk, cfad(X), is plotted in Figure 48.

The non-bond was similarly simulated in the thermal contact boundary: a function was developed where 1.59 mm [0.0625 in] at the center of the boundary used the realistic values of 3.1 MPa [450 psi] for the contact pressure and 70 GPa for the reduced modulus, while the remainder of the boundary used the same 0.4950 ratio identified above. Again, a 0.254 mm [0.01 in] transition region was used between these two values. This function, pressure over elastic modulus, PoE(x), Figure 49, was then supplied in the "pressure" field and 1.0 was supplied in the
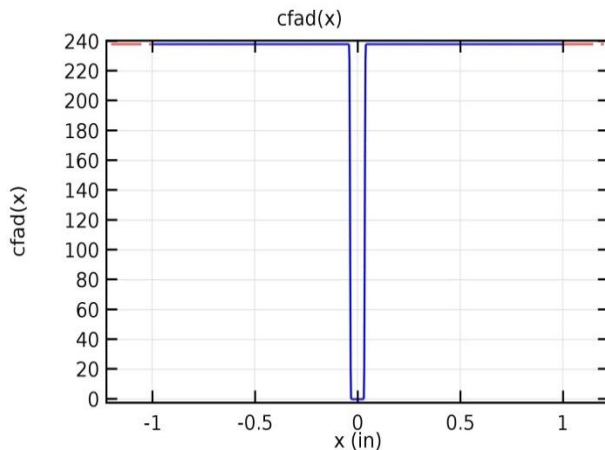
Figure 48 Function used to define thermal conductivity of the thin layer to produce an adiabatic disc
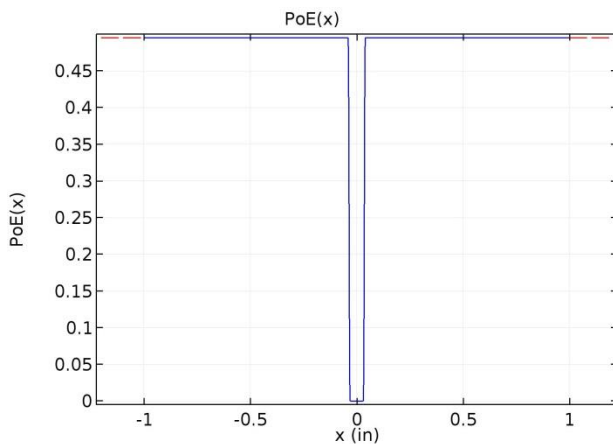
Figure 49 Pressure over Elastic modulus function used to simulate a non-bond in the thermal contact model

"elastic modulus" field of the thermal contact menu.

To simulate the non-bond directly in the base model, a geometric entity was inserted at the center of the plate immediately below the fuel. Figure 50 shows this geometry, with the non-bond appearing in black. The non-bond was assigned aluminum properties, as well, with the thermal conductivity set to 0.001 [W/m K] to model extremely poor conductivity, approaching adiabatic.

This new geometric entity required re-meshing of the model. The default settings for Finer and Extra Fine within the semi-conductor menu were unable to generate a useable mesh, however. By increasing the setting for maximum growth rate to 1.2, and directing the meshing of the non-bond first, and the remaining domains after, the mesh in Figure 51 was produced.

This mesh has 32,428 quadrilateral elements, with an average quality of 0.858, and a minimum of 0.0619. The Extra Fine mesh had 59,381 elements with an average quality of 0.9132 and a minimum of 0.1659.

7.1.4 Modeling Fuel Segregation

A fuel segregation, which introduced higher heat flux as well as a region with significantly lower thermal conductivity, was modeled with the addition of a geometric feature. The built in aluminum properties were used, except that the thermal conductivity was lowered. The legacy hotspot model used a thermal conductivity for the fuel segregation that was 27.9% of the fuel and cladding, but for simplicity 25% of the value for aluminum was used in this model. The energy generation rate for the fuel segregations was taken from the legacy models. At 0.417 mm [.0164 in] long and the thickness of the fuel, the fuel segregation was located at the center of the model and is shown in red in Figure 52.
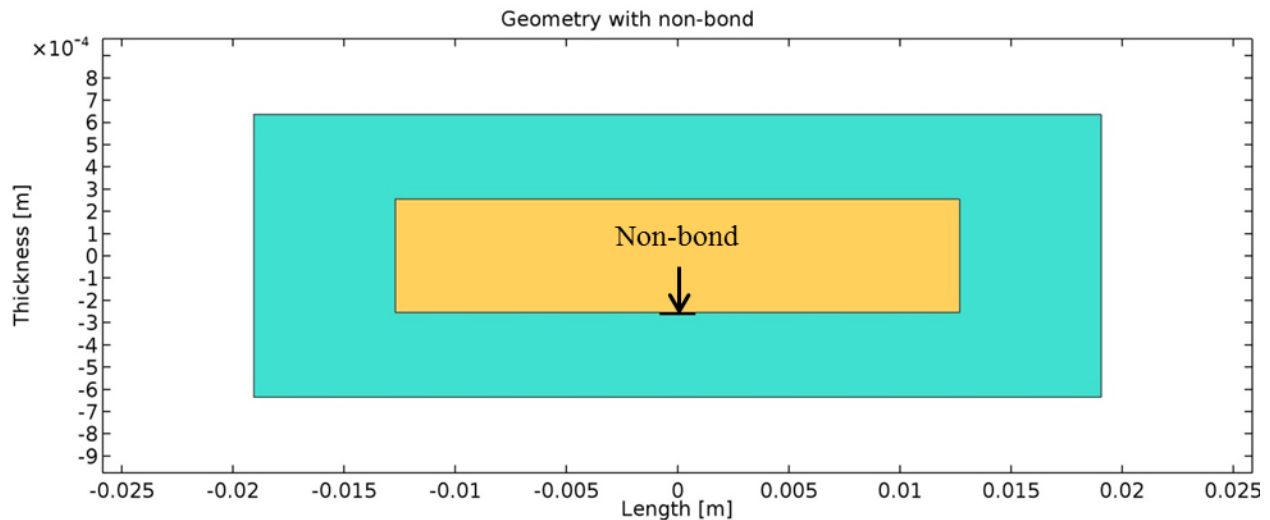
Figure 50 Base model with an adiabatic disc (Note: thickness is exaggerated)

94
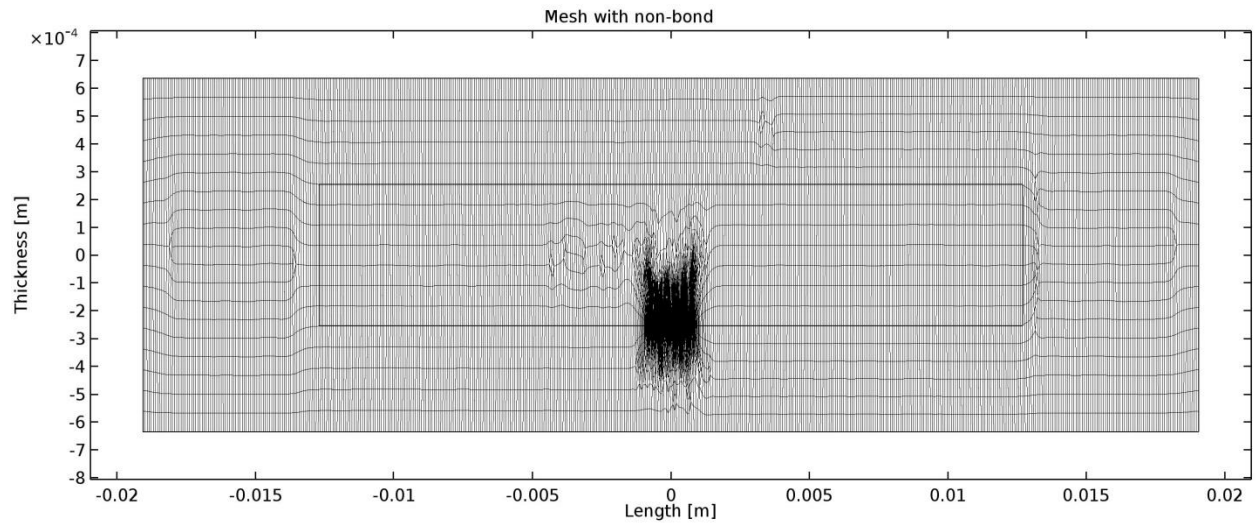
Figure 51 Mesh of the base model with a non-bond (Note: thickness is exaggerated)
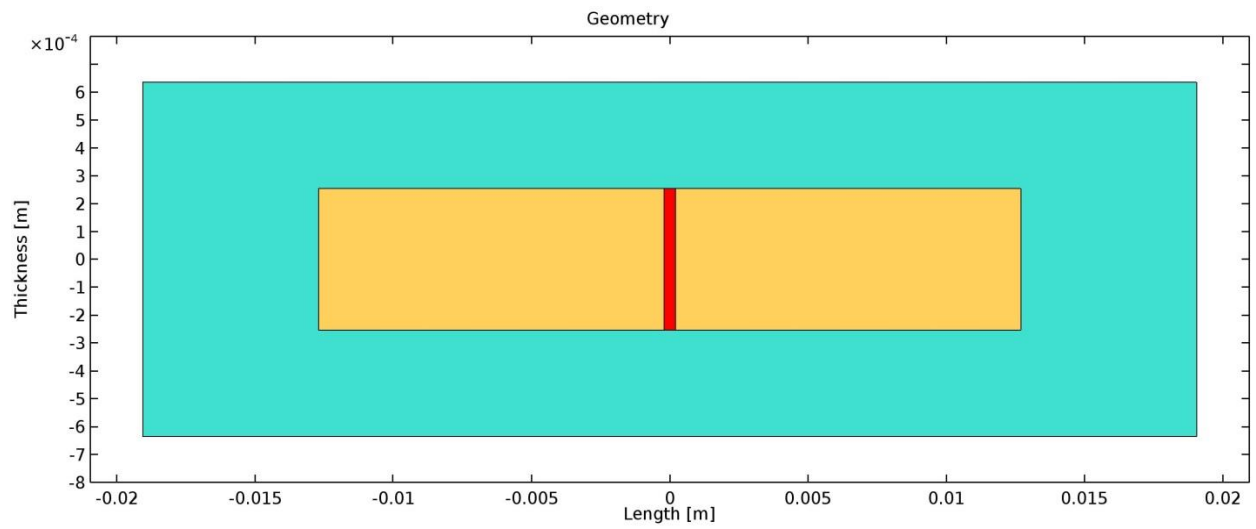
Figure 52 Geometry model with the inclusion of a fuel segregation at the center of the fuel (Note: thickness is exaggerated)

95

Adding the fuel segregation required the regeneration of the mesh. For the model with the geometric entity for a non-bond, the Finer mesh had 32,878 elements with an average quality of 0.8618 and a minimum of 0.155. The Extra Fine mesh had 58,632 elements with an average quality of 0.913 and a minimum of 0.2035. With only the fuel segregation, but not the non-bond, Finer had 9,467 elements with an average quality of 0.9575 and a minimum of 0.5206. The Extra Fine mesh had 34,019 elements, with an average quality of 0.9678 and a minimum of 0.4889.

7.2 Results and Discussion

The analysis examines the temperature distribution, the behavior of the heat fluxes, and energy balances within each model. The visual appearance of the results is very similar, and in some cases indistinguishable between the three modeling options (base, thin layer, and thermal contact). As such, a representative image of the results will be provided when multiple images will not provide additional information, and tabulated data will be used to capture the other results for comparison. To aid in presentation of the results, abbreviations found in Table 5 will be used in figures and tables.

7.2.1 Base, Thin Layer (TL), and Thermal Contact (TC)

The three models were first compared without any non-bonds or fuel segregations.

7.2.1.1 Temperature

Temperature fields from all cases are visually indistinguishable from the base model shown in Figure 53. Subtracting TL or TC from the base case, as in Figure 54, shows that the differences

Table 5 Abbreviations and descriptions of the different cases modeled

Case	Abbreviation	Description
Base	Base	Base model without a special boundary layer
Thin Layer	TL	Base model with the thin layer feature along the lower fuel boundary
Thermal Contact	TC	Base model with the thermal contact feature along the lower fuel boundary
with adiabatic disc/non-bond	wad/wnb	TL or TC including a small region of lower conductivity in the modified boundary
with fuel segregation	wfs	A model with a small fuel region with higher heat generation and lower conductivity

96
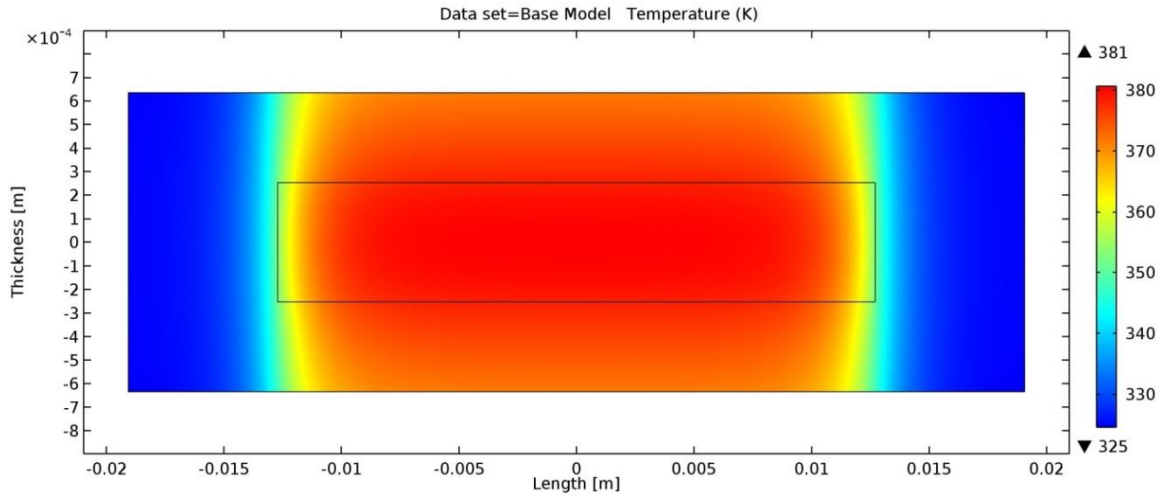
Figure 53 Temperature distribution from base model (Note: thickness is exaggerated)
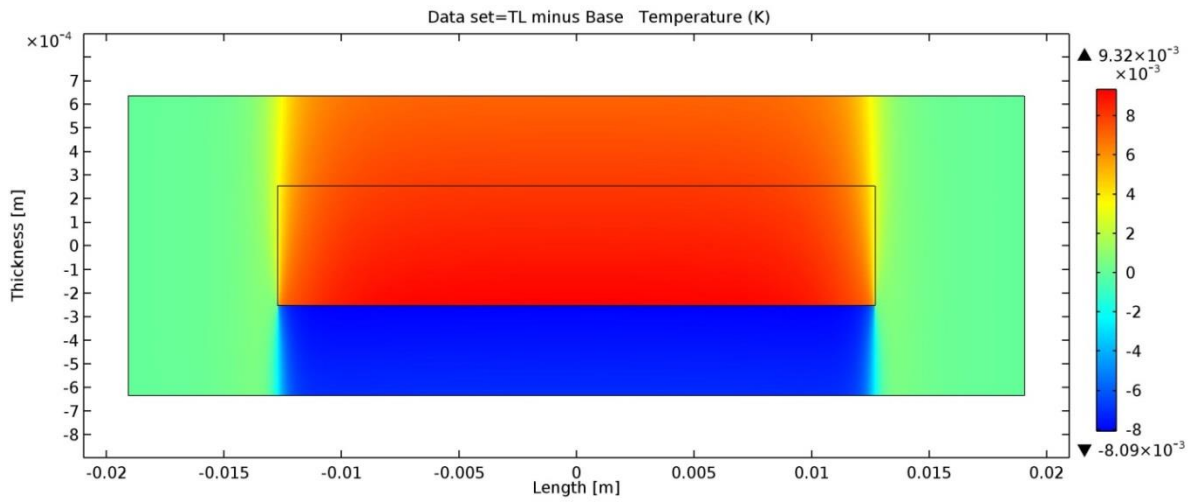
Figure 54 Thin Layer temperature results after subtracting the base case results show almost no difference (Note: thickness is exaggerated)

97

are more than 5 orders of magnitude less than the actual temperatures. This suggests that the approach taken to make TL and TC mimic the un-altered boundary were effective.

7.2.1.2 Flux

Of primary concern in evaluating TL and TC is their ability to accurately determine the heat flux in the presence of sharp gradients caused by non-bonds and fuel segregations. First, however, their performance in the absence of sharp gradients was evaluated.

Figure 55 shows the conductive heat flux magnitude of the base model. Similar plots of TC and TL are visually indistinguishable from this plot. Subtracting the base model from them shows an approximately 1% variation at the edges of the layer. This variation is shown in Figure 56 which plots the flux magnitude for each case at the edge of the boundary.

Interestingly, these minor differences in the *domain* flux magnitudes do not reflect the significant differences in the *boundary* flux across the layers indicated in Figure 57. These differences depend on the mesh. In Figure 58 the TL line is generated using the extra fine mesh, while TC is from the finer mesh. Both fluxes still drop at the end of the boundary layer. However, TL, with the more refined mesh begins to oscillate closer to the edge, and falls in line with the base model results sooner.

7.2.1.3 Energy Balance

The results of performing an energy balance, shown in Table 6, reveal that when the entire model is included, the energy production and rejection is balanced for all 3 cases with all 3 meshes. Within the fuel, the energy balance is slightly off for TC and TL with less energy leaving the fuel boundaries than is produced within the fuel. Additionally, both show the same error in energy
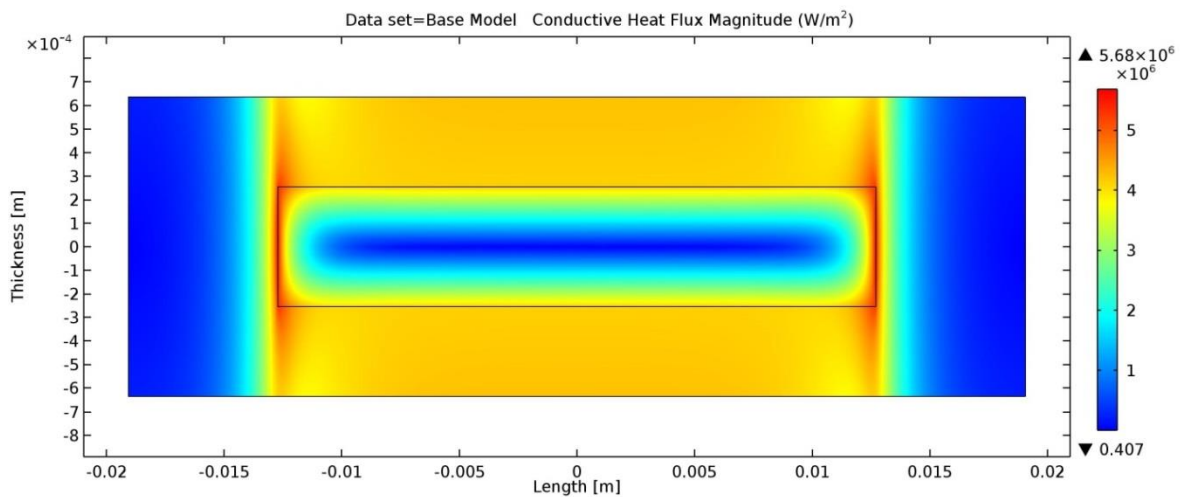
Figure 55 Conductive heat flux magnitude of the base model (Note: thickness is exaggerated)

98
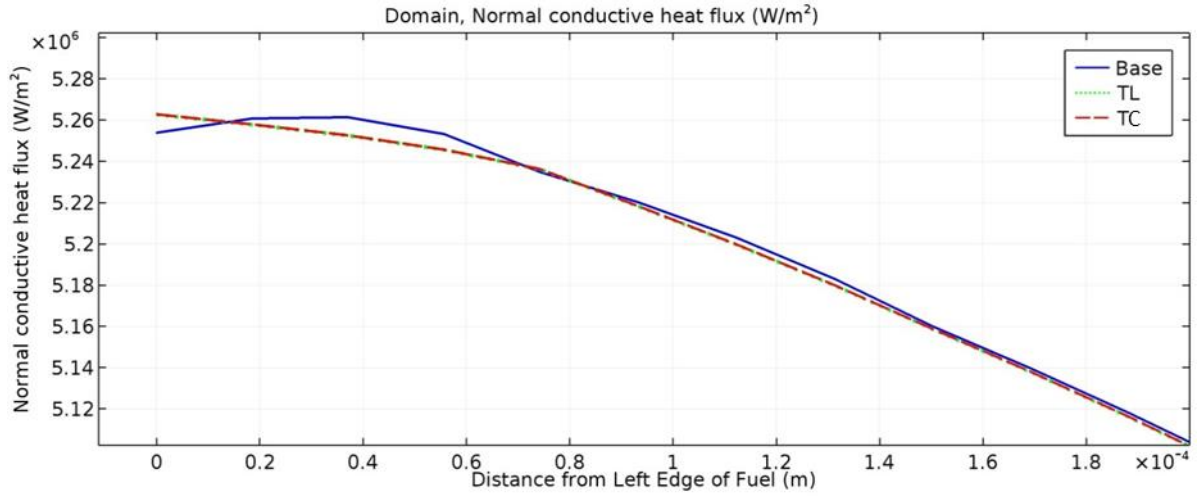
Figure 56 Domain conductive heat flux magnitude of Base, TL, and TC at the edge of the boundary
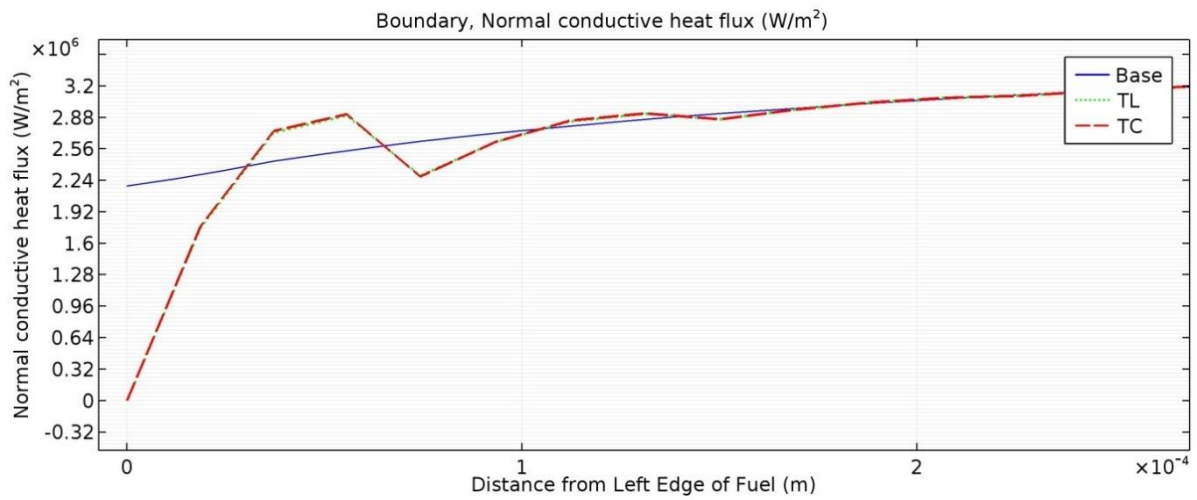
Figure 57 Normal conductive flux across the boundary. TC overlays TL.
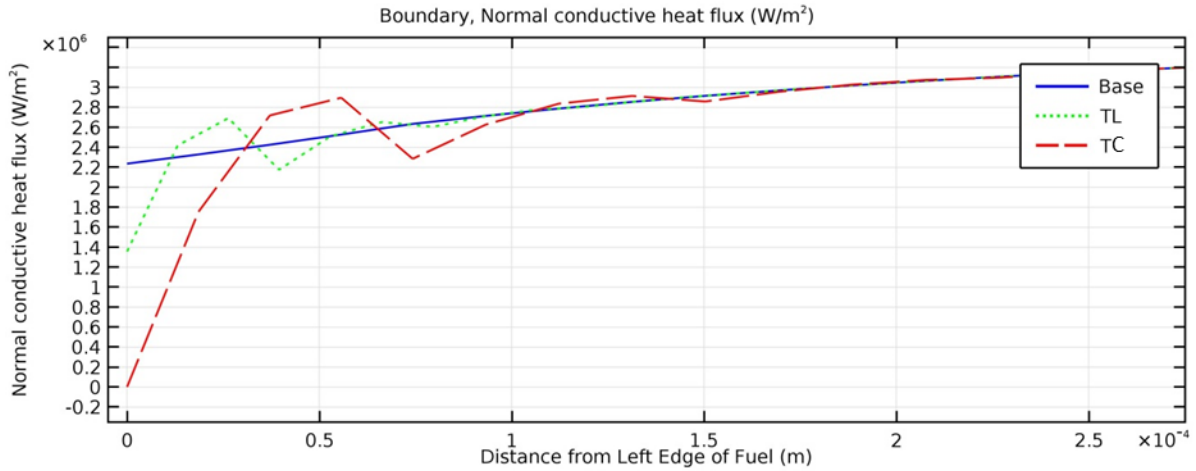
Figure 58 Normal conductive heat flux across the boundary. In this plot TL was generated from the extra fine mesh, and shows that the refined mesh tracks better with the base.

Table 6 Energy Balance of the Base, TL and TC models

	Base			TC & TL		
	Fine	Finer	Extra Fine	Fine	Finer	Extra Fine
Fuel	0.00%	0.00%	0.00%	0.08%	0.02%	0.01%
Whole Model	0.00%	0.00%	0.00%	0.00%	0.00%	0.00%

Energy Balance: % Difference in Energy Generation and Energy Leaving

balance. The difference in heat transfer shows up, as expected from Figure 54, as less heat leaving through the bottom boundary of the fuel, and more, but not enough to make up the difference at the bottom, leaving through the top. That the entire model is in balance while the fuel is not indicates that the lost energy is made up somewhere else in the model. Additionally, the results indicate that as the mesh becomes tighter, the error in energy balance is reduced.

The preceding results quantify variations attributable to the specialized TC and TL models relative to the base boundary model without hotspot or non-bond attributes added.

7.2.2   Base with adiabatic disk (wad), TL wad, and TC with non-bond (wnb)

Non-bonds were simulated in the base model, thin layer (TL) and the thermal contact (TC) layer. The results for each are presented here.

7.2.2.1   *Temperature*

Introduction of a non-bond produces a localized hotspot as shown in Figure 59. The intensity of the hotspot depends on the conductivity through the non-bond. To see the effect of a non-bond on the temperature distribution relative to a defect-free plate, Figure 60 shows the base model results subtracted from the non-bond results. The results shown in Figure 59 and Figure 60 both come from the TL wad model. Similar results were obtained for the TC wnb model. Table 7 shows the maximum temperatures for each of these models with non-bonds as well as how they compare to the defect free base model.

7.2.2.2   *Flux*

Figure 61 shows the magnitude of the conductive heat flux for TL with an adiabatic disc. Note that the majority of the information is washed out in the color pallet due to the very high flux on
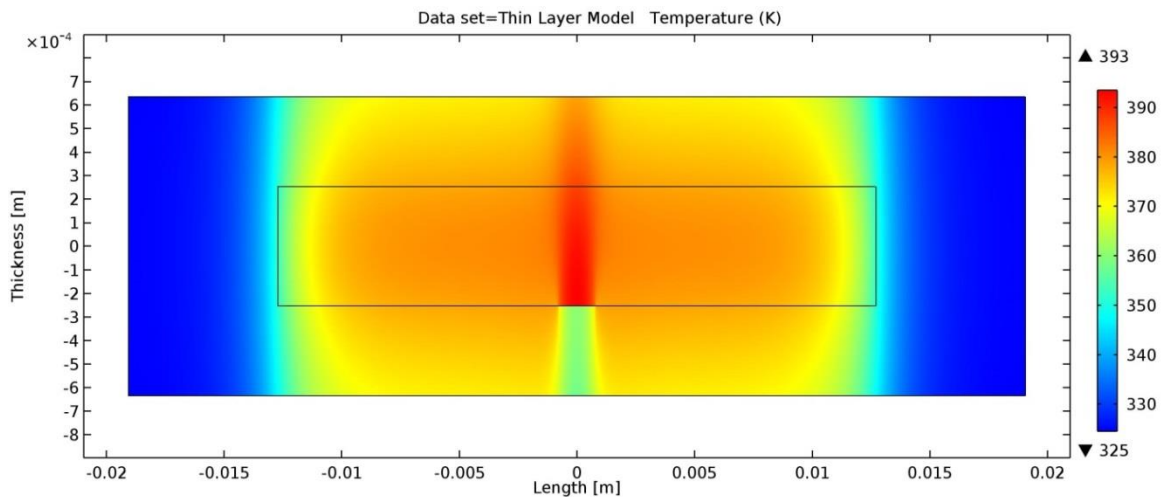
Figure 59 Temperature distribution of the thin layer model with an adiabatic disc (Note: thickness is exaggerated)

101
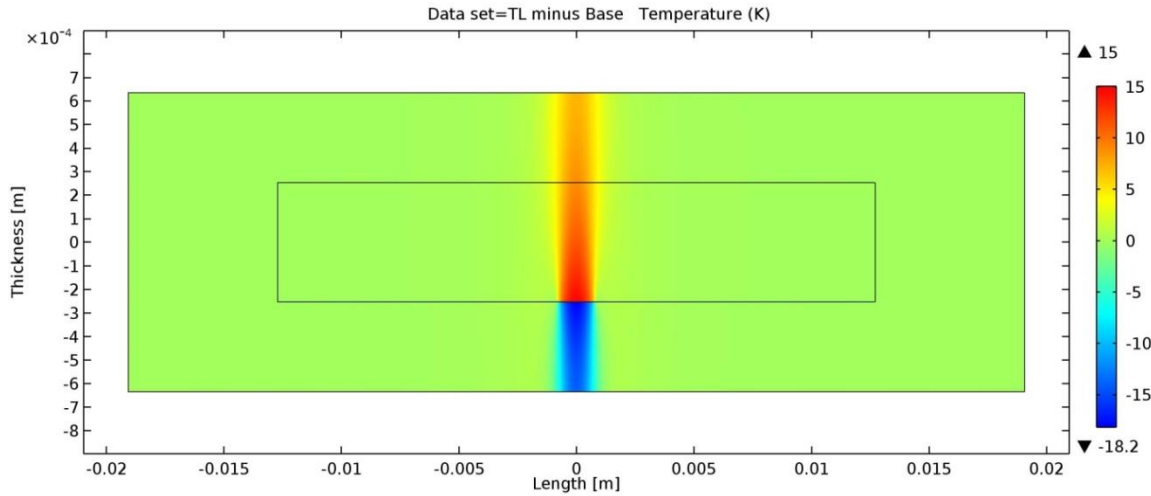
Figure 60 Temperature increase over the base model caused by an adiabatic disc in the thin layer model (Note: thickness is exaggerated)

Table 7 Temperature Results for Base wad, TL wad and TC wnb

Temperature Results in K			
	Base wad	TL wad	TC wnb
maximum	393	393	390
minus Base	14.4	15	11.6

102
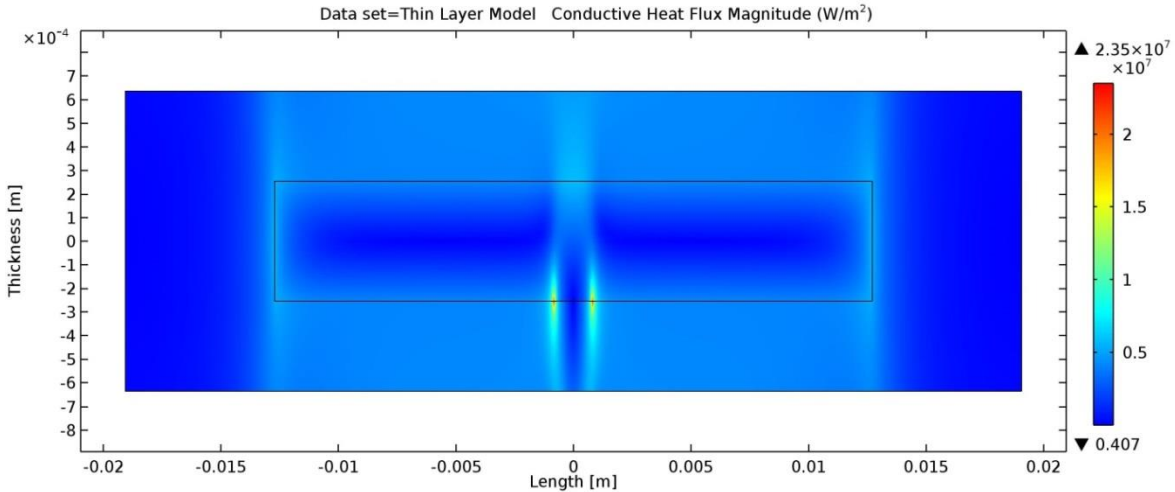
Figure 61 Domain conductive heat flux magnitude for the thin layer with an adiabatic disc (Note: thickness is exaggerated)

 the edges of the adiabatic disc. The flux at these edges is approximately 4 times greater than the maximum flux seen in the models without a non-bond. Figure 62 shows the boundary, normal conductive heat flux for TL wad, TC wnb, and base wad along the modified boundary for the finer mesh. These boundary, normal heat flux peaks are more severe than the domain, conductive heat flux peaks for each case.

Figure 63 shows how each of the 3 approaches handles the discontinuity in conductivity at the non-bond. Both TC and TL experience lower peaks and oscillations in flux, while the base has a smooth rise in flux, but to a not-shown peak of 1.6×10^8 W/m^2.

Nine evenly-spaced, 6.35 mm [0.25 in] cut lines were introduced to the model for use in analyzing heat flux. These cut lines were placed at the center of the fuel, moving across the altered boundary, toward the bottom of the plate as shown in Figure 64. The fifth cut line was placed so that it coincided with the altered boundary. These lines allow examination of the heat flux at locations other than the boundary at greater detail than is available through the heat flux magnitude surface plots

Domain heat fluxes normal to these cut lines were plotted for all three non-bond models. Figure 65, Figure 66, and Figure 67 show the normal flux, with the key showing the plots from the center of the plate, down to the bottom. The solid pink line shows the flux across the altered boundary. The spikes are most severe at this location and taper off further away from the boundary. The peaks for the base wad, approximately -9×10^7 W/m^2, are cut off so the details of the other curves can be seen. Each of these figures is plotted on the same scale for comparison.

103
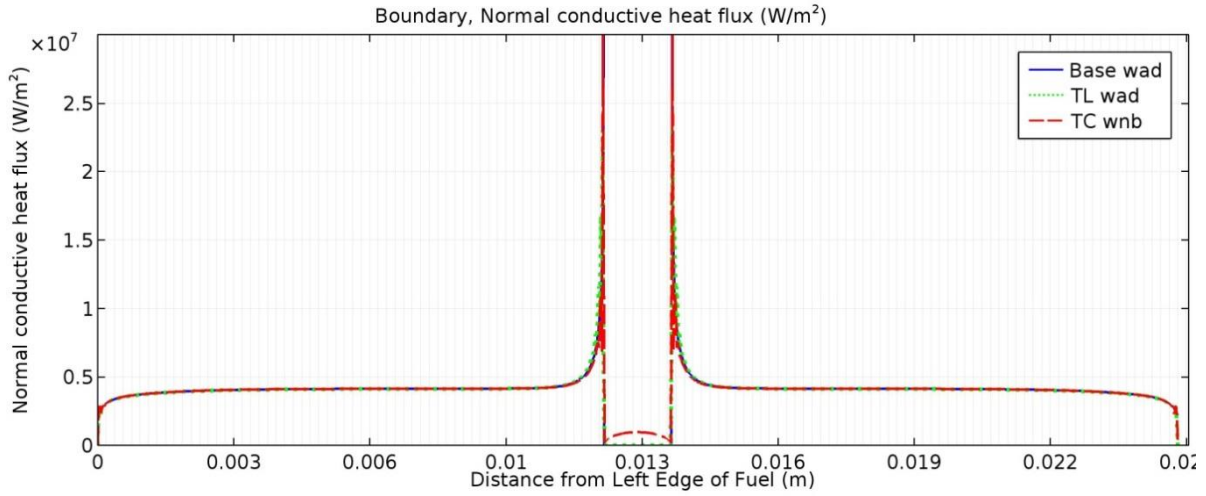
Figure 62 Normal conductive heat flux through the boundary for all three models with simulated non-bonds
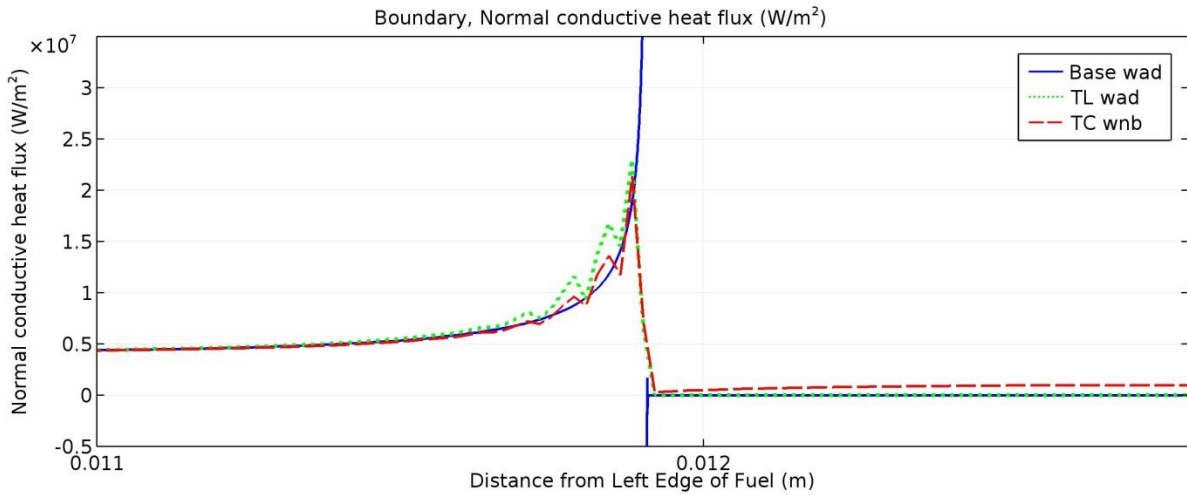
Figure 63 Magnified plot of the oscillations experienced by TL wad and TC wnb at the edge of the simulated non-bond
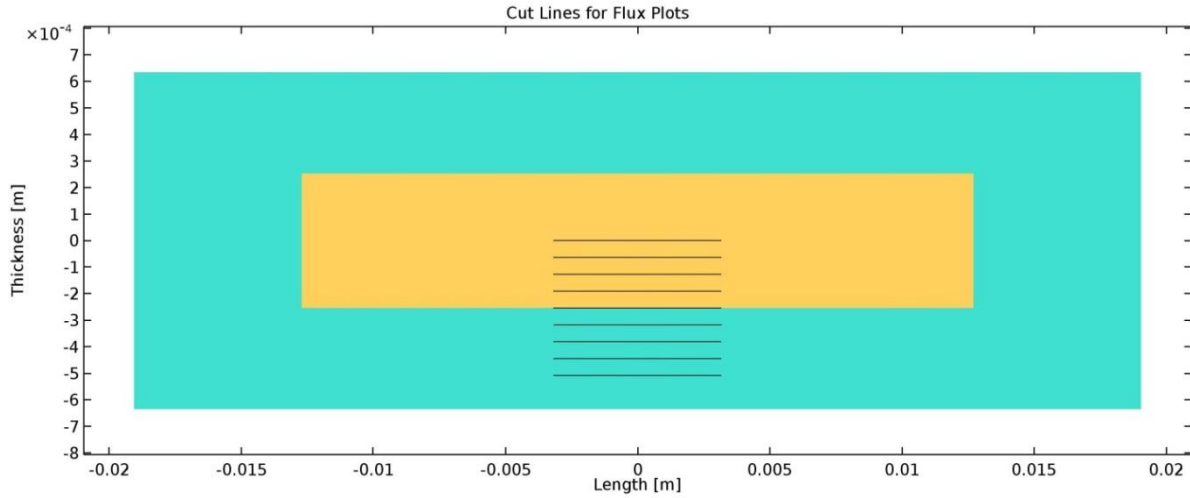
Figure 64 Geometry with cut lines plotted (Note: thickness is exaggerated)
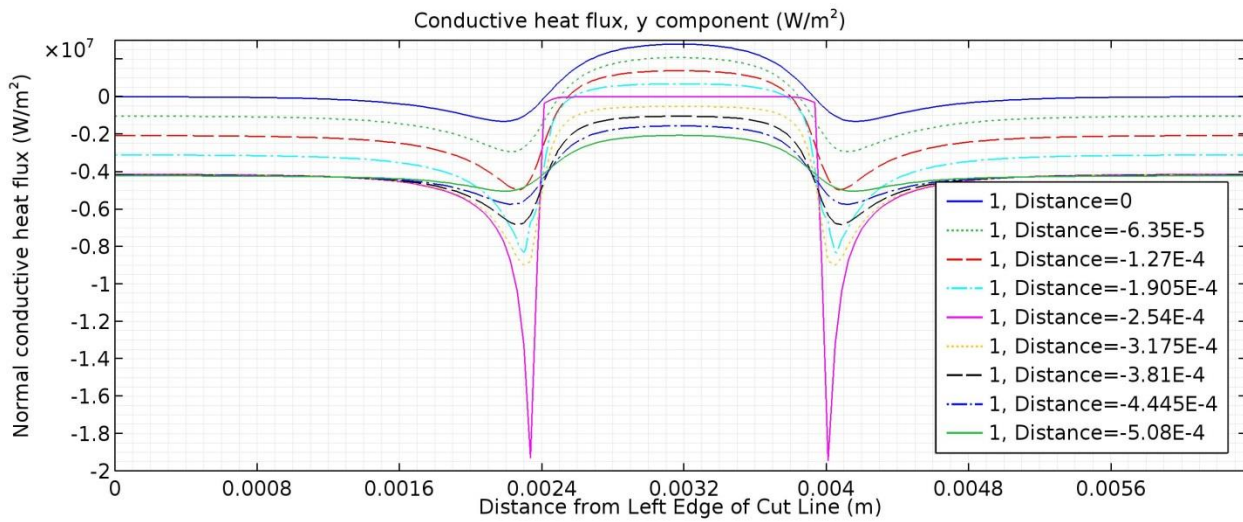
Figure 65 Domain conductive heat flux normal to the cut lines for TL wad
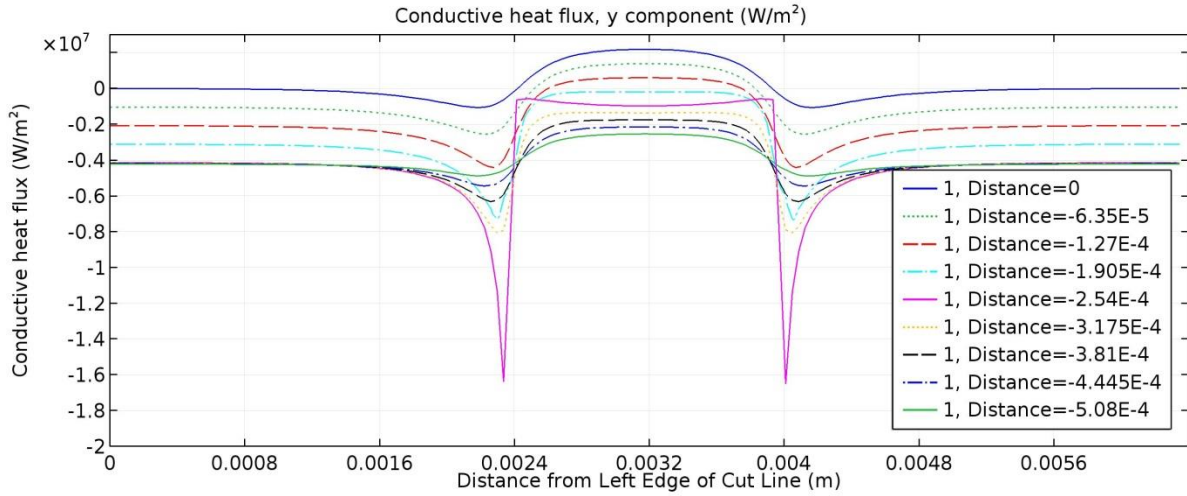
Figure 66 Domain conductive heat flux normal to the cut lines for TC wnb
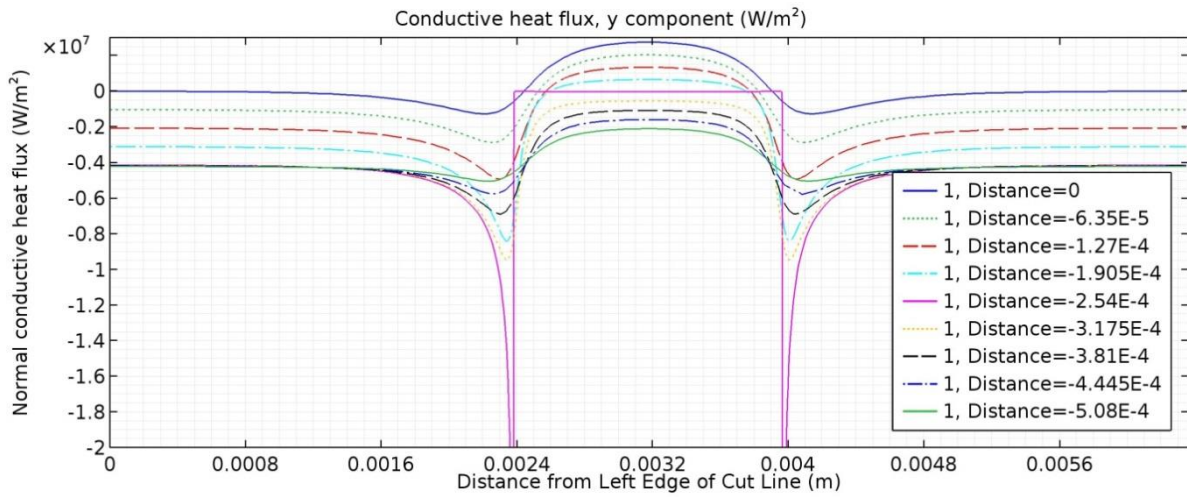
Figure 67 Domain conductive heat flux normal to the cut lines for the Base wad

106

Each plot shows behavior that would be expected—heat moving up and away from the non-bond directly above it, and pouring around the edges of the non-bond. In the base and TL plots, the flux is 0 across the non-bond, as expected for an adiabatic disk, while the TC allows some heat through. Similarly, the flux parallel to the cut lines shown in Figure 64 are offered in Figure 68, Figure 69, and Figure 70. These flux plots behave as expected: above the non-bond, heat flows away from the center of the plate, while below heat rushes in to fill the cooler area below the non-bond. Additionally, the slopes on the TL adiabatic disc are more severe. Again, the peak for the base wad is not shown, but also reaches approximately 9×10^7 W/m^2.

7.2.2.3 *Energy Balance:*

The energy balances over the whole model and over the fuel do not change by introducing the non-bonds in TL and TC, but the inclusion of a non-bond in the base model does affect the energy balance. As expected, in TL and TC less energy leaves through the bottom boundary of the fuel, but it is balanced by energy leaving through the top boundary. Interestingly, refinement in the base wad mesh does not affect the energy balance. The results are tabulated in Table 8.

7.2.3 Base, TL, TC with Fuel Segregation (wfs)

A fuel segregation, with 25% of the thermal conductivity and approximately 10 times the heat generation, was added to determine how the higher heat generation and lower thermal conductivity would affect the thin layer and thermal contact models. The fuel segregation was first added to the models that did not contain non-bonds. Section 7.2.4 describes when both a fuel segregation and a non-bond are present.
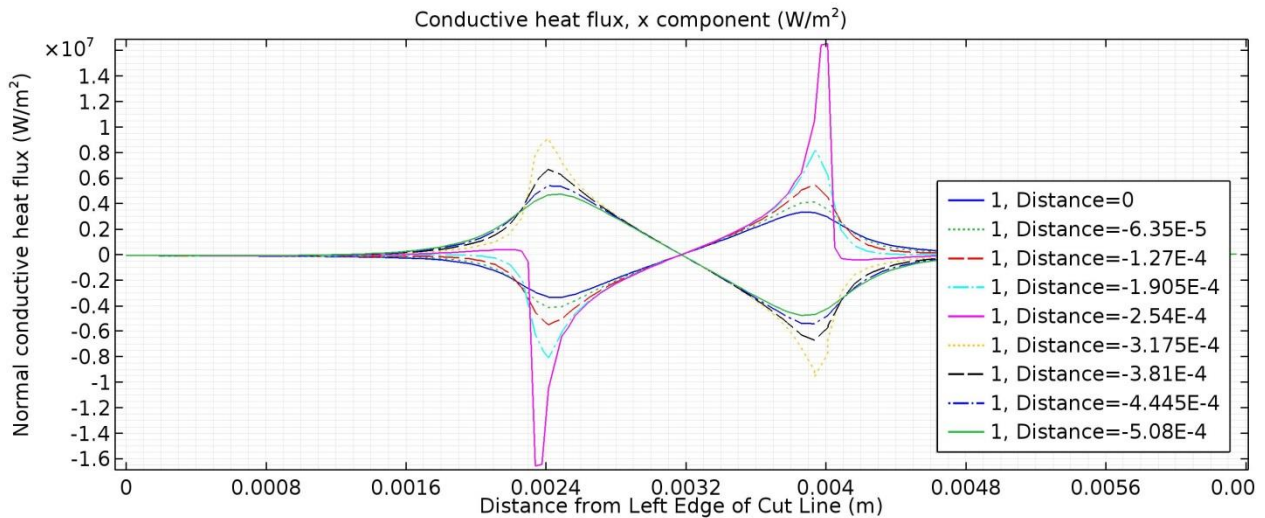
Figure 68 Domain conductive heat flux parallel to the cut lines for TL wad

107
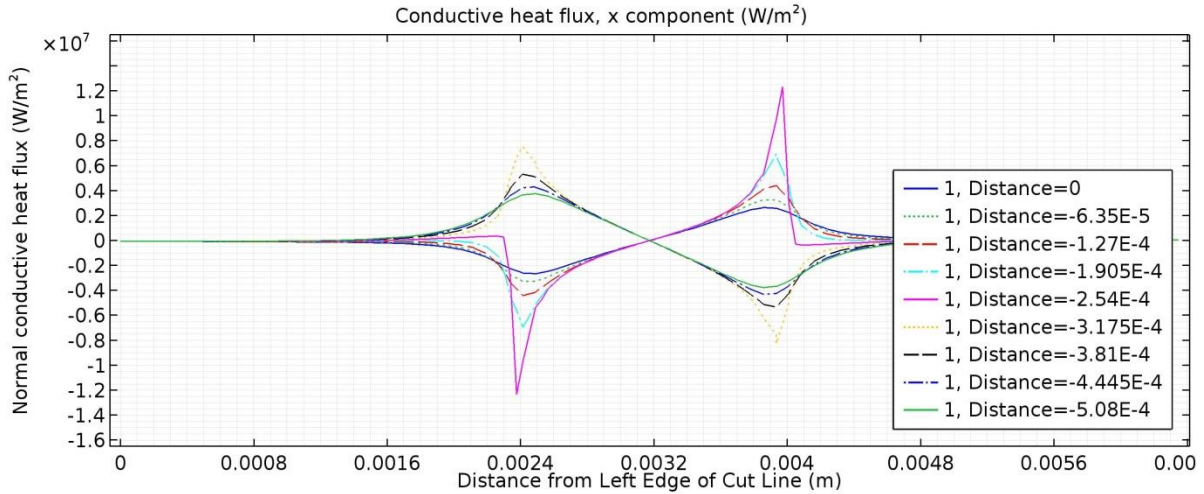
Figure 69 Domain conductive heat flux parallel to the cut lines for TC wnb
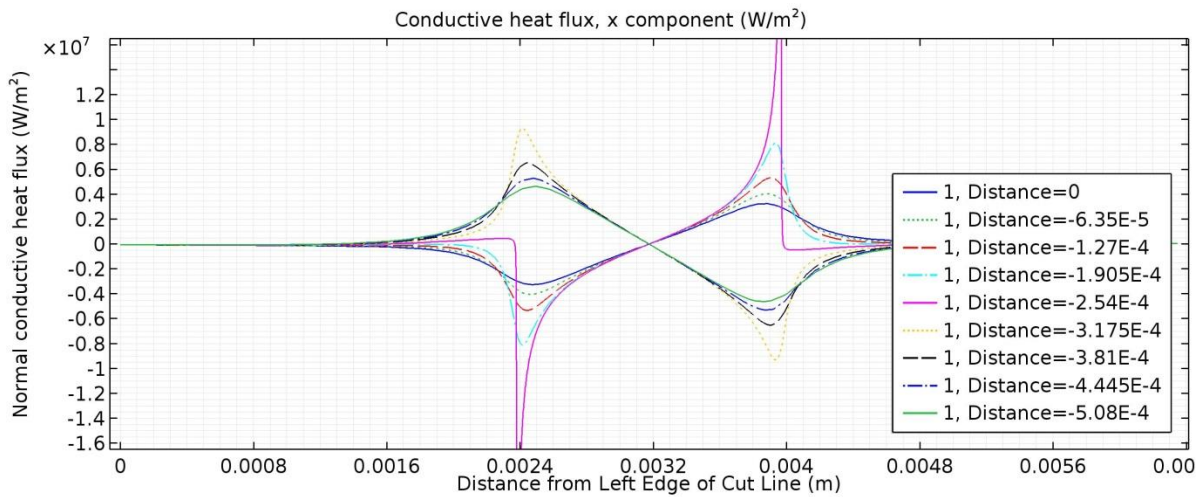
Figure 70 Domain conductive heat flux parallel to the cut lines for Base wad

Table 8 Energy balance for the base with an adiabatic disc, thermal contact layer with a non-bond and the thin layer with an adiabatic disc

	Energy Balance Error with adiabatic disc/non-bond			
	Base wad		TL wad & TC wnb	
	Finer	Extra Fine	Finer	Extra Fine
Fuel	0.06%	0.06%	0.02%	0.01%
Whole Model	0.00%	0.00%	0.00%	0.00%

7.2.3.1 Temperature

Without the presence of a non-bond, the temperature fields produced by all three models were again visually indistinguishable from Figure 71. To see the effect of these fuel segregations on the base model, the base model temperature field was subtracted from these results as presented in Figure 72. The fuel segregation causes a larger increase in temperature than does a non-bond by itself. In comparing TL wfs and TC wfs to Base wfs, the difference in temperature is a maximum of 0.281 K.

7.2.3.2 Flux

Including a fuel segregation increases the conductive heat flux magnitude. Figure 73 shows how the flux surrounding the fuel segregation washes out the flux from the remainder of the fuel in the color palette. Comparing TC wfs and TL wfs to Base wfs, the fluxes are visually indistinguishable. Taking the difference between them demonstrates that the maximum variation is approximately 1% of the maximum value.

Using the cut lines shown in Figure 64, the effect of the fuel segregation on the domain, normal heat flux can be examined, Figure 74. As expected, the solid blue line, which is vertically in the center of the model has 0 flux. As the cut lines move further down the model the flux gradually increases. The greatest peak is at the boundary between the clad and the fuel segregation, the solid pink line. The discontinuity of thermal conductivity and heat generation between the fuel and the fuel segregation leaves a sharp transition in the flux, as well.

A plot of boundary, normal heat flux (along the altered boundary) for the base case, TL and TC,
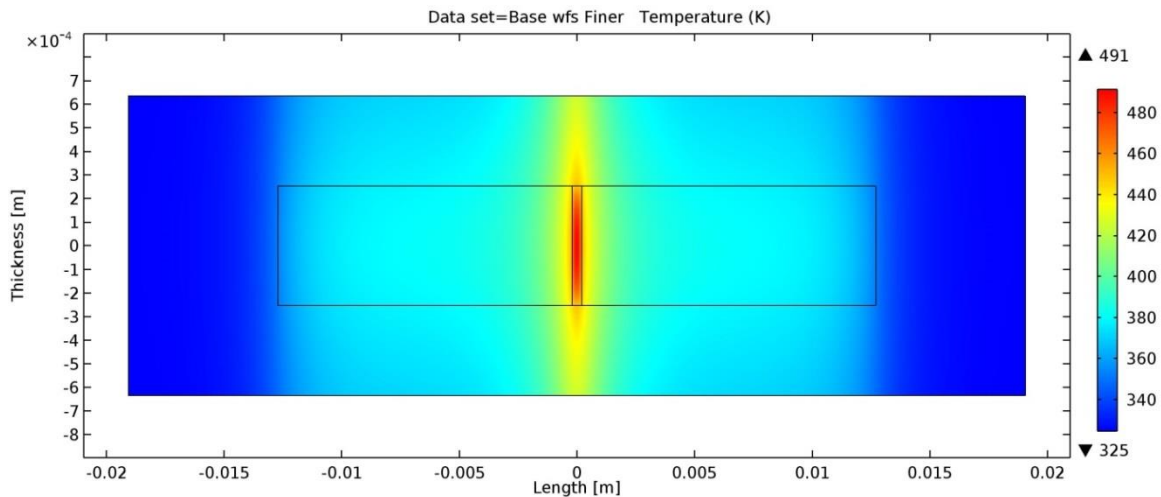
Figure 71 Temperature field in the base model when including a fuel segregation (Note: thickness is exaggerated)
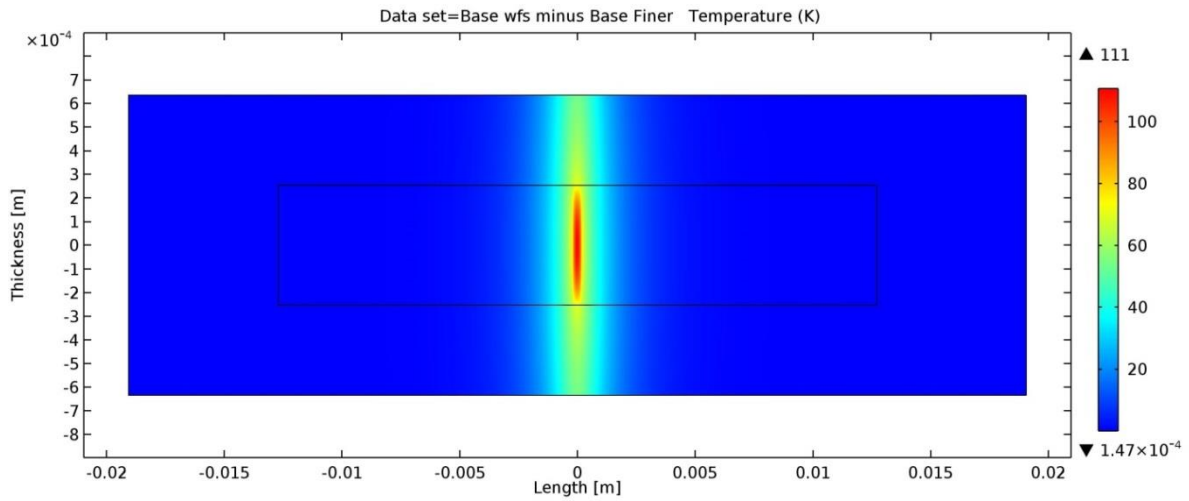
Figure 72 Temperature increase caused by the inclusion of fuel segregation in the base model (Note: thickness is exaggerated)
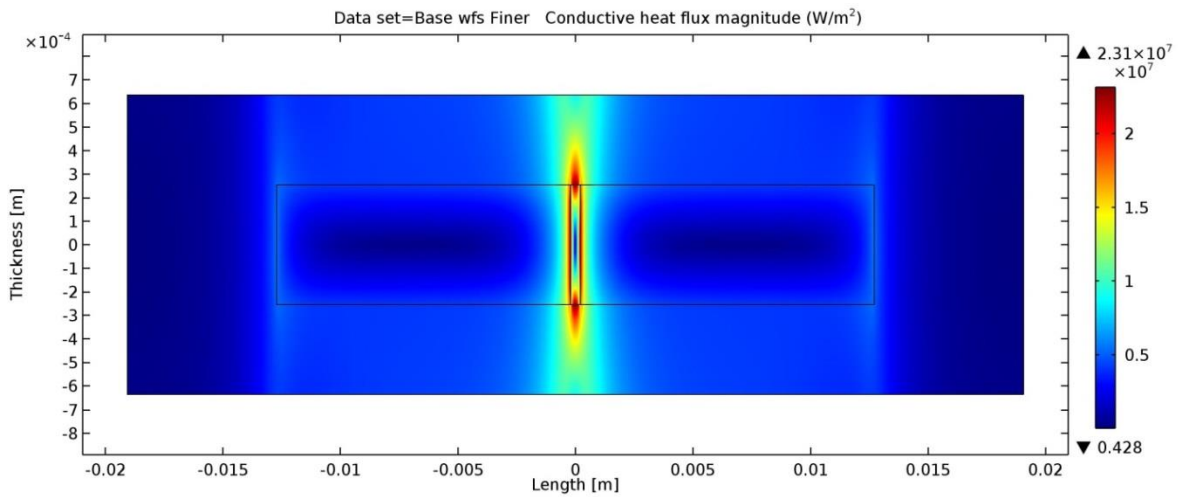
Figure 73 Conductive heat flux magnitude for the base model with a fuel segregation included (Note: thickness is exaggerated)
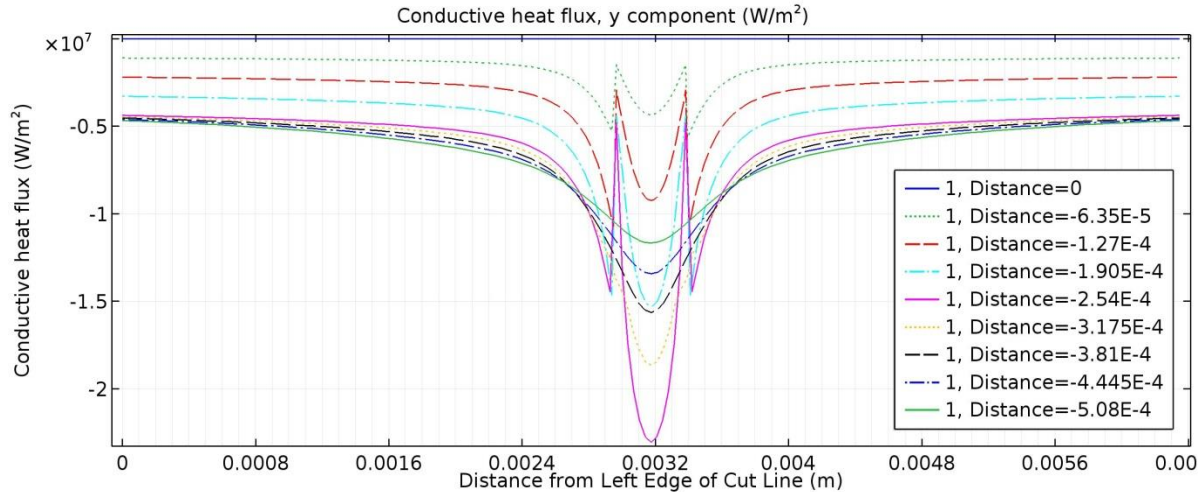
Figure 74 Domain conductive heat flux normal to the cut lines for Base wfs

Figure 75, shows the expected peak due to the high heat generation, as well as oscillation near the edges of the fuel segregation-fuel boundary. Magnification of the peak, Figure 76, shows that each of the cases handles the discontinuity in thermal conductivity from fuel segregation to fuel slightly differently, with both TC and TL experiencing a more severe transition. TL and TC also exhibit oscillations in flux resulting from the discontinuity.

7.2.3.3   *Energy Balance:*

Performing an energy balance on these models shows a bigger discrepancy in the fuel segregation model results than has been observed in the previous models. Table 9 shows the results of the energy balance, omitting the base model because the entries were all 0. The negative indicates that more heat is leaving through the boundaries than is actually generated within the domain.

All of the foregoing results quantify the special thin layer and thermal contact model performance when used to replace a normal FEA modeling approach for simulation of a fuel segregation.

7.2.4   **Base wfs wad, TL wfs wad, and TC wfs wnb**

Introducing a non-bond to the models with a fuel segregation brings the model closer to the worst case scenario.

7.2.4.1   *Temperature*

The introduction of a non-bond below the fuel segregation causes another increase in temperature. The temperature results are summarized in Table 10. Figure 77 shows a typical temperature field generated with a non-bond and a fuel segregation.
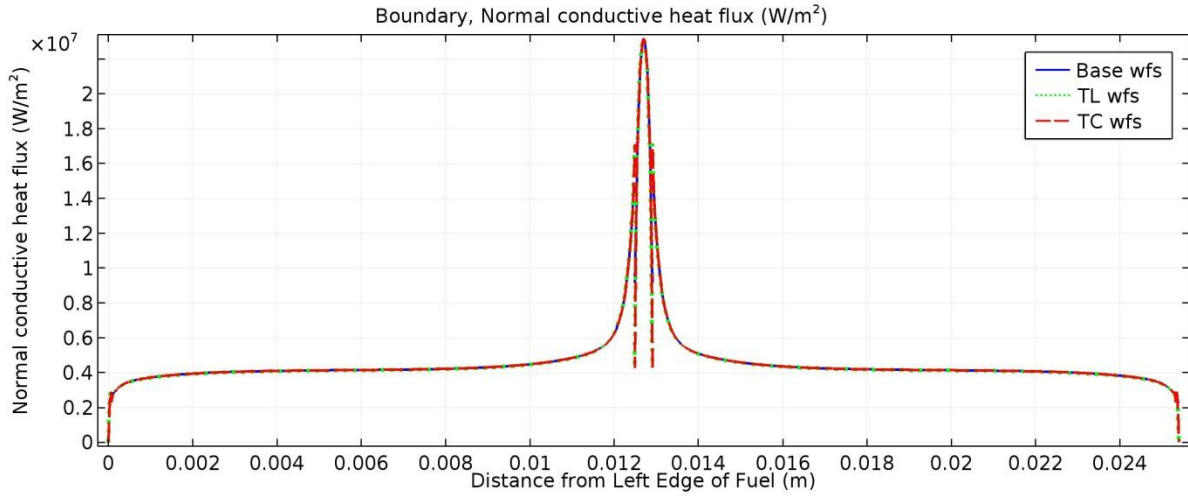
Figure 75 Boundary heat flux for all three models with a fuel segregation
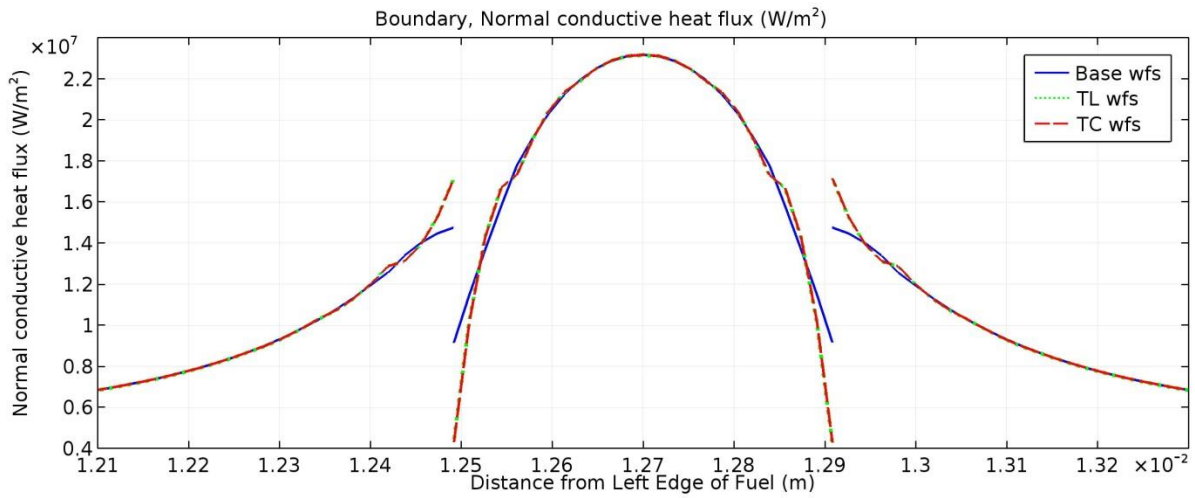
Figure 76 Magnified boundary heat flux for all three models with a fuel segregation

Table 9 Energy balance for TL and TC with a fuel segregation

Energy Balance Error with fuel segregation		
Domain	TL wfs & TC wfs	
	Finer	Extra Fine
Fuel Segregation (FS)	-0.23%	-0.12%
Fuel + FS	0.02%	0.01%
Whole Model	0.00%	0.00%

Table 10 Temperature results with a fuel segregation and a non-bond

	Temperature Results in K		
	Base wfs wad	TL wfs wad	TC wfs wnb
maximum	546	548	537
minus Base wfs	97.4	99.4	87
minus Base	167	169	157
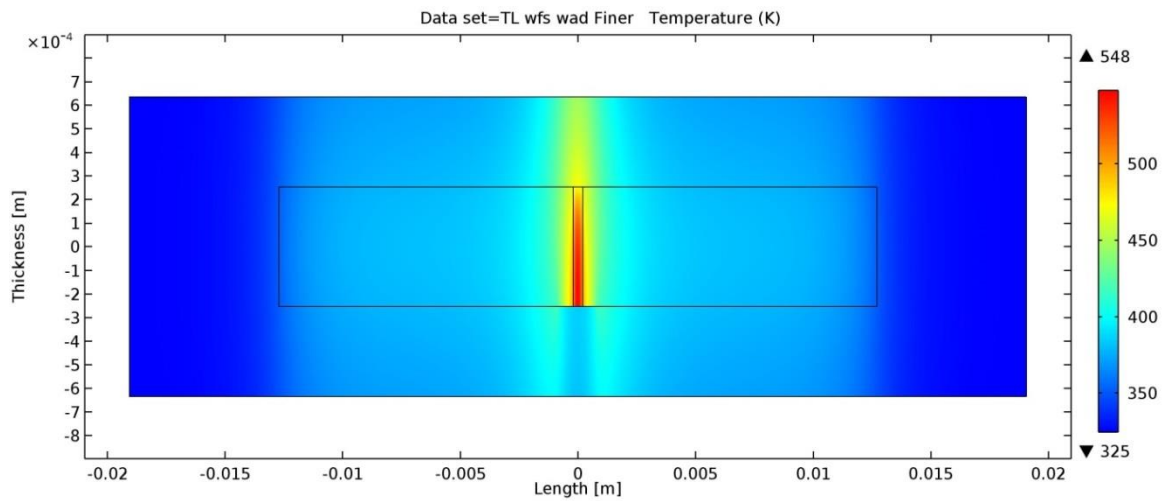
Figure 77 Temperature field generated with the thin layer model with a fuel segregation and an adiabatic disc (Note: thickness is exaggerated)

113

To see the effect the non-bond has on the temperature, Figure 78 shows the base model with a fuel segregation subtracted from the thin layer with both an adiabatic disc and a fuel segregation. Similarly, to see the effect of both the non-bond and the fuel segregation, Figure 79 shows the base model without a fuel segregation subtracted from this same thin layer with both an adiabatic disc and a fuel segregation.

7.2.4.2   Flux

The domain heat flux normal to the cut lines in Figure 64, is plotted in Figure 80, Figure 81, and Figure 82. A number of features of the domain heat flux can be observed. First, the spikes at the edges of the non-bonds are about twice what they were without the fuel segregation, but follow the same pattern of diminishing away from the interface layer. The discontinuity in thermal conductivity and heat generation causes a jump at the edges of the fuel segregation, but no visual oscillations or other distortions are apparent. Finally, all plots use the same axis, for comparison, and the peaks of a few plots are cut so the details in the curves can be seen.

As with the last set of flux plots that had non-bonds, the behavior is as expected: the fuel segregation produces a positive flux (that is, a flux moving upward) in the center of the plate, which appears as a hump in the center of each of the curves above the pink curve. At the edge of the fuel segregation for these same curves, the flux changes drastically, as the thermal conductivity goes up 4 times the value in the fuel segregation. The flux remains positive, as the curves are followed away from the center, until they approach the edge of the non-bond where they drop below 0, indicating that the flux is pointed downward.
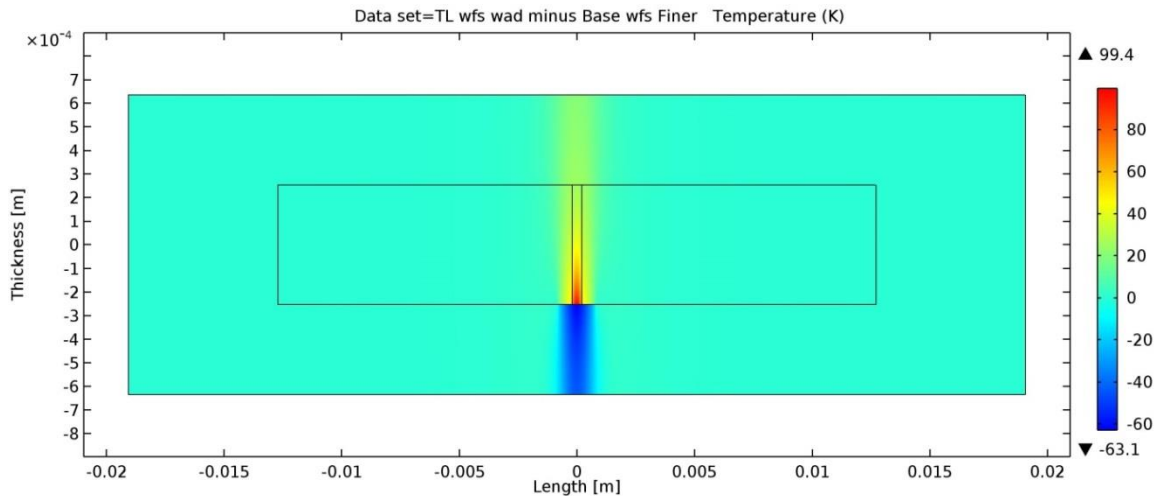
Figure 78 Temperature increase caused by the introduction of the adiabatic disc below the fuel segregation (Note: thickness is exaggerated)

114
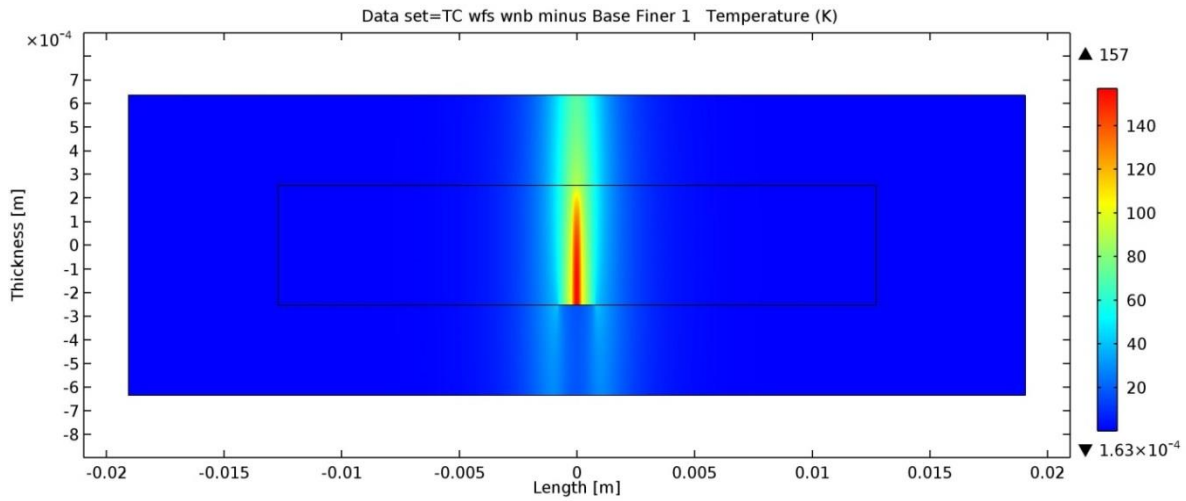
Figure 79 Temperature increase caused by the presences of both an adiabatic disc and a fuel segregation (Note: thickness is exaggerated)
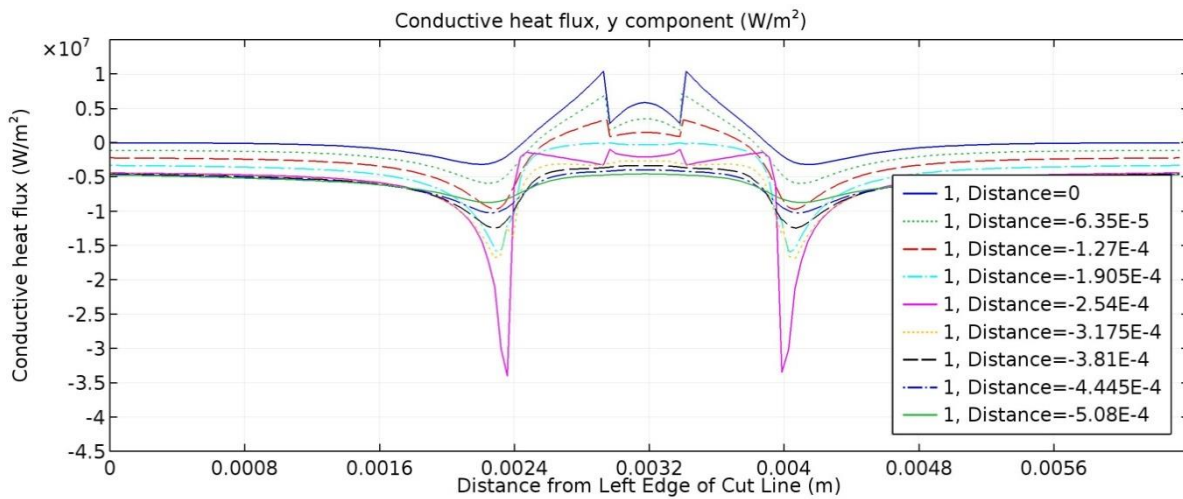
Figure 80 Domain heat flux normal to the cut lines for the thermal contact model with a fuel segregation and a non-bond
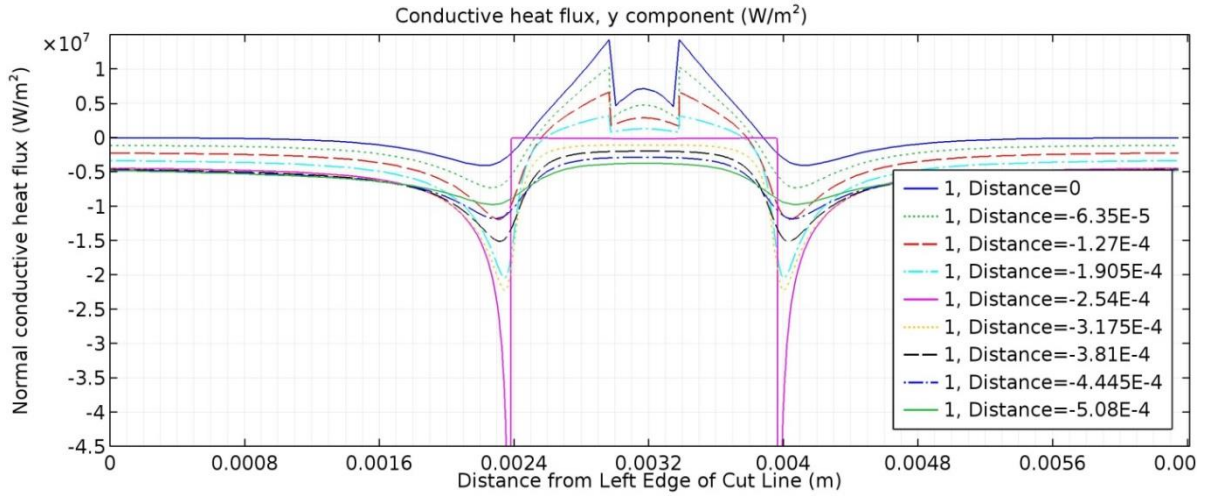
Figure 81 Domain heat flux normal to the cut lines for the thin layer model with a fuel segregation and an adiabatic disc
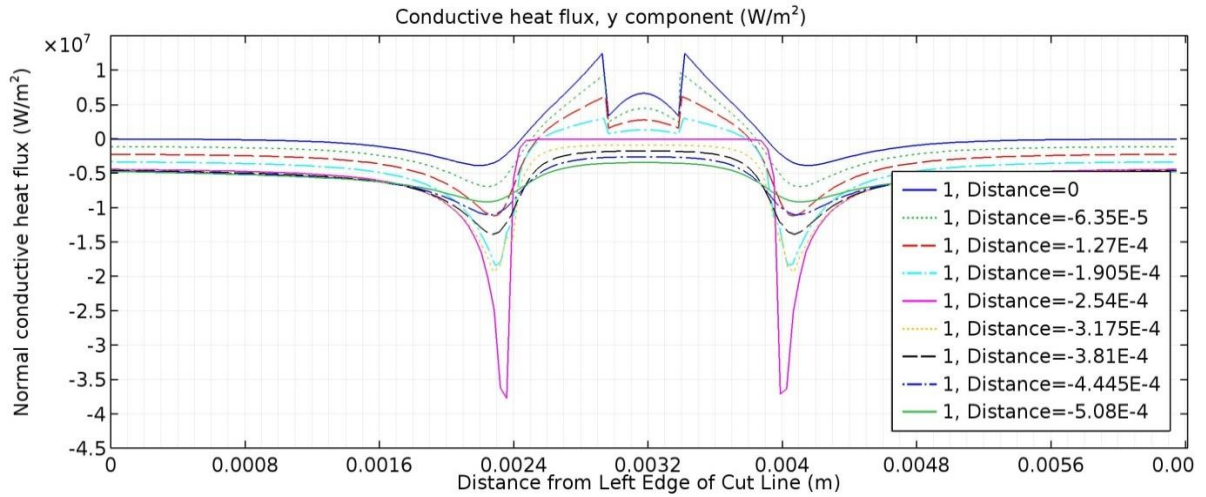
Figure 82 Domain heat flux normal to the cut lines for the Base with a geometric adiabatic disc and fuel segregation

116
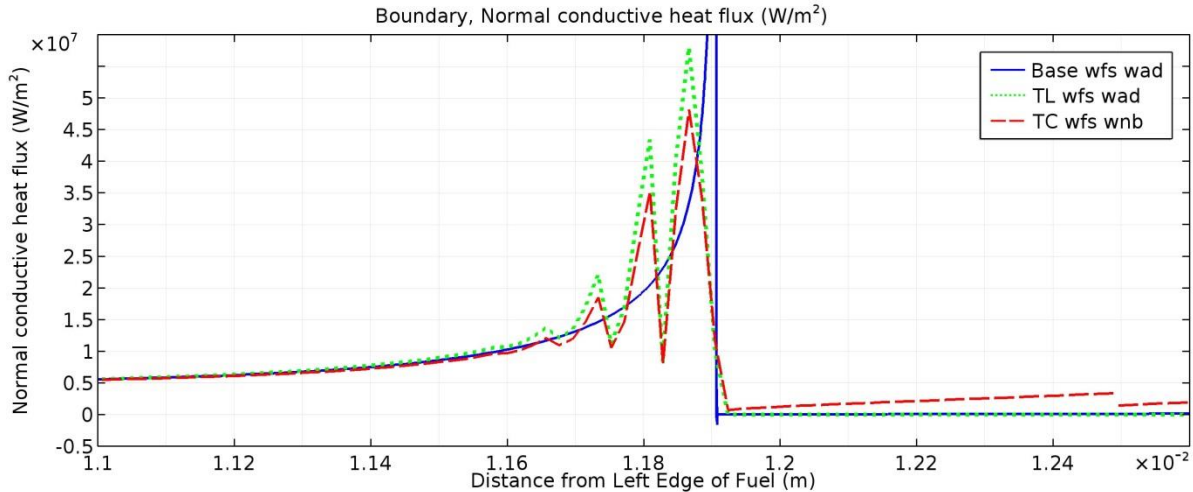
Figure 83 Boundary heat flux for all 3 models with a fuel segregation and non-bond

As observed previously, the boundary heat flux, as opposed to the domain heat fluxes shown in the previous figures, experiences more severe distortions in the form of oscillations in the flux in both TC and TL. Figure 83 shows these oscillations in the boundary, normal heat flux by magnifying the plot in the area immediately around the edge of the non-bond. The peaks of the base wfs wad reach approximately 4.25×10^8 W/m^2 and are cut off because including them makes the other features of the plot indiscernible.

7.2.4.3 *Energy Balance*

An energy balance on each of the domains shows that, across the entire model, the energy is balanced as indicated in Table 11. The simulated non-bonds in TL and TC do not appear to affect the energy balance across the combined fuel and fuel segregation.

The energy balance appears to improve with the simulated non-bonds when compared to the models with only the fuel segregation presented in Table 9. It is possible that this apparent improvement is simply a case of errors cancelling one another. Also of interest is that the base wfs wad has no error within the fuel segregation, but does show error in the combined fuel and fuel segregation, and the refinement in mesh does not appear to affect that error, as presented in Table 11.

These results suggest that both the thin layer and thermal contact models have essentially equivalent performance when including both a fuel segregation and a non-bond. Both experience oscillations not experienced by the base wfs wad model, and both have smaller spikes in flux than the base wfs wad. The energy balance in the TC and TL models is worse across the fuel segregation and better across the combined fuel and fuel segregation than the base wfs wad model.

117

Table 11 Energy balance for the 3 models with fuel segregations and simulated non-bonds

Domain	% Difference in Energy Generation and Energy Leaving					
	Base wfs wad		TC wfs wnb		TL wfs wad	
	Finer	Extra Fine	Finer	Extra Fine	Finer	Extra Fine
Fuel Segregation (FS)	0.000%	0.000%	-0.055%	-0.030%	0.001%	0.000%
Fuel + FS	0.046%	0.046%	0.019%	0.010%	0.019%	0.010%
Whole Model	0.000%	0.000%	0.000%	0.000%	0.000%	0.000%

7.2.5 TC Comparisons

The previous models were all run with the thermal contact model settings of slope equal to 0.2 and average surface asperity height equal to 1 μm. To see the effect of these settings on temperature, flux, and energy balance, these values are varied for both TC wfs and TC wfs wnb. Slope values of 0.01, 0.2, and 1 were used. The average asperity height, equivalent to the average roughness of the surface, is unknown within the non-bond, so values of 0.1, 1, and 10 μm, a range encompassing typical rolling surface finishes, were used. As explained in section 7.1.3, the ratio of p/E' was adjusted for each slope value to force C_{tc} to 1with the intention of minimizing the influence of the thermal contact boundary outside of the non-bond region.

The effect of slope has been removed from the calculation by forcing C_{tc} to equal 1. This becomes apparent by examining the differences in maximum temperature between the base wfs and TC wfs shown in Table 12. The asperity height has an almost proportional effect on the difference while slope has no effect. Plots of the boundary normal heat flux also show that the flux aligns along asperity height, with no discernable difference between different slopes at the same asperity height.

The introduction of a non-bond produces higher temperatures. Table 13 shows how the difference in maximum temperatures between the base wfs and the TC wfs wnb changes with both the slope and asperity height. Interestingly, while the differences are still larger along asperity height, they are no longer constant for all slopes. Recall that in the region of the non-bond values for *p* and *E'* were set to be realistic, not only for C_{tc} to be 1, so the slope does affect the conductivity. Again, the asperity height has the largest impact.

Figure 84 and Figure 85 show the boundary, normal conductive heat flux of these models. The numerical oscillations in the boundary flux are much more severe for the 0.1 μm asperity height, while there seems to be little difference between the 1 and 10 μm. Also, by an asperity height of 10 μm, the thermal contact model is very close to adiabatic in the non-bond region. The actual contact conductance values, in units identical to a heat transfer coefficient, are calculated with the slope, asperity heights, and a 3.7 MPa contact pressure in Table 14.

Table 12 Temperature difference [K] between TC models with different values of slope and asperity height and the base model

slope	Asperity Height		
	0.1	1	10
m=1	0.017	0.172	1.68
m=0.2	0.017	0.172	1.68
m=0.01	0.017	0.172	1.68

Table 13 Maximum temperature difference [K] of the TC models with non-bonds compared to the base model both with a fuel segregation

slope	Asperity Height		
	0.1	1	10
m=1	43.4	85.9	99.5
m=0.2	46.4	87.4	99.8
m=0.01	49.4	88.7	99.9
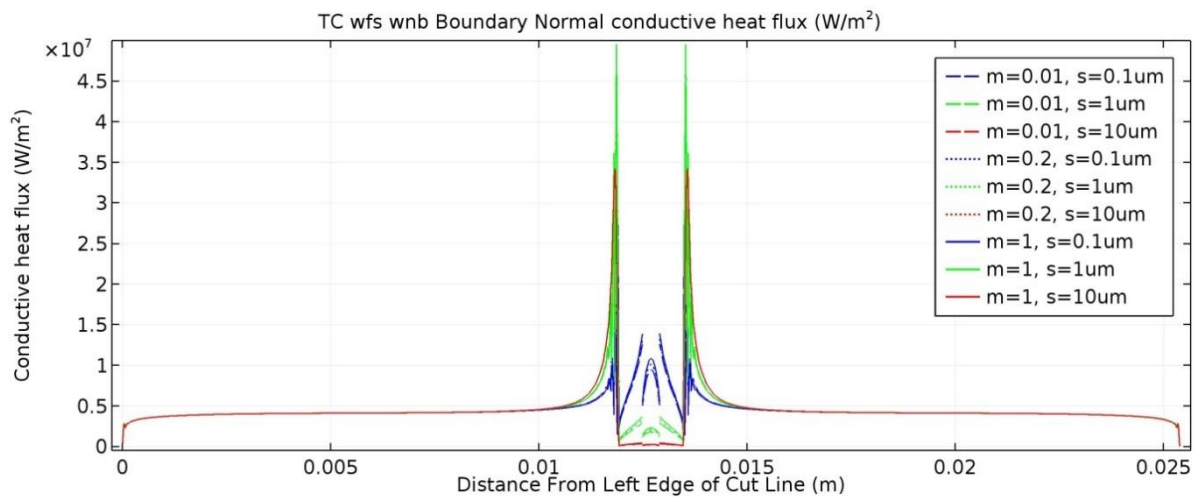
Figure 84 Boundary normal conductive heat flux for the different TC comparison cases

119
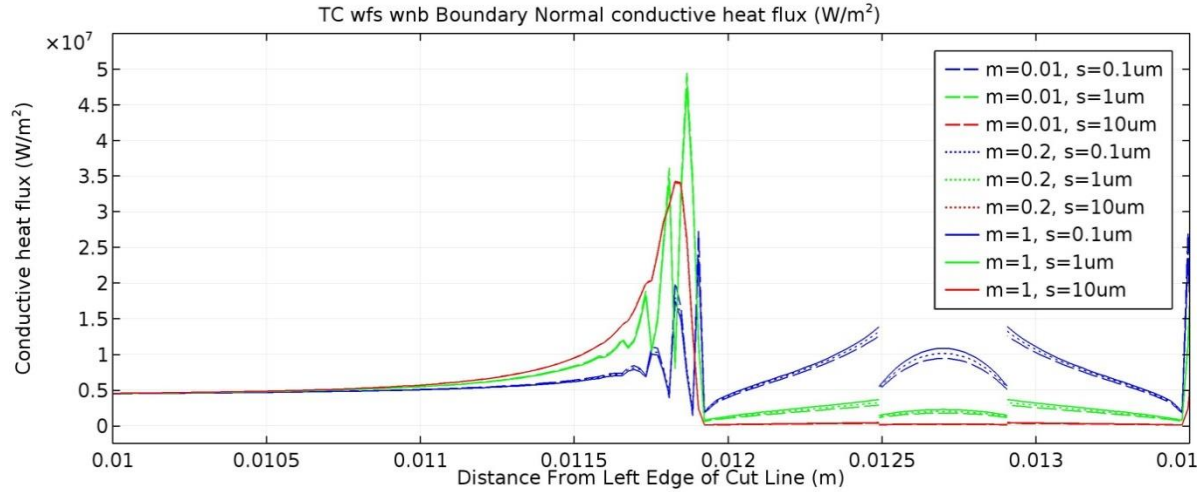
Figure 85 Magnified view of the boundary normal conductive heat fluxes showing the oscillations approaching the non-bond

Table 14 Thermal contact conductance for each combination of slope and asperity height

h (W/[m^2*K])		asperity height (μm)		
		0.1	1	10
Slope	1	4.72E+05	4.72E+04	4.72E+03
	0.2	4.29E+05	4.29E+04	4.29E+03
	0.01	3.58E+05	3.58E+04	3.58E+03

120

7.2.6 Adaptive Mesh Refinement

An additional case used the adaptive mesh refinement (AMR) feature in the mesh building sequence. This feature adjusts the mesh while the solution is being determined by increasing the element density in regions of high gradients to help ensure that an appropriate resolution is obtained. The AMR feature required the use of triangular elements, and resulted in a significantly more refined mesh, for example in the case of the TL wfs wad, the resulting mesh had 371,794 elements (compared with the 36,759 in the Extra Fine model, and 9,445 in the Finer model).

AMR was used on TL wad and TL wfs wad. Differences within maximum temperature between AMR and Finer/Extra Fine mesh models were less than 1 K, however, the boundary, normal flux behavior near the non-bond edge showed more significant differences. Figure 86 shows the reduction in oscillations obtained by using AMR over the Finer mesh. Figure 87 shows that this reduction is not as significant when comparing the Extra Fine model to the AMR. Figure 88 provides the domain flux across the cut lines introduced in Figure 64 for the TL wad AMR. The differences within the domain flux between AMR and Finer are not as apparent as in the boundary flux. Similar results are obtained with the models that include a fuel segregation, Figure 89. An energy balance across the AMR models shows the finer meshes reduce the errors, Table 15.

7.2.7 Element Order

Further comparisons were made based on which element order was used. The default, and that used for all other cases in this effort, was the quadratic basis function. The TL wfs wad Finer model was recomputed using a cubic and quartic basis function. Again, these changes produced very similar temperature fields, but different boundary flux behaviors. Figure 90 shows smoothing of the oscillations in the boundary, normal flux at the edge of the non-bond as the element order increases. The transitions between steps in thermal conductivity and heat generation in the domain fluxes are sharper in the higher order basis functions, Figure 91, Figure 92, and Figure 93. Changing the element order also changes the energy balance across the fuel segregation, and the combined fuel plus fuel segregation, Table 17.

Table 15 Energy balance for TL wfs wad both with and without adaptive mesh refinement

| | % Difference in Energy Generation and Energy Leaving | | | |
| Domain | Thin Layer wfs wad | | with AMR | |
	Finer	Extra Fine	Finer	Extra Fine
Fuel Segregation (FS)	0.0009%	0.0002%	0.0000%	0.0000%
Fuel + FS	0.0190%	0.0101%	0.0014%	0.0005%
Whole Model	0.0000%	0.0000%	0.0000%	0.0000%
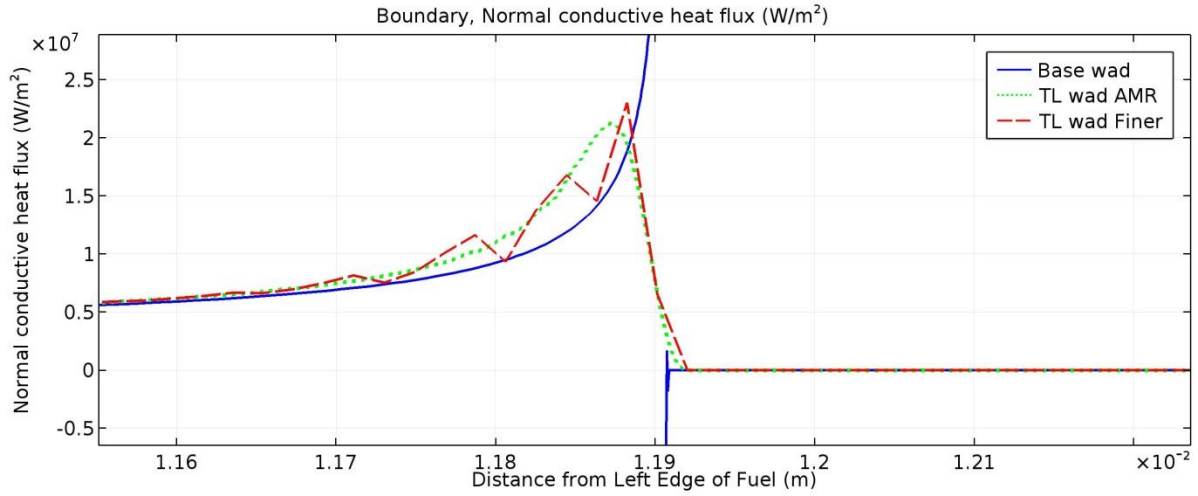
Figure 86 Comparison of boundary, normal flux for the base model, Finer mesh model, and AMR model with an adiabatic disc
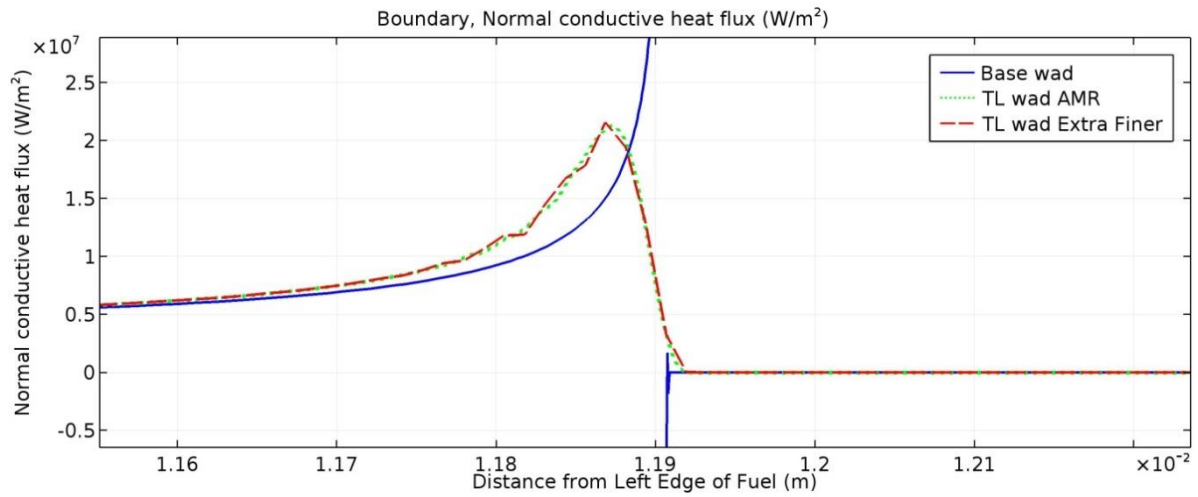
Figure 87 Comparison of boundary, normal flux for the Base, Extra Fine mesh, and AMR models with an adiabatic disc
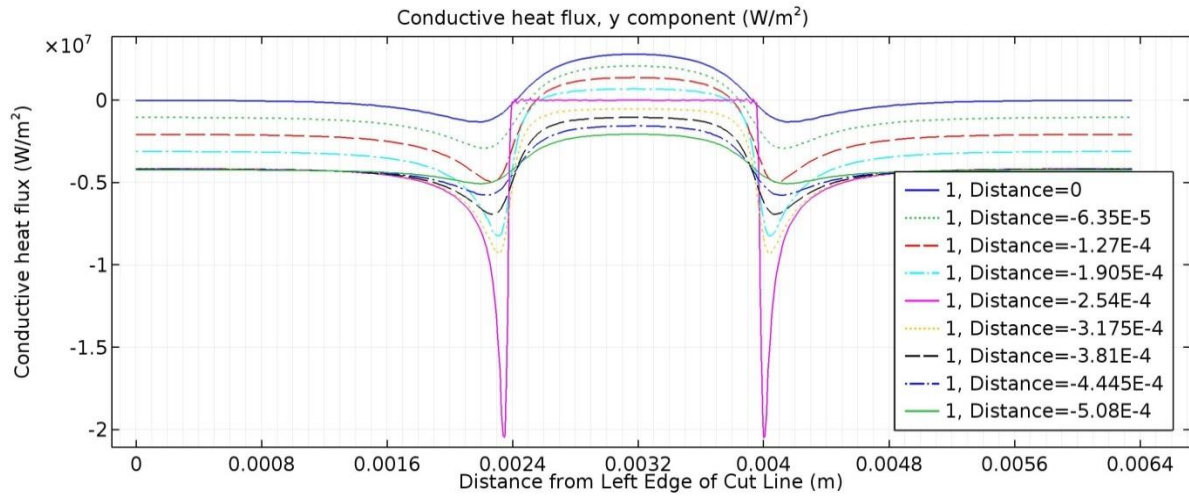
Figure 88 TL wad AMR domain flux across the cut lines
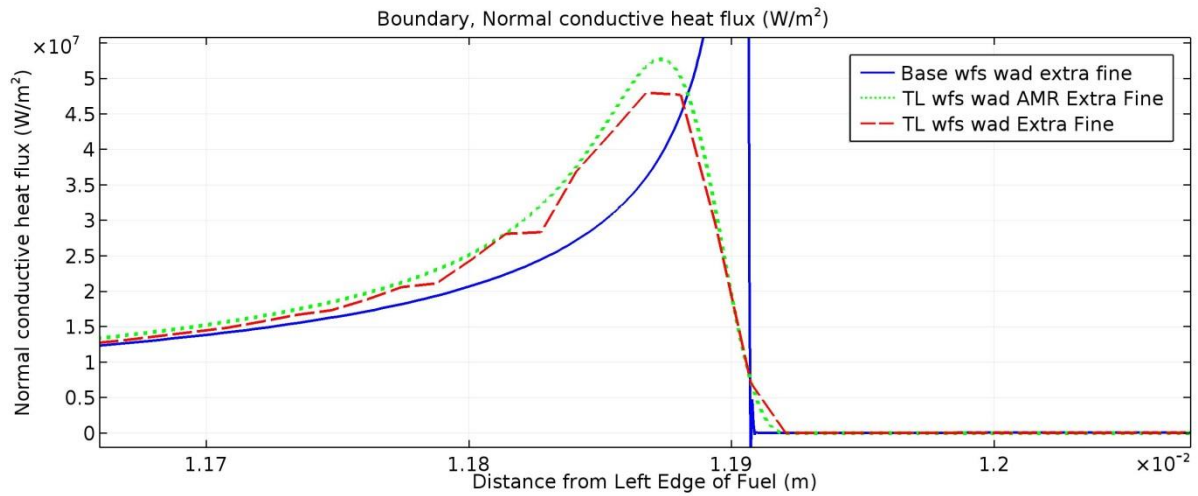
Figure 89 Comparison of boundary, normal flux for the Base, Extra Fine mesh, and AMR models wfs wad
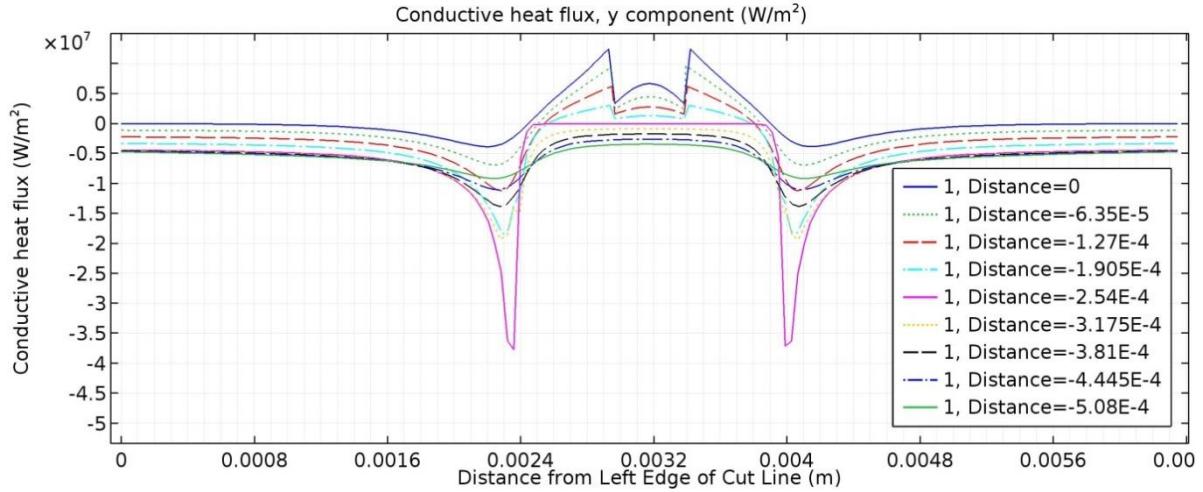
Figure 90 Comparison of quadratic, cubic, and quartic basis functions for boundary, normal flux of TL wfs wad Finer
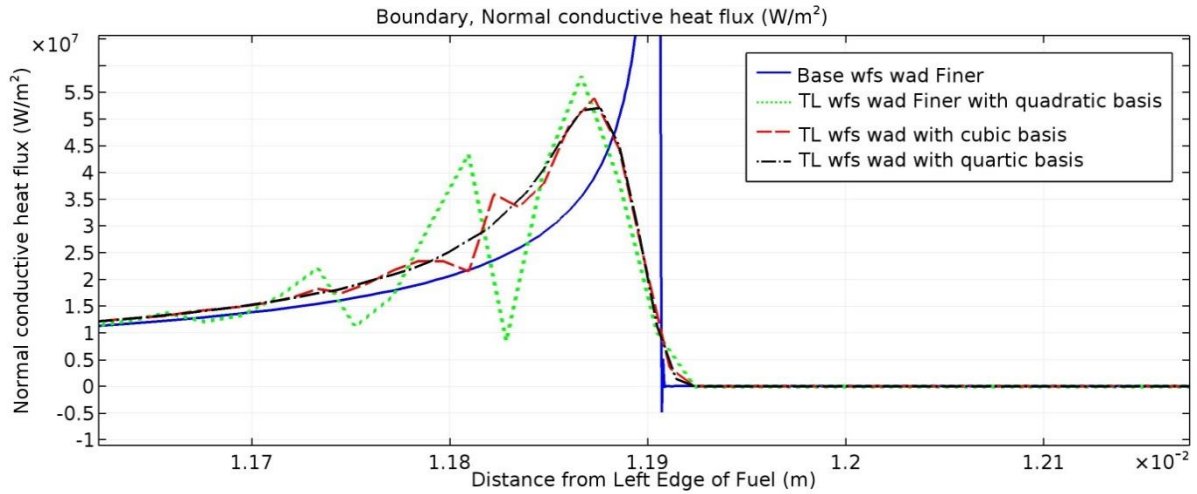
Figure 91 Domain conductive heat flux normal to the cut lines for the quadratic basis function TL wfs wad Finer model
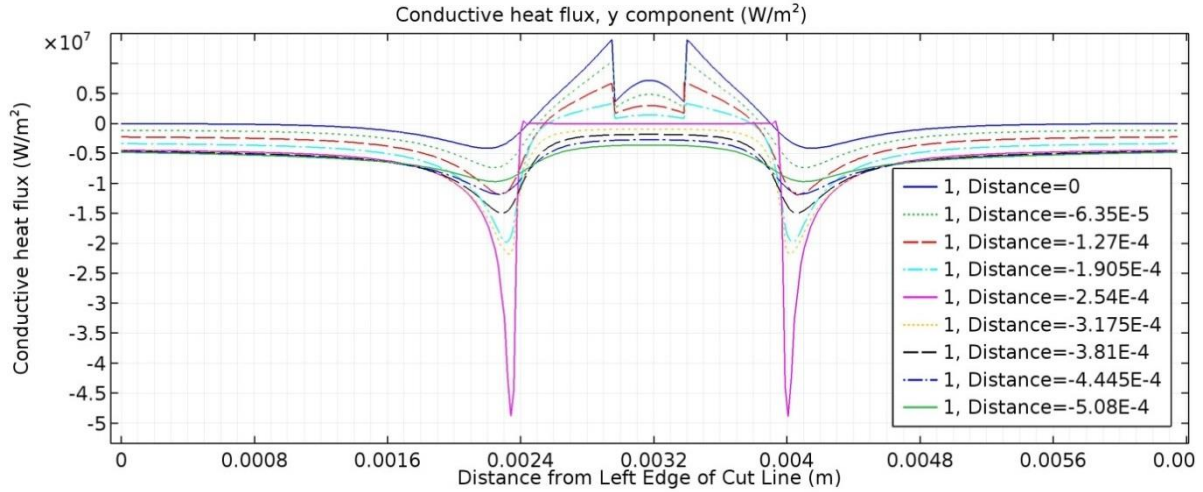
Figure 92 Domain conductive heat flux normal to the cut lines for the cubic basis function TL wfs wad Finer model
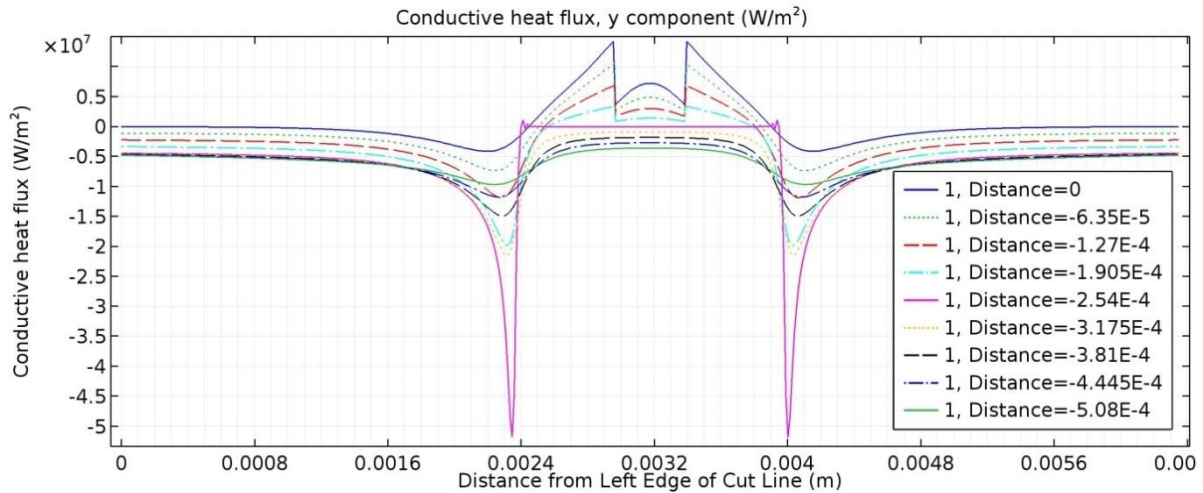
Figure 93 Domain conductive heat flux normal to the cut lines for the quartic basis function TL wfs wad Finer model

125

7.3 Considerations for TC

As discussed in section 4.2, thermal contact conductance models are developed with the implicit assumption that heat transfer is only taking place through the small area of true contact. In the case of a non-bond, the majority of the conduction is taking place around the non-bond. This results in the flux vectors bending around the non-bond instead of all bending through the location of thermal contact in a typical joint, per Figure 94. In the standard thermal contact conductance description and experiment, at some distance from the thermal contact, the flux vectors are parallel, and constrict through the contact area. In the non-bond description, the flux vectors diverge as they mostly go around the non-bond.

At the microscopic level, the interior of the non-bond (that is, away from the edges) has the typical appearance of thermal contact conductance, with multiple contact points between the two surfaces. However, with thin cladding, the tacit assumption of heat flux normal to the contact plane is not satisfied. By examining the degree to which the flux is not parallel, that is, what portion of the heat flux magnitude is still moving across the cladding rather than out to the coolant at the exterior edge of the surface, the degree to which this tacit assumption is not being satisfied can be quantified. These results are shown in Table 16.

While these two cases, standard thermal contact and non-bond contact, differ, what determines the actual conductance across the interface is the actual contact area between the surfaces. Thermal contact conductance models determine this contact area through semi-empirical relationships that use contact mechanics. The parameter C_{tc} is, in one way, a coefficient of true contact or a ratio of true to apparent contact. Viewed in this way, the difference between a standard thermal contact configuration and a non-bond configuration would not appear to affect the resulting conductivity in the non-bond region.

Additionally, the manufacturing process ensures that the surface topology on either side of a non-bond is close to a mirror image of the other side. The manufacturing process is such that where no non-bond exists, the material has flowed to perfect contact, with material from the cladding bonding with the fuel. Thus, it is likely that where a non-bond exists the material has also flowed to nearly perfect contact, as well, but not bonded. As such, while this situation is not

Table 17 Energy Balance for TL wfs wad using different basis functions

% Difference in Energy Generation and Energy Leaving Domain	TL wfs wad Finer		
	Quadratic	Cubic	Quartic
Fuel Segregation (FS)	0.001%	0.000%	0.000%
Fuel + FS	0.019%	-0.048%	-0.016%

Table 16 Percent of heat flux flowing across the cladding at the cold and hot surfaces

	cold	hot
TC wnb	65.8%	20.7%
TC wfs wnb	21.6%	27.2%

126
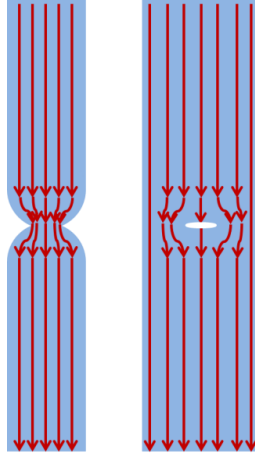
Figure 94 Standard thermal contact (left) versus non-bond thermal contact (right)

entirely consistent with the assumptions of TCC, the results from using TCC are likely still conservative, but less so than using an adiabatic disc.

7.4   Conclusions

The thermal contact and thin layer options in COMSOL are compared with a conventional fine mesh FEA modeling approach. Differences in temperature, conductive heat fluxes, or energy balances are assessed for an array of cases. Spikes and oscillations are observed along the non-bond boundary in both boundary and domain heat flux for the thin layer and thermal contact models that are not physical. Domain energy balances, and the rate at which the distortions diffuse within the computational domain fluxes, diminish the influence of the oscillating features on the temperature field in regions of interest away from the non-bond edge. Using adaptive mesh refinement, as well as user controlled tighter meshing reduces and can eliminate these oscillations. Additionally, use of higher order elements has an effect similar to tighter meshing.

Both thin layer and thermal contact modeling options are similar in performance, but the thermal contact model offers flexibility that make it the more appealing option for this assessment. First, the thermal contact model allows for the inclusion of structural mechanic effects on the conductivity across the non-bond. While including structural mechanics is outside of the scope of this current effort, it should eventually be incorporated into the model. Similarly, the thermal contact model can be used to account for the heat transfer through accumulated fission gases in the non-bond. This aspect is also outside the scope of the current project, which focuses exclusively on initial operating conditions, however, it will also need to be incorporated in the future. Finally, and most relevant right now, using the thermal contact model provides a direct estimate of the conductivity of the non-bond. If the thin layer were used, a value for the conductivity across the non-bond would still be needed.

127

Chapter 8   2D, Narrow Coolant Channel Model Development

A 2D, narrow coolant channel model was developed to simulate the fuel plate and coolant channel. Development of the model included gathering necessary data for construction of the model, evaluation of computation times for different configurations of the model, and examination of pressure drops, coolant velocities, temperatures, and mass and energy balances associated with turbulence models and mesh refinement.

8.1   Model Features

The model consists of a fluid coolant channel surrounding a solid fuel plate, Figure 95, and is representative of a nominal, flat fuel plate. The aspect ratio of the model is very large. To aid in visualization, the view is set so that the y-axis is magnified 100 times relative to the x-axis in images that show the entire plate. Each domain of the model, as well as associated boundaries are described in the following sections. A number of different works were consulted in the development of this model, and discussions of the efforts used by the different authors are included within each sub-section as appropriate.

8.1.1   Coolant

8.1.1.1   Dimensions

The coolant domain within the model encompasses the fuel plate and represents half of a coolant channel above and below a fuel plate plus some distance upstream and downstream of the fuel plate. It is 0.8128 m [32 in] long and 2.54 mm [0.10 in] thick. It extends 0.1016 m [4 in]
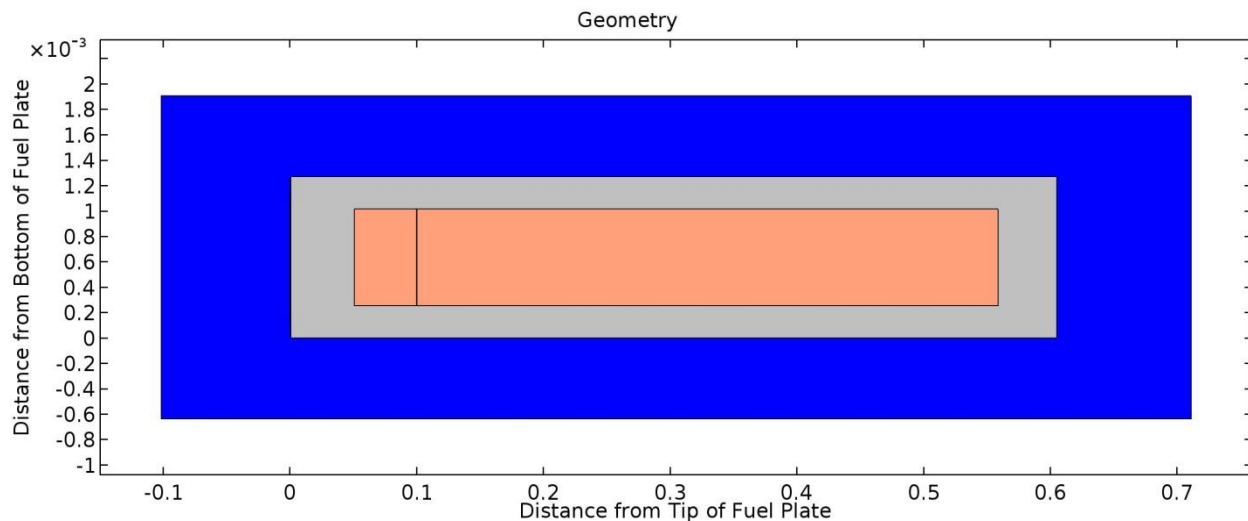
Figure 95 Model geometry with coolant in blue, clad in gray, fuel in orange, and a fuel segregation (only used in identified cases) in red, but here only appears as a line in the fuel (Note: thickness is exaggerated)

128

upstream from the tip of the fuel plate, and 0.1016 m [4 in] downstream from the end of the fuel plate.

Based on the drawings, the nominal thickness, or gap, for the coolant channel between each fuel plate is 1.27 mm [0.05 in]. [14] observed that by accounting "…for fuel element manufacturing tolerances; fuel plate deflections; thermal expansion; and oxide buildup" the actual channel gap may reduce to 0.889 mm [0.035 in] on one side of a plate. In the model used for this study, however, no effort has been made to account for these phenomena.

[36] used a coolant domain that extended 2.67 cm [1.05 in] upstream and 25.39 cm [10 in] downstream. [36] explained that "this extension is necessary to allow the flow to expand and relax the transverse pressure gradient downstream of the fuel plate. This allows one to impose a uniform pressure boundary condition at the global flow outlet of the model."

To examine the effect of coolant domain length downstream of the end of a fuel plate, three variations of the model (0.8128 m [32 in], 1.067 m [42 in], and 1.321 m [52 in] coolant domain lengths) were run using the SST turbulence model with a "Normal" mesh. Figure 96 shows the pressure recovery just past the end of the fuel plate along the top boundary of the coolant channel. This boundary represents the centerline of the coolant channel between two fuel plates, and is measured from the tip of the fuel plate. Figure 97 shows the pressure recovery through the centerline of a fuel plate measured from the end of the fuel plate. In both cases, the pressure is fully recovered, and stabilized for all three lengths before the end of the nominal (0.8128 m [32 in]) model length.
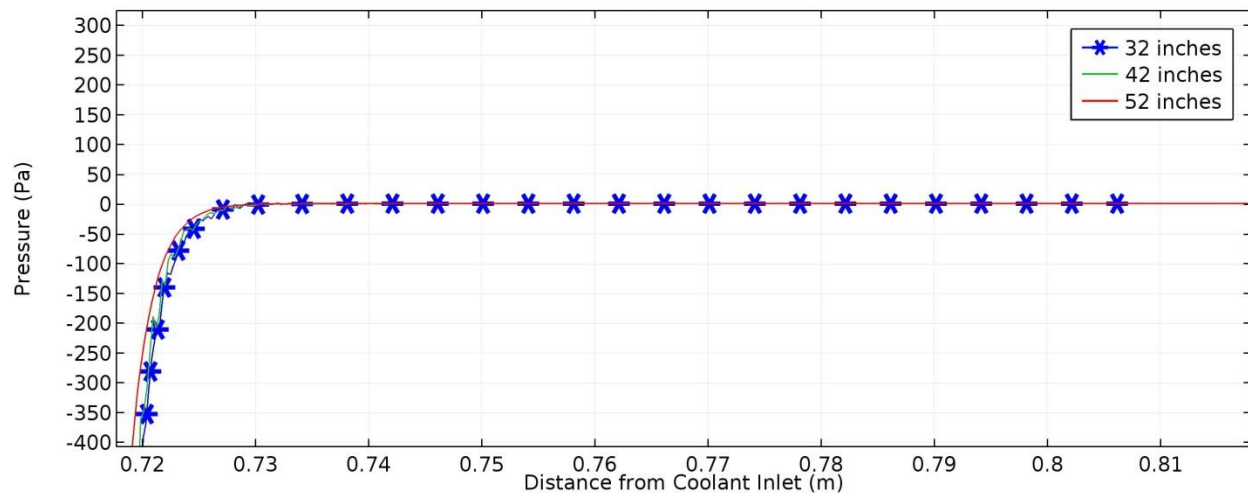
Figure 96 Pressure recovery at the top of the model, or the center line of a coolant channel between two fuel plates, for 3 different lengths of coolant domain measured from the tip of the fuel plate

129
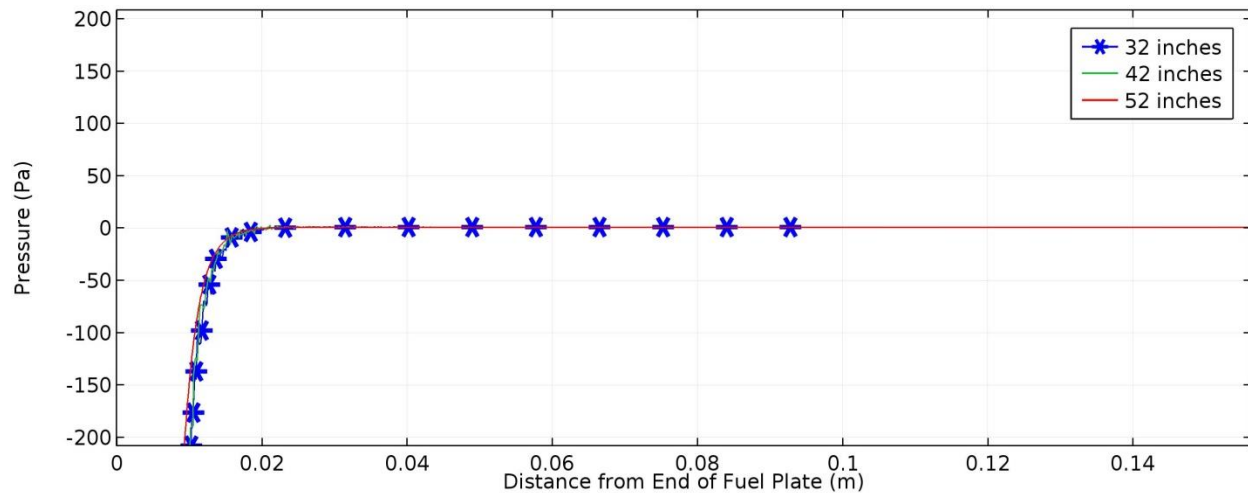
Figure 97 Pressure recovery at the center line of the model, which is the centerline through a fuel plate, for 3 different lengths of coolant domain measured from the end of the fuel plate

8.1.1.2 Materials

The coolant domain uses COMSOL's built-in liquid water which uses temperature dependent viscosity, heat capacity, density, thermal conductivity, and speed of sound.

[36] compared using water with constant fluid properties and fluid properties from the National Institute of Standards and Technology (NIST) which vary with temperature. The NIST fluid properties yielded consistently lower temperatures along the clad surface because of the increase in thermal conductivity and decreased viscosity of water as the temperature increased.

8.1.1.3 Physics

The coolant was assigned to both non-isothermal fluid flow and heat transfer in fluids physics nodes. The fluid flow node includes selection of turbulence models. As discussed in section 6.2.2, a number of different turbulence models are available within COMSOL. The meshing and solver requirements differ from one turbulence model to the next. This necessitated using a separate study for each turbulence model. The default parameters were used for each of the turbulence models.

8.1.1.4 Boundaries

The top and bottom boundaries are periodic and were set to symmetric for both fluid flow and heat transfer. The left hand side boundary is the inlet boundary, and was set to 322 K [120°F] with an inlet velocity of 8.525 m/s [27.97 ft/sec].

Most previous researches have used an inlet coolant velocity close to 15.8 m/s [52 ft/s]. [89] used 15.88 m/s citing [14]'s 52 ft/s. The authors of [88] used 15.8 m/s, and [36] used 15.85 m/s also citing [14]. In [36], however, because the inlet geometry height was twice the channel geometry

height, a value of 7.925 m/s was used so that the average coolant velocity within the channel was 15.85 m/s. With regard to the 52 ft/s, [14] makes the following statement: "Based on typical measured pressure drops through the core (upon which fuel element flow-rate estimates can be made) and discussions with HFIR staff, a normal (steady-state) flow rate of 16,500 gal/min (1.04 m^3/s) was selected for initializing the vessel core portion of the model. The design data were normalized to this value, thus preserving the designed flow distribution. As indicated in Fig. 8 [reproduced as Figure 8 in section 2.1], the bulk of the flow is through the fuel region, resulting in an average inlet flow velocity of ~52 ft/s (1.58 m/s [sic])."

A new effort was made to determine the flow velocity within the coolant channels. Re-examining Figure 8, it can be seen that the flow rate through the fuel region is 0.84623 m^3/s [13,413 gallons/min]. Later in [14] it states, "During HFIR normal operation the flow rate through the fuel element is estimated to be 13,277 gal/min (0.838 m^3/s)." With these flow rates established, the area through which the flow is passing can be used to determine the coolant velocity. [14] provides the radii for the inner dimensions of each fuel element as 0.06913 m as the inner element inner radius, 0.128 m as the inner element outer radius, 0.1492 m as the outer element inner radius, and 0.2111 m as the outer element outer radius.

Using these radii, a flow area of 0.1065 m^2 is calculated. This represents the area immediately upstream and downstream of the fuel plates. Once the flow enters the coolant channels between the fuel plates, the total flow area will be reduced to ½ of this area. These areas provide an inlet flow velocity of 7.944 m/s and an average in-channel velocity of 15.89 m/s for the 13,413 gallons/min flow rate. This inlet velocity was used as the nominal value in the sensitivity analysis reported in Chapter 11, but the inlet velocity reported initially, 8.525 m/s, was used for all results reported in this section, unless otherwise noted.

An inlet temperature of 322 K [120°F] [14, 88, 36] has been used previously. Additionally a value of 327 K [128.9°F] was used by [36].

The right hand side boundary is the exit. It was assigned an outflow condition as well as a convective heat transfer condition, and given a uniform pressure of 0 Pa. Where the coolant comes into contact with the fuel plate, the boundaries were all set to the no-slip condition. These boundary conditions are in line with what previous researchers have done.

8.1.2   Cladding

8.1.2.1   Dimensions
The fuel plate measures 0.6096 m [24 inches] long, 1.27 mm [0.05 inches] thick, and has a semi-circle tip with a radius of 0.635 mm [0.025 inches]. It is centered within the coolant.

Table 18 Clad specific heat and thermal conductivity values used in the final model

| Thermal Conductivity | | | | | Specific Heat | | | |
| Temp | (W/m-K) | | | | Temp | (J/kg K) | | |
F	Al	6061	<Clad>		F	Al	6061	<Clad>
82.4	237	175	181		80	900	900	900
442.4	237	196	200		440	996	988	988
802.4	226	194	197		980	1147	1126	1130

8.1.2.2 Material

The fuel plate cladding is composed of 6061 aluminum. In the model, the COMSOL built-in aluminum material was used initially.

Following [14], the clad specific heat and thermal conductivity of the built in aluminum were changed in the final model to reflect the <Clad> values in Table 18. [36] used a value of 167 W/m-K for the clad thermal conductivity. [89] lists the SSHTC as using a value of 167.88 W/m-K, which is the same value used in the legacy hotspot model.

8.1.2.3 Physics

The cladding was assigned to the heat transfer in solids node.

8.1.2.4 Boundaries

The outer boundaries were assigned a no-slip condition, as mentioned above. The continuity condition was assigned to the boundaries between the cladding and the fuel for the base model. When a non-bond was modeled, the bottom boundary between the fuel and the cladding was assigned the thermal contact boundary condition. Within this boundary layer, the Mikic elastic correlation was used with an average asperity roughness of 1 μm, an average slope of 0.20, and a function was defined as previously described for modeling a non-bond in section 7.1.3.

8.1.3 Fuel

8.1.3.1 Dimensions

The fuel measures 0.508 m [20 inches] long, 0.762 mm [0.03 inches] thick, and is centered within the cladding.

8.1.3.2 Material

The fuel is a cermet composed of aluminum 1100 and U_3O_8. As with the cladding, in the model, the built-in aluminum material was used initially.

Again following [14], values for thermal conductivity and heat capacity in Table 19 were used for the fuel properties in the final model.

Table 19 Specific heat and thermal conductivity values used for the fuel in the final model [14]

Thermal Conductivity				Specific Heat			
Temp		(W/m-K)		Temp		(J/kg K)	
F	Al	In Elem	Out Elem	F	U3O8	In Elem	Out Elem
80.3	237	177	159	80	285	762	724
260.3	237	176	158	440	331	846	804
900	226	174	158	980	339	963	913

[36] used 132.06 W/m-K for the fuel thermal conductivity. [89] lists the SSHTC values of 132.06 and 110.07 W/m-K for inner and outer elements respectively. The legacy hotspot model used 167.87 W/m-k.

8.1.3.3 Physics

The fuel was assigned to the heat transfer in solids node. It was also given the domain condition of heat generation. For the initial runs, a constant value of heat generation was used. These values were $5.6 \times 10^7, 5.6 \times 10^8$ and 5.6×10^9 W/m^3. These numbers represent 1%, 10%, and 100% of the heat generation based on 85 MW total power generation, and uniform power production by the total fuel-meat/filler volume in the core [89].

Following [89], the constant heat generation rate was replaced by a heat generation density profile in the final model. This profile was developed based on the output of the SSHTC used at the HFIR. Figure 98 shows the profile and Table 20 shows the development of the power density profile as well as a check that these values correctly account for the total power production and the distribution of power between the inner and outer fuel elements. These values were computed based on a power level of 85 MW.

Previous researchers have used other approaches. [84] did a similar calculation using SSHTC output values from one edge of the plate to generate the heat production profile. Additionally, [84] divided the fuel section of the model up into 19 separate subdomains to account for the different generation levels. [35] took into account a 1% variance in power production due to fuel load tolerances, and 9% allowance for power tilt resulting from the influences of experiments within the reactor.

[36] used the power density distribution shown in Figure 99, with a spike in power near the core axial center. [36] explained that the spike in the center "…is not a physical phenomenon that occurs in the High Flux Isotope Reactor. Instead it is part of a strategy used by the developers of the Steady State Heat Transfer Code to model the thermal consequences of fuel defects." [84] used a constant heat generation rate of 2.658×10^9 W/m^3; this was shown by [89] to be the result of an error related to the active area for the heat transfer area of the fuel plates.
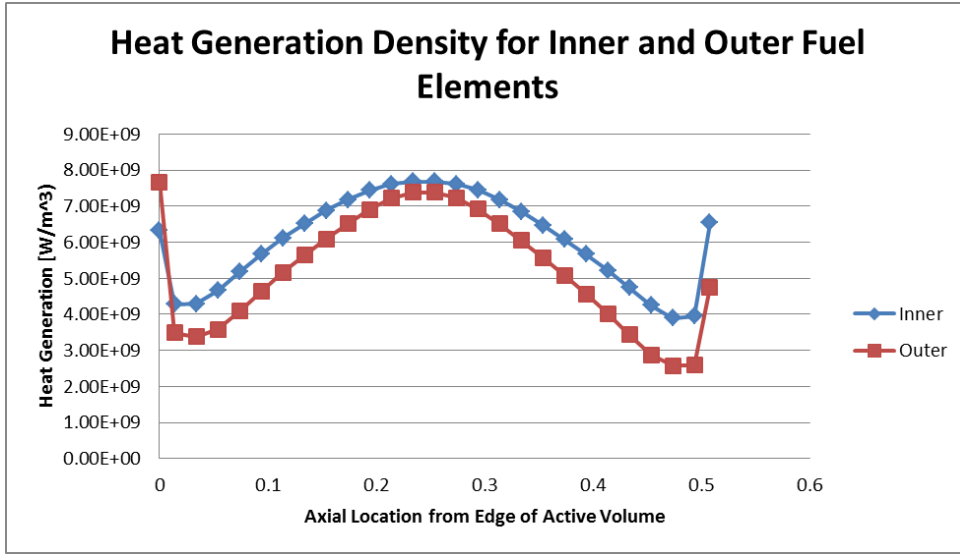
Figure 98 Profile of heat generation density for both inner and outer fuel plates and elements
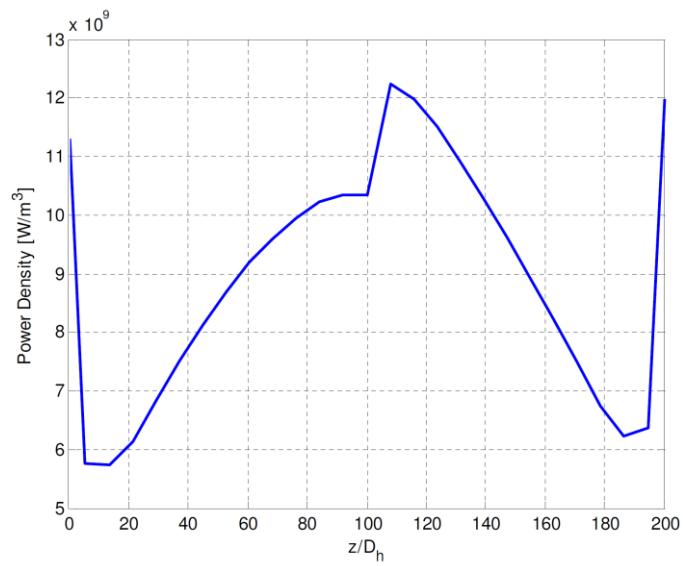
Figure 99 Power density distribution used by [2]

134

Table 20 Calculations and check for inner and outer fuel plate heat generation rates

Axial location (m)	Multiplier Inner	Multiplier Outer	Height	volume Inner	volume Outer	Power Density [w/m^3] Inner	Power Density [w/m^3] Outer	Power Production [w] Inner	Power Production [w] Outer
0	1.13	1.369	0.007	4.24E-07	3.81E-07	6.33E+09	7.67E+09	2.68E+03	2.92E+03
0.014	0.763	0.623	0.017	1.03E-06	9.25E-07	4.27E+09	3.49E+09	4.40E+03	3.23E+03
0.034	0.767	0.603	0.02	1.21E-06	1.09E-06	4.30E+09	3.38E+09	5.20E+03	3.67E+03
0.054	0.832	0.639	0.02	1.21E-06	1.09E-06	4.66E+09	3.58E+09	5.65E+03	3.89E+03
0.074	0.925	0.729	0.02	1.21E-06	1.09E-06	5.18E+09	4.08E+09	6.28E+03	4.44E+03
0.094	1.012	0.828	0.02	1.21E-06	1.09E-06	5.67E+09	4.64E+09	6.87E+03	5.04E+03
0.114	1.092	0.922	0.02	1.21E-06	1.09E-06	6.12E+09	5.16E+09	7.41E+03	5.62E+03
0.134	1.163	1.008	0.02	1.21E-06	1.09E-06	6.51E+09	5.64E+09	7.89E+03	6.14E+03
0.154	1.228	1.088	0.02	1.21E-06	1.09E-06	6.88E+09	6.09E+09	8.33E+03	6.63E+03
0.174	1.282	1.164	0.02	1.21E-06	1.09E-06	7.18E+09	6.52E+09	8.70E+03	7.09E+03
0.194	1.329	1.233	0.02	1.21E-06	1.09E-06	7.44E+09	6.90E+09	9.02E+03	7.51E+03
0.214	1.36	1.289	0.02	1.21E-06	1.09E-06	7.62E+09	7.22E+09	9.23E+03	7.85E+03
0.234	1.373	1.319	0.02	1.21E-06	1.09E-06	7.69E+09	7.39E+09	9.32E+03	8.03E+03
0.254	1.372	1.319	0.02	1.21E-06	1.09E-06	7.68E+09	7.39E+09	9.31E+03	8.03E+03
0.274	1.361	1.291	0.02	1.21E-06	1.09E-06	7.62E+09	7.23E+09	9.23E+03	7.86E+03
0.294	1.33	1.237	0.02	1.21E-06	1.09E-06	7.45E+09	6.93E+09	9.02E+03	7.53E+03
0.314	1.282	1.164	0.02	1.21E-06	1.09E-06	7.18E+09	6.52E+09	8.70E+03	7.09E+03
0.334	1.223	1.081	0.02	1.21E-06	1.09E-06	6.85E+09	6.05E+09	8.30E+03	6.58E+03
0.354	1.156	0.996	0.02	1.21E-06	1.09E-06	6.47E+09	5.58E+09	7.84E+03	6.07E+03
0.374	1.086	0.907	0.02	1.21E-06	1.09E-06	6.08E+09	5.08E+09	7.37E+03	5.52E+03
0.394	1.011	0.814	0.02	1.21E-06	1.09E-06	5.66E+09	4.56E+09	6.86E+03	4.96E+03
0.414	0.931	0.717	0.02	1.21E-06	1.09E-06	5.21E+09	4.02E+09	6.32E+03	4.37E+03
0.434	0.847	0.614	0.02	1.21E-06	1.09E-06	4.74E+09	3.44E+09	5.75E+03	3.74E+03
0.454	0.759	0.514	0.02	1.21E-06	1.09E-06	4.25E+09	2.88E+09	5.15E+03	3.13E+03
0.474	0.695	0.46	0.02	1.21E-06	1.09E-06	3.89E+09	2.58E+09	4.72E+03	2.80E+03
0.494	0.705	0.463	0.017	1.03E-06	9.25E-07	3.95E+09	2.59E+09	4.07E+03	2.40E+03
0.508	1.169	0.849	0.007	4.24E-07	3.81E-07	6.55E+09	4.75E+09	2.78E+03	1.81E+03

Power per Plate:	186374 143971
Power per Element:	3.19E+07 5.31E+07
Percent:	37.5% 62.5%
Total Power Produced:	8.50E+07

8.1.3.4   *Boundaries*

All boundaries of the fuel were as described in the section 8.1.2.4.

8.1.4   **Fuel Segregation**

A few test cases were run with a fuel segregation, though the majority of the results presented in this chapter were from runs without a fuel segregation or a non-bond. Both the non-bond and the fuel segregation are used in the sensitivity analysis, Chapter 11.

8.1.4.1   *Dimensions*

The fuel segregation was set to the full thickness of the fuel 0.762 mm [0.03 inches], and a length of 0.0208 mm [0.0082 inches].

8.1.4.2   *Material*

Initially the fuel segregation was assigned the built-in aluminum material properties, but with a thermal conductivity equal to 59.5 W/m-K, ¼ the unsegregated fuel value.

Following the SSHTC as described in [89], 46.9 W/m-k was used for the thermal conductivity of the fuel segregation in the final model. This is also the same value used in the legacy hotspot model.

8.1.4.3   *Physics*

The fuel segregation was assigned to the heat transfer in solids node. It was also given the domain condition of heat generation. For the initial runs, a constant value of heat generation, 5.6×10^{10} W/m^2, was used, equal to 10 times that generated in the fuel.

Following the legacy model, this was later changed to 10.3 times the nominal fuel generation rate at the location of the fuel segregation. Previous researchers have used different generation rates for the fuel segregation. [36] used 10 times the fuel generation rate. [84] used 1.2 times.

8.1.4.4   *Boundaries*

All boundaries of the fuel segregation match those described in the section on cladding, with the non-bond coincident with the fuel segregation.

8.2   **Meshing**

COMSOL's Physics-controlled meshing feature was used for all cases. This resulted in a wide range of domain mesh elements from approximately 10,000 for the coarsest algebraic model, to 3,500,000 for the finest 2 equation model that could be run. Table 21 provides the number of domain elements for each of the different turbulence models and mesh sizes. No entries are provided for SST over Finer, because the computer did not have sufficient memory to run those models. In the case of k-ω, the solution failed to converge for the extra fine grid. Low-Re models with grids over Normal, and all L-VEL and Spalart-Allmaras models would not run, producing an error shortly into the solution process. In some cases, these errors could be avoided by

changing model parameters such as dimensions or inlet velocity, but because these changes moved the model away from the desired target, the results from those changed models are not included here.

Because the different turbulence models approximate the physics in different ways, the mesh used for the study also differed. Figure 100 shows the difference in appearance for the different mesh sizes as well as how the different turbulence models use different meshes for the same mesh size.

8.3   Other Model Features to Report

All other features not mentioned previously were left to the default settings within COMSOL. This means that for both heat transfer and fluid flow physics, consistent stabilization with both streamline and crosswind diffusion was used. Additionally linear discretization in heat transfer, and P1+P1—which is first order elements for velocity and pressure (as opposed to P2+P1 which is second order for velocity, first for pressure; and P3+P2 which is 3rd order for velocity, 2nd order for pressure)—were used.

8.4   Results

The following section covers the various results produced by the different models. All of these results, unless noted otherwise, were from the initial models which used the built-in values for aluminum as described in the model parameters section as well as a constant heat generation rate and a 0.8128 m [32 inch] coolant domain. The presentation focuses primarily on the comparison of the different turbulence models and mesh refinement.

Table 21 Domain mesh elements for the different turbulence models and different mesh sizes

| | Domain Mesh Elements | | | | |
	SST	k-e	k-w	yPlus	Low-Re
Extremely Coarse	73,798	41,240	41,240	29,752	58,020
Extra Coarse	109,269	49,088	49,088	34,988	88,418
Coarser	157,246	72,638	72,638	39,038	130,640
Coarse	208,533	112,816	112,816	60,155	175,262
Normal	634,844	149,926	149,926	97,890	563,418
Fine	1,616,228	506,118	506,118	129,917	***
Finer	1,965,096	1,410,156	1,410,156	470,892	***
Extra Fine	3,643,822	1,785,694	***	1,396,998	***
Extremely Fine	***	3,444,530	***	1,752,646	***
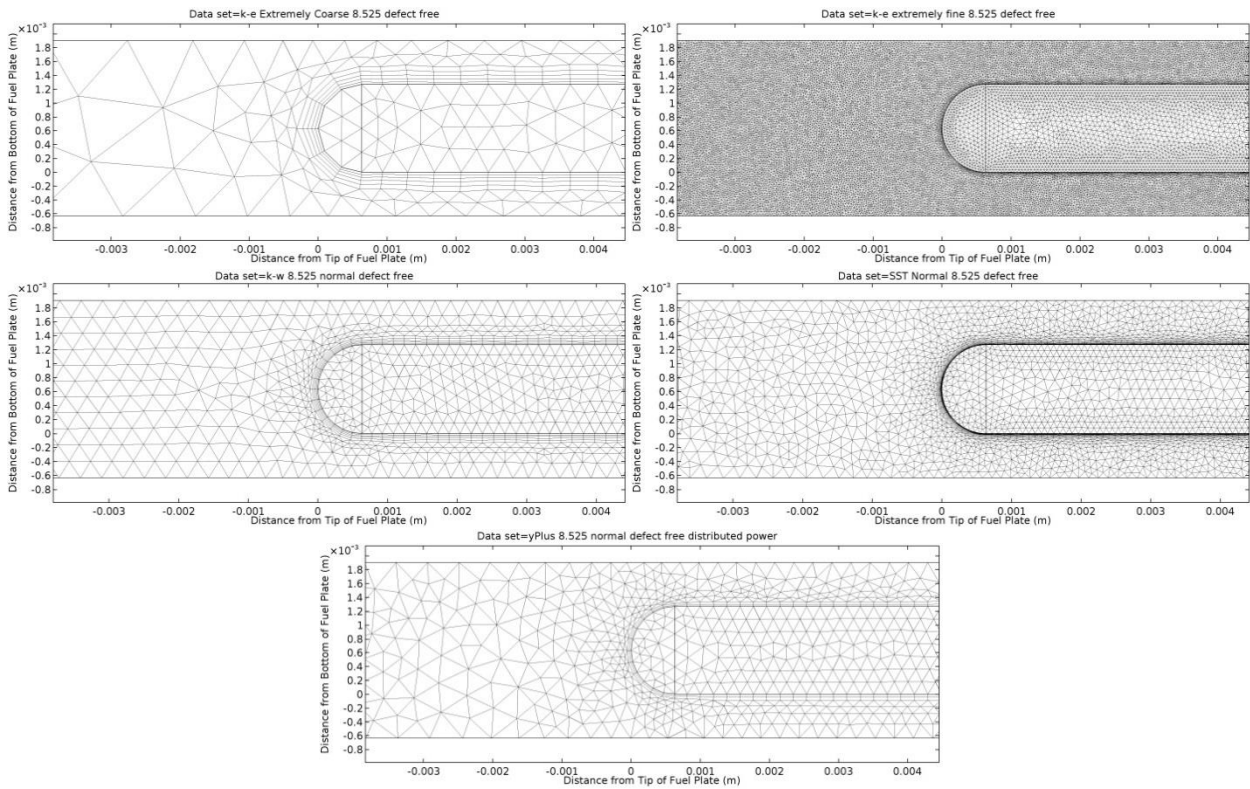
Figure 100 Examples of different meshes used. Top left: Extremely Coarse k-ϵ ; Top Right: Extremely Fine k-ϵ; Center Left: Normal k-ω; Center Right: Normal SST; Bottom: Normal yPlus
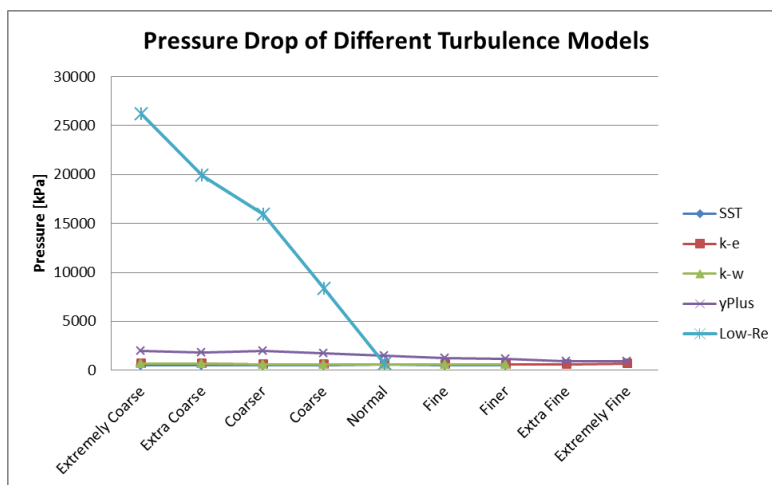
Figure 101 Pressure drop for different turbulence models shown against mesh size

138

8.4.1 Pressure Drop

Pressure drops for the turbulence models at different mesh refinements are shown in Figure 101. Pressure drop in the Low-Re model decreases dramatically as the grid is refined, and obscures the differences in the other models. Figure 102 shows the pressure drop zoomed in on the lower pressure results, and Figure 103 shows the results without either Low-Re or yPlus.

8.4.2 Temperature

Figure 104 shows the maximum temperature within each model. Three of the 2-equation turbulence models are relatively close in their temperature results, while the Low-Re (also a 2-equation model) only approaches the other 2-equation models once at the Normal mesh size. Focusing on the tighter group, Figure 105, it can be seen that k-ϵ and k-ω produce similar results.

8.4.3 Velocity

The same behavior continues in Figure 106 which shows the maximum velocity in the models. The tighter grouping of k-ϵ, k-ω, and SST relative to Low-Re and yPlus is clear. Removing those two models and zooming in, Figure 107, SST and k-ϵ appear to track fairly closely.

8.4.4 Balances

8.4.4.1 Mass

All of the models at all mesh sizes produce mass errors (inlet mass flow rate minus outlet mass flow rate) of approximately 1.2%. Plotting the results, Figure 108, requires a very tight y-axis to see any difference between the models—all of the results fall within close to one hundredth of one percent of one another.
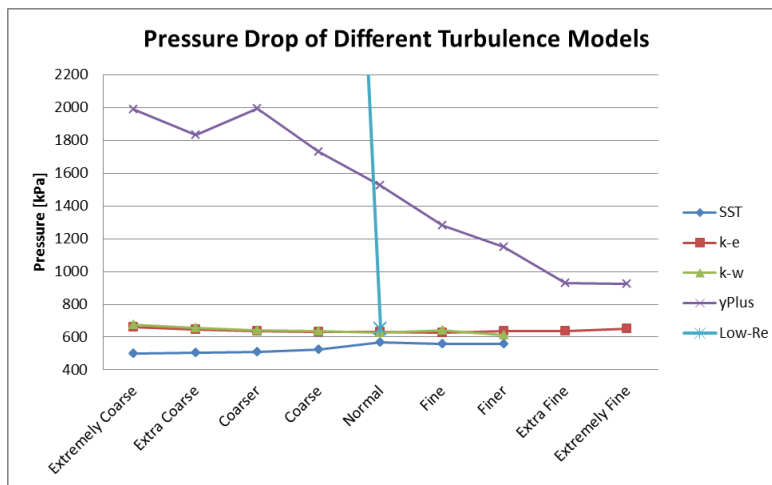
Figure 102 Zoomed pressure drop for different turbulence models

139
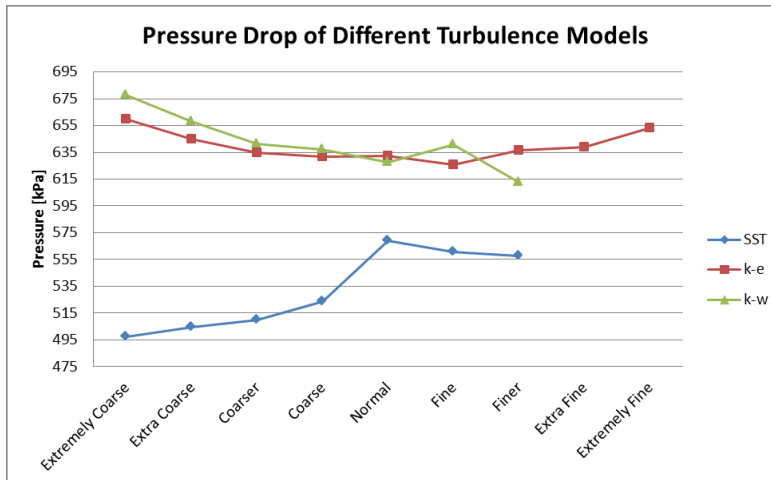
Figure 103 Zoomed pressure drop of k-ϵ, k-ω, and SST turbulence models
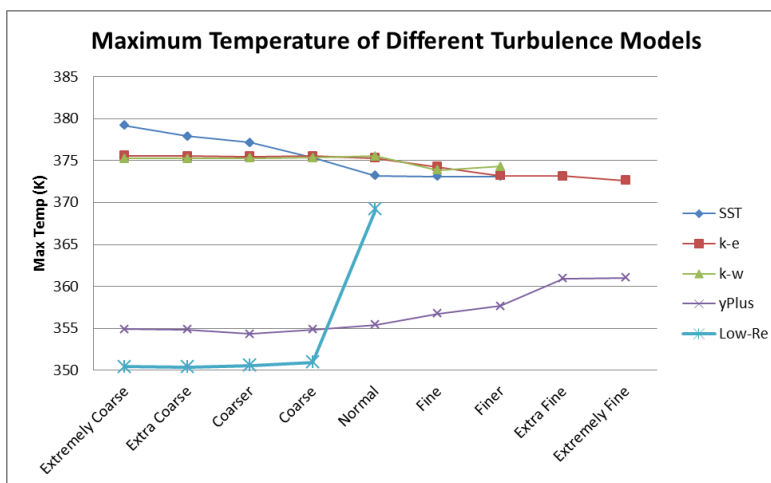
Figure 104 Maximum temperature of different turbulence models

140
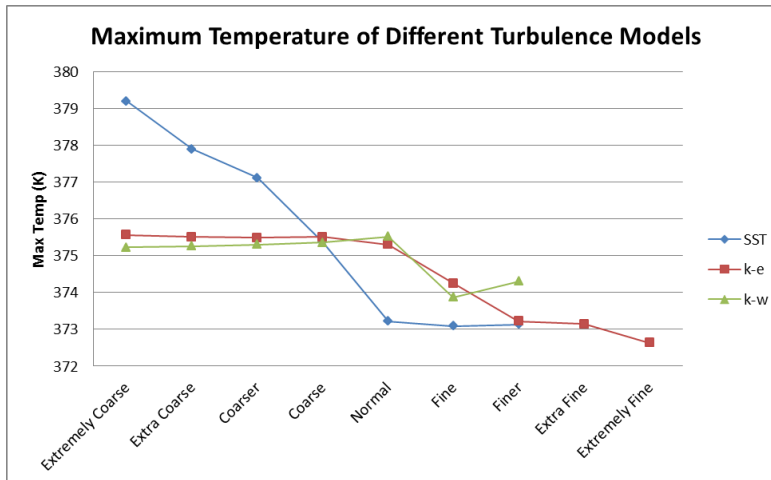
Figure 105 Zoomed maximum temperature for the tight group of k-ϵ, k-ω, and SST
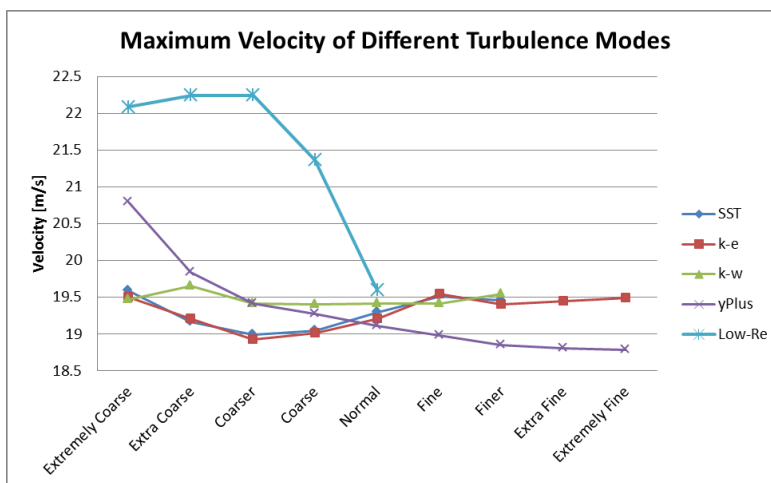
Figure 106 Maximum velocity of the different turbulence models

141
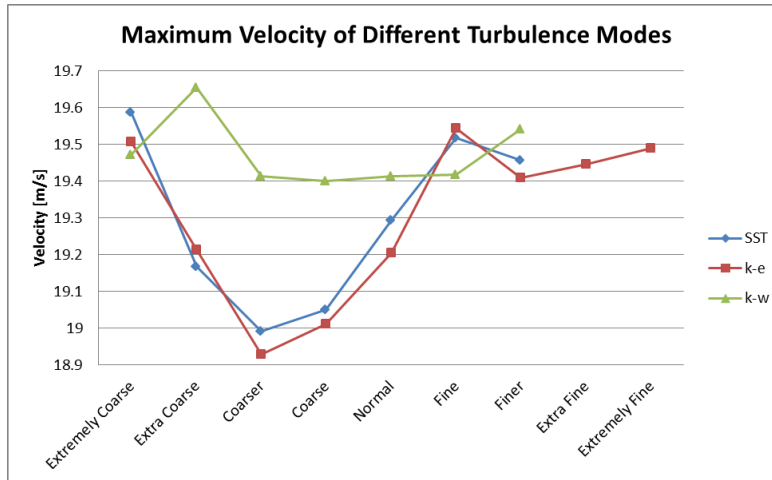
Figure 107 Zoomed maximum velocity focusing on k-ϵ, k-ω, and SST

8.4.4.2 Energy

The error in the energy balance (net energy leaving the system minus energy generated within the system) is dramatic in the Low-Re turbulence model, large mesh size results, surpassing 30% in the extremely coarse mesh. Figure 109 shows that this error decreases rapidly with mesh refinement to Normal where it is comparable to the other models. Figure 110 shows the results without the Low-Re where it can be seen again that the k-ϵ, k-ω, and SST are grouped away from yPlus. Figure 111 shows those three models with k-ϵ and k-ω tracking closely.

8.4.5 Run Time

All of the models were run on a Dell PC with an i7-4790, 8 core, 3.6 GHz processor and 16 GB RAM. The run times in minutes for each model are shown in Table 22. As expected, the algebraic model ran fastest, followed by k-ϵ, k-ω, Low-Re and finally SST.

8.5 Narrow Coolant Channel Model Development Conclusion

The development of the narrow coolant channel model has been detailed. Sources and previous work have been discussed as relevant to each of the components of the model. A number of different turbulence models have been compared using initial parameters. The k-ϵ, k-ω, and SST turbulence models were similar. yPlus required the least calculation time and SST the most. These preliminary assessments inform later studies where parameters are refined for the verification, validation, and sensitivity assessments in coming chapters.
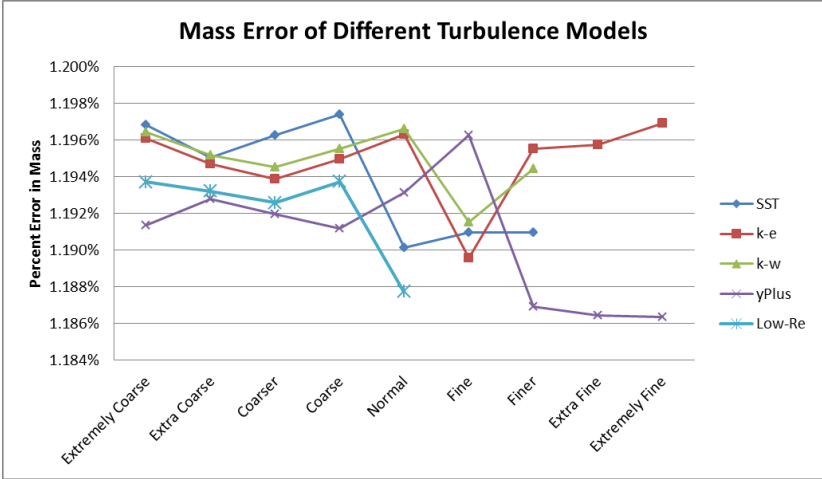
Figure 108 Mass error of the different turbulence models
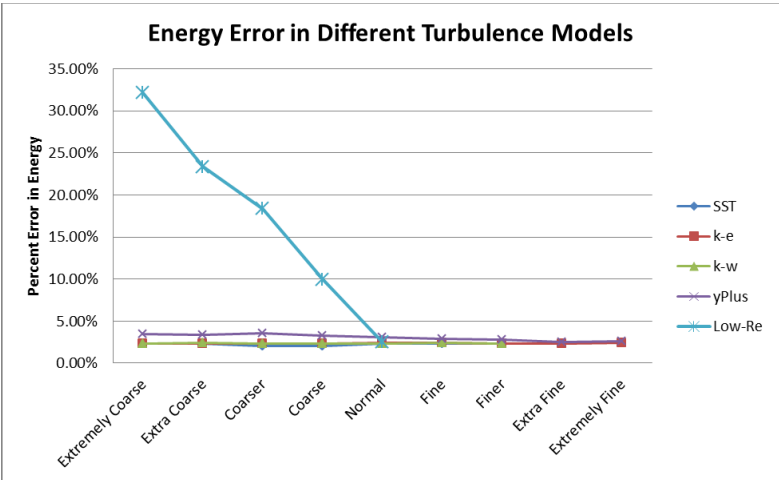
Figure 109 Energy error of the different turbulence models

143
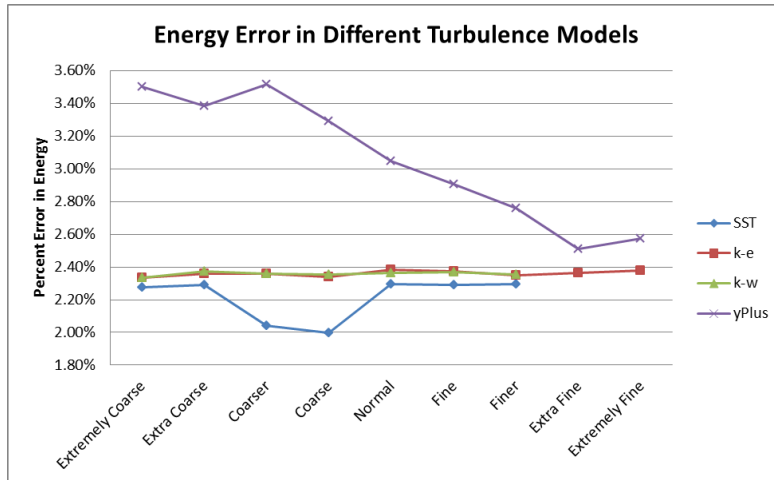
Figure 110 Energy error of different turbulence model without the Low-Re results
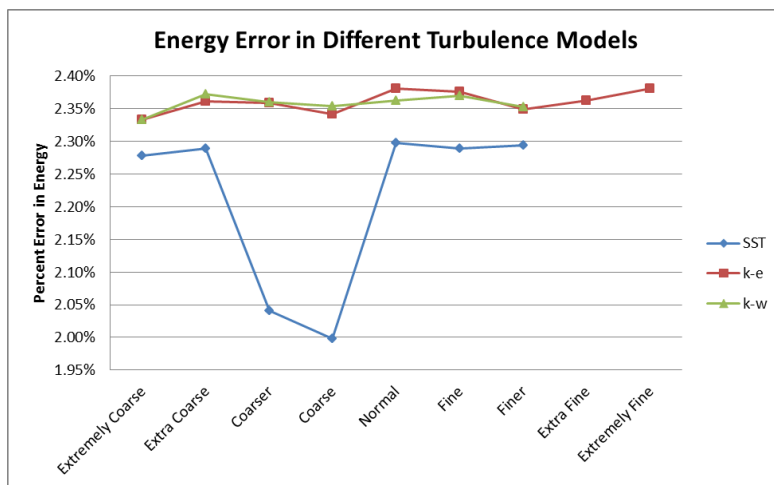
Figure 111 Zoomed energy error focusing on k-ϵ, k-ω, and SST turbulence models

144

Table 22 Run times for the different turbulence models at different mesh sizes in minutes

		Run Time in Minutes		
SST	k-e	k-w	yPlus	Low-Re
6.3	2.4	4.1	0.8	3.5
3.9	2.0	2.6	0.6	3.1
13.1	1.7	3.2	0.6	4.4
24.8	2.3	3.8	0.9	6.7
37.4	3.5	4.9	2.4	71.1
223.8	19.5	18.0	1.6	***
274.5	121.2	62.6	16.4	***
1558	100.8	***	39.7	***
***	378.9	***	62.3	***

Chapter 9   Verification

Verification is the process of ensuring that a code is solving the equations it is supposed to solve (code verification) and determining how well it does so (solution verification). The approach to verification of the hotspot multiphysics simulation will consist of verification in stages—starting with the simplest form of the code and progressing to more and more complicated levels of verification.

9.1   Code Verification

The method of manufactured solutions (MMS) has been identified as an effective approach to code verification. In essence, the method consists of choosing *a priori* the solution that one wishes the code to produce, $S(\vec{x})$, known now as the manufactured solution. The partial differential equations (PDEs) that the code solves are written as an operator, L, and are then allowed to operate on the solution, $L(S(\vec{x})) = Q$. The resulting terms, Q, are then added to the original differential equations as source terms, and the code is asked to solve this modified set of equations. If the code is working correctly, it will reproduce the manufactured solution, and it will do so with an expected, relatively constant order of accuracy [90].

Once a code has demonstrated that it correctly solves the equations, it must be determined how well it does so. That question can be answered, in part, by determining how the actual order of convergence compares with the theoretical order of convergence.

For this project, there are two areas that must be verified: heat transfer and fluid mechanics. Each of these areas is verified at steady state in two dimensions. Heat transfer is the easier of these two as it has only one governing equation and fewer options to explore. The fluid portion is complicated by the presence of multiple equations which require multiple manufactured solutions. Verification will proceed, as possible within COMSOL, with isothermal laminar flow, which has the continuity and two momentum equations, non-isothermal laminar flow, which introduces an energy equation, isothermal turbulent (RANS) flow, which has one or two additional PDEs for turbulent variables, and then non-isothermal turbulent (RANS) flow, which adds an energy equation for a total of 5 or 6 PDEs. Once each component is verified independently, the whole process is repeated with the physics coupled together.

9.1.1   Verification of Heat Transfer in Solids
As explained in section 6.3.1, heat transfer in solids within COMSOL is governed by

$$\rho C_p \left(\frac{\partial T}{\partial t} + \vec{u}_{trans} \cdot \nabla T \right) + \nabla \cdot (\vec{q} + \vec{q}_r) = -\alpha T : \frac{DS}{Dt} + Q$$

where the colon is known as the "double dot product" and is defined by $a : b = \sum_n \sum_m a_{nm} b_{nm}$. This project focuses on a steady state simulation with no translation of the solid material, so the

first term on the left can be eliminated. The first term on the right can also be eliminated because thermoelastic effects are not being considered here. The radiative heat flux can also be ignored. This leaves

$$\nabla \cdot \vec{q} = Q,$$

where $\vec{q} = -k\nabla T$.

In two dimensions, with a constant thermal conductivity, this becomes

$$Q = -k\left(\frac{\partial^2 T}{\partial x^2} + \frac{\partial^2 T}{\partial y^2}\right).$$

The solution to this equation is a temperature field, $T(x, y)$. By using MMS, we first identify the solution,

$$T(x, y) = 60\sin(2\pi x) + 60\sin(2\pi y) + 300. \tag{12}$$

COMSOL offers symbolic differentiation, so the source term, Q, is generated directly as written above—by taking the second derivative of the temperature field in both x and y direction, adding them and multiplying by the thermal conductivity. This verification procedure is done assuming that COMSOL's built-in differentiation is done correctly. By performing the source term generation within the code, verification activities gain flexibility, as the only change needed to use different manufactured solutions is to enter the solution itself, and the code will generate the required source term. This procedure is used for all code verification activities, except where noted otherwise. With a 1x1 domain, this solution appears as Figure 112.

The computational domain was divided into increasingly fine grids using square, mapped elements, starting with a 5x5 grid and doubling edge node density to a 1280x1280 grid. The source term identified above was added in as a heat source, and each boundary was assigned a Dirichlet boundary condition, with the temperatures determined from the manufactured solution. The error (the discrete solution minus the manufactured solution) for each of these grids was plotted as shown in Figure 113.

The scale of the errors decreases with each refinement. Additionally, the average of the error across the surface, as determined by the absolute value of the difference between the discrete solution and the manufactured solution, was also calculated for each grid size and plotted against the number of divisions in one side of the domain. This plot, Figure 114, indicates that this model, with quadratic elements, has an order of convergence of 3. These results are typical of an ideal code.
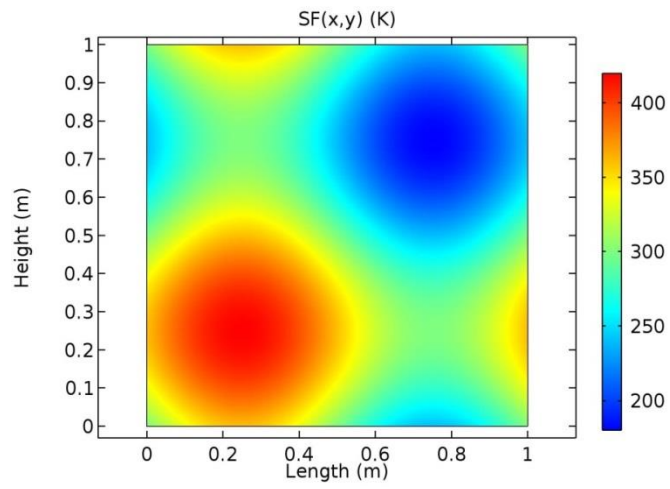
Figure 112 T(x,y) manufactured solution for heat transfer in solids code verification
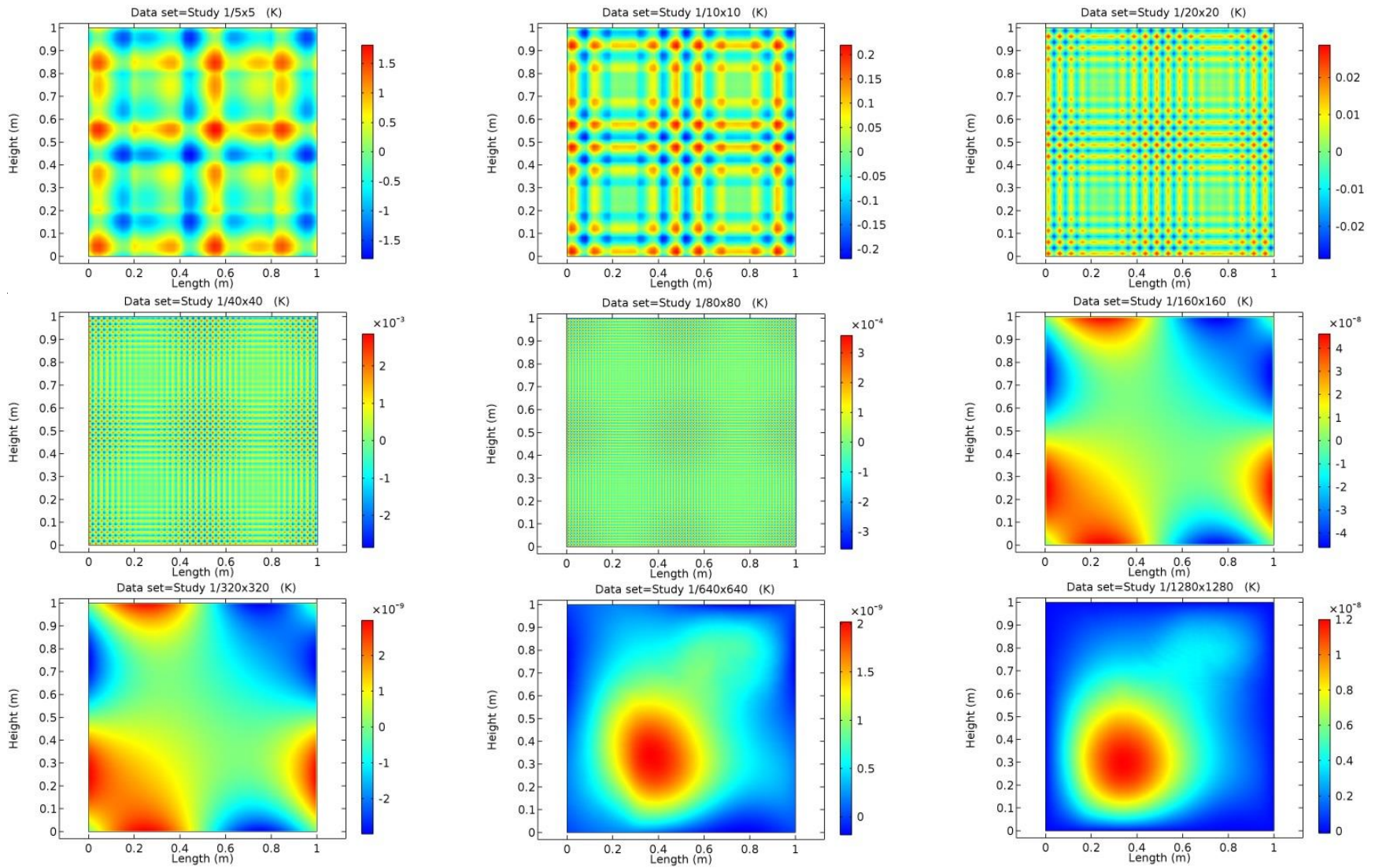
Figure 113 Error (discrete solution minus manufactured solution) for grids from 5x5 to 1280x1280

149

From these results, a numerical error can be predicted for an unknown solution using Richardson extrapolation to complete solution verification. However, the numerical error for the coupled heat transfer and fluid flow modules, not the heat transfer module alone, is the quantity needed.

9.1.2 Verification of Fluid Flow

Verification of fluid flow calculations proved more challenging than heat transfer. Several manufactured solutions were identified, source terms were generated and the solver was run, but the solutions would not converge. The generation of the source terms was carefully checked, but even when the source term appeared to be free of error, the solutions still would not converge. Attempts to use different boundary conditions also proved fruitless. The challenge appeared to result from the sensitivity of the solver, but the exact source of the sensitivity was difficult to identify.

Eventually, a manufactured solution developed by Eca was implemented [91]. This solution was designed to mimic flow over a flat plate, including the presence of a boundary layer. With the same source term generation technique used above, and with appropriate boundary conditions, this solution converged. A number of other manufactured solutions that converged were developed and implemented with the solution from [91] as a guide. The following section, 9.1.2.1, discusses these manufactured solutions and the results from using them.

9.1.2.1 Isothermal, Laminar Flow

As explained in section 6.2.1, COMSOL solves the following equations for isothermal, laminar flow,

$$\frac{\partial \rho}{\partial t} + \nabla \cdot (\rho \vec{u}) = 0$$
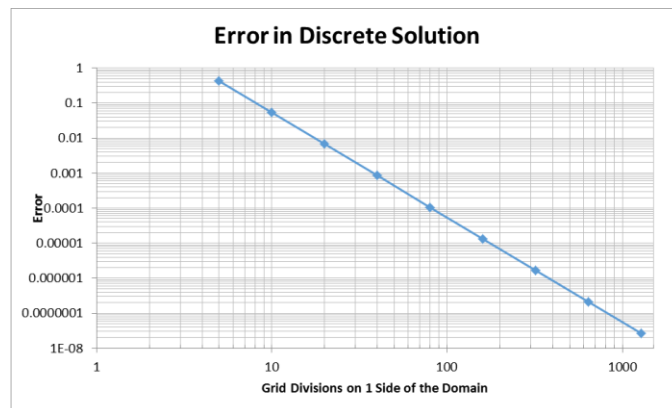
Figure 114 Error in discrete solution as a function of domain grid divisions showing a convergence order of 3

150

$$\rho \frac{\partial \vec{u}}{\partial t} + \rho \vec{u} \cdot \nabla \vec{u} = -\nabla p + \nabla \cdot \mu (\nabla \vec{u} + (\nabla \vec{u})^T) + \vec{F}$$

The flow of interest is steady, so the first term of each equation can be eliminated. Additionally, the flows being examined are 2 dimensional, and initially assumed to have constant material properties, so the equations can be rewritten as

$$\text{continuity: } \rho \left(\frac{\partial u}{\partial x} + \frac{\partial v}{\partial y} \right) = 0$$

$$\text{x} - \text{momentum: } \rho \left(u \frac{\partial u}{\partial x} + v \frac{\partial u}{\partial y} \right) = -\frac{\partial p}{\partial x} + \mu \left(2 \frac{\partial^2 u}{\partial x^2} + \frac{\partial^2 u}{\partial y^2} + \frac{\partial^2 v}{\partial xy} \right) + F_x$$

$$\text{y} - \text{momentum: } \rho \left(u \frac{\partial v}{\partial x} + v \frac{\partial v}{\partial y} \right) = -\frac{\partial p}{\partial y} + \mu \left(\frac{\partial^2 v}{\partial x^2} + 2 \frac{\partial^2 v}{\partial y^2} + \frac{\partial^2 u}{\partial xy} \right) + F_y.$$

In a real fluid, the viscous term is reduced further by use of the continuity equation. However, some manufactured solutions require a source term in the continuity equation, so retention of all viscous terms is prudent.

The manufactured equations will each contain a source term based on the manufactured solution, as indicated by the "ms" subscript, as

$$Q_{mass} = \nabla \cdot (\rho \overrightarrow{u_{ms}})$$

$$F_x = \rho \left(u_{ms} \frac{\partial u_{ms}}{\partial x} + v_{ms} \frac{\partial u_{ms}}{\partial y} \right) + \frac{\partial p_{ms}}{\partial x} - \mu \left(\frac{\partial^2 u_{ms}}{\partial x^2} + 2 \frac{\partial^2 u_{ms}}{\partial y^2} + \frac{\partial^2 v_{ms}}{\partial xy} \right)$$

$$F_y = \rho \left(u_{ms} \frac{\partial v_{ms}}{\partial x} + v_{ms} \frac{\partial v_{ms}}{\partial y} \right) + \frac{\partial p_{ms}}{\partial y} - \mu \left(\frac{\partial^2 v_{ms}}{\partial x^2} + 2 \frac{\partial^2 v_{ms}}{\partial y^2} + \frac{\partial^2 u_{ms}}{\partial xy} \right)$$

9.1.2.1.1 Eca

[91] designed a manufactured solution for verification of wall-bounded, incompressible, turbulent flows. To simulate the wall, they used a similarity variable, $= \frac{4y}{x}$, and the error function for the x-direction velocity. Their non-dimensionalized flow had a Reynolds number of 10^6, with flow and pressure manufactured solutions given by

$$u_{ms} = \text{erf}(\eta)$$

$$v_{ms} = \frac{1}{4\sqrt{\pi}} \left(1 - e^{-\eta^2} \right)$$
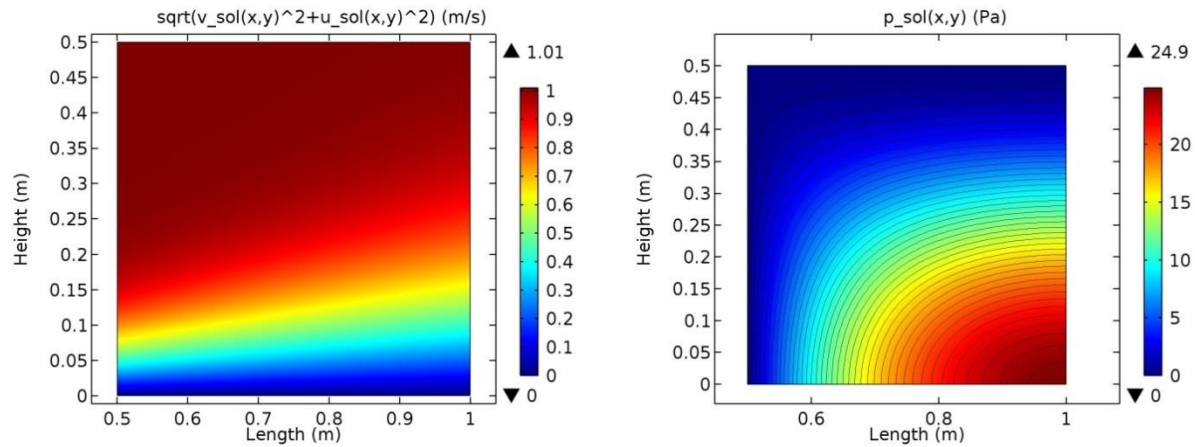
Figure 115 Velocity and pressure field from [91]'s manufactured solution

$$p_{ms} = \frac{\rho U_1^2}{2} \ln(2x - x^2 + 0.25) \ln(4y^3 - 3y^2 + 1.25)$$

where U_1 is the reference velocity and is set equal to 1. The velocity solutions were chosen to ensure the continuity equation did not require a source term, that is, it still equaled zero. These velocity and pressure fields are shown in Figure 115.

Because initial interest is in verifying the laminar flow, the Reynolds number was changed to 500, and these manufactured solutions were entered into COMSOL. The domain was constructed to match that used by [91], $0.5 \leq x \leq 1, 0 \leq y \leq 0.5$. The same grid refinement used in the heat transfer analysis was used here, a mapped 5x5 for the first and doubling the edge node density up to 320x320. P1+P1, P2+P1 and P3+P2 element orders were examined. The relative convergence tolerance was increased from 1e-3 to 1e-6, though this did not produce observable differences in results. Figure 116 shows the error in pressure for grids from 5x5 to 160x160. As the refinement increases, the details of the error are washed out by the presence of a relatively large error in the bottom right hand corner. In the 320x320 study, which is not pictured, that corner shows an error of 15.5 Pa, more than half of the true value.

These same results are reproduced using a constant color scale in Figure 117. The overall error appears to be improving, or remaining constant, while the error in the bottom right hand corner continues to grow as the grid is refined. Similar behavior is observed in the error in the velocity field as seen in Figure 118 and Figure 119.

By plotting the average error, defined here as the absolute value of the discrete solution minus the manufactured solution, against the edge grid refinement, it can be seen that the order of convergence is not constant. Where the average temperature error in the heat transfer module showed a grid convergence of order 3, the fluid velocity and pressure field do not show constant

152
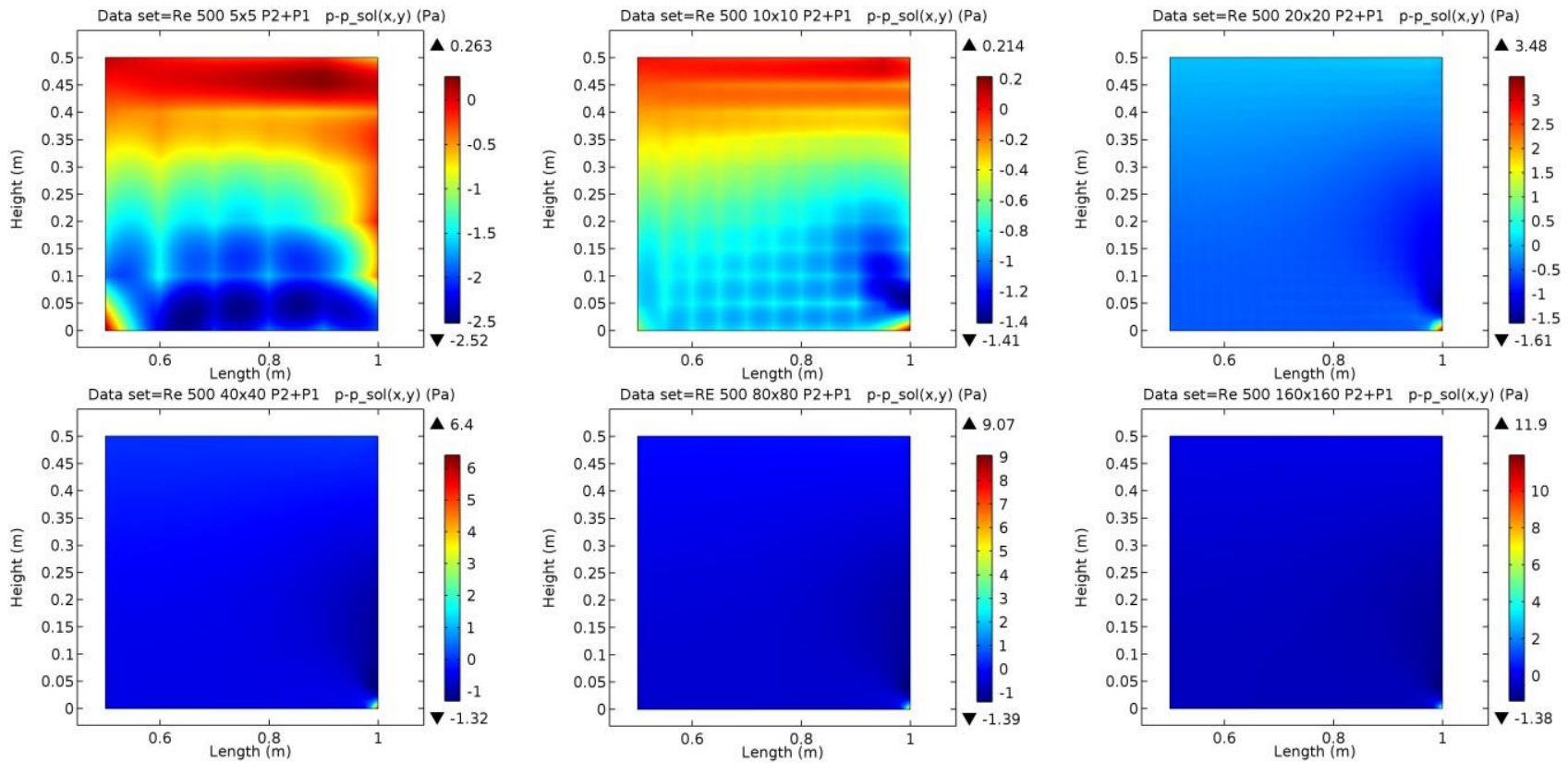
Figure 116 Error in pressure field for grids from 5x5 to 160x160
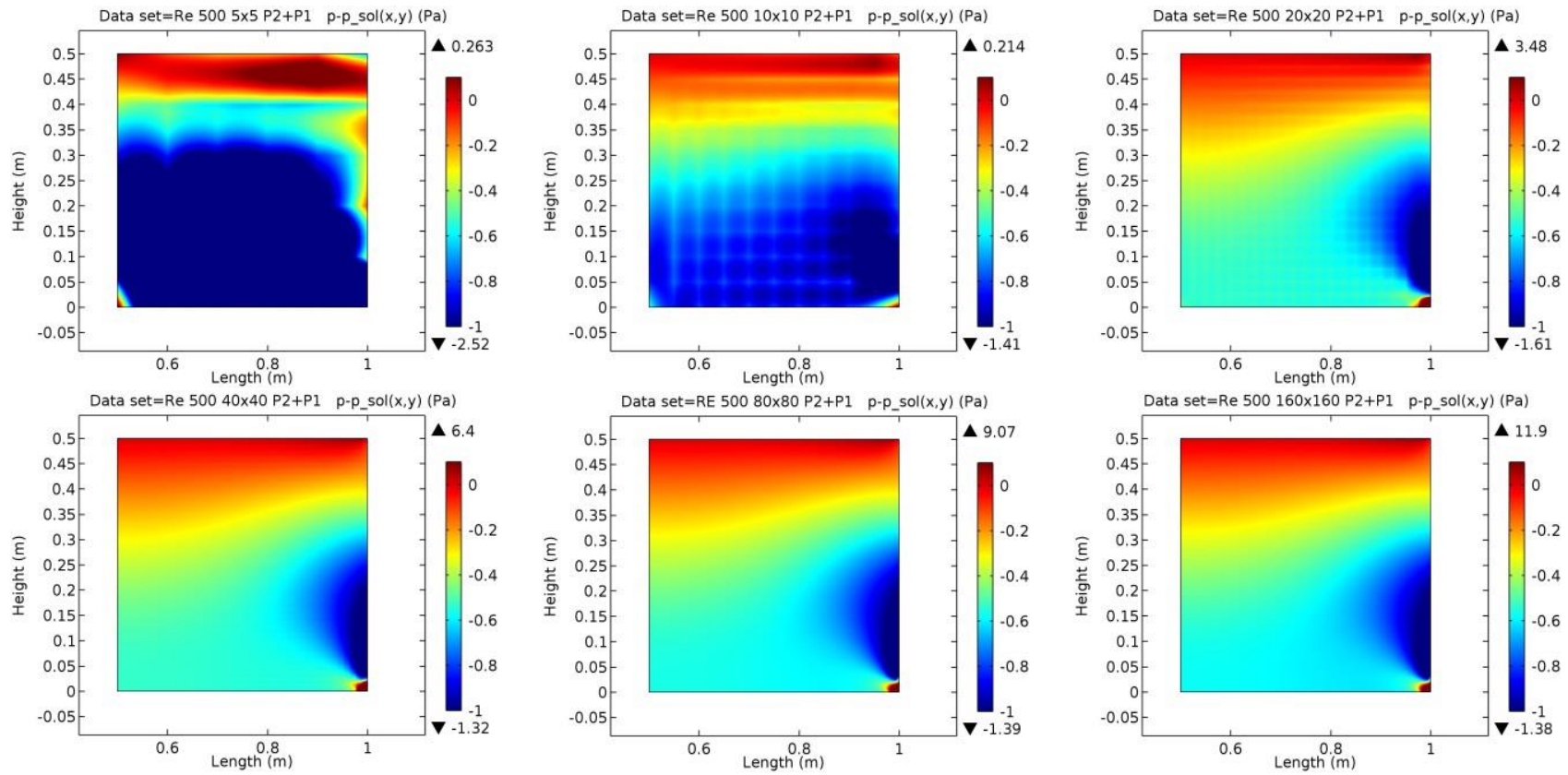
Figure 117 Error in pressure field with a constant color bar for grids 5x5 to 160x160
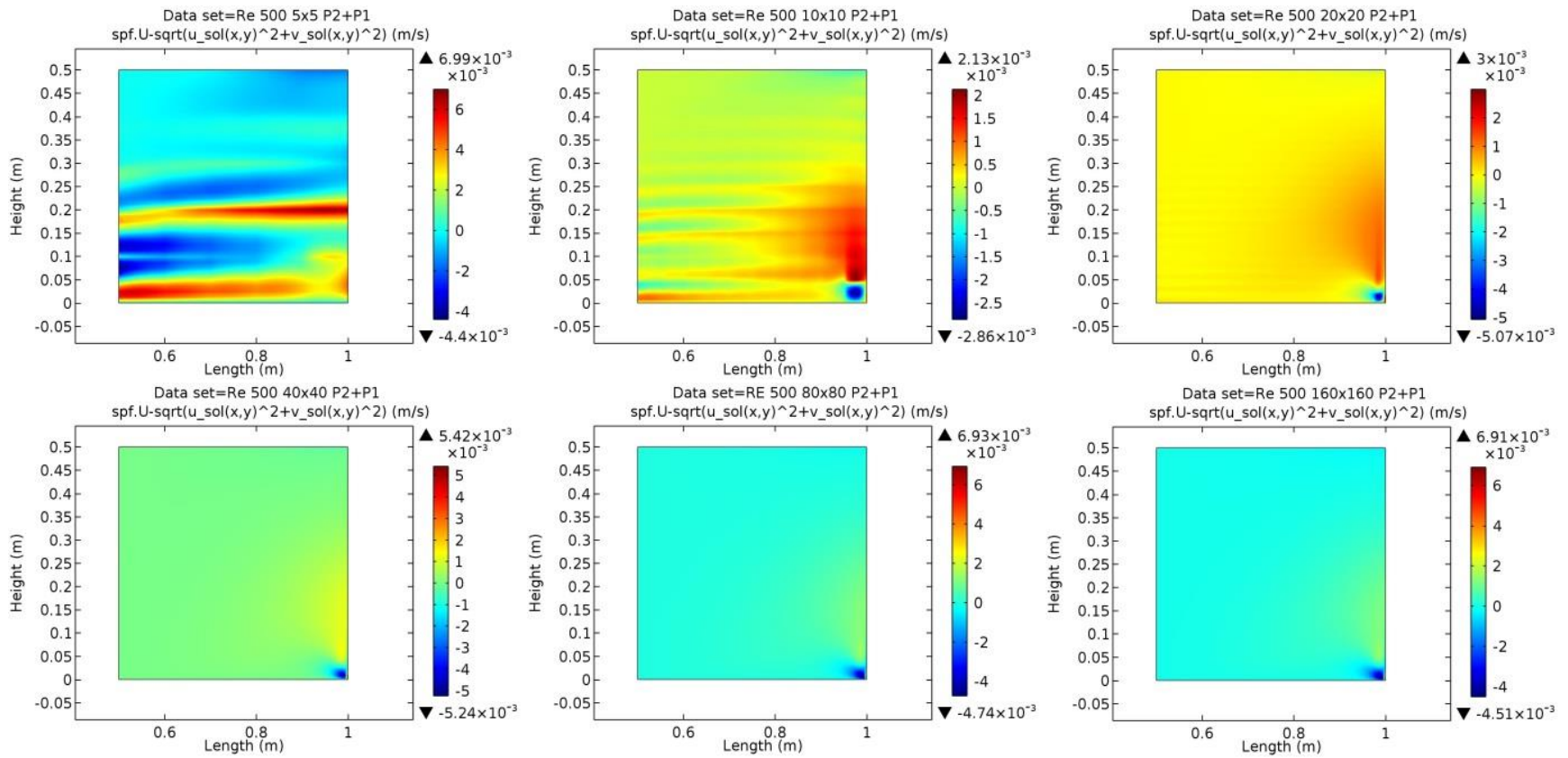
Figure 118 Error in velocity field for grids 5x5 to 160x160

155
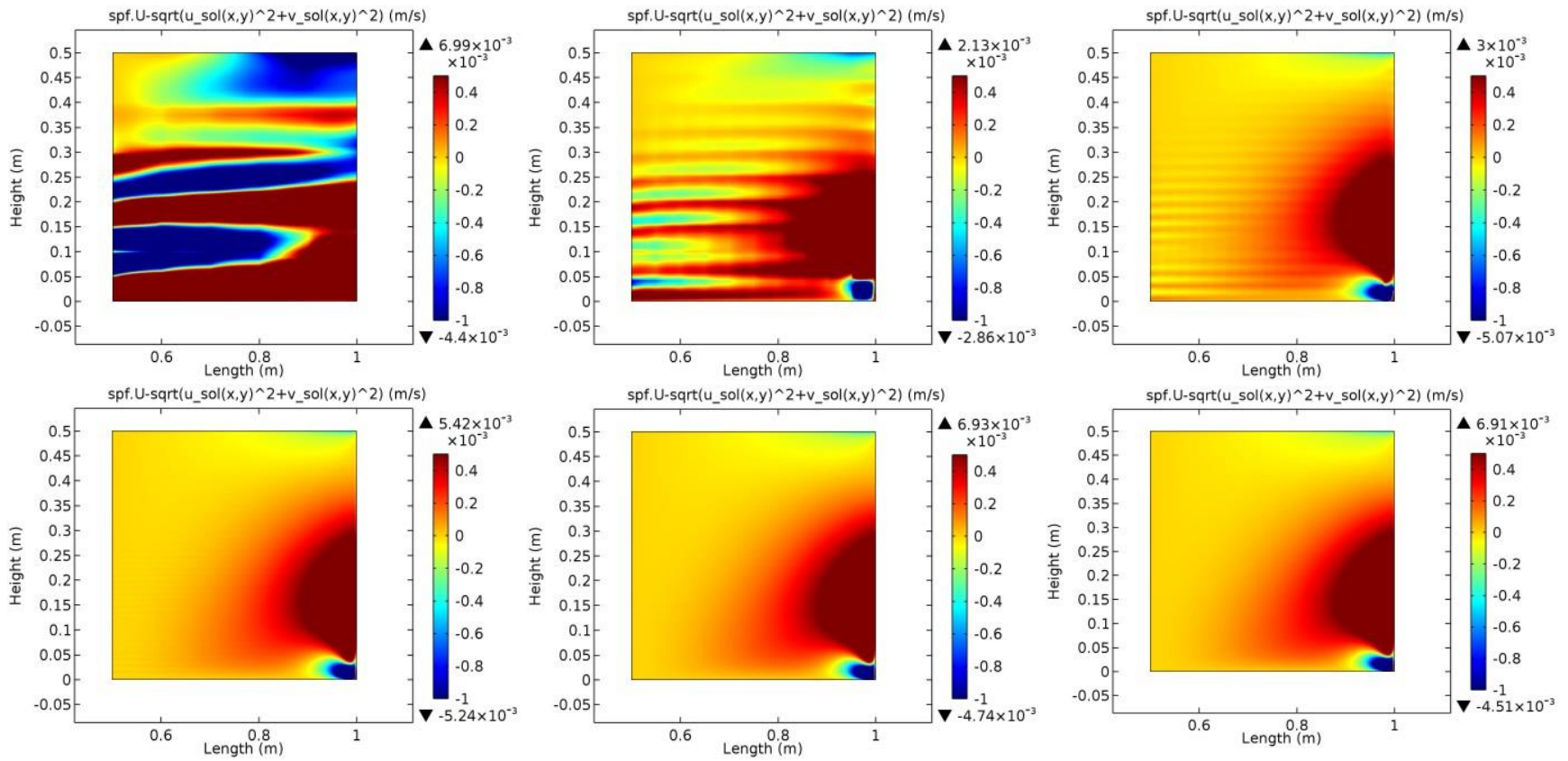
Figure 119 Error in velocity field using a constant color bar for grids 5x5 to 160x160
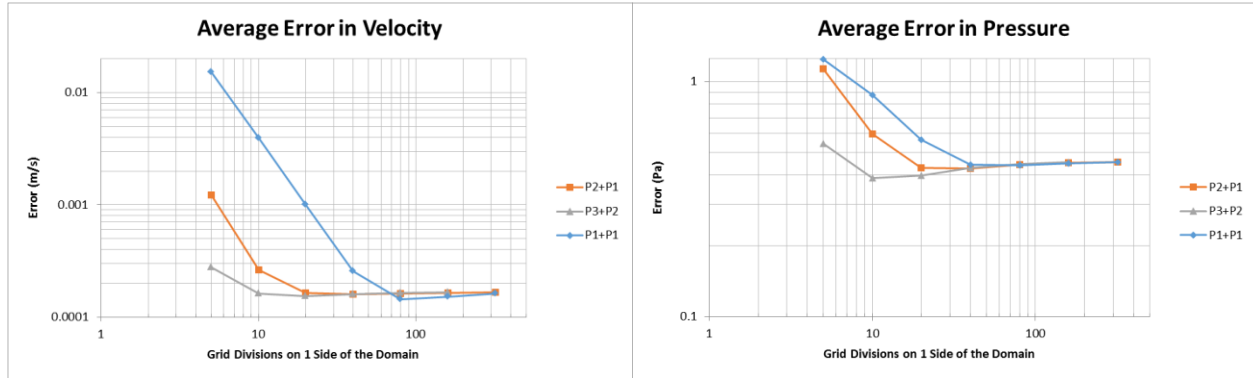
Figure 120 Average error in velocity and pressure against grid refinement

convergence across all grid refinements, Figure 120.

Richards 1

After working with the manufactured solution from [91], it was supposed that part of the earlier challenge with convergence of attempted manufactured solutions was how widely the manufactured pressure fields differed from those that could exist with a given velocity field (even if that velocity field itself was physically impossible). As such, to generate manufactured solutions that could converge, the following steps were taken. Solutions for the velocity components were chosen. The boundaries of the domain were assigned those velocities, and the simulation was run. While the simulation generally did not converge, the pressure field for the final iteration was examined, and a pressure solution that resembled that final shape was introduced as the manufactured solution for the pressure. This technique yielded the following solution,

$$u_{ms} = 2\cos(xy) + 2$$

$$v_{ms} = \sin(xy)$$

$$p_{ms} = \rho \cos\left(\frac{x\pi}{2}\right)^4 \cos\left(\frac{y\pi}{2}\right)^4,$$

which will be referred to as Richards 1. Reynolds number was set to 1,000, and the domain to $0 \leq x \leq 1, 0 \leq y \leq 1$. The velocity and pressure field generated by these solutions are shown in Figure 121. The velocity field in this solution does not satisfy the continuity equation, and thus requires the introduction of a source term within the code. COMSOL provides access to the equations that are solved within the Equation View of the models. By adding the source term, $Q_{mass} = \rho \left(\frac{\partial u_{ms}}{\partial x} + \frac{\partial v_{ms}}{\partial y}\right)$, to the continuity equation, the following results were generated. All results presented used the same grid refinement procedure identified previously. This simulation would not converge when all initial conditions were 0. However, when the initial conditions

157
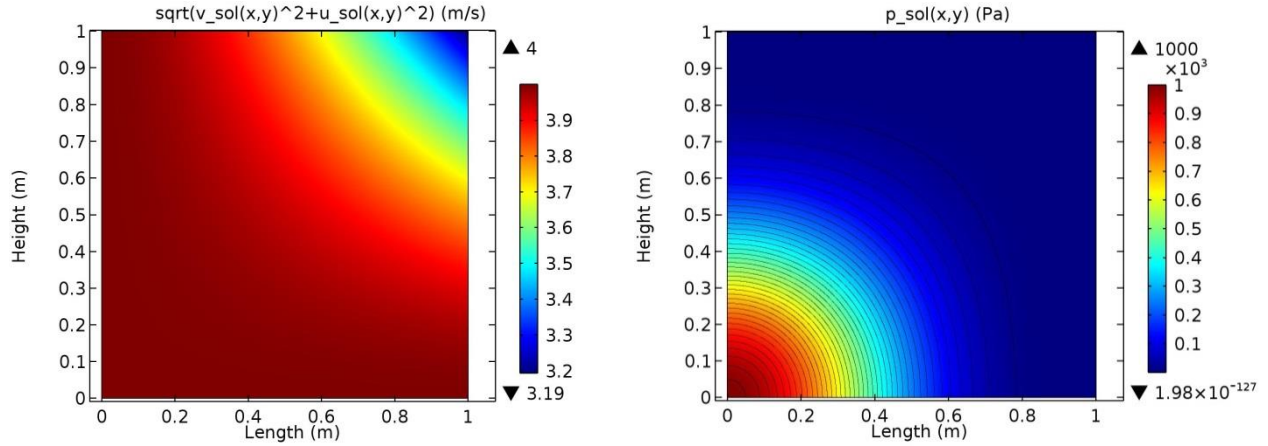
Figure 121 Velocity and pressure field from Richards 1 manufactured solution

were set to 1% of the manufactured solution, the solutions did converge. The left and bottom boundaries were set as inlets with the manufactured solutions as inlet velocities and the right and top as outlets with the manufactured solution as outlet pressure.

The pressure results did not visually change from one grid to the next, but the magnitude of the pressure error did. Figure 122 shows a plot of the average error from the 5x5 grid. The velocity error did change with grid refinement, Figure 123. Whereas with the manufactured solution from [91] the bottom right hand corner of the grids showed an increasing error with grid refinement beyond the 10x10 grid, Richards 1 shows an error along the top boundary towards the left that does not vary significantly (remains constant within 2.5%) from the 20x20 grid and beyond.

Figure 124 shows the average error in velocity and pressure against grid refinement. Three of the four curves show inconsistent orders of convergence, as was seen with the solution from [91]. The exception is that pressure with linear discretization shows a near-constant order of convergence of approximately 1 for all levels of refinement tested.

9.1.2.1.2   Richards 2
Continuing with the procedure described above, another manufactured solution, Richards 2, was generated

$$u_{ms} = 2\cos(xy) + \frac{1}{x^2 + 0.25} + 2.2$$

$$v_{ms} = \sin(xy)$$

$$p_{ms} = \rho\left(\cos\left(\frac{xy\pi}{2}\right)^4 - x\right)$$

158
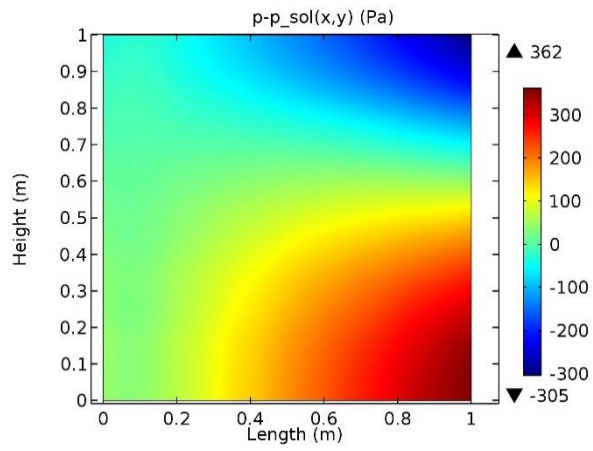
Figure 122 Typical average error in pressure, in this case from the 5x5 grid
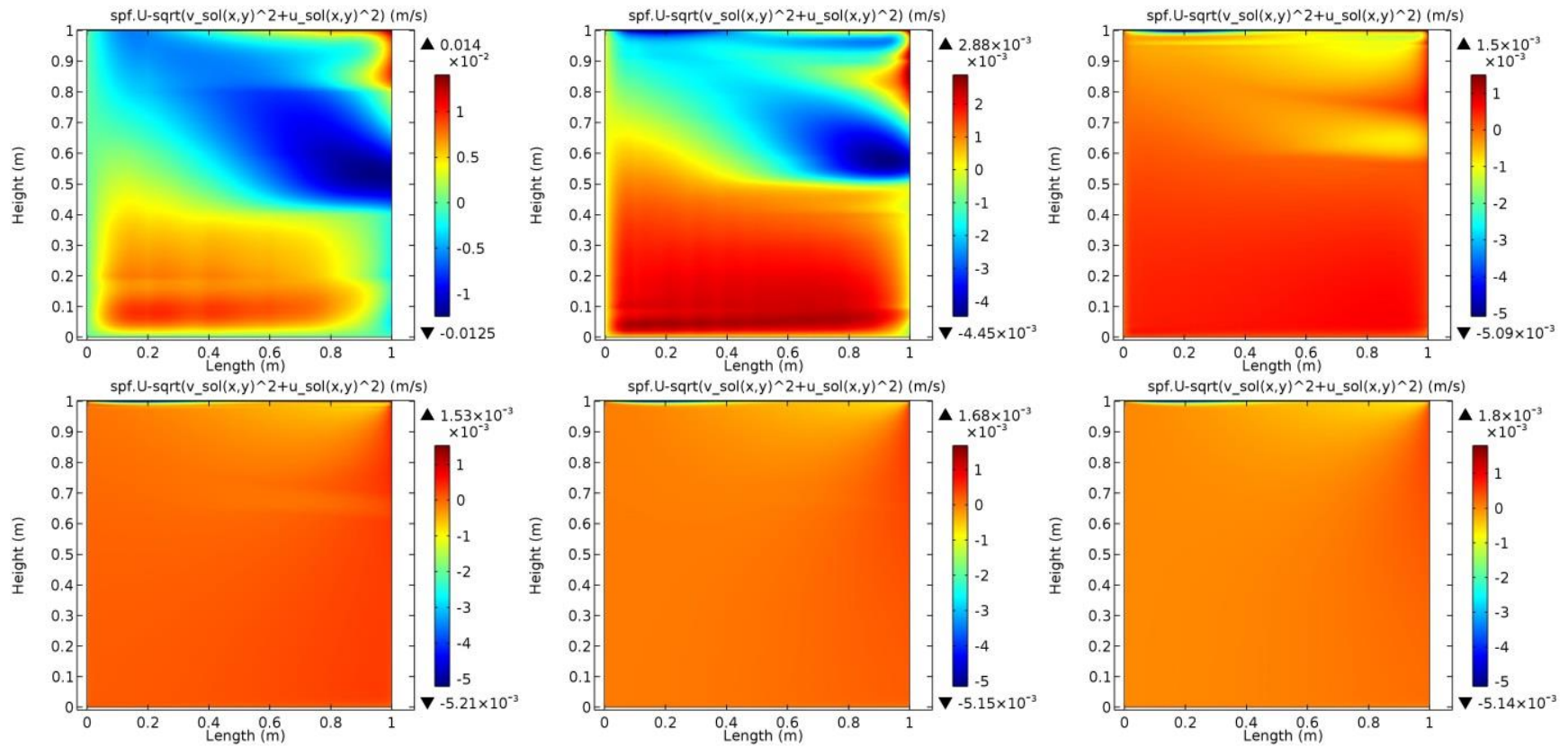
Figure 123 Average error in velocity from grids from 5x5 to 160x160
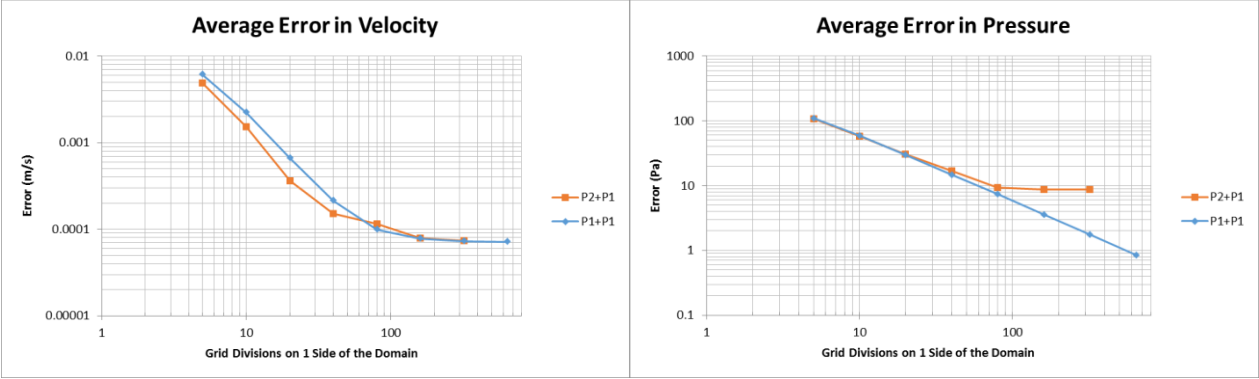
Figure 124 Average error in pressure and velocity against grid refinement
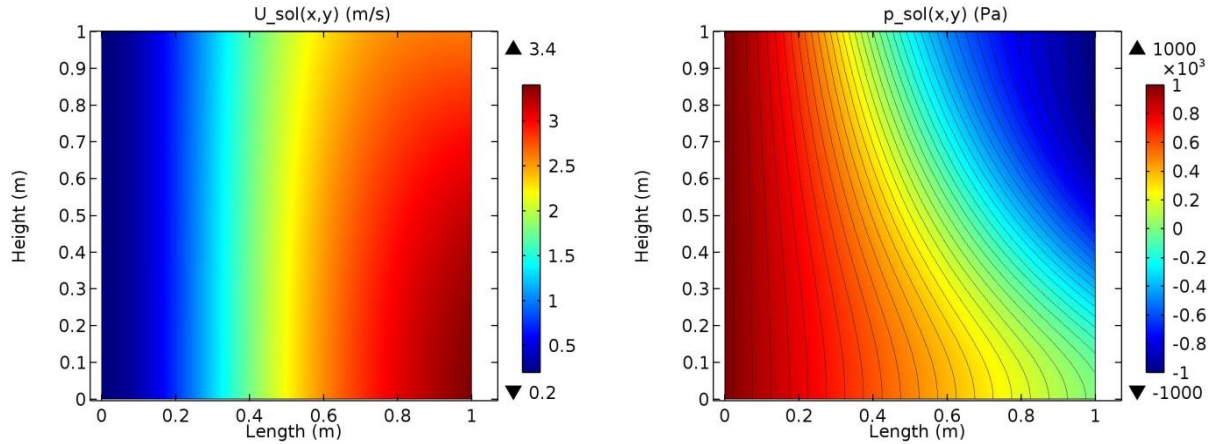
Figure 125 Manufactured solutions of velocity and pressure for Richards 2

This solution, Figure 125, would not converge with initial values of 0 or 1% of the manufactured, solution, but would with 10% of the manufactured solution as the initial values.

Images of the error in velocity show similar results to the previous two cases: initial wide distribution of error that is reduced with increasing grid refinement, with one region (the top, left side again) showing a slow increase in error magnitude. Similarly, the error in the pressure does not change visually, though the size of the error is reduced with grid refinement. Figure 126 shows the average error in velocity and pressure versus grid refinement level, indicating the same behavior as seen above: a portion where the code shows a relatively constant order of convergence at lower grid refinements in fluid velocity, but then levels off (or increases), while the error in pressure shows a more constant order of convergence across grid refinement.

9.1.2.1.3 Richards 3
A final manufactured solution, Richards 3, was generated that contained discontinuous first and second derivatives. The solutions were given by

$$u_{ms} = \sin(\pi\, y)\left(1 - \frac{1}{10^{|x-y|}}\right)$$

$$v_{ms} = \sin(\pi\, x)\left(1 - \frac{1}{10^{|x-y|}}\right)$$

$$p_{ms} = \rho\left(\frac{1}{2^{|x-y|}}\right).$$

These equations describe the flow and pressure shown in Figure 127. This manufactured solution produced results that differ significantly from the previous cases. Most notable is the lack of reduction in average error with increasing grid refinement, Figure 128. In this simulation, free
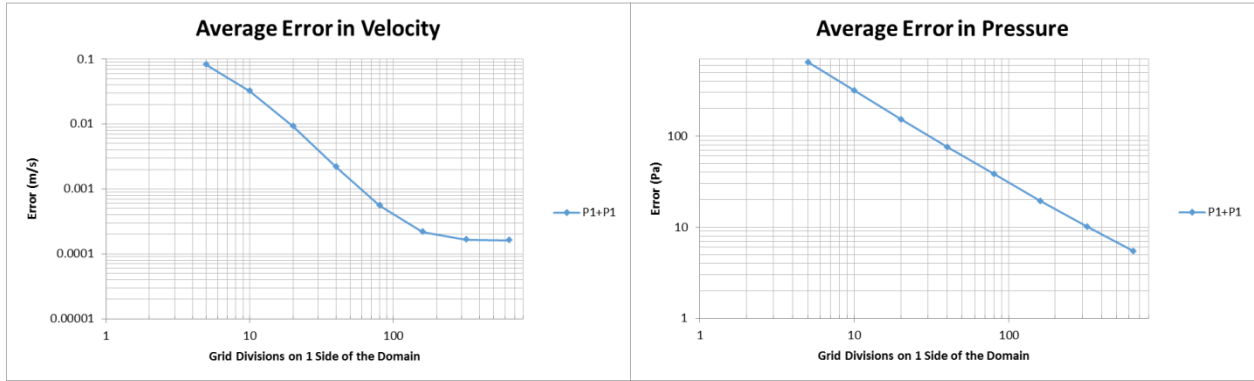
Figure 126 Average error in velocity and pressure for Richards 2 manufactured solution
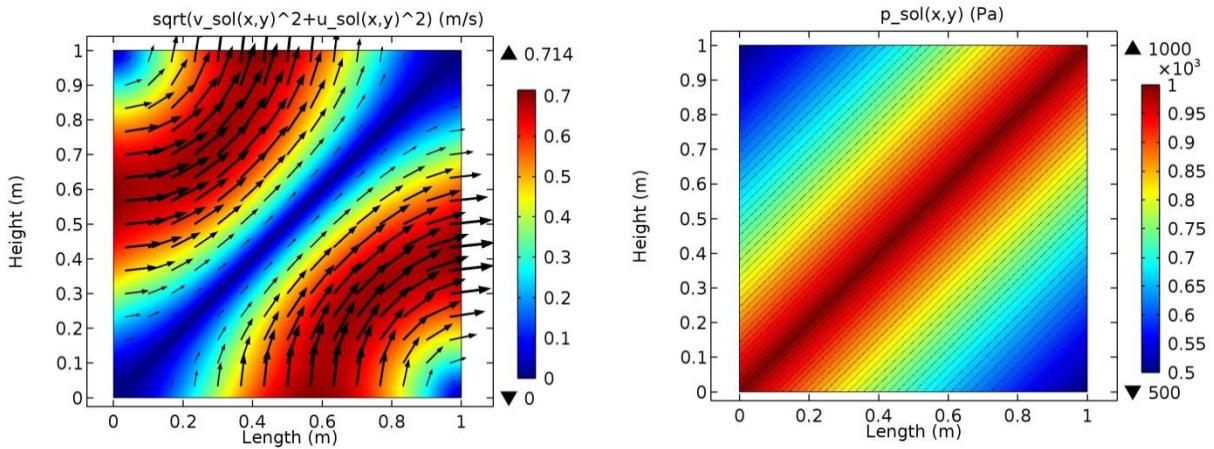
Figure 127 Velocity and pressure fields for Richards 3 manufactured solution

163
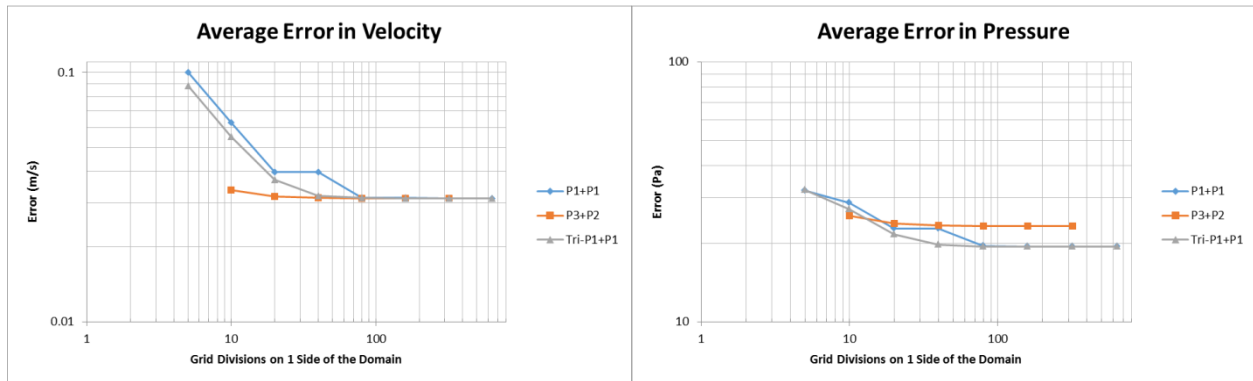
Figure 128 Average error in velocity and pressure for Richards 3 manufactured solution

triangles were also used to see if they improved the error reduction. The results indicate that they offer no advantage at higher resolutions, and only minor improvement at lower resolution.

9.1.2.1.4 Isothermal, Laminar Orders of Convergence

The preceding results can be summarized by the orders of convergence for each of the cases examined at each of the grid refinements, Figure 129. Because the solution is known, the order of convergence, p, can be calculated as

$$f_{exact} = f_1 + \frac{f_1 - f_2}{r^p - 1},$$

where the subscripts indicate the level of refinement (1 indicating the more refined solution), r is the refinement ratio, and f is the solution.

9.1.2.1.5 Efforts to Improve Grid Convergence

In an ideal code, the order of convergence would be a constant at the theoretical order of convergence for the solution method used. A number of steps were taken to determine if certain options within COMSOL would result in orders of convergence that remained closer to a constant value across various grid sizes.

A first observation was that the errors in each of the simulations were largest along the boundaries. Four different evaluations were made to see if the boundary error causes the decline in order of convergence with grid refinement. The error along the boundary was removed from the error of the whole simulation; the errors at single points—an arbitrary location (in the lower left quadrant of the domain) and at the center of the domain—were examined; and the maximum error in the simulation was also examined. These results are plotted in Figure 130 along with the original P1+P1 results for comparison.

164
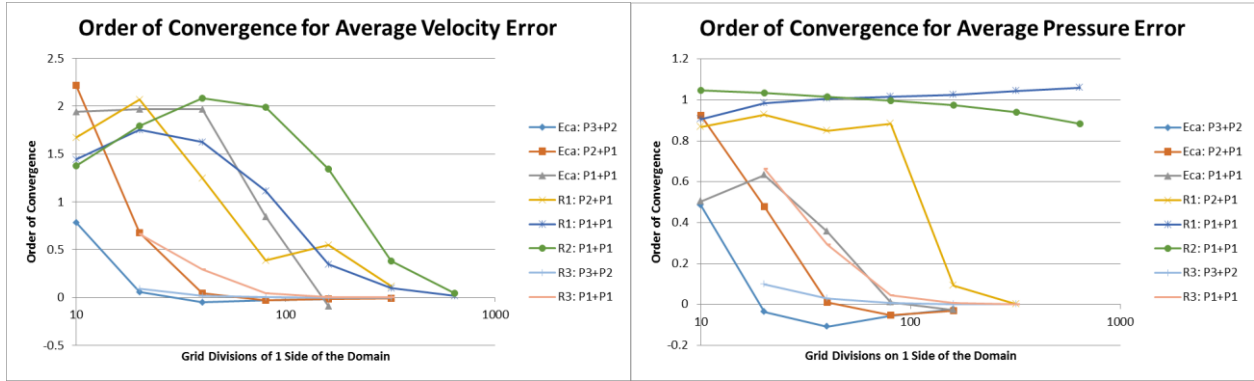
Figure 129 Orders of convergence for the average velocity and pressure errors for various cases against grid refinement
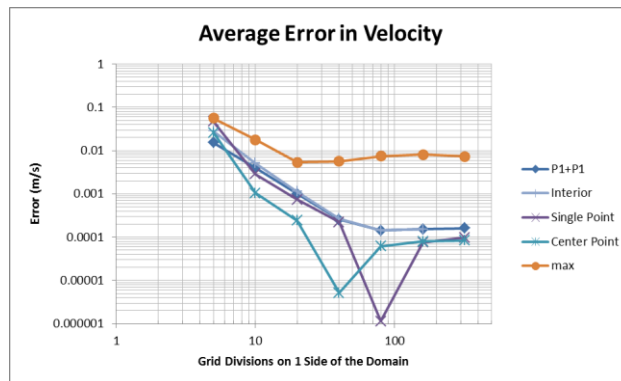
Figure 130 Average error in velocity for P1+P1 along with the interior error, errors at 2 single points, and the maximum error

165

A second potential source of error examined was the artificial dissipation, known as stabilization in COMSOL. The Navier-Stokes equations are non-linear and inherently unstable. To provide stability COMSOL and other codes introduce artificial dissipation. COMSOL offers 3 types of artificial dissipations—crosswind and streamline, which are referred to as consistent stabilization and isotropic diffusion, which is known as inconsistent stabilization. The two consistent options provide artificial dissipation that decreases as the solution approaches the convergence criteria. When working properly, this allows for the effect of the artificial dissipation to be minimal, ideally non-existent, on the final solution. Isotropic dissipation is constant throughout the solution and does change the final solution.

Several simulations were run with various combinations of discretization and artificial dissipation. The P1+P1 discretization was unstable in the absence of artificial dissipation, with only isotropic diffusion (for a 160x160 grid, and an artificial diffusion coefficient of 0.25 and 0.5), and with only crosswind diffusion. With only streamline diffusion, the simulation was stable. Results are plotted in Figure 131 beside the P1+P1 results from the default (both crosswind and streamline) simulation results. In addition, the P2+P1 simulation was stable without any artificial stabilization. It is also plotted in Figure 131 beside the default P2+P1 simulation results.

The simulations were run using the 4 different solvers COMSOL offers. The results were identical to the first 7+ digits. The velocities, pressure, and density were increased by a factor of 1,000 to offset the effect of any unseen constant in the solution process. The results were again identical, when divided by 1,000.

Finally, as explained above, in each of the simulations, the manufactured source terms are calculated using COMSOL's symbolic differentiation. These terms were replaced with the analytical terms generated by [91]. The results were identical. These efforts indicate that none of the attempted changes were the source of the non-constant orders of convergence.

9.1.2.2 *Non-Isothermal, Laminar Flow*
The next step in the verification process was to introduce temperature variation into the flow. Within COMSOL this is accomplished by using both the Laminar Flow and Heat Transfer in Fluids physics nodes. The flow equations are the same as were used in the previous section. The heat transfer equation is also the same as used earlier, reproduced below, however, the translational term that was neglected earlier becomes important now.

$$\rho C_p \left(\frac{\partial T}{\partial t} + \vec{u}_{trans} \cdot \nabla T \right) + \nabla \cdot (\vec{q} + \vec{q}_r) = -\alpha T : \frac{DS}{Dt} + Q.$$

The heat transfer source term for the manufactured solution now is written as

166
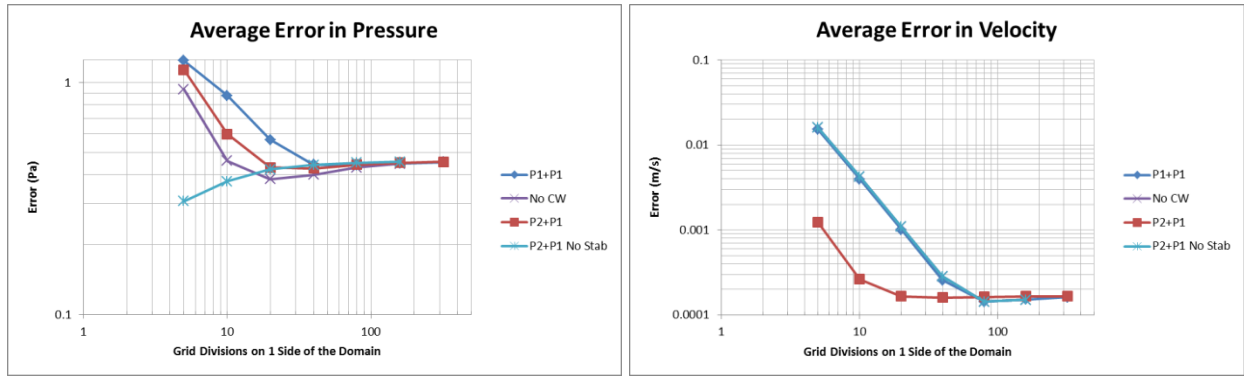
Figure 131 Average Error in Pressure (left) and Velocity (right) for the default P1+P1 and P2+P1 plotted beside P1+P1 without crosswind stabilization (No CW) and P2+P1 without any stabilization

$$Q = -k \left(\frac{\partial^2 T_{ms}}{\partial x^2} + \frac{\partial^2 T_{ms}}{\partial x^2} \right) + \rho C_p \left(u_{ms} \frac{\partial T_{ms}}{\partial x} + v_{ms} \frac{\partial T_{ms}}{\partial y} \right).$$

Constant values for ρ, C_p, and k were used. The constant density removed the transfer of information from the Heat Transfer in Fluids node to the Laminar Flow node. Flow information, however, still transferred to Heat Transfer in Fluids from Laminar Flow.

9.1.2.2.1 Richards 1

Richards 1 velocity and pressure solutions were used with an added temperature solution,

$$T_{ms} = 300 + 5 \cos(\pi x) + 5 \sin(\pi y).$$

This temperature solution can be seen in Figure 132.

The average error in velocity and pressure for the different refinement levels are shown in Figure 133. The errors obtained with the same manufactured solution in section 0— without the heat transfer—are also included for comparison sake. The results are similar, but are not identical. In both cases, P1+P1 results are displayed.

Linear elements were used for the heat transfer in liquids physics node. The error in average temperature is shown in Figure 134. An order of convergence of between 1.7 and 1.9 is seen for all grids except for the 640x640. These results can be compared to a nearly constant value of 3 obtained with quadratic elements and no coupling when verifying heat transfer in solids.

9.1.2.3 Isothermal, Turbulent Flow

Where the evaluation of non-isothermal flow resulted in 4 coupled equations (mass, two momentum, and energy), isothermal turbulence presents 4 or 5 coupled equations. The first

167
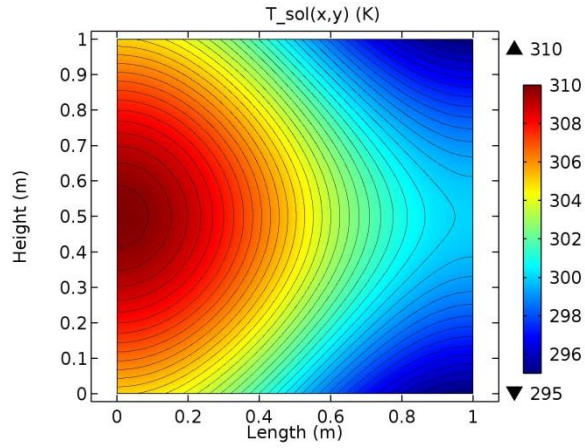
Figure 132 Temperature field for Richards 1 manufactured solution
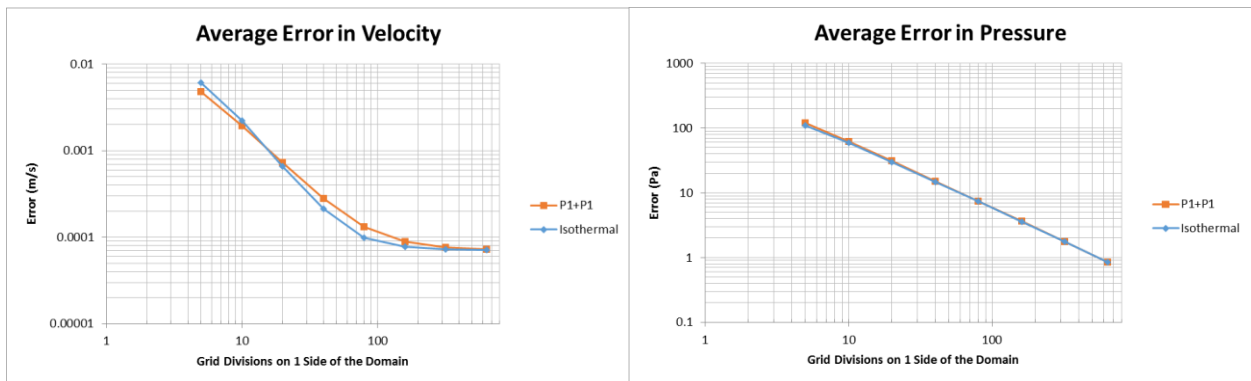
Figure 133 Average error in velocity and pressure for Richards 1 manufactured solution with non-isothermal flow and isothermal flow

168
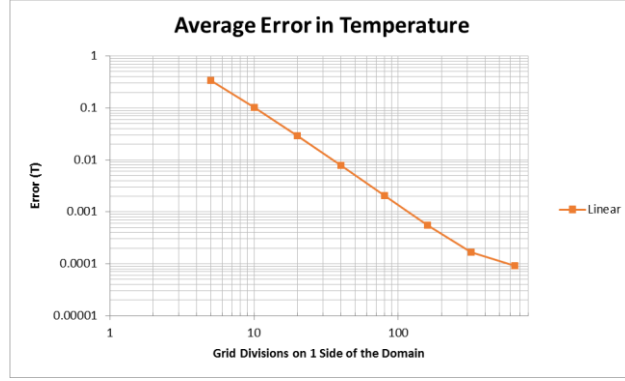
Figure 134 Average error in temperature for Richards 1 manufactured solution

three equations are similar to those used in the isothermal laminar flow, except that Reynolds averaging has been applied. When the equations are simplified, they are given as

$$\text{continuity: } \rho \left(\frac{\partial u}{\partial x} + \frac{\partial v}{\partial y} \right) = 0$$

$$\text{x} - \text{momentum: } \rho \left(u \frac{\partial u}{\partial x} + v \frac{\partial u}{\partial y} \right) = -\frac{\partial p}{\partial x} + (\mu + \mu_T) \left(2 \frac{\partial^2 u}{\partial x^2} + \frac{\partial^2 u}{\partial y^2} + \frac{\partial^2 v}{\partial xy} \right) + F_x$$

$$\text{y} - \text{momentum: } \rho \left(u \frac{\partial v}{\partial x} + v \frac{\partial v}{\partial y} \right) = -\frac{\partial p}{\partial y} + (\mu + \mu_T) \left(\frac{\partial^2 v}{\partial x^2} + 2 \frac{\partial^2 v}{\partial y^2} + \frac{\partial^2 u}{\partial xy} \right) + F_y.$$

Again, using these equations as operators on the manufactured solutions, subscripted "ms", the following source terms are identified

$$Q_{mass} = \rho \left(\frac{\partial u_{ms}}{\partial x} + \frac{\partial v_{ms}}{\partial y} \right)$$

$$F_x = \rho \left(u_{ms} \frac{\partial u_{ms}}{\partial x} + v_{ms} \frac{\partial u_{ms}}{\partial y} \right) + \frac{\partial p_{ms}}{\partial x} + (\mu + \mu_T) \left(\frac{\partial^2 u_{ms}}{\partial x^2} + 2 \frac{\partial^2 u_{ms}}{\partial y^2} + \frac{\partial^2 v_{ms}}{\partial xy} \right)$$

$$F_y = \rho \left(u_{ms} \frac{\partial v_{ms}}{\partial x} + v_{ms} \frac{\partial v_{ms}}{\partial y} \right) + \frac{\partial p_{ms}}{\partial y} + (\mu + \mu_T) \left(\frac{\partial^2 v_{ms}}{\partial x^2} + 2 \frac{\partial^2 v_{ms}}{\partial y^2} + \frac{\partial^2 u_{ms}}{\partial xy} \right).$$

In the previous equations, μ_T is the turbulence viscosity. Each turbulence model determines this value differently and thus, needs to be verified separately. Only the yPlus model will be examined here.

9.1.2.3.1 yPlus

The yPlus turbulence model calculates μ_T from a non-dimensionalized wall distance, y^+. A local Reynolds number,

$$\text{Re} = \frac{\rho U d_w}{\mu},$$

where d_w is the distance to the nearest wall. d_w is determined by a solution node, Wall Distance Initialization, which solves

$$\nabla G \cdot \nabla G + \sigma_w G(\nabla \cdot \nabla G) = (1 + 2\sigma_w)G^4$$

for G, a reciprocal wall distance. The local Reynolds number is then used to solve the following equations for y^+,

$$\text{Re} = y^+ u^+$$

with

$$u^+ = \begin{cases} y^+, & y^+ \leq y^* \\ y^* + \dfrac{1 - \chi_y}{2\kappa^2(y^+ - y^*)} + \dfrac{1}{\kappa}\log\left(\chi_y + 2\kappa(y^+ - y^*)\right), & y^+ > y^*, \end{cases}$$

where $y^* = B - \frac{1}{\kappa}(\log(4\kappa) - 1)$ and $\chi_y = \sqrt{1 + 4\kappa^2(y^+ - y^*)^2}$. B and k are model parameters. y^+ is then used to calculate the nondimensionalized effective viscosity, $v+$, by

$$v^+ = \begin{cases} 1, & y^+ \leq y^* \\ \dfrac{1 + \chi_y}{2}, & y^+ > y^*. \end{cases}$$

The turbulent viscosity is then determined by

$$\mu_T = v^+\mu - \mu.$$

Within COMSOL, the procedure differs slightly from that presented in the reference manual and here. The differences include conditional statements that prevent certain values from being less than 0 and division by 0, and that force a minimum of 0.001 for u^+ when calculating y^+.

Because μ_T is determined with algebraic equations instead of differential equations, the method of manufactured solutions cannot be used to force a solution. Instead, the procedure for verification uses MMS for the flow equations, and checks the simulation solution values of y^+ against values calculated outside of the solution, but still within COMSOL. The simulation solutions value of μ_T was used in the momentum forcing functions. Finally, because the yPlus

Figure 135 Average error in velocity, pressure and yPlus for Eca yPlus turbulent case plotted against grid refinement

model depends on wall distance, the manufactured solution from [91] was used (since Richards 1, 2 and 3 do not have walls).

Figure 135 shows the average error in velocity, pressure and yPlus for a Reynolds number of 5×10^5. The solution would not converge for grids higher than 80x80. These results, combined with those in laminar flow suggest that the other turbulence models are unlikely to demonstrate more constant orders of convergence. No code verification using the other turbulence models is performed here. However, solution verification for the other turbulence models is performed in section 9.2.

9.1.3   Coupling
The next step in verification is examining the coupling of different domains and physics.

9.1.3.1   *Coupling Heat Transfer across Domains*
Earlier in heat transfer, both by itself and in non-isothermal flow, the thermal conductivity was assumed constant which allowed it to be removed from under the partial derivative in the heat equation. When considering heat transfer across two different materials, this conductivity must remain in the derivative. The source term for the heat equation, then is given as

171
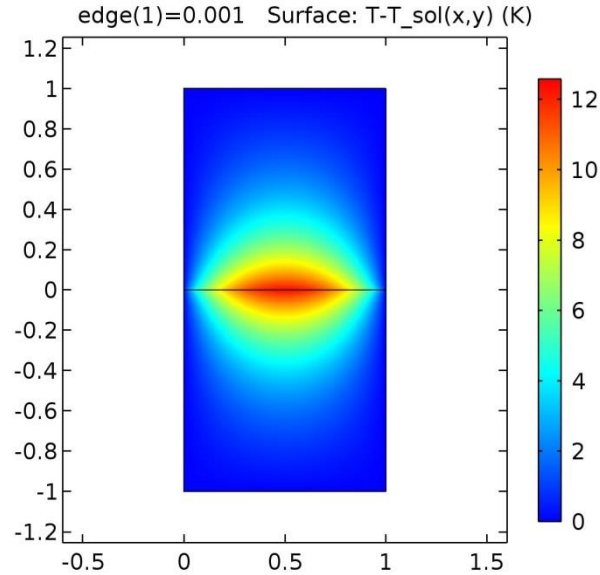
Figure 136 Energy error (simulation results minus manufactured solution) at interface between solids resulting from differentiation of a discontinuity

$$Q = \frac{\partial}{\partial x}\left(-k\frac{\partial T}{\partial x}\right) + \frac{\partial}{\partial y}\left(-k\frac{\partial T}{\partial y}\right).$$

To account for the change in thermal conductivity within the manufactured solution, a piecewise function was created within COMSOL.

$$k_{ms} = \begin{cases} k_1, & \in \text{Domain 1} \\ k_2, & \in \text{Domain 2} \end{cases}$$

This function is differentiated as part of the source term for the heat equation. COMSOL's symbolic differentiation appears to do one-sided differentiation on either side of a discontinuity. This one sided approach produces a function that does not include the Dirac delta that results from the derivative of a step function. This lack in the source term of the manufactured solution produces temperature errors at the interface between the two domains, as seen in Figure 136.

To partially correct for this error, a transition in thermal conductivity between the two domains is included in the thermal conductivity function. This transition is smooth to the second derivative and has a length that can be adjusted. To examine the effect of introducing this transition on the error, a model was created with a block of aluminum, $k = 238\frac{W}{m\,K}$ connected to a block of iron, $k = 76.2\frac{W}{m\,K}$. The manufactured solution from the heat transfer code verification was reused. The length of the transition was varied, along with the grid size. The thermal conductivity of the iron was also varied. The maximum error from these results is plotted in Figure 137.
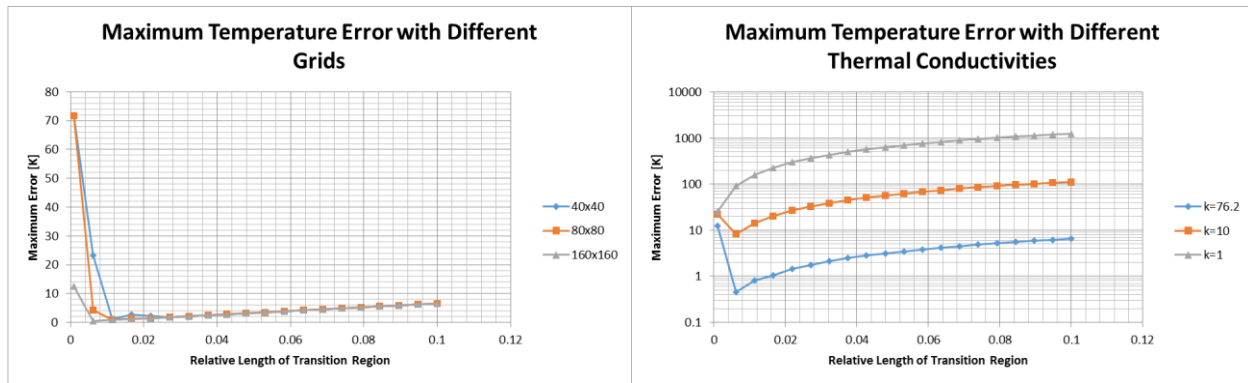
Figure 137 Maximum temperature error with different grids (left) and with different thermal conductivities for grid 160x160 (right)

As a reminder these errors are associated with a manufactured solution which has an average temperature of 300 K and a temperature variation of ±60 K. A few conclusions can be drawn. First, the smaller the transition, the smaller the error, up to a point. Beyond that point the error rapidly rises as the impulse in the derivative is lost. Second, the size of the error is not significantly affected by the grid size, except at the smaller end of the transition, where tighter grids allow for smaller errors. Finally, the greater the difference across the discontinuity, the larger the error that results.

Figure 138 shows the temperature error as the grid is refined at a number of different transition lengths. It can be seen that the challenge with differentiating the discontinuity controls the size of the error. There appears to be a range of transition lengths and grid size combinations where the order of convergence appears close to constant. Outside of these combinations, grid refinement does not appear to affect the error.

With these conclusions in hand, a similar analysis was performed on a block of still water coupled to a block of aluminum. A greater range of grids and transition lengths was examined. The manufactured solution is the same as used in the non-isothermal, laminar flow, which experiences temperature variations of ± 10 K. The maximum errors produced from this simulation are shown in Figure 139. Similar conclusions are drawn here, noting that refining the grid further, and carefully reducing the transition length decreases the error.

9.1.3.2 *Coupling Heat Transfer across Domains with Laminar Flow*
Finally, the heat transfer and fluid flow physics, along with the different domains are all coupled together. Using the same manufactured solution for fluid velocity from [91], and the same manufactured solution for temperature from the non-isothermal flow extended through the entire length of the model (block of water adjacent to a block of aluminum), the simulation was run with heat transfer in solids and non-isothermal flow in the fluid. The same grid refinement scheme was used as well as transition lengths.

173
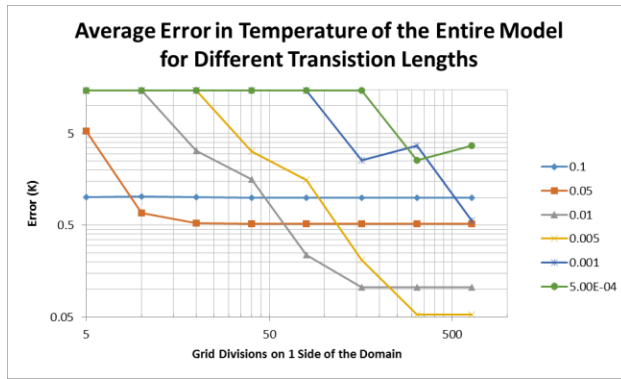
Figure 138 Average error in temperature of the entire model for 2 solids coupled together
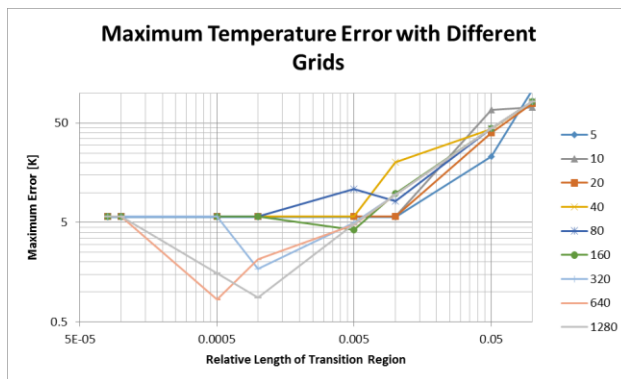
Figure 139 Maximum temperature error with a liquid and a solid domain coupled for various grids

174
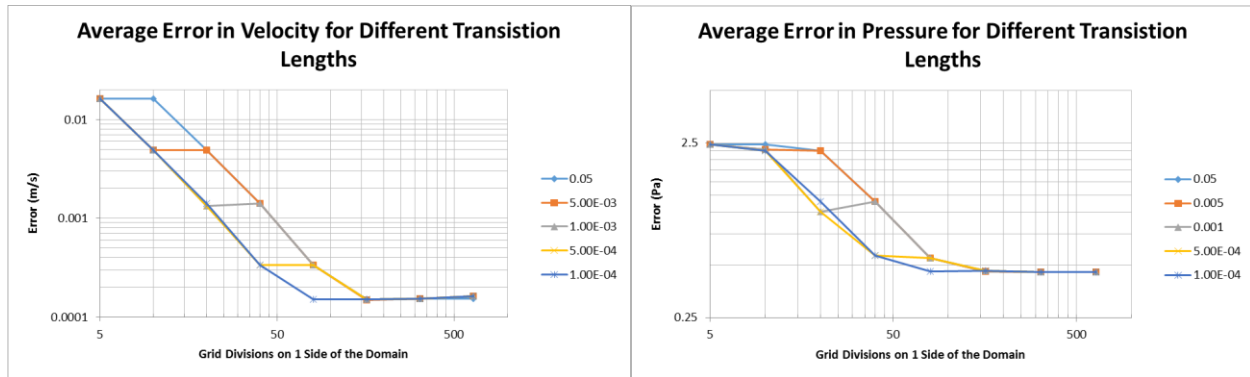
Figure 140 Average error in velocity and pressure for different transition lengths against grid divisions for the coupled heat transfer and laminar flow model

Figure 140 shows the average error in velocity and pressure for these simulations. Comparing these with Figure 120, which is the same flow field but isothermal, it can be seen that the combined transition lengths yield a velocity error that is essentially the same. The pressure error is larger in this coupled model compared to the isothermal flow model for all grids up to 80x80 at which point it coincides with those in the isothermal flow.

Figure 141 shows the average error in temperature for the fluid, solid, and entire model. Here the effects of coupling are much more apparent than in velocity and pressure. Where the verification of heat transfer in solids by itself shows a linear drop (on a log-log plot) of temperature error with decrease in grid size, Figure 113, in this coupled simulation the temperature error only decreases up to the 40x40 grid.

The orders of convergence for each of these simulations is shown in Figure 142. Again, in an ideal code, these lines would each be constant at the theoretical order of convergence for the solution method being used.

9.1.4 Code Verification Conclusion

The process of code verification was performed on the relevant portions of COMSOL's heat transfer and CFD modules. The method of manufactured solutions was applied in a series of increasingly complex simulations. Dirichlet boundary conditions were used in each of the simulations.

Heat transfer in solids was verified, producing a nearly constant order of convergence against a wide range of grid refinements.

The isothermal, laminar flow was subject to 4 different manufactured solutions. In each case, the order of convergence for average error in velocity dropped to essentially 0 with increasing grid refinement, while the average error in pressure did the same in all but 2 cases. In those cases, the

175
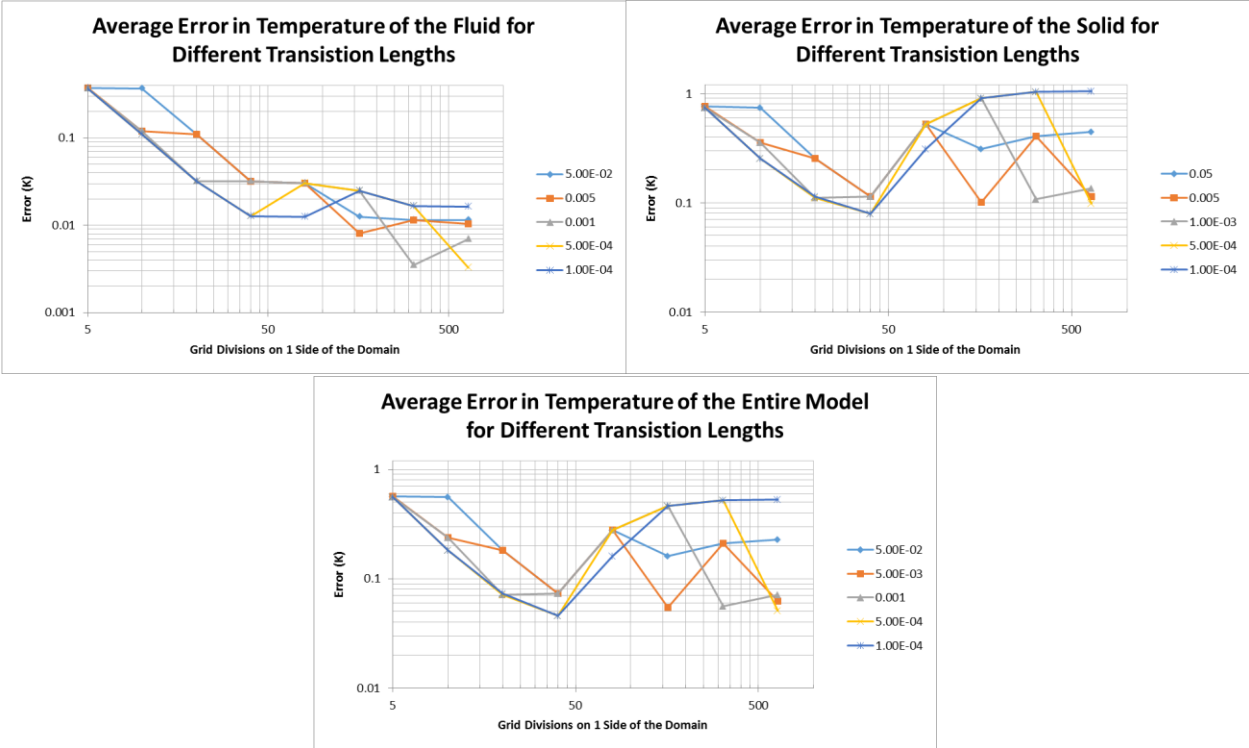
Figure 141 Average error in temperature for the fluid, solid, and total model for the coupled simulation
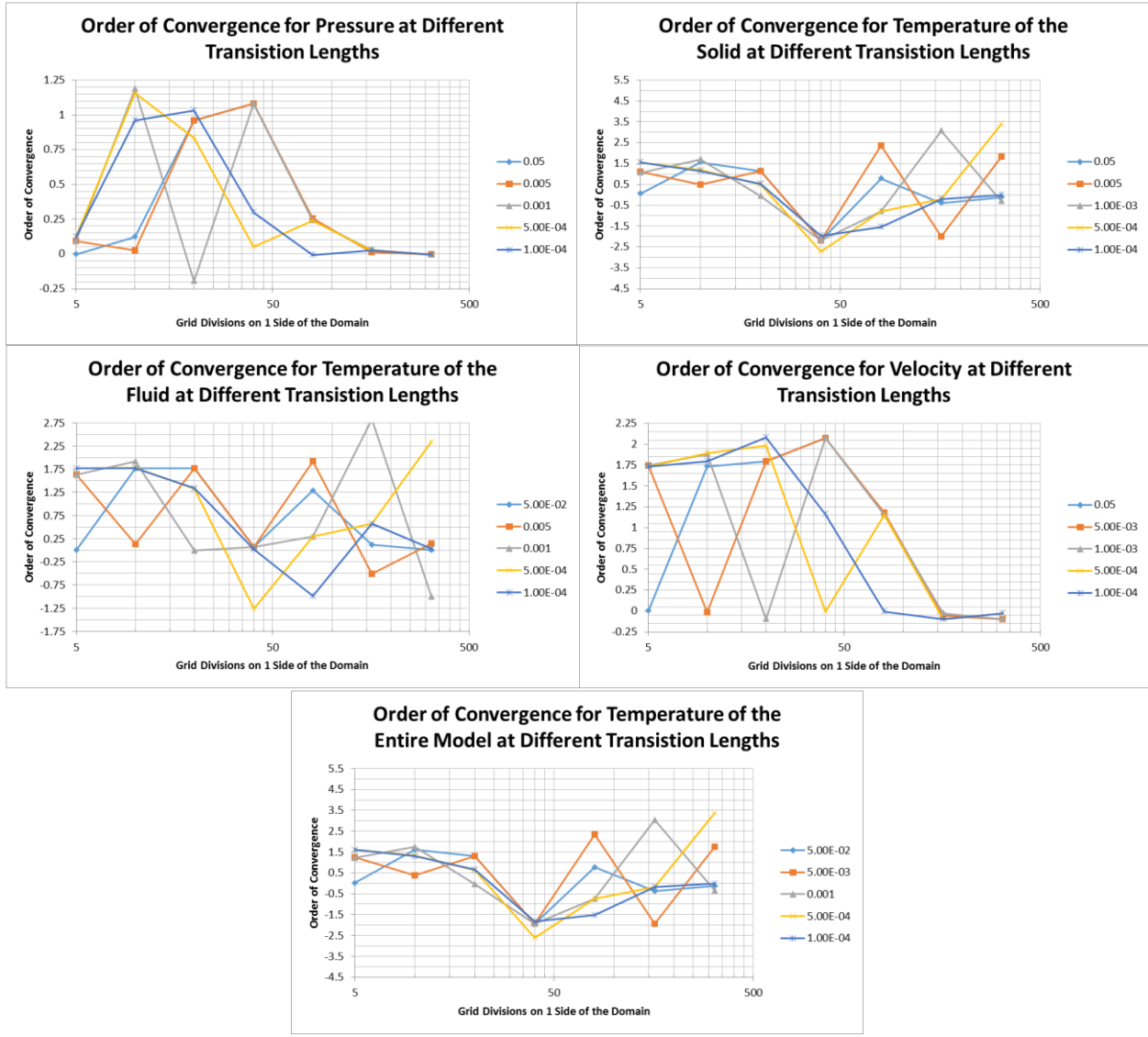
Figure 142 Orders of convergence for velocity, pressure, and temperature in the coupled model

177

order of convergence was nearly constant across the range of grids tested. A number of efforts were made to improve these results, including examining only the interior node values, removing the default artificial dissipation, using different solvers, excluding constants, and using analytical source terms. None of these efforts resulted in appreciable differences in the solutions.

Non-Isothermal laminar flow was subject to a single manufactured solution. The results were similar to the isothermal laminar flow with respect to flow properties. The temperature results were similar to those for heat transfer. The isothermal, turbulent flow, yPlus RANS model was subject to a single manufactured solution. It did not converge beyond an 80x80 grid, and the results in velocity error and pressure error show more variability in order of convergence than did laminar isothermal flow with the same manufactured solution.

The process of code verification with the method of manufactured solutions was also applied to coupling of both solid and fluid domains with heat transfer physics. Coupling two domains introduced discontinuities in thermal conductivity which increases error relative to a single domain and causes the order of convergence to be close to zero except in a specific combination of grid size and transition length. Increasing the difference in thermal conductivities between the two domains increases the error. Thermal conductivity of water is very low compared to that of aluminum, and thus coupling the two materials produces a large error in the temperature predictions. These errors in heat transfer are caused by COMOL's handling of the discontinuity in the source term of the manufactured equations, and may not also be an error in the coupling approach in the code.

The flow physics and heat transfer with two domains were examined. The coupling reduces the temperature error in the fluid. This reduction in error occurs because of the size of the flow heat source term relative to the conduction heat source term. The temperature error in the solid is increased. The error in velocity is essentially unchanged from the isothermal case, while the error in pressure increases. The order of convergence for fluid velocity is largely the same, while for pressure and temperature the orders of convergence become less constant across grid refinement than the models that are not coupled.

Opportunity still exists to further code verification of COMSOL's heat transfer and CFD modules. Different boundary conditions; other turbulence models such as isothermal, non-isothermal, and in conjugate heat transfer; temperature dependent material properties, all could be tested. These tests would strengthen the verification of the modules. Additionally, a partnership with COMSOL enabling a more thorough investigation into why the models do not exhibit the expected nearly constant orders of convergence may prove valuable and may enable more precise numerical error estimates than can currently be made.

9.2 Solution Verification

Following code verification, which seeks to demonstrate that a particular code solves the equations it is supposed to solve, solution verification seeks to quantify the uncertainty in the calculated solution of those equations. In an ideal code that shows a constant order of convergence under grid refinement, the accuracy of the solution can be arbitrarily required and met through grid refinement. This is limited by computational resources available and by round off error, but, in general, the solution can be made as accurate as desired.

9.2.1 Numerical Uncertainty by Grid Convergence Index [92]

The ultimate output from solution verification is an estimate of the numerical uncertainty associated with a given solution from a particular grid. If the exact solution, f_{exact}, is known beforehand, the discretization error, ϵ, is given by

$$\epsilon = f_1 - f_{exact} \tag{13}$$

where, f_1 is the simulation solution. In most cases of interest, the solution is not known before hand, and an error must be estimated. The simplest form of error estimation can be used when the simulation is run on 2 different grids.

$$\epsilon_{12} \cong f_2 - f_1$$

where 1 indicates the finer of the two grids. In essence, this estimation assumes that the finer solution is in fact the exact solution. By solving on a third grid, three different error estimates are available, ϵ_{12}, ϵ_{13}, ϵ_{23}. From these error estimates, an order of convergence, p, can be calculated by solving

$$\frac{\epsilon_{23}}{r_{23}^p - 1} = r_{12}^p \left(\frac{\epsilon_{12}}{r_{12}^p - 1} \right)$$

where the r's indicate grid refinement ratios.

Numerical error and uncertainty estimates can be made using different techniques depending on p. When p is relatively consistent across different grids, Richardson extrapolation can be used to estimate a more accurate solution,

$$f_{exact} \cong f_1 + \frac{f_1 - f_2}{r^p - 1}$$

where r is the refinement ratio between grids 1 and 2, as in $r = \frac{h_2}{h_1}$, where h is some representative mesh element dimension. With this estimate of f_{exact} a numerical error can be estimated using equation (13). This numerical error can then be converted into a numerical uncertainty by multiplying it by a factor of safety, F_s. [92] recommends a factor of safety of 1.25

for solutions that exhibit near constant p close to the theoretical p for the solution technique being used and 3 for all other cases. The steps in determining numerical uncertainty can be combined into a single relationship expressed by

$$\text{GCI} = F_s \frac{|\epsilon|}{r^p - 1},$$

where GCI is the grid convergence index, and with a proper F_s can be considered as a $\pm$ uncertainty interval at the 95% confidence level in CFD applications [92].

9.2.2 Least Squares GCI [93]

Challenges with the GCI approach arise when p is not constant across multiple grids. [93] developed a method for estimating numerical uncertainty in cases where using the standard GCI method is questionable, such as when observed p is difficult to determine, degraded, or noisy. Their approach involves using least squares to estimate a value for p, calculating a standard deviation for that estimated p and using those two values, as well as the spread in the solution results to estimate a numerical uncertainty. This process requires solutions from at least 4 different grids. The following procedure is taken almost verbatim from [93]:

1. Determine ϵ_ϕ:

   • Solve
   $$\delta_{RE} = \alpha_v h_i^p$$
   in the least-squares sense with and without weights to obtain δ_{RE}, p and the standard deviations of the two fits, σ. If any of the fits exhibits $0.5 \leq p \leq 2$, $\epsilon_\phi = \delta_{RE}$. If both fits exhibit $0.5 \leq p \leq 2$, the value of δ_{RE} selected corresponds to the fit with the smallest standard deviation.

   • If the observed order of grid convergence $p > 2$, solve
   $$\delta_1 = \alpha_v h_i$$
   and
   $$\delta_2 = \alpha_v h_i^2$$
   in the least-squares sense with and without weights and determine the standard deviations of the four fits, σ. ϵ_ϕ is obtained from the fit that exhibits the smallest standard deviation.

   • If the observed order of grid convergence $p < 0.5$ or is impossible to establish, solve
   $$\delta_1 = \alpha_v h_i$$
   $$\delta_2 = \alpha_v h_i^2$$
   and
   $$\delta_{12} = \alpha_{v,1} h_i + \alpha_{v,2} h_i^2$$
   in the least-squares sense with and without weights and determine the standard deviations of the six fits σ. ϵ_ϕ is obtained from the fit that exhibits the smallest standard deviation.

180

2. Determine a data range parameter

$$\Delta_\phi = \frac{(\phi_i)_{max} - (\phi_i)_{min}}{n_g - 1}$$

to assess the quality of the fit used to obtain the error estimate ϵ_ϕ.

3. Determine the safety factor from p, σ, and Δ_ϕ:

- If $0.5 \leq p \leq 2$ and $\leq \Delta_\phi$, $F_s = 1.25$.
- Otherwise, $F_s = 3$.

4. Obtain the uncertainty from ϵ_ϕ and the safety factor F_s using the values of σ and Δ_ϕ to distinguish between "good" and "bad" error estimates:

- For $\sigma < \Delta_\phi$:

$$U_\phi(\phi_i) = F_s \epsilon_\phi(\phi_i) + \sigma + |\phi_i - \phi_{fit}|$$

- For $\sigma \geq \Delta_\phi$:

$$U_\phi(\phi_i) = 3\frac{\sigma}{\Delta_\phi} \left(\epsilon_\phi(\phi_i) + \sigma + |\phi_i - \phi_{fit}|\right).$$

The α_v's and p's for solving the δ's are determined as follows:

with the number of grids, n_g, and weights,

$$w_i = \frac{\dfrac{1}{h_i}}{\sum_{i=1}^{n_g}\left(\dfrac{1}{h_i}\right)}$$

minimize

$$S_{RE}(\phi_0, \alpha_v, p) = \sqrt{\sum_{i=1}^{n_g} w_i \left(\phi_i - (\phi_0 + \alpha_v h_i^p)\right)^2}.$$

This is obtained from

$$\frac{\partial S_{RE}}{\partial \phi_0} = 0, \qquad \frac{\partial S_{RE}}{\partial \alpha} = 0, \qquad \frac{\partial S_{RE}}{\partial p} = 0.$$

This leads to a system of non-linear equations

$$\phi_0 = \sum_{i=1}^{n_g} w_i \phi_i - \alpha_v \sum_{i=1}^{n_g} w_i h_i^p,$$

$$\alpha = \frac{\sum_{i=1}^{n_g} w_i \phi_i \, h_i^p - \left(\sum_{i=1}^{n_g} w_i \phi_i\right)\left(\sum_{i=1}^{n_g} w_i h_i^p\right)}{\sum_{i=1}^{n_g} w_i h_i^{2p} - \left(\sum_{i=1}^{n_g} w_i h_i^p\right)^2},$$

$$\sum_{i=1}^{n_g} w_i \phi_i h_i^p \log(h_i) - \phi_0 \sum_{i=1}^{n_g} w_i h_i^p \log(h_i) - \alpha_v \sum_{i=1}^{n_g} w_i h_i^{2p} \log(h_i) = 0$$

that has a standard deviation given by

$$\sigma_{RE} = \sqrt{\frac{\sum_{i=1}^{n_g} n_g w_i \left(\phi_i - \left(\phi_0 + \alpha_v h_i^p\right)\right)^2}{n_g - 3}}.$$

*Note that [2] states that to calculate the unweighted values, simply replace the w_i with 1, however, this leaves the estimated exact solution, ϕ_0, and α incorrect. [92] offers the correction

$$\phi_0 = \frac{1}{n_g}\left(\sum_{i=1}^{n_g} \phi_i - \alpha_v \sum_{i=1}^{n_g} h_i^p\right)$$

$$\alpha = \frac{n_g \sum_{i=1}^{n_g} \phi_i \, h_i^p - \left(\sum_{i=1}^{n_g} \phi_i\right)\left(\sum_{i=1}^{n_g} h_i^p\right)}{n_g \sum_{i=1}^{n_g} h_i^{2p} - \left(\sum_{i=1}^{n_g} h_i^p\right)^2}.$$

In the standard deviation calculation, $n_g w_i = 1$.

Continuing with [93]'s process:

To determine the values for calculating δ_1, essentially assuming an order of convergence equal to one, minimize

$$S_1(\phi_0, \alpha) = \sqrt{\sum_{i=1}^{n_g} w_i\left(\phi_i - \left(\phi_0 + \alpha_v h_i\right)\right)^2}.$$

This leads to a system of liner equations

$$
\begin{bmatrix} 1 & \sum_{i=1}^{n_g} w_i h_i \\ \sum_{i=1}^{n_g} w_i h_i & \sum_{i=1}^{n_g} w_i h_i^2 \end{bmatrix} \begin{bmatrix} \phi_0 \\ \alpha_v \end{bmatrix} = \begin{bmatrix} \sum_{i=1}^{n_g} w_i \phi_i \\ \sum_{i=1}^{n_g} w_i \phi_i h_i \end{bmatrix}
$$

That has a standard deviation given by

$$
\sigma_1 = \sqrt{\frac{\sum_{i=1}^{n_g} n_g w_i \left(\phi_i - (\phi_0 + \alpha_v h_i) \right)^2}{n_g - 2}}.
$$

*Again, [93]'s description of the unweighted calculation leads to an error. [92] did not cover this calculation. The following system of linear equations was determined to be correct.

$$
\begin{bmatrix} n_g & n_g \sum_{i=1}^{n_g} h_i \\ \sum_{i=1}^{n_g} h_i & n_g \sum_{i=1}^{n_g} h_i^2 \end{bmatrix} \begin{bmatrix} \phi_0 \\ \alpha_v \end{bmatrix} = \begin{bmatrix} \sum_{i=1}^{n_g} \phi_i \\ \sum_{i=1}^{n_g} \phi_i h_i \end{bmatrix}.
$$

Continuing with [93]'s process:

To determine the values for calculating δ_2, essentially assuming an order of convergence equal to two, minimize

$$
S_2(\phi_0, \alpha_v) = \sqrt{\sum_{i=1}^{n_g} w_i \left(\phi_i - (\phi_0 + \alpha_v h_i^2) \right)^2}.
$$

This leads to a system of liner equations

$$
\begin{bmatrix} 1 & \sum_{i=1}^{n_g} w_i h_i^2 \\ \sum_{i=1}^{n_g} w_i h_i^2 & \sum_{i=1}^{n_g} w_i h_i^4 \end{bmatrix} \begin{bmatrix} \phi_0 \\ \alpha_v \end{bmatrix} = \begin{bmatrix} \sum_{i=1}^{n_g} w_i \phi_i \\ \sum_{i=1}^{n_g} w_i \phi_i h_i^2 \end{bmatrix}
$$

That has a standard deviation given by

183

$$\sigma_1 = \sqrt{\frac{\sum_{i=1}^{n_g} n_g w_i \left(\phi_i - (\phi_0 + \alpha_v h_i^2) \right)^2}{n_g - 2}}.$$

*The same correction is necessary as in the previous system of equations.

Continuing with [93]'s process:

To determine the values for calculating δ_{12}, minimize the function

$$S_{12}(\phi_0, \alpha_{v,1}, \alpha_{v,2}) = \sqrt{\sum_{i=1}^{n_g} w_i \left(\phi_i - (\phi_0 + \alpha_{v,1} h_i + \alpha_{v,2} h_i^2) \right)^2}.$$

This leads to a system of linear equations

$$\begin{bmatrix} 1 & \sum_{i=1}^{n_g} w_i h_i & \sum_{i=1}^{n_g} w_i h_i^2 \\ \sum_{i=1}^{n_g} w_i h_i & \sum_{i=1}^{n_g} w_i h_i^2 & \sum_{i=1}^{n_g} w_i h_i^3 \\ \sum_{i=1}^{n_g} w_i h_i^2 & \sum_{i=1}^{n_g} w_i h_i^3 & \sum_{i=1}^{n_g} w_i h_i^4 \end{bmatrix} \begin{bmatrix} \phi_0 \\ \alpha_{v,1} \\ \alpha_{v,2} \end{bmatrix} = \begin{bmatrix} \sum_{i=1}^{n_g} w_i \phi_i \\ \sum_{i=1}^{n_g} w_i \phi_i h_i \\ \sum_{i=1}^{n_g} w_i \phi_i h_i^2 \end{bmatrix}$$

that has a standard deviation given by

$$\sigma_{12} = \sqrt{\frac{\sum_{i=1}^{n_g} n_g w_i \left(\phi_i - (\phi_0 + \alpha_{v,1} h_i + \alpha_{v,2} h_i^2) \right)^2}{n_g - 3}}.$$

*The same corrections are necessary, removing the weights, and multiplying the diagonal and the upper right triangle by the number of grids for the unweighted calculations.

This concludes [93]'s procedure. The entire procedure was programmed into a MATLAB file, supplied in Appendix A: Least Squares GCI.

[93] evaluated this procedure on 4 different CFD test cases, using two turbulence models, and over 20 grid refinements per case. 4 different quantities of interest were examined for each simulation. The simulations were manufactured solutions, flow over a flat plate, flow over a

backward step, and flow past a tanker. In general, the results indicated that the procedure does produce uncertainty estimates that encompass the true value 95% (or more) of the time.

9.2.3 The Advanced Neutron Source Reactor Thermal Hydraulic Test Loop
Keeping in mind the V&V goal of determining a model error with uncertainty, the next step would normally be to subject the model in question to a series of grid refinements and estimate a numerical error using one of the preceding methods, or another acceptable method. This numerical error would then be combined with the results from validation to produce the model error estimate with uncertainty. Unfortunately, there are no relevant experimental data for a HFIR fuel plate. Experimental data with similar features to the HFIR fuel plate and coolant channel were identified. As a surrogate for the HFIR fuel plate model, a model of that experiment was created, and solution verification and validation were performed with that model and experimental data.

The advanced neutron source reactor (ANSR) thermal hydraulic test loop (THTL) was an experimental facility designed to "…simulate a full-length coolant subchannel of the core, allowing experimental determination of thermal limits under the expected ANSR thermal-hydraulic conditions" [94]. Table 23 shows a comparison of HFIR properties with properties from the ANSR THTL experiments that were simulated. Of the simulated experiments, only FE331A10 had data for temperature measurements along the length of the test section; the results for the other experiment only report the inlet and outlet conditions. Figure 143 plots the temperature data reported on FE331A10. As the plot indicates, the temperature was measured on the outside of the test section, while the other temperatures reported were calculated based on the measured inlet and outlet temperatures, and power applied to the test section.

9.2.3.1 THTL COMSOL Model
A 2D model of the THTL was created in COMSOL, Figure 144. The model contains two domains, a water coolant domain and an aluminum test section domain. The water domain extends 12.7 mm upstream and downstream of the aluminum, starting and ending at the approximate location of the pressure taps on the THTL test section [94]. It is 0.635 mm thick. The aluminum test section is 507 mm long, 2.54 mm thick, and uses the built-in COMSOL properties for aluminum, except for the thermal conductivity which has been replaced with a function that follows Table 24.

Only half of the test section is modeled and the top of the water domain was set to a symmetric boundary condition. All bottom boundaries were thermally insulated, and the remaining boundary conditions were established based on the information provided from the experiment (see Table 23). The entire lower length of the coolant domain was given the "wall" boundary condition with roughness.

k-ϵ , k-ω, and SST turbulence models were run. Compressible, low Mach number (Ma<0.3)

Table 23 Comparison of the HFIR conditions with modeled experiments from the ANSR

		HFIR	ANSR FE331A10	FE105B06
Coolant Channel	thickness [mm]	1.27	1.27	
	width [mm]	81/73*	12.7	
	length [mm]	610	507	
	Inlet Pressure [MPa]	3.33	2.318	2.226
	Outlet Pressure [MPa]	2.61	1.701	1.72
	Pressure Drop [MPa]	0.724	0.617	0.506
	Inlet Velocity [m/s]	7.944	18.5	15.43
	Inlet Temperature [C]	48.9	45.75	44.69
	Outlet Temperature [C]	69.4	169.17	154.35
	Ave Heat Flux [MW/m^2]	2.26/1.94*	12.031	9.099

*inner/outer plate

Measured and Calculated Temperatures for THTL Run FE331A10
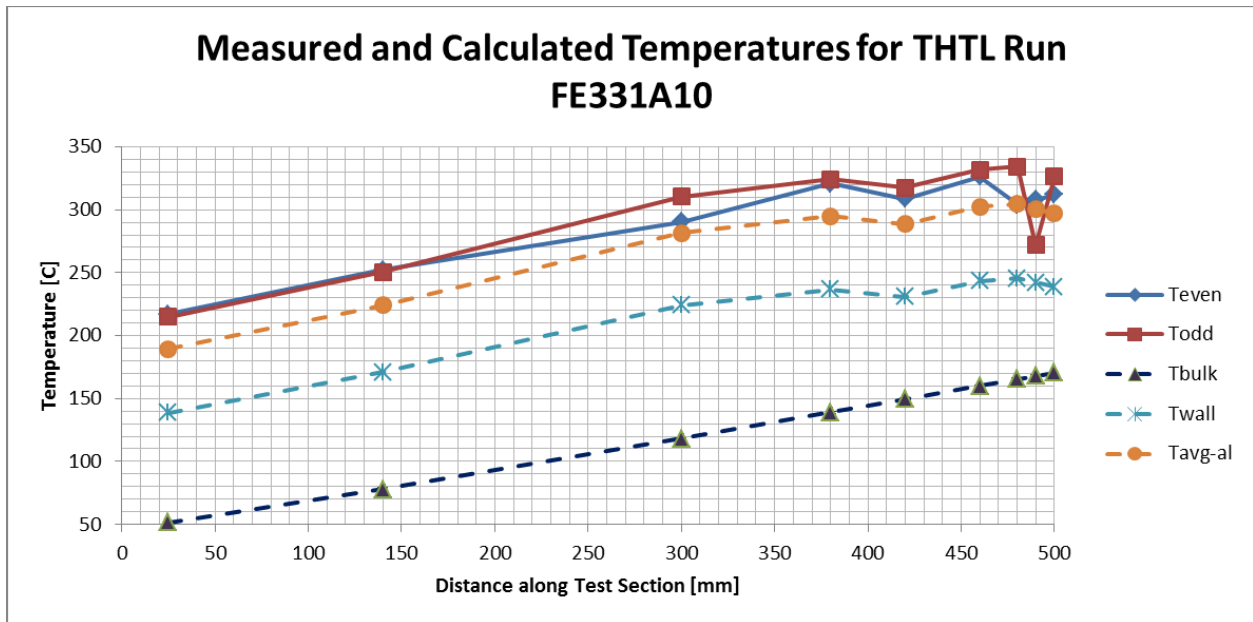
Figure 143 Measured (solid lines) and calculated (dashed lines) temperatures for one of the ANSR THTL experiments

186
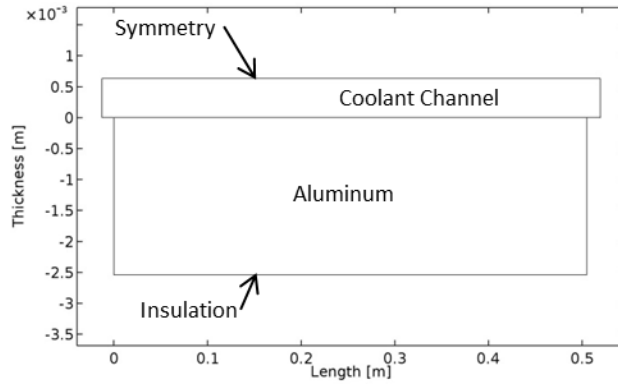
Figure 144 Simplified, 2D THTL model consisting of a coolant channel (the upper domain) and an aluminum test section (the lower domain)

Table 24 Material properties for aluminum 6061-T6 [95]

Temperature [C]	Thermal Conductivity [W/ (m K)]	Heat Capacity [J/(kg K)]	Density [kg/m^3]	Thermal Expansio n [e-6/K]	Young's Modulus [GPa]	Yield Stress [Mpa]	Poisson's Ratio
0	162	917	2703	22.4	69.7	277.7	
98	177	978	2685	24.6	66.2	264.6	
201	192	1028	2657	26.6	59.2	218.6	0.33
316	207	1078	2630	27.6	47.8	66.2	
428	223	1133	2602	29.6	31.7	17.9	
571	253	1230	2574	24.2	0	0	

187

Table 25 Domain elements for each of the grid sizes used for the three turbulence models

Grid Size	Domain Element	
	k-ϵ & k-ω	SST
Normal	73309	257706
Fine	197860	637231
Finer	540066	770752
Extra Fine	693799	1295605
Extremely Fine	1373929	1489957

flow with density determined by the heat transfer module and with a P1+P1 discretization were used. Uniform heat generation was used based on the reported experimental average heat flux.

The experimental data provide both inlet and exit pressures, and either inlet and exit, or average fluid velocities. Inlet and exit temperatures were also provided. All of these values would over-constrain the simulation, so the inlet temperature and velocity as well as the exit pressure were supplied to the simulation, and the inlet pressure and exit temperature, as well as temperatures along the length of the test section when they were available in the experimental results, were examined as the quantities of interest.

The pressure drop was used as a gauge for adjusting the wall roughness in the k-ϵ and k-ω models. COMSOL's SST model provides no way to adjust for wall roughness. The inlet velocity and exit pressure were set in the simulation and a wall roughness was selected. The simulation was run and the pressure drop was determined by subtracting the prescribed exit pressure from the maximum pressure in the simulation. The wall roughness was then adjusted to bring the pressure drop from the simulation closer to the reported experimental pressure drop. This was repeated until the error in pressure drop (simulated minus experimental) was less than 0.1%. In cases where only an average velocity was supplied with the experiment, the inlet velocity was first adjusted until the average velocity error was below 0.1%, and then the pressure was adjusted.

After this tuning was completed, the simulations of the experiments were run at each of the built-in mesh sizes, normal through extremely fine. Table 25 provides the domain mesh elements for each of the sizes.

Figure 145 shows a comparison of the temperatures reported for the experiment and the results from the simulations for the wall at the solid-fluid interface, for the external surface of the test section, and for the bulk temperature for the experiment with the centerline temperature from the simulation for k-ϵ. The markers in the plots indicate the experimental values while the lines without markers indicate the simulation values. The test section has two measured values because it was instrumented on both sides at the same axial locations. These two are
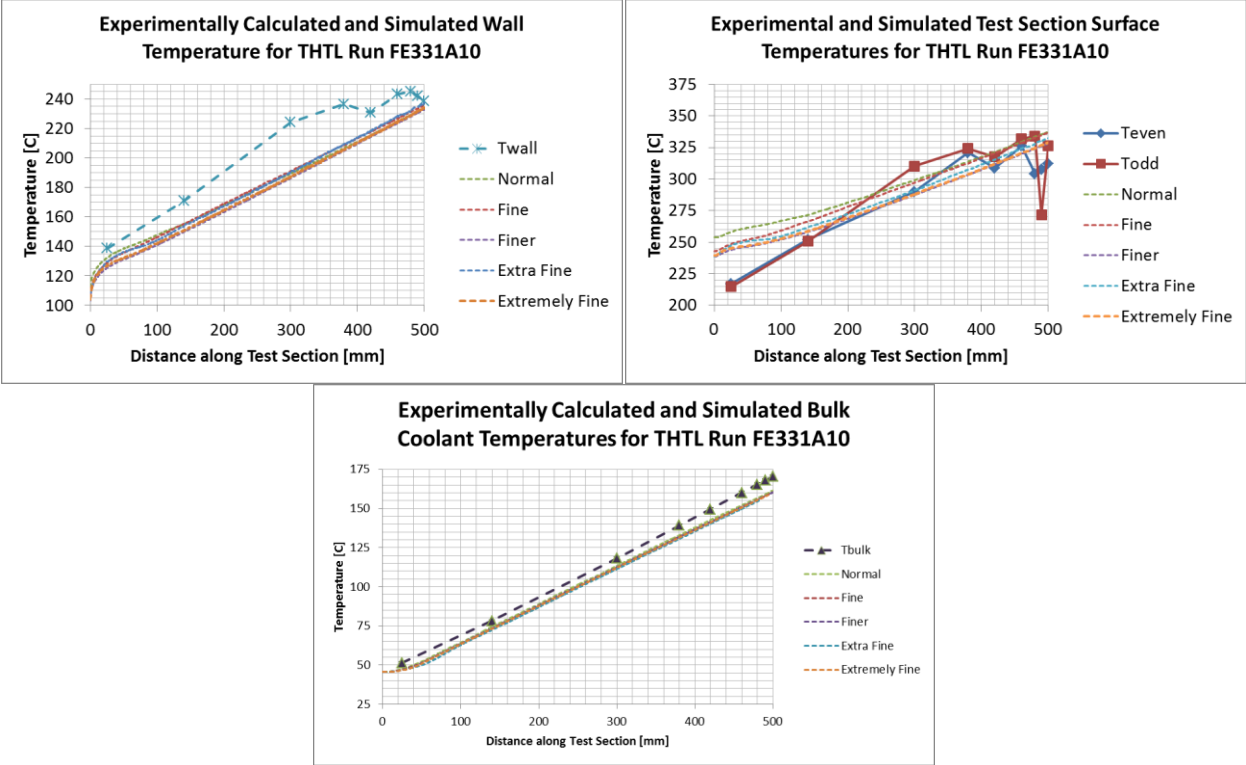
Figure 145 Experimental and simulation temperatures for the wall, test section surface, and the bulk/centerline for k-ϵ

distinguished from each other by "even" and "odd" corresponding to the thermocouple number given in the report. The results for k-ω are very similar. The temperatures predicted with SST were higher for both the wall and test section and are provided in Figure 146.

9.2.3.2 THTL Numerical Uncertainty

Numerical uncertainty was calculated for each grid at each location where the experimental results were reported. Initially, the GCI method was attempted. The observed orders of convergence were sufficiently noisy (ranging from -8 to 17 in the worst cases) for these local values, that the least squares GCI method was required. This noisy p is consistent with the code verification results observed previously.

The MATLAB code in Appendix A was used to calculate the uncertainties at a 95% confidence level. Values for h were determined using

$$h_i = \frac{1000}{\sqrt{N_{DE}}}$$

where N_{DE} is the number of domain elements in a given mesh, Table 25.

In addition to the uncertainties, the MATLAB code in Appendix A: Least Squares GCI also supplies the user with the calculated standard deviation of the selected fit and the p value used. Figure 147, Figure 148, and Figure 149 show the k-ϵ simulated values for the centerline temperature, the test section surface temperature, and the coolant-test section interface wall temperature along with the 95% confidence bands. The uncertainties in the first three charts of the quad-plot were calculated from (1) all 5 grids, (2) the 4 remaining grids without the normal, and (3) without the extremely fine grids. The final chart (4) in each quad-plot was generated by using the minimum uncertainty of the three preceding plots. Similar plots for the k-ω and SST simulations are presented in Appendix B: Numerical Uncertainty Plots for THLT k-ω and SST.

Uncertainty for local values is expected to be higher than for average, integral or global values. As stated previously, for each of these simulations, the inlet velocity and temperatures as well as the exit pressure were prescribed. The inlet pressure and exit temperature were determined from the simulation solutions. Numerical uncertainty, $\pm U_{95\%}$, for these values were also calculated, Table 26.

The final row in Table 26 presents the order of convergence that had the best fit, as identified by the smallest standard deviation. A non-integer number in this row represents the order of convergence that the solver identified based on the convergence data. An integer value of 1 or 2 indicates that the solver identified an order of convergence that was greater than 2. The code then used an order of convergence of 1 or 2, whichever was the better fit, and reported that number. If the order of convergence was less than 0.5, or if the solver could not identify an order of

190
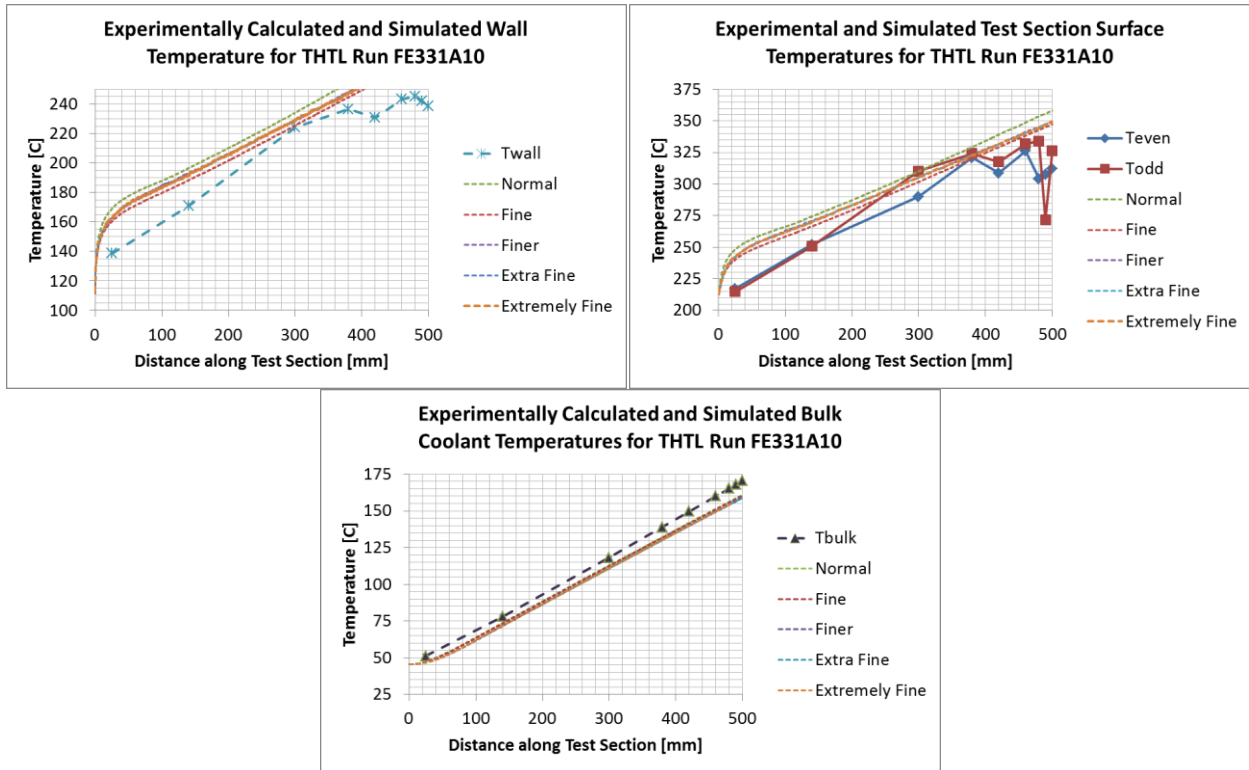
Figure 146 Experimental (with marker) and simulation (no marker) temperatures for the wall (fluid-solid interface), test section surface, and the bulk/centerline for SST
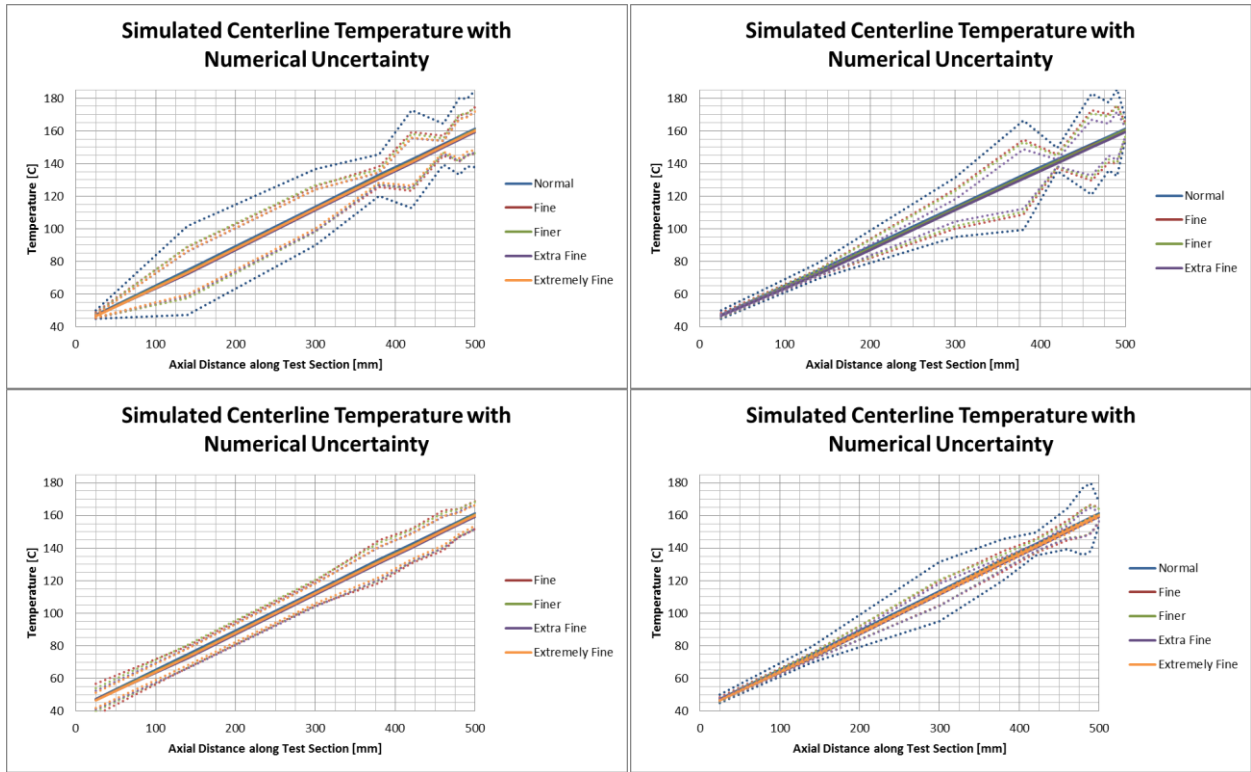
Figure 147 Numerical uncertainty (±U$_{95\%}$) in k-ε centerline temperature for different grids
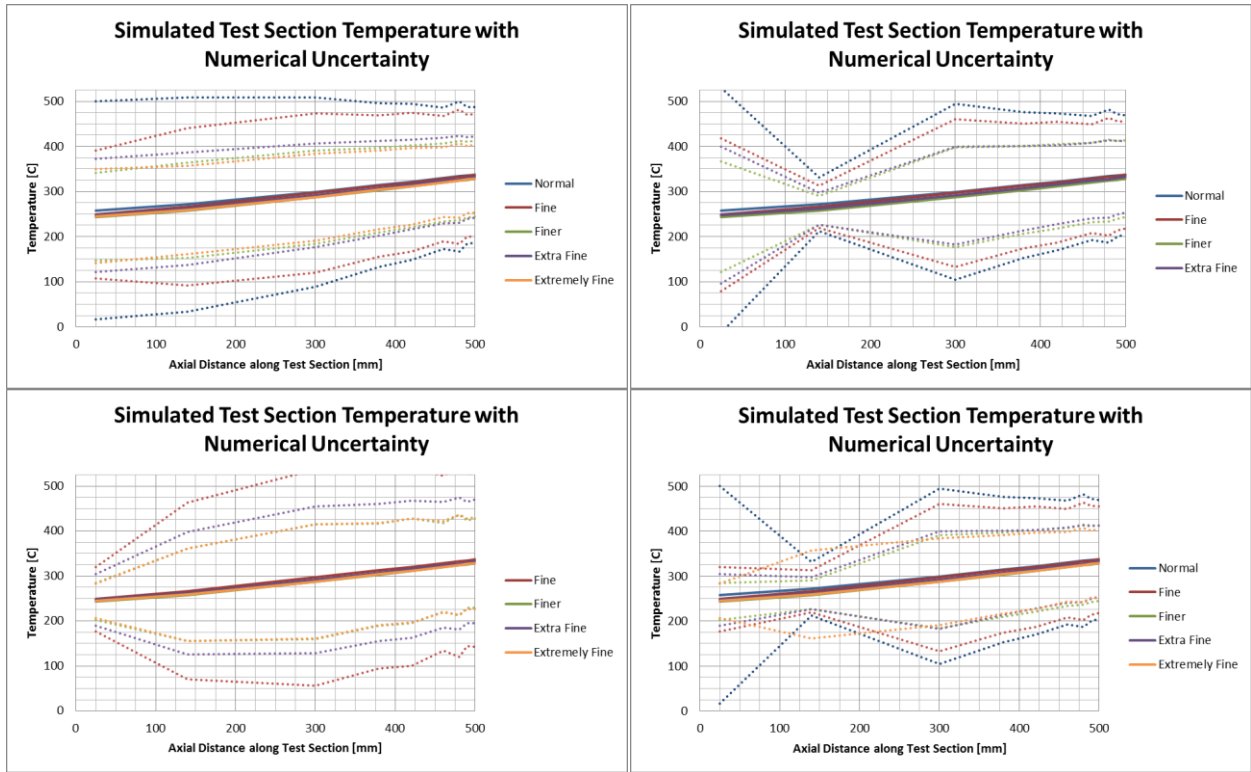
Figure 148 Numerical uncertainty ($\pm U_{95\%}$) in k-ϵ test section temperature for different grids
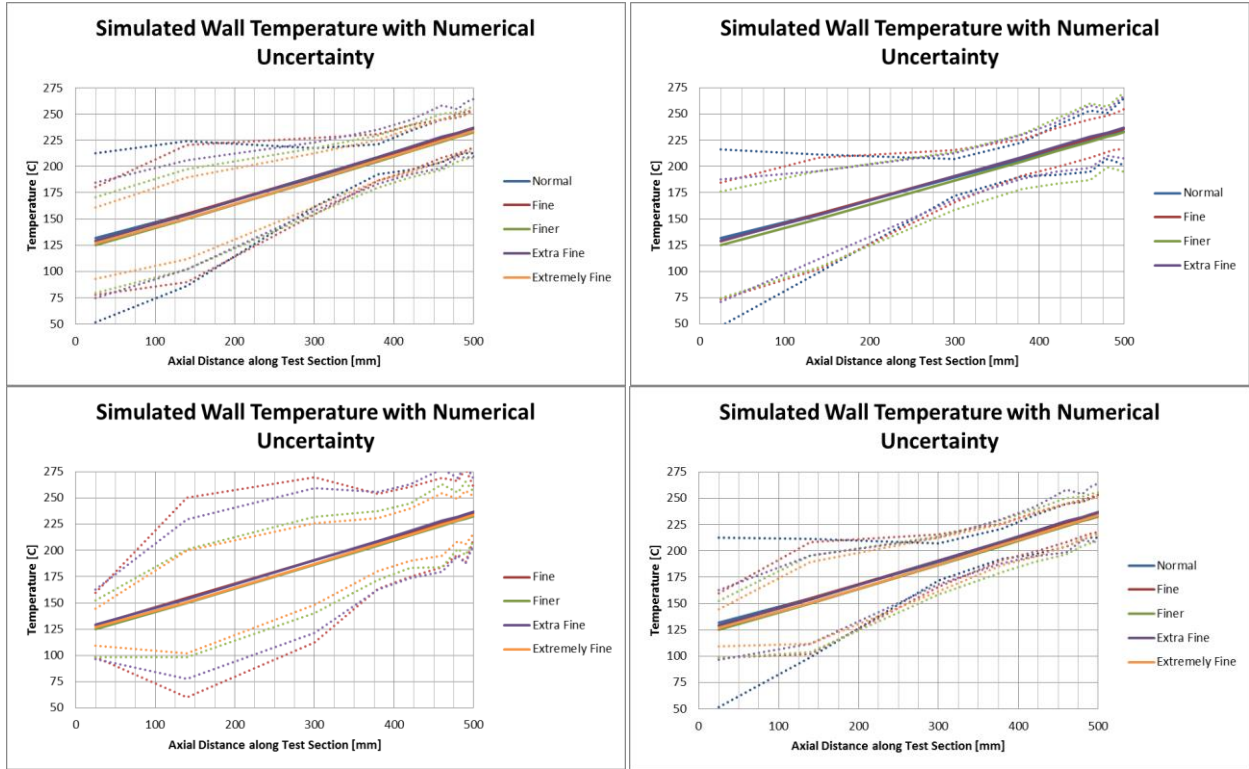
Figure 149 Numerical uncertainty (±U$_{95\%}$) in k-ϵ wall temperature for different grids

convergence, then values of 1, 2 and a two term expansion with first and second order of convergence were examined. The standard deviations were compared for each of these, and the best fit was selected. In this last case, a value of 11-16 is presented in the "p" row. 11 and 12 indicate the $p=1$ unweight or weighted, respectively, was the best fit. 13 and 14 are similar with $p=2$ unweighted and weighted. 15 and 16 indicate the two term expansion with first and second order was the best fit, again, unweighted and weighted.

Table 26 Numerical Uncertainties, $\pm U_{95\%}$ for the exit temperature and inlet pressure for each of the three turbulence models

Grid	k-e		k-w		SST	
	Temperature [C]	Pressure [MPa]	Temperature [C]	Pressure [MPa]	Temperature [C]	Pressure [MPa]
Normal	1.56	0.392	5.08	0.588	0.9	0.661
Fine	1.1	0.364	4.75	0.452	2.13	0.347
Finer	1.4	0.26	4.23	0.462	1.08	0.401
Extra Fine	1.44	0.324	3.37	0.329	0.95	0.422
Exremely Fine	1.14	0.25	3.24	0.335	1.04	0.424
SD	0.13	0.024	0.31	0.029	0.13	0.03
P	2	2	13	2	2	2

Chapter 10 Validation

10.1 Validation Efforts

Validation is the process of establishing how well a mathematical model describes reality. It ideally consists of a validation experiment which seeks to accurately measure reality, D, for data, provide an experimental uncertainty, U_D, and an input parameter uncertainty, U_{input}. Often, however, validation depends on pre-existing experimental results instead of a custom designed validation experiment, and may lack information about the uncertainties and other features of the experiment. The results of verification and the validation experiment (or pre-existing data) are combined to determine an error, E, in the numerical solution, and a validation uncertainty, U_{val}. The combination of error and validation uncertainty represent an estimate of the modeling error. The process is illustrated in Figure 150.

Because no validation experiment exists for the HFIR fuel plate and coolant channel, an estimate for the model error was derived from the ANSR THTL experiment and data. Table 23 in section 9.2.3, lists the conditions of the HFIR and the ANSR THTL experiment for comparison. No experimental uncertainty for the temperature and pressure measurements was reported with the ANSR THTL data. In another paper that reports on ANSR THTL experiments, the experimental uncertainty in the temperature measurement is reported at ±2% at the 95% confidence level with two standard deviations [96].

The test section temperature measurements were made by thermocouples held against the side of
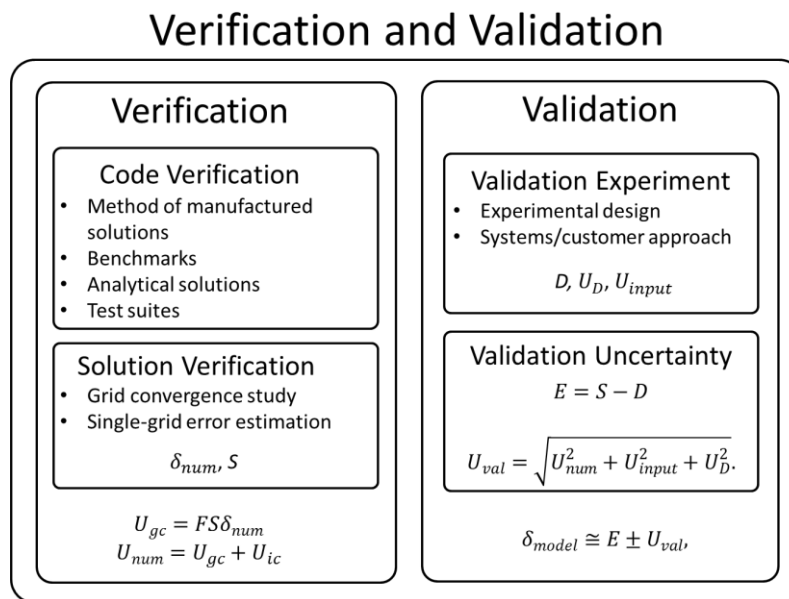
Figure 150 Summary of a verification and validation process

196

the test section. Two thermocouples were placed opposite one another at each axial location. In a perfect experiment and with this configuration, the thermocouple pairs would provide identical readings once the experiment was at steady state. Two data sets were identified where the temperatures from these pairs of thermocouples are reported. The first set comes from a zero-power run—that is, there was no heating of the test section. In this run, the thermocouple pairs differed by 3.26°C at most, with an average difference of 0.48°C and a standard deviation of 1.54°C. If it is assumed that the test section supply water was at a constant temperature and that all 18 test section thermocouples were measuring the same temperature, the standard deviation is 0.94°C out of 36.3°C. Changing this to a percentage using an absolute scale gives a standard deviation of 0.3041%. At the 2 standard deviation level, this would provide an uncertainty of ±0.6%. This is well below the reported ±2%. Additionally, each of the measurements overlaps the others when ±2% is applied to them.

In the other data set available, the test section was heated, so the thermocouples were not all measuring the same temperature. Using the difference between the measured temperatures for each thermocouple in a pair may provide some indication of the uncertainty in their measurements. The thermocouple pairs showed a standard deviation of 3.23% difference, with the largest difference being over 6%. With this information, a number of possibilities exist. First, the test section is not symmetric in its temperature distribution, that is, the temperatures that each thermocouple in a pair measures is not the same. Second, the temperatures are the same and (1) there is a problem with the measurement system or (2) the uncertainty in the measurement of the thermocouples is greater than 2%. The required uncertainty to make the confidence intervals overlap for the pair with the greatest difference is slightly lower than the calculated standard deviation in temperature difference. Without further information, it is not possible to know the source of the difference, but it will be assumed that the temperature measurements for the ANSR THTL data have a 95% confidence interval of 3.25%.

The modeling error as described in Figure 150 is given by

$$\delta_{model} \cong (S - D) \pm \sqrt{U_{num}^2 + U_{exp}^2}$$

where *S* is the simulation results and no parameter uncertainty is included. The modeling error as a function of position for the THTL experiment is shown in Figure 151, Figure 152, and Figure 153 for the k-ε model. Similar plots for k-ω and SST can be found in Appendix C: Model Error and Uncertainty Plots for THTL.

The same approach to determining the modeling error with uncertainty can be made with the average values of inlet pressure and exit temperature. [96] reports a 95% confidence interval for the pressure of 5.8% which was used here. These pressure and temperature results are shown in Table 27.
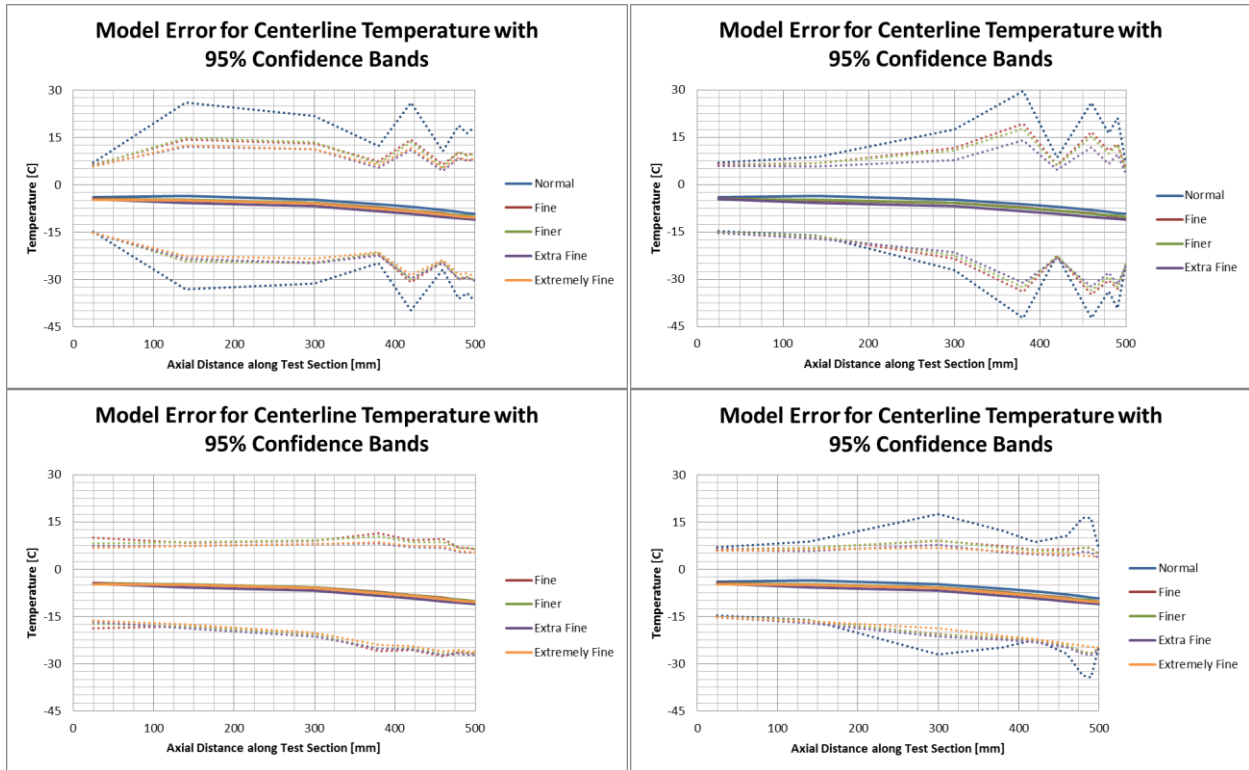
Figure 151 Modeling error with ±U$_{95\%}$ confidence intervals for k-ϵ centerline temperature for different grids

198
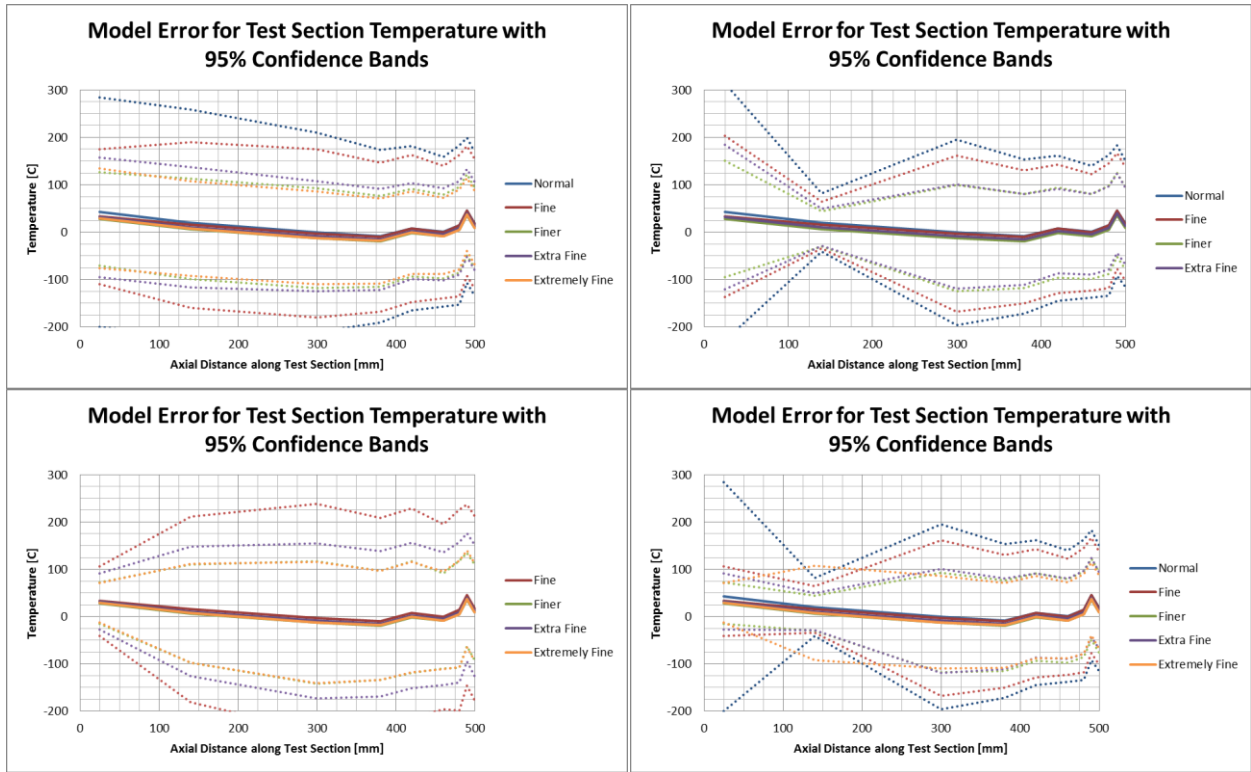
Figure 152 Modeling error with ±U$_{95\%}$ for test section temperature for different grids
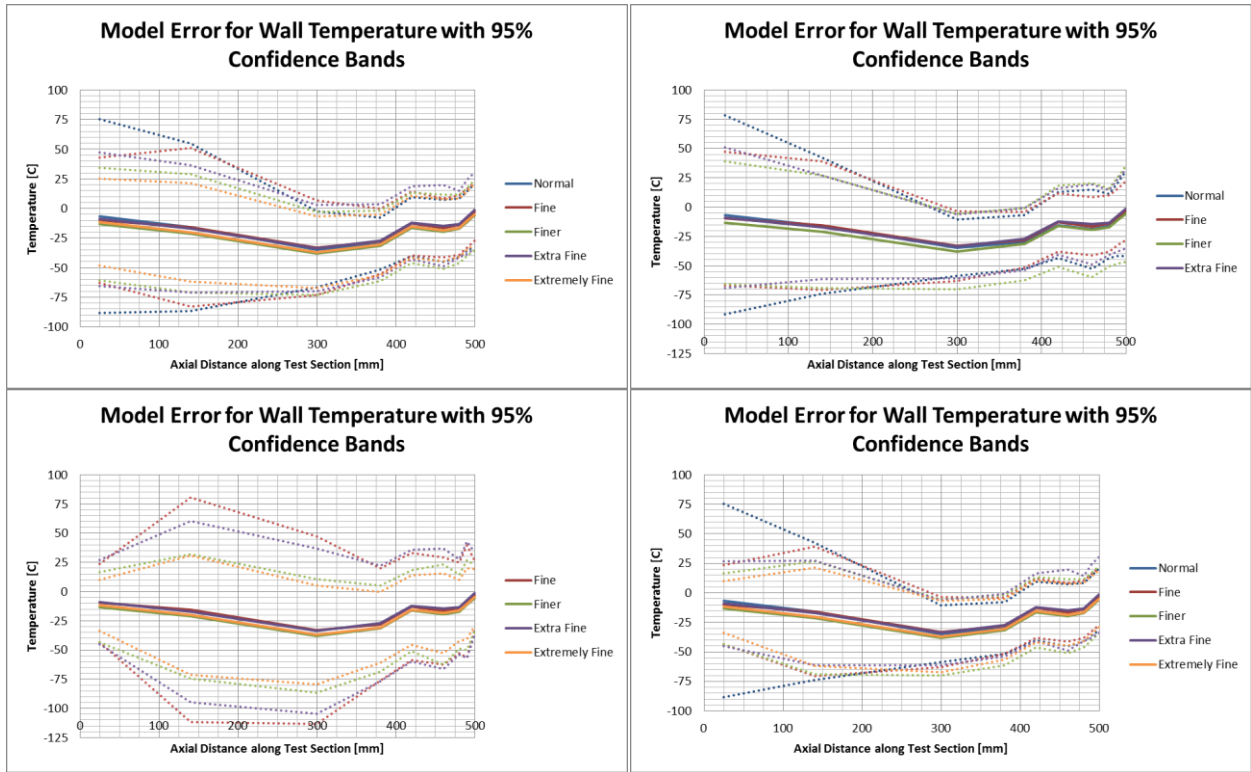
Figure 153 Modeling error plus 95% confidence intervals for test section temperature for different grids

Table 27 Modeling error and uncertainty for average exit temperature and inlet pressure for the three turbulence models

| | k-e | | | | k-w | | | | SST | | | |
| | T [C] | | P [MPa] | | T [C] | | P [MPa] | | T [C] | | P [MPa] | |
	δ	U95%	δ	U95%	δ	U95%	δ	U95%	δ	U95%	δ	U95%
Normal	-0.109	14.5	-0.038	0.415	-0.21	15.2	-0.005	0.603	0.112	14.4	-0.11	0.6748
Fine	-0.024	14.4	-0.036	0.388	-0.127	15.1	-0.016	0.471	-0.08	14.5	-0.043	0.3718
Finer	-0.062	14.4	-0.013	0.293	-0.052	15	-0.013	0.481	0.183	14.4	-0.044	0.4225
Extra Fine	0.117	14.4	-0.036	0.351	0.196	14.8	-0.043	0.356	0.16	14.4	-0.047	0.4428
Extremely Fine	-0.021	14.4	-0.018	0.284	0.177	14.7	-0.044	0.361	0.175	14.4	-0.047	0.4452

10.2 V&V Conclusion

The purpose of verification and validation is to establish confidence with a goal to provide an estimate of the model error and the uncertainty for a given quantity of interest. With those pieces of information, the decision maker can choose how to proceed. If the modeling error and uncertainties are acceptable for the quantity of interest and application of the results, the model can be used with confidence. If the modeling error is too large, the mathematical model used ought to be revisited. If the uncertainty is too large, the largest component of the uncertainty (numerical, experimental, parameter, etc.) may be an appropriate focus for efforts in uncertainty reduction. A review of this V&V effort may provide some insight in approaches to reduce overall uncertainty in the hotspot evaluation even though the exercise is for a uniformly heated channel.

10.2.1 Verification

10.2.1.1 Code Verification

The method of manufactured solutions was used for code verification. The heat transfer module performed as expected with a nearly constant order of convergence across all grids. The fluid flow module, with laminar flow and yPlus turbulence model showed orders of convergence that were not well behaved with grid refinement for all quantities of interest. Coupling heat transfer and flow did not improve the quality of the order of convergence. See section 9.1.4 for a more detailed discussion of the results from code verification.

10.2.1.2 Solution verification

Solution verification was performed on two sets of ANSR THTL experimental data. Numerical uncertainty and 95% confidence bands were calculated for the simulation results using the least squares GCI approach.

Numerical uncertainty was larger for local values than for average values of temperature. The average of the local uncertainty values calculated for k-ϵ was ±9.7% with a standard deviation of 9.2% and a maximum of 51%. For the average exit temperature, the average uncertainty was ±0.28% with a standard deviation of 0.12% and a maximum of 0.48%. Numerical uncertainty in average inlet pressure was larger at between 20 and 31%.

10.2.2 Validation

An estimated model error with an associated numerical uncertainty in that error was determined for the ANSR THTL 2D model. The size and behavior of the modeling error differed for each of the 3 experimental results to which the simulation was compared, with errors ranging from almost -37°C to 46°C. In the local cases, the uncertainty in the modeling error was dominated by the numerical uncertainty, accounting for 60% on average for the centerline temperature, 99% for the test section temperature, and 83% for the wall temperature.

The average values had smaller errors, with errors in exit temperature of less than 0.05%. The error in exit pressure was larger, at less than 5%. In the average exit temperature, the experimental uncertainty accounted for between 94%-100% of the model error uncertainty, while in the average inlet pressure the experimental uncertainty accounted for between 20% -40% of the model error uncertainty.

10.2.3 Concluding Thoughts

The model used for this V&V effort is not an entirely accurate representation of the THTL. While efforts were made to ensure the fidelity of the model to the actual THTL experiments, a number of discrepancies exist between the test and the model. The thermocouples and associated measurement hardware (and software) are not modeled. While a roughness was included in the wall functions for the k-ϵ and k-ω models, the thermal conductivity and reduced flow area caused by oxide buildup was not modeled. Additionally, the observed, though not fully explained challenges the experimenters experienced with the thermocouples were not modeled. The largest source of modeling error may have been the use of a constant heat generation rate in the model compared to joule heating of an Al 6061 test section with electrical and thermal conductivity that vary with temperature. It is possible within COMSOL to model joule heating of the test section. Doing so, however, adds additional complexity through the coupling of another physics to the problem, moving the validation effort further from the true quantity of interest.

Even if the model were a perfect representation of the ANSR THTL experiments, it would still only be a surrogate for a true validation experiment for this work. This is because the ANSR THTL differs in a number of ways from HFIR fuel plate and coolant channels. Main differences include physical dimensions, heat fluxes, energy generation densities, and flow rates. These differences suggest care must be taken in applying this model error and uncertainty to results from the narrow channel model. Additional ANSR THTL experiment results at different conditions may enable extrapolating the model error and uncertainty to some of the HFIR conditions, but thus far, the experimental results that can be found only report on inlet and outlet conditions, not temperature measurements along the length of the test section where uncertainties are greater. Additional results may also help to reduce the uncertainty in the local temperature measurements. Beyond the differences between the ANSR THTL and the HFIR, the true quantity of interest is not generically the wall temperature within a HFIR coolant channel, but rather the wall temperature over a hot spot caused by a coincident fuel segregation and non-bond. In the absence of non-bond and fuel segregation experimental data, no effort has been made to validate the hotspot portion of the hotspot model.

Other methods are available for reducing the model uncertainty if that is desired. Numerical uncertainty is the largest source of model uncertainty for the local temperature results. This is a consequence of the noisy order of convergence across the various grids used. Ideally this uncertainty could be reduced by further refining the grids. An improved grid or more controlled

grid refinement approach may make some improvement, but appear unlikely to make significant improvement based on the experience during code verification, where a structured, constant refinement ratio study resulted in noisy orders of convergence. A number of different attempts were made to improve these results as reported in section 9.1, but none were successful. Instead, reducing this uncertainty may require a better solution algorithm, or at least a significant effort working with the developers at COMSOL in identifying the source of the challenge and possible solutions.

In the average temperature results, the experimental uncertainty (as opposed to the numerical uncertainty) was responsible for the bulk of the model error uncertainty. If this uncertainty is too great, an additional experiment must be designed to bring down the experimental uncertainty.

As a final note, with all of these critiques made, the temperatures calculated, in general, were within a few degrees of each other for most of the grids at most locations and were close to the experimental data. The experimental data and the corresponding calculated values lie well within the predicted numerical uncertainty for the local temperature values. The role of V&V is to provide confidence to the decision maker and may identify priorities for improved modeling based on a thorough characterization of contributors to uncertainty.

Chapter 11 2D Narrow Coolant Channel Hotspot Sensitivity Analysis

This section describes the 2D narrow coolant channel hotspot sensitivity analysis. A brief introduction to sensitivity analysis is first provided, section 11.1. Later sections describe the purpose and goals of this analysis, section 11.2, the tools and methods used, sections 11.3 through 11.4, and the results acquired, section 11.5. A number of appendices provide more details about various aspects of the study and additional results.

11.1 Sensitivity Analysis

A sensitivity analysis (SA) seeks to determine how the variation in the output of a model depends on the uncertainty of the input parameters. Because of the different ways of viewing the variation in output and uncertainty in input, the term "SA" can convey a number of different meanings. Primary among these different meanings are the two categories of SA: local and global. Within these categories are a number of different methods and techniques that can provide different kinds of information.

11.1.1 Local Sensitivity

Local sensitivity is focused on "…the local impact of the [parameters] on the model" [97]. It is best described mathematically as

$$S_i = \frac{\partial Q}{\partial x_i}$$

where S_i is the sensitivity of Q, some quantity of interest, to x_i, an input parameter, about some value of x_i. These derivatives can be calculated directly in a forward manner, or with the use of an adjoint of the model.

11.1.2 Global Sensitivity

In global sensitivity, the sensitivity of the quantity of interest to the inputs is determined across a range of inputs. Specifically, "Global SA apportions the output uncertainty to the uncertainty in the input factors, described typically by probability distribution functions that cover the factors' ranges of existence" [97]. In essence, the global sensitivity analysis determines the effect of varying multiple parameters simultaneously while local sensitivity, as expressed by the partial derivatives of the quantity of interest, holds all but one parameter constant at a given time. This study focusses on a global SA of the 2D narrow channel hotspot model described in Chapter 8.

11.2 Purpose of this SA

The purpose of this SA is to identify the parameters that have the greatest impact on the hot side, cold side and maximum temperatures in the fuel plate. These quantities of interest are defined as follows. Hot Side Temperature: the temperature on the surface of the fuel plate directly above the center of the fuel segregation opposite from the non-bond; Cold Side Temperature: the

temperature on the surface of the fuel plate directly below the center of the fuel segregation on the same side as the non-bond; Maximum Temperature: the highest temperature within the fuel plate.

11.2.1 Input Parameters

The 2D narrow channel model contains many different parameters. An initial review of those parameters yielded 35 potential candidates. These parameters are listed in Appendix D: Parameters for Sensitivity Analysis.

A down-select from these 35 parameters to the final 18 parameters was made in conjunction with ORNL's Research Reactor Division. The final parameters used are also presented in the same appendix. In addition to the identified parameters, ranges for each parameter were identified with RRD as well.

11.2.2 Methods Used

Sandia National Lab's Dakota, a software suite for optimization, SA, and uncertainty quantification, was used to perform the sampling of the model. The following section describes Dakota and how it was implemented in this study.

11.3 Dakota

The "about" page of the Dakota website states the following:

"The Dakota toolkit provides a flexible, extensible interface between analysis codes and iterative systems analysis methods. Dakota contains algorithms for:
- optimization with gradient and non-gradient-based methods;
- uncertainty quantification with sampling, reliability, stochastic expansion, and epistemic methods;
- parameter estimation with nonlinear least squares methods; and
- sensitivity/variance analysis with design of experiments and parameter study methods.

These capabilities may be used on their own or as components within advanced strategies such as hybrid optimization, surrogate-based optimization, mixed integer nonlinear programming, or optimization under uncertainty" [98].

For this study, the sampling with sensitivity analysis is used.

11.3.1 Components

As described above, Dakota is an interface between the optimization/SA/UQ tools supplied with Dakota and a user's code. In order for the interface to work correctly, a number of components had to be coupled together. These included an input file, a BASH script, two MATLAB functions, and the narrow coolant channel COMSOL model. Each of these new components is reproduced and described below.

11.3.1.1 Dakota Input File

The Dakota input file is the set of instructions that directs Dakota what to do. This file is reproduced below.

```
#  DAKOTA INPUT FILE - input_test1.in
# This file samples a number of parameters and drives MATLAB
# which then drives comsol. It provides the results in a
# table that can be analyzed later.
# Here we use the MATLABTest1
# analysis driver that calls MATLAB for each function evaluation

environment,
        tabular_data
                tabular_data_file = 'simulation_results_tabulated.dat'
        results_output
                results_output_file = 'similation_out_simplified'
        write_restart = 'simulation_sampler.rst'

# Simulation Method for providing training points
method,
        id_method = 'SimulationMethod'
        model_pointer = 'SimulationModel'
        sampling
                seed =1234
                sample_type lhs
                samples = 380
        output verbose

# Simulation Model
model,
        id_model = 'SimulationModel'
        single
                interface_pointer = 'SimulationInterface'




variables,
        uniform_uncertain = 18
        lower_bounds 0.02    .049    0.09    0.5     0.5     19.478 0.25    0.004  0.056  0.0
        0.1     0.0     0.88    5.15    7.15    2.345   5.067   120
        upper_bounds    0.033 0.051   0.11    0.75    0.75    20.478 0.75    0.018  0.0688 1.0
        10      1000    1.12    13.081 8.425   2.8666 6.193   135
        descriptors     'Th_f'  'Th_p' 'Th_w' 'PL'    'FL_y' 'L_f'   'FL_x' 'L_fs' 'L_nb'
        'FSL_x'         'sig'   'p_nb' 'Q_f'   'Q_fs' 'v_in'  'p_out' 'k_sand' 't_in'
```

```
interface,
        id_interface = 'SimulationInterface'
        analysis_driver = 'MATLABTest1_simulator.sh'
        fork,
        parameters_file = 'params.in'
        results_file   = 'results.out'


responses,
        response_functions = 6
                descriptors 'hot' 'cold' 'max'    'NetFlux' 'NetGen' 'EngError'
        no_gradients
        no_hessians
```

The input file is divided into 6 sections: environment, method, model, variables, interface, and responses. The environment section specifies the location and format of output as well as directing the creation of a restart file. The method section indicates that sampling is performed using the Latin hypercube sampling method to take 380 samples. The random number generator is directed to use a specific seed to ensure the results are repeatable. The variables section describes the parameters that are sampled and supplied to the model as inputs. In particular, each of the parameters is described as being uniformly distributed over the range provided, though other distributions can be prescribed. The interface section provides the link to the analysis driver, in this case a BASH script that Dakota calls to run the model. Dakota provides the parameters to the model in a file called 'parameters.in' and looks for the results from the model in a file called 'results.out'. The responses section indicates that Dakota is to look for 6 responses from the model and that no gradients or hessian are provided by the model.

In effect, this input file directs Dakota to generate 380 samples of the parameters using Latin hyper cube sampling, run COMSOL and collect 6 values as responses. This input file does not direct Dakota to do anything with these results beyond saving them in a tabular format.

11.3.1.2 BASH Script
Dakota initiates a COMSOL run by calling the BASH Script below.

```
#!/bin/csh -f
# Simulator for Dakota-->MATLAB-->COMSOL
# Mike Richards 3 Nov 16
# adapted from
# bvbw 10/24/01
```

Brian M. Adams, 11/17/2005; 5/11/2009

$argv[1] is params.in.(fn_eval_num) FROM Dakota
$argv[2] is results.out.(fn_eval_num) returned to Dakota

Assuming MATLAB .m files and any necessary data are in ./
from which DAKOTA is run

Set up working directory
----

strip function evaluation number for making working directory

set num = `echo $argv[1] | cut -c 11-`

mkdir workdir.$num

copy parameters file from DAKOTA into working directory
cp $argv[1] workdir.$num/params.in

copy any necessary .m files and data files into workdir
cp MATLABTest1.m MATLABTest1_wrapper.m workdir.$num/

RUN the simulation from workdir.num
----
launch MATLAB with command mode (-r)

cd workdir.$num

echo MATLAB -nodesktop -nodisplay -nosplash -r "MATLABTest1_wrapper('params.in', 'results.out'); exit"

MATLAB -nodesktop -nodisplay -nosplash -r "MATLABTest1_wrapper('params.in', 'results.out'); exit"

----
write results.out.X and cleanup
----
mv results.out ../$argv[2]

cd ..

209

```
\rm -rf workdir.$num
```

This script is adapted from an example found in the samples supplied with Dakota. It begins by creating a working directory within which to carry out the simulation and moves all the necessary files to that directory. It copies the input parameters from Dakota and passes them into the MATLAB function described in the next section. It then moves the results file created by MATLAB back to the original directory where Dakota can collect the results. Finally it removes the working directory and its contents.

11.3.1.3 MATLAB Functions

Two MATLAB functions are used for this study. The first, reproduced below is the "wrapper" that accepts the input parameters produced by Dakota, supplies them to the second function, MATLABTest1, reproduced below as well, and returns the results. Both of these files were adapted from a simple example supplied with Dakota.

```matlab
function MATLABTest1_wrapper(params,results)

% READ params.in (or params.in.num) from DAKOTA and set MATLAB variables
%
% read params.in (no aprepro) -- just one param per line
% continuous design, then U.C. vars
% --> 1st cell of C has values, 2nd cell labels
% --> variables are in rows 2-->19
% --> row 47 contains the sample identification number
%----------------------------------------------------------------

fid = fopen(params,'r');
C = textscan(fid,'%n%s');
fclose(fid);

for i =1:18
    x(i) = C{1}(i+1);
end
run_number = C{1}(47)

%----------------------------------------------------------------
% CALL analysis code to get the function value
%----------------------------------------------------------------

[f] = MATLABTest1(x);

%----------------------------------------------------------------
% WRITE results.out
%----------------------------------------------------------------
```

```matlab
fid = fopen(results,'w');
fprintf(fid,'%20.10e %20.10e %20.10e %20.10e %20.10e %20.10e f\n', f(1),
f(2), f(3), f(4), f(5), f(6));

fclose(fid);
```

```matlab
function f = MATLABTest1(x)

    addpath('/opt/comsol/comsol52a/multiphysics/mli');
    mphstart;

    try
        model = mphopen('/home/ej4/COMSOL
Models/2DSA/NarrowChannel/NCMwHSforSA2mesh.mph');
    catch
        msg = 'error opening file'
        for i=1:6
            f(i)=NaN;
        end
        return
    end

    model.param.set('Th_f', strcat(num2str(x(1)), '[in]'), 'Thickness of
fuel');
    model.param.set('Th_p', strcat(num2str(x(2)), '[in]'), 'Thickness of the
fuel plate');
    model.param.set('Th_w', strcat(num2str(x(3)),'[in]'), 'Thickness of the
coolant channel');
    model.param.set('PL', x(4), 'How the place is centered in the coolant');
    model.param.set('FL_y', x(5), 'How the fuel is centered in the plate');
    model.param.set('L_f', strcat(num2str(x(6)),'[in]'), 'Total fuel
length');
    model.param.set('FL_x', x(7), 'How the fuel is centered left and right
within the cladding');
    model.param.set('L_fs', strcat(num2str(x(8)),'[in]'), 'length (diameter)
of fuel segregation');
    model.param.set('L_nb', strcat(num2str(x(9)),'[in]'), 'length (diameter)
of non-bond');
    model.param.set('FSL_x', x(10), 'Location of fuel segregation and non-
bond as a percentage of fuel length');
    model.param.set('sigma', strcat(num2str(x(11)), '[um]'), 'asperity
height');
    model.param.set('p_nb', strcat(num2str(x(12)), '[psi]'), 'contact
pressure');
    model.param.set('Q_f', x(13), 'heat generation multiplier');
    model.param.set('Q_fs', x(14), 'fuel segregation power generation
multiplier');
    model.param.set('V_in', strcat(num2str(x(15)),'[m/s]'), 'Fluid inlet
velocity');
    model.param.set('p_out', strcat(num2str(x(16)), '[MPa]'), 'coolant exit
pressure');
```

211

```matlab
    model.param.set('k_sand_eq', strcat(num2str(x(17)), '[um]'), 'wall
roughness in sand equivalent');
    model.param.set('T_in', strcat(num2str(x(18)),'[degF]'), 'Fluid inlet
temperature');

    try
        msg = 'I am trying'
        model.sol('sol1').run;
    catch
        msg = 'I failed'
        for j=1:6
            f(j) = NaN;
        end
        return
    end

    f(1) = model.result().numerical('pev1').getReal();
    f(2) = model.result().numerical('pev2').getReal();
    f(3) = model.result().numerical('max1').getReal();
    f(4) = model.result().numerical('gev1').getReal();
    f(5) = model.result().numerical('gev2').getReal();
    f(6) = (f(5)-f(4))/f(5);
    clear model
```

The second function gains access to the COMSOL mph commands, a series of java methods, by adding the path to those commands, and then connects to a local COMSOL server. Before this connection can be created, a local COMSOL server must be initiated. This is accomplished with the command "comsolmph" at the command line in Windows or "comsol server" in Linux. In Windows, this server will remain open as MATLAB repeatedly connects and disconnects from the server for each of the samples run by Dakota. In Linux, however, once MATLAB disconnects from the server, the server closes. To prevent this from happening, it is necessary to first connect another instance of MATLAB to the server and leave this connection open and running through Dakota's entire run.

Once connected to the server, MATLAB opens the narrow channel model, updates all of the parameters with those supplied from Dakota, and runs the simulation. The quantities of interest are then calculated within COMSOL and the results are returned to the wrapper function (which returns them to Dakota). At both opening the file and running the model, error handling is provided in case something prevents the simulation from running to completion. Examples of errors that have been observed are file permissions from an already-open COMSOL model, license errors when insufficient MATLAB or COMSOL licenses are available, and meshing errors that occur when the fuel segregation is too close to the edge of the fuel meat for the mesh to be generated. When these, or other errors occur, the function returns NaN and Dakota continues its run. Upon completion, these failed simulations are easily detected, and the simulations can be run manually to identify and correct the source of the error.

As a final note, the restart file generated by Dakota has proven very valuable. When errors occur that are not caught, Dakota shuts down. The restart file can be used to restart Dakota from where it shut down without having to repeat all of the earlier simulations.

11.3.1.4 Dakota Output
The output from this Dakota input file provides several items including the correlations between parameters and results, a table of the sample parameter values with corresponding results, and statistics about the study. Of these, the current study only uses the table of sample parameter values and results.

11.4 Post-Processing
The tabular output data from the Dakota simulation sample study were fed into SAS's JMP, a statistical analysis suite. JMP can be used to generate surrogate models (or response curves) that can be used in place of the COMSOL model to estimate the quantities of interest. The benefit of such an approach is that the surrogate model can be economically incorporated into the SSHTC or other codes where the COMSOL model cannot be. In addition to these surrogate models, JMP identifies which parameters have the largest effect on the quantities of interest.

JMP offers a number of different forms for surrogate models. Those that are ideal for interpolation and extrapolation from the parameter samples are the linear, quadratic, and cubic polynomials and the Gaussian Process model.

11.4.1 Polynomial Surrogate Models
The polynomial surrogate models are the most basic and easy to visualize of the surrogate models. They include linear, quadratic, and cubic relationships—further degree polynomials can also be computed, but the effects of interactions generally decreases quickly after the second degree. Their form is provided by the following equations

$$F_{linear}(\vec{x}) \cong c_0 + \sum_{i=1}^{n} c_i x_i$$

$$F_{quadratic}(\vec{x}) \cong c_0 + \sum_{i=1}^{n} c_i x_i + \sum_{i=1}^{n}\sum_{j>i}^{n} c_{ij}(x_i + b_i)(x_j + b_j)$$

$$F_{cubic}(\vec{x}) \cong c_0 + \sum_{i=1}^{n} c_i x_i + \sum_{i=1}^{n}\sum_{j>i}^{n} c_{ij}(x_i + b_i)(x_j + b_j)$$
$$+ \sum_{i=1}^{n}\sum_{j>i}^{n}\sum_{k>j}^{n} c_{ijk}(x_i + b_i)(x_j + b_j)(x_k + b_k)$$

213

where $\vec{x}$ is the set of parameter coordinates for the quantity of interest being estimated. As can be seen, the linear model only captures the first order effects of the parameters and does not capture the effects that result from interactions between the parameters. The quadratic model will capture second order effects due to interaction between two parameters and the cubic third order effects due to interaction between sets of three factors.

A minimum number of samples, n_c, based on the number of parameters, n, in the study, must be computed in order to develop each of these surrogates.

$$n_{c_{linear}} = n + 1$$

$$n_{c_{quadratic}} = \frac{(n+1)(n+2)}{2}$$

$$n_{c_{cubic}} = \frac{(n^3 + 6n^2 + 11n + 6)}{6}$$

11.4.2 Gaussian Process Surrogate Model
The Gaussian process surrogate model developed by JMP is given by

$$F_{Gaussian}(\vec{x}) = \mu_\mu + \sum_{i=1}^{n_c} c_i e^{\sum_{j=1}^{n} \theta_j (x_j - x_{ij})^2}$$

where μ_μ is the mean of all sample value results, c_i is the coefficient determined for each sample point, θ_i is the weight given to each of the parameters in the model, x_j is the jth parameter value in the $\vec{x}$ input, and x_{ij} is the jth parameter value of the ith sample used to develop the model. It can be seen that this equation contains $1 + n_c$ terms, and that all but one of the terms contains an exponential function that itself contains n terms. These equations are quite long (close to 90 pages at 12 point font with 380 samples and 18 parameters, for example). The Gaussian Process model requires approximately $2n_{c_{quadratic}}$ samples in order to be developed.

A step-by-step description of the process for running this study is included in Appendix E: Step-by-step of Sensitivity Analysis to aid in reproducing or modifying this effort.

11.5 Results
380 samples were run on a single node of ORNL's Libby cluster to provide $2n_{c_{quadratic}}$ samples. It took approximately 2 days to complete this study. 379 of those samples ran without incident. Sample number 378, however, threw an error. That sample places the fuel segregation at location 0.99976 (almost to the edge of the fuel meat, but not exactly at the edge). This caused the meshing operation to fail. This parameter was manually changed to 0.99925 (still within the same grid of the Latin hyper cube) and run manually. The output from all 380 samples was used

214

to develop 3 response functions: a linear polynomial, a quadratic polynomial, and a Gaussian process function.

11.5.1 Linear Polynomial

The linear polynomial response function has 19 terms, 1 for each parameter and an intercept term. The coefficient for each parameter is a statistical determination, and as such has a distribution that is treated as if it were a normal distribution. Figure 154 shows the coefficients, along with statistical information, for each of the parameters for the hot side temperature. Not included in this table is the intercept, which has a value of 151.3 K, and a standard error of 46.17 K. The figure graphically indicates the effect each parameter has on the final temperature estimate. As can be seen, the location of the fuel segregation is the most important factor in determining the temperature, this is followed by the thickness of the fuel meat, the size of the fuel segregation, the location of the fuel plate within the coolant channel (which corresponds with the coolant channel gap on one side of a fuel plate), the power level of the fuel, the power level of the fuel segregation, the inlet temperature of the water, the inlet velocity of the water, and the width of the coolant channel (which corresponds to the width of the coolant channel on both sides of a plate, or the coolant channel gap). The other parameters have small effects, and cannot be said to be statistically different from 0.

Figure 155 provides some indication of the quality of the linear surrogate model. A perfect model would have all of the observations, black dots, collapse on the solid red line. The further

Sorted Parameter Estimates

Term	Estimate	Std Error	t Ratio		Prob>|t|
FSL_x	29.802551	1.30718	22.80		<.0001*
Th_f	1455.8693	100.6406	14.47		<.0001*
L_fs	1051.6209	93.3677	11.26		<.0001*
PL	52.928708	5.230797	10.12		<.0001*
Q_f	42.943321	5.44749	7.88		<.0001*
Q_fs	1.1858629	0.164764	7.20		<.0001*
t_in	0.4600862	0.08712	5.28		<.0001*
v_in	-4.289568	1.024667	-4.19		<.0001*
Th_w	135.94928	65.37325	2.08		0.0383*
sig	0.2445551	0.132055	1.85		0.0649
FL_y	7.3255081	5.224384	1.40		0.1617
k_sand	1.1905815	1.159985	1.03		0.3054
p_nb	-0.001215	0.001307	-0.93		0.3533
L_nb	-91.73794	102.1157	-0.90		0.3696
p_out	1.5621261	2.505166	0.62		0.5333
Th_p	304.9192	653.38	0.47		0.6410
L_f	0.2002883	1.307912	0.15		0.8784
FL_x	0.3569143	2.612311	0.14		0.8914

Figure 154 Coefficients (here labeled "Estimate") for each parameter (here labeled "Term") along with statistical information sorted by significance for the linear surrogate model

215
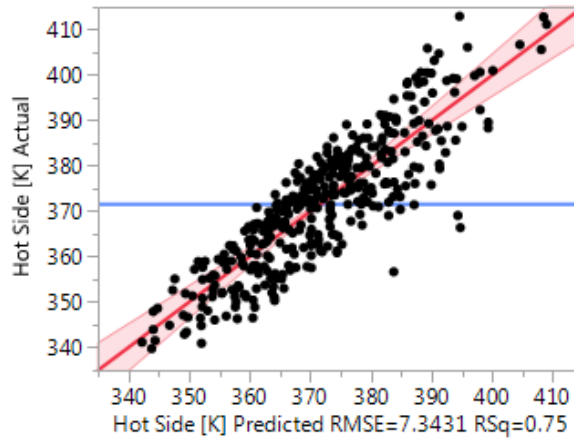
Figure 155 Linear surrogate "Predicted" versus simulation "Actual" hot side temperatures

the observations are from the red line, or the larger the number of observations that depart from it, the less trustworthy the surrogate is. The pink bands represent the 95% confidence intervals for the surrogate model and are based on the standard errors reported for the coefficients for each of the parameters. To aid in visually evaluating the model, Figure 156 plots the residuals, the difference between the temperatures determined by COMSOL and the temperature predicted by the linear surrogate. This visual quality is captured numerically in the r-squared value of 0.75.

11.5.2 Quadratic Polynomial

The quadratic polynomial response function has 190 terms, 1 for each parameter, 1 for each parameter squared, 1 term for each interaction between parameters, and an intercept term. Like with the linear polynomial, the coefficient for each parameter or combination of parameters is a statistical determination. Figure 157 shows the coefficients, along with statistical information, for each of the approximately 34 most significant parameters and combinations of parameters for the hot side temperature. Not included in this table is the intercept, which has a value of 193.5 K, and a standard error of 24.3 K. The figure graphically indicates the effect each parameter has on the final temperature estimate. As can be seen, the location of the fuel segregation is the most important factor in determining the temperature both as a primary factor and as a squared term, this is followed by the thickness of the fuel meat, the location of the fuel plate within the coolant channel (which corresponds with the width of a coolant channel on one side of a fuel plate), the size of the fuel segregation, the power level of the fuel segregation, the power level of the fuel, the inlet temperature of the water, the inlet velocity of the water, and so on. The parameters and combinations of parameters in black and those that are not included in the figure have small effects, and cannot be said to be statistically different from 0.

216
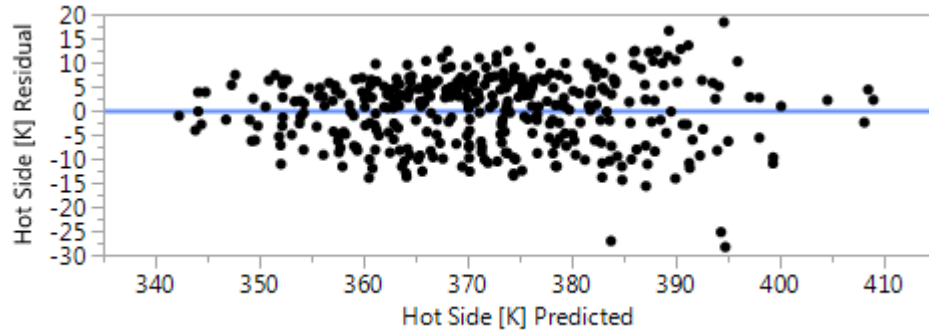
Figure 156 Residual, simulation values minus surrogate values for the linear surrogate of hot side temperature

Sorted Parameter Estimates

Term	Estimate	Std Error	t Ratio		Prob>|t|
FSL_x	29.793777	0.667497	44.64		<.0001*
(FSL_x-0.49987)*(FSL_x-0.49987)	-83.21083	2.640211	-31.52		<.0001*
Th_f	1496.5951	51.8692	28.85		<.0001*
PL	59.384043	2.517774	23.59		<.0001*
L_fs	1053.1975	53.34966	19.74		<.0001*
Q_fs	1.4387114	0.081237	17.71		<.0001*
Q_f	43.961771	2.751856	15.98		<.0001*
t_in	0.5054234	0.045378	11.14		<.0001*
v_in	-4.411863	0.512144	-8.61		<.0001*
(PL-0.625)*(FSL_x-0.49987)	66.017539	9.34223	7.07		<.0001*
(Th_f-0.0265)*(FSL_x-0.49987)	997.34774	188.6045	5.29		<.0001*
(PL-0.625)*(PL-0.625)	192.2723	41.89435	4.59		<.0001*
FL_y	11.999976	2.732609	4.39		<.0001*
(L_fs-0.011)*(Q_fs-9.11574)	73.788867	20.33853	3.63		0.0004*
(Th_w-0.1)*(FSL_x-0.49987)	-417.6124	121.5456	-3.44		0.0007*
(L_fs-0.011)*(FSL_x-0.49987)	-612.0075	181.9384	-3.36		0.0009*
(Th_f-0.0265)*(PL-0.625)	2325.2786	742.0506	3.13		0.0020*
(FL_y-0.62501)*(v_in-7.78747)	22.227373	7.443129	2.99		0.0032*
(v_in-7.78747)*(k_sand-5.62998)	-4.366844	1.497068	-2.92		0.0040*
(FL_x-0.50001)*(p_nb-500.038)	-0.013691	0.005019	-2.73		0.0070*
(Th_p-0.05)*(FL_x-0.50001)	-7009.976	2587.494	-2.71		0.0074*
(L_fs-0.011)*(Q_f-1)	1689.4766	688.9726	2.45		0.0151*
(FSL_x-0.49987)*(Q_f-1)	23.360982	9.604689	2.43		0.0159*
(FL_x-0.50001)*(k_sand-5.62998)	10.399105	4.412388	2.36		0.0195*
(FL_x-0.50001)*(p_out-2.60582)	-21.43258	9.198203	-2.33		0.0209*
(L_f-19.978)*(FSL_x-0.49987)	-5.005279	2.250565	-2.22		0.0273*
(L_fs-0.011)*(p_nb-500.038)	0.3671945	0.175205	2.10		0.0374*
(Th_f-0.0265)*(L_fs-0.011)	29404.856	14090.38	2.09		0.0382*
sig	0.1382786	0.066262	2.09		0.0382*
(Th_f-0.0265)*(FL_y-0.62501)	-1517.382	731.2261	-2.08		0.0393*
(Th_f-0.0265)*(v_in-7.78747)	-290.8514	144.23	-2.02		0.0451*
(FL_x-0.50001)*(Q_fs-9.11574)	1.2487752	0.619942	2.01		0.0454*
(Th_f-0.0265)*(Q_f-1)	1533.084	771.397	1.99		0.0483*
L_nb	104.75775	53.14603	1.97		0.0502
(Th_p-0.05)*(Th_w-0.1)	121338.05	63758.39	1.90		0.0585

Figure 157 Coefficients (here labeled "Estimate") for each parameter (here labeled "Term") along with statistical information sorted by significance for the quadratic surrogate model for hot side temperature

218

As in the linear surrogate, Figure 158 and Figure 159 give a visual indication of the quality of this model. The reported r-squared value of 0.98 provides a quantitative evaluation.

The quality of the surrogate model, as measured by its ability to predict the outcomes generated by the simulation model, improves from the linear to quadratic model. This is apparent both visually and from the r-squared values of 0.75 and 0.98. This improvement results primarily from the quadratic model's ability to capture the curvature in the heat generation profile used in the fuel meat. This can be seen in the presence of the FSL_x^2 2nd position in the list of influential terms.

To help in interpreting this model, and to give a sense of the nature of interactions between the parameters, Appendix H: Graphical Display of Parameter Interactions is provided.

11.5.3 Gaussian Process Model

The Gaussian process model has 381 terms. The first term is the mean value for the model. The remaining terms account for each sample's contribution to the model, thus with 380 samples, there are 381 terms.

Figure 160 shows "Jackknife" predicted temperatures vs simulation temperatures. The jackknife temperatures are computed by substituting the parameters for one sample into the Gaussian Process prediction equation with one modification to the equation: the term in the model that is derived from the sample point being evaluated is excluded. Technically, this is a pseudo jackknife approach. In a true jackknife, the entire Gaussian process model would be recomputed without the sample data from the specific sample being evaluated. This, however, would require 381 separate Gaussian process models being developed. The jackknife (or pseudo jackknife) approach is necessary because, by the Gaussian Process, if the sample's term in the equation were included, the predicted temperature would exactly match the sample temperature. This
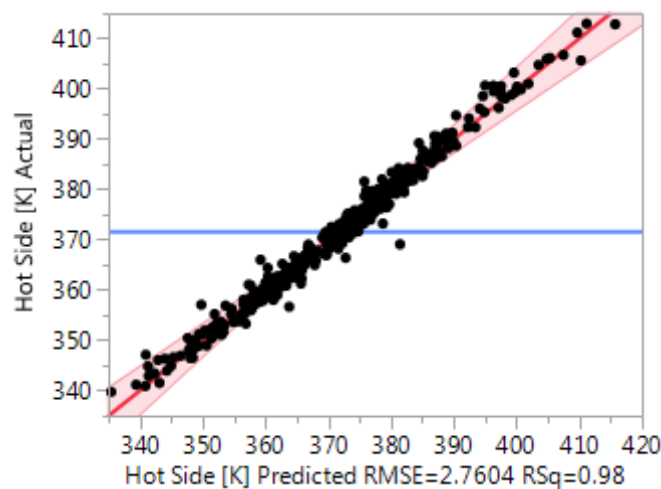
Figure 158 Quadratic surrogate "Predicted" versus simulation "Actual" hot side temperatures

219
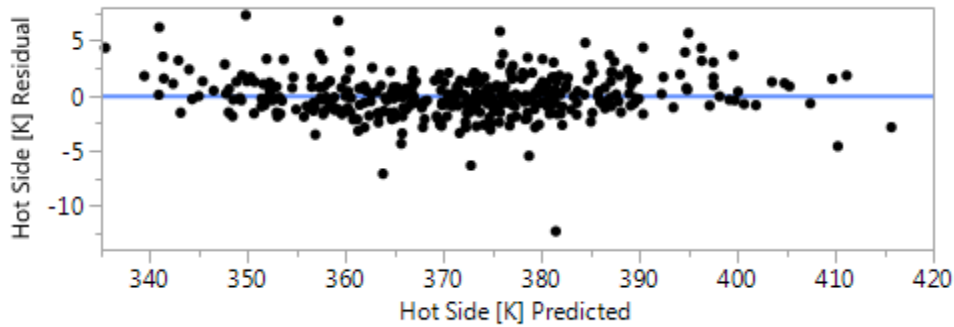
Figure 159 Residual, simulation values minus surrogate values for the quadratic surrogate of hot side temperature

means that there are no residuals for the Gaussian Process model, and that a Gaussian Process model has an r-squared of 1. These metrics are not meaningful and are thus typically not reported. For comparison sake, the difference between the pseudo-jackknife predicted temperature and the simulation temperature can be plotted, as with the residuals, as in Figure 161. This plot, however, may give the impression that the prediction model is actually worse than it is. A more robust, though more time consuming method to gathering this same kind of information is to take additional samples and compare those results to what the surrogate predicts. Because the primary purpose of this effort was to determine the most important parameters, and was not to necessarily identify the best prediction model, this work has not been done.

Table 28 lists the θ values for the parameters. It also lists the total sensitivity and the main effect of each parameter. The main effect is the portion of the variability in the temperature that can be attributed to the parameter alone. The total sensitivity is the portion of the variability that can be attributed to the parameter plus the portion that can be attributed to that parameter's interactions with other parameters (Note that the total sensitivity can, and does add up to more than 1 because it includes the sensitivity of the interactions in each of the interacting parameters' value).

The same set of information (surrogate models and their quality metrics) is provided for the Cold Side Temperature and Maximum Temperature in Appendix F: Additional Results from the Sensitivity Analysis

11.5.4 Model Comparison

When the linear, quadratic and Gaussian Process models for the hot side temperature are compared, 8 parameters as identified as significant (to the $p \leq 0.05$ level, and Total Sensitivity greater than 1%) by all 3. These 8 are FSL_x, Th_f, L_fs, PL, Q_f, Q_fs, t_in, and v_in. The linear model also includes Th_w, while the quadratic model includes FL_y by itself, and interactions that include Th_w, k_sand, Th_p, and p_nb. Each of these interactions is between
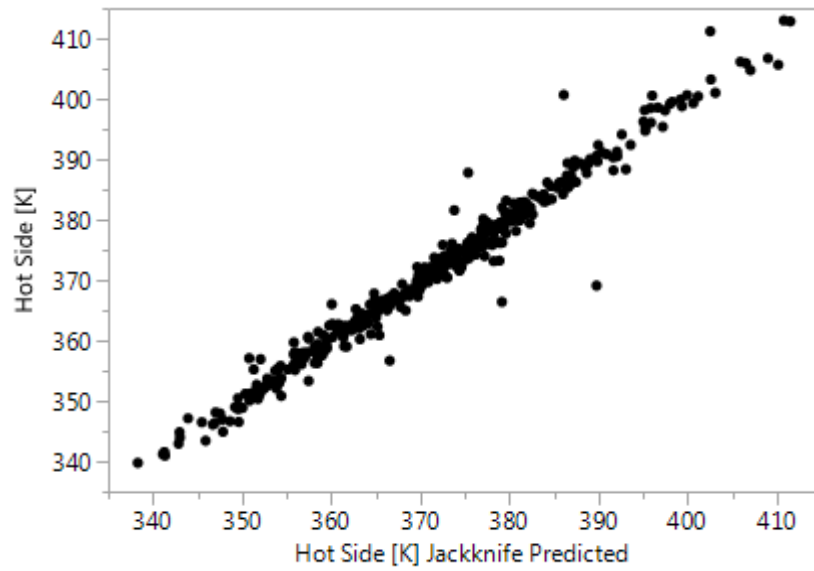
Figure 160 Gaussian Process jackknife predicted versus simulation actual hot side temperatures
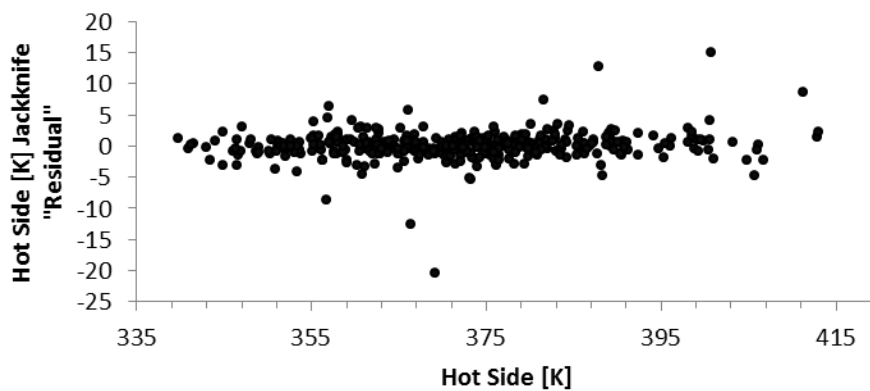
Figure 161 "Residual" plot using jackknife values from the Gaussian process prediction surrogate model

Table 28 θ values, total sensitivity and main effects for the Gaussian process prediction

Parameter	θ	Total Sensitivity	Main Effect
FSL_x	2.4115592	0.53626	0.5007244
Th_f	397.62114	0.15485	0.1435125
PL	1.8005143	0.09937	8.44E-02
L_fs	385.22104	0.09247	8.35E-02
Q_fs	0.0015378	0.06321	5.64E-02
Q_f	1.19E+00	0.0454	4.14E-02
t_in	4.41E-05	1.96E-02	1.91E-02
v_in	0.0186534	0.01199	0.010906
L_f	2.165245	0.00959	1.07E-03
Th_w	79.966795	0.00341	0.0012586
FL_y	0.0491185	0.00337	3.08E-03
k_sand	5.41E-03	9.49E-04	1.33E-04
sig	2.56E-05	0.00081	7.40E-04
Th_p	1984.0386	0.00042	0.0001772
L_nb	2.4686357	0.0003	0.0002776
p_nb	9.73E-11	0.00001	7.60E-06
FL_x	2.47E-04	0	1.44E-06
p_out	0.0002142	1.60E-06	1.50E-06

the parameter listed and one of the 8 identified by all of the models. By using the total sensitivity of the Gaussian Process model, the normalized cumulative effect of the most to the least important parameters, Table 29, can be examined. As can be seen, the first 5 parameters account for over 90% of the variation.

Making the same comparisons for the cold side temperature reveals 9 common parameters: FSL_x, Th_f, t_in, Q_f, L_fs, v_in, Q_fs, Th_w, and sig. The linear model also includes L_nb, while the quadratic model includes PL, L_nb, and p_nb by themselves and the interaction of FL_x and p_out. Considering the normalized, cumulative total sensitivity, Table 30, the first 4 parameters account for almost 90% of the total variation.

With the 3 models for maximum temperature, the following 6 parameters are significant for all: L_fs, Q_fs, Th_f, Q_f, FSL_x, PL. The linear model also includes sigma, while the quadratic model includes v_in, t_in, and p_nb by themselves, and interactions with L_nb, Th_p, FL_x, FL_y, and p_out with each other or one of the other significant parameters. Table 31 shows the total and normalized, cumulative sensitivities from the Gaussian model and indicates that the first 4 parameters are responsible for over 90% of the variation.

Table 29 Total Sensitivity and Normalized, Cumulative Total Sensitivity of the parameters for the hot side temperature

Gaussian	Total Sensitivity	Normalized Cumulative
FSL_x	0.5363	0.5147
Th_f	0.1549	0.6633
PL	0.0994	0.7586
L_fs	0.0925	0.8474
Q_fs	0.0632	0.9080
Q_f	0.0454	0.9516
t_in	0.0196	0.9704
v_in	0.0120	0.9819
L_f	0.0096	0.9911
Th_w	0.0034	0.9944
FL_y	0.0034	0.9976
k_sand	0.0010	0.9985
sig	0.0008	0.9993
Th_p	0.0004	0.9997
L_nb	0.0003	1.0000
p_nb	0.0000	1.0000
FL_x	0.0000	1.0000
p_out	0.0000	1.0000

Table 30 Total Sensitivity and Normalized, Cumulative Total Sensitivity of the parameters for the cold side temperature

Gaussian	Total Sensitivity	Normalized Cumulative
FSL_x	0.6789	0.6617
Th_f	0.1441	0.8021
t_in	0.0596	0.8601
Q_f	0.0375	0.8967
L_fs	0.0297	0.9256
v_in	0.0211	0.9462
Q_fs	0.0191	0.9648
sig	0.0118	0.9763
Th_w	0.0113	0.9872
PL	0.0052	0.9923
L_f	0.0030	0.9953
L_nb	0.0026	0.9978
p_nb	0.0019	0.9996
Th_p	0.0003	0.9999
FL_y	0.0001	1.0000
k_sand	0.0000	1.0000
FL_x	0.0000	1.0000
p_out	0.0000	1.0000

Table 31 Total Sensitivity and Normalized, Cumulative Total Sensitivity of the parameters for the maximum temperature

Gaussian	Total Sensitivity	Normalized Cumulative
L_fs	0.3848	0.3618
FSL_x	0.3109	0.6540
Q_fs	0.1900	0.8327
Th_f	0.0927	0.9198
Q_f	0.0471	0.9641
PL	0.0144	0.9776
v_in	0.0062	0.9834
sig	0.0050	0.9882
t_in	0.0036	0.9915
L_f	0.0034	0.9948
L_nb	0.0021	0.9967
Th_w	0.0020	0.9986
p_nb	0.0012	0.9998
k_sand	0.0002	1.0000
Th_p	0.0000	1.0000
FL_y	0.0000	1.0000
FL_x	0.0000	1.0000
p_out	0.0000	1.0000

Comparing the parameters' effects on the 3 different quantities of interest the following observations can be made:

- 4 of the top 5 parameters are the same for each quantity of interest.

- The location of the fuel segregation (FSL_x) is the most important for hot temperature and cold temperature and second most important for maximum temperature.

- Using the top 5 parameters for the hot side will account for 90% of the variation in hot side temperature, 85% of the variation in cold side temperature, and 93% of the variation in maximum temperature.

- Using the top 6 parameters increases the percent of variation represented to 95%, 89%, and 97%, respectively.

11.5.5 Energy Balance

In addition to the hot side, cold side, and maximum temperatures, a whole-model energy balance, reported as an error, (Energy Generated – Net Energy Flux)/Energy Generated, was provided for each simulation. The "Energy Generated" term does not include the work done by pressure changes or viscous dissipation. Figure 162 shows the distribution of these errors with both a box plot and a histogram. Table 32 shows the mean, standard deviation, minimum and maximum values, and Table 33 shows the total sensitivity and main effects, as determined from a Gaussian Process model of the energy balance error, for each of the parameters. It is interesting to note that approximately half of the variability of the error comes from the thickness of the fuel and coolant channel, and that the coolant parameters (channel thickness, inlet temperature and velocity) also account for about half of the variability.
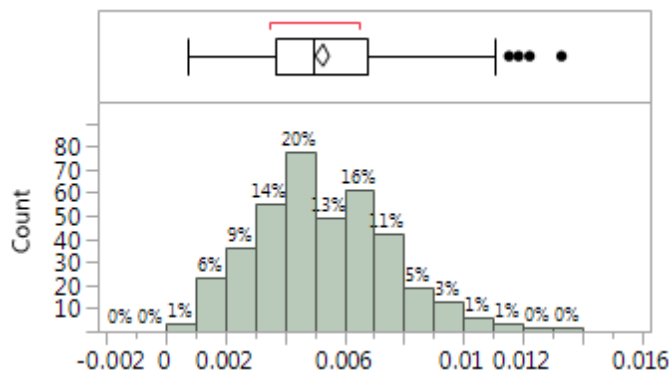
Figure 162 Distribution of energy balance errors

Table 32 Statistics for energy balance errors

Energy Balance Statistics	
Mean	0.00528
Std Dev	0.00225
maximum	0.01331
minimum	0.00075

225

Table 33 Total Sensitivity and Main Effects of the parameters on the energy balance error

Parameter	Total Sensitivity	Main Effect
Th_f	0.3263	0.3005
Th_w	0.2421	0.2092
v_in	0.1630	0.1330
t_in	0.0928	0.0814
PL	0.0791	0.0538
Q_f	0.0758	0.0699
Th_p	0.0200	0.0144
FL_x	0.0173	0.0115
L_nb	0.0096	0.0013
L_f	0.0063	0.0017
FSL_x	0.0059	0.0005
p_out	0.0041	0.0022
p_nb	0.0030	0.0004
Q_fs	0.0023	0.0002
k_sand	0.0010	0.0001
sig	0.0005	0.0005
FL_y	0.0001	0.0001
L_fs	0.0000	0.0000

11.5.6 Grid Convergence

The set of 380 samples were run at 4 different mesh density levels to determine the influence of the mesh on the surrogate models. The mesh density was controlled by a model parameter n_op which is used throughout the mesh generation. For n_op greater than 4, the number of elements present in a given mesh is approximately 2,000*n_op. In order to gain better control of mesh generation, and to reduce the calculation time, the built-in "physics controlled" mesh generation used during the development of the 2D Narrow Channel Model was replaced with a "user controlled" mesh generation sequence. This change was supported by partitioning the geometry of the original model, though all of the physics settings were left as originally described in section 8.1. The changes to the geometry construction and details of the mesh generation sequence are provided in Appendix G: Sensitivity Analysis Model and Mesh Description. All results reported previously have been from a setting of n_op = 50.

Samples were run for n_op values of 8, 16, 32, and 50. Results similar to those reported above for the other mesh densities can be found in Appendix F: Additional Results from the Sensitivity Analysis. As reported above, sample 378 causes an error at every mesh density level. FSL_x was

changed to 0.9990 for 32, 0.998 for 16, and 0.9965 for 8. For 8 this positioning takes the sample out of the required Latin hyper cube bin which runs from .99736 to 1. Sample 129 also failed for 8 due to the fuel segregation being too close to the inlet side for the mesh. FSL_x was changed from 0.002842 to 0.0035 in that case.

Table 34 lists the LogWorth (the $\log_{10}(p)$) of the parameters at each of the grids tested for the linear surrogate model, hot side temperature. This ranks the parameters by their significance in affecting the hot side temperature. In this table, the relative position of each parameter is compared to the position of that same parameter at an n_op of 50. Parameters that have moved up in position are colored red; those that have moved down are colored blue. This color coding helps to indicate that which parameters are most significant does not change as the mesh density of the COMSOL model is changed.

A similar comparison done for the quadratic hot side model is shown in Table 35. Because the quadratic model has 190 terms, only those that are significant to the $p \leq 0.05$ level were included in the table. The first 11 terms are the same at all grid levels. These terms are the same as, or combinations of the 8 most significant parameters of the linear model. The remaining terms on the table contain combinations with parameters that, by themselves, are not significant.

Table 36 presents similar information, using the total sensitivity as the comparison metric, for the Gaussian process model. It is interesting to note that the parameter L_fs, the size of the fuel segregation, has a decreasing total sensitivity level with increasing mesh density. Additionally, with the exception of PL and L_fs switching positions, all grid levels share the same 11 parameters as the most important and in the same order.

Similar tables are available for the cold side and maximum temperatures in Appendix F: Additional Results from the Sensitivity Analysis.

11.6 SA Conclusion

SA has been discussed as a general practice. Its application to plate fuel hotspots has been addressed. A sensitivity analysis involving 18 parameters and 3 quantities of interest has been performed using Dakota as a driver. A series of scripts and files have been presented that controlled the effort in deriving these results from the 2D narrow coolant channel COMSOL model. The most influential parameters for each of the quantities of interest have been identified. Three surrogate models, linear, quadratic, and Gaussian Process, have been developed and metrics indicating their fidelity to the high resolution multiphysics COMSOL model outputs have been indicated. The relationships between the models and their sensitivity to the parameters have been discussed.

An energy balance sensitivity analysis has also been performed and discussed. The average energy balance error is about 0.5% and has a range from about -0.07% to 1.33%. The surrogate

Table 34 LogWorth for each parameter at different grid refinement levels for the linear, hot side temperature.

Parameter	n_op (Grid Refinement)			
	50	32	16	8
FSL_x	71.184	73.224	71.615	70.803
Th_f	37.003	37.532	37.395	36.622
L_fs	24.695	25.242	25.15	25.575
PL	20.626	21.377	18.578	19.009
Q_f	13.418	13.805	13.459	13.747
Q_fs	11.446	11.555	11.594	11.408
t_in	6.653	6.852	6.913	6.701
v_in	4.448	4.484	4.676	4.461
Th_w	1.417	1.628	0.82	0.837
sig	1.188	1.162	1.151	1.024
FL_y	0.791	0.798	0.908	0.846
k_sand	0.515	0.528	0.501	0.486
p_nb	0.452	0.436	0.46	0.431
L_nb	0.432	0.552	0.421	0.647
p_out	0.273	0.262	0.268	0.244
Th_p	0.193	0.172	0.252	0.218
L_f	0.056	0.086	0.105	0.024
FL_x	0.05	0.072	0.047	0.133

Table 35 LogWorth for the significant (p ≤ 0.05) parameters at each of the grid refinement levels for the quadratic, hot side temperature.

	n_op						
50		**32**		**16**		**8**	
FSL_x	101.934	FSL_x	101.779	FSL_x	102.003	FSL_x	102.609
FSL_x*FSL_x	76.663	FSL_x*FSL_x	75.118	FSL_x*FSL_x	76.358	FSL_x*FSL_x	77.23
Th_f	70.631	Th_f	70.059	Th_f	71.301	Th_f	71.133
PL	57.62	PL	57.453	PL	54.005	PL	55.517
L_fs	47.177	L_fs	47.289	L_fs	48.812	L_fs	49.368
Q_fs	41.357	Q_fs	40.65	Q_fs	41.62	Q_fs	42.065
Q_f	36.251	Q_f	35.617	Q_f	36.458	Q_f	37.054
t_in	21.774	t_in	21.475	t_in	22.858	t_in	22.639
v_in	14.571	v_in	13.971	v_in	15.602	v_in	14.307
PL*FSL_x	10.533	PL*FSL_x	10.83	PL*FSL_x	9.947	PL*FSL_x	10.918
Th_f*FSL_x	6.471	Th_f*FSL_x	6.899	Th_f*FSL_x	6.48	Th_f*FSL_x	6.481
PL*PL	5.094	PL*PL	5.053	FL_y	4.928	PL*PL	5.605
FL_y	4.729	FL_y	3.715	PL*PL	4.7	FL_y	4.854
L_fs*Q_fs	3.435	L_fs*FSL_x	3.409	Th_w*FSL_x	4.14	Th_w*FSL_x	3.846
Th_w*FSL_x	3.139	L_fs*Q_fs	3.402	L_fs*Q_fs	3.952	L_fs*Q_fs	3.807
L_fs*FSL_x	3.032	Th_f*PL	3.172	L_fs*FSL_x	3.386	L_fs*FSL_x	3.505
Th_f*PL	2.699	Th_w*FSL_x	3.168	FL_y*v_in	2.429	Th_f*PL	2.69
FL_y*v_in	2.495	v_in*k_sand	2.236	Th_f*PL	2.267	FL_y*v_in	2.413
v_in*k_sand	2.402	FSL_x*Q_f	1.998	FL_x*p_nb	2.204	Th_p*FL_x	2.368
FL_x*p_nb	2.157	Th_p*FL_x	1.93	Th_p*FL_x	2.152	FL_x*p_nb	2.047
Th_p*FL_x	2.133	FL_x*k_sand	1.925	L_f*FSL_x	2.047	L_f*FSL_x	1.955

Table 36 Total sensitivity for parameters at different grid refinement levels for the Gaussian Process, hot side temperature.

	n_op			
	50	32	16	8
FSL_x	0.536256	0.528123	0.538401	0.541638
Th_f	0.154853	0.154116	0.155125	0.156389
PL	0.099366	0.095213	0.087946	0.088471
L_fs	0.092467	0.096974	0.098946	0.10317
Q_fs	0.063211	0.063549	0.064047	0.060197
Q_f	0.045403	0.045752	0.045208	0.047014
t_in	0.019588	0.020284	0.021627	0.022709
v_in	0.011985	0.013777	0.012931	0.011491
L_f	0.009594	0.01161	0.008549	0.003848
Th_w	0.003406	0.005025	0.003401	0.003676
FL_y	0.003369	0.003146	0.003277	0.003661
k_sand	0.000949	0.001557	0.000878	0.000004
sig	0.000806	0.000862	0.000657	0.000193
Th_p	0.000419	0.00029	0.000079	0.000192
L_nb	0.000299	0.000453	0.000382	0.000004
p_nb	0.000015	0.000119	0.000002	0.000007
FL_x	0.000002	0.00023	0.000007	0
p_out	0.000002	0.000155	0.000001	0.000001

model's sensitivity to mesh density has been examined. The order of the significant parameters did not change with changing grid density, with a single exception where 2 adjacent parameters switched places.

These results provide insight into the physics by themselves, as well as informing the development of future fuel plate designs by helping to identify which parameters are most critical to the quantities of interest. The 5 most influential parameters account for approximately 90% of the variation in the quantities of interest.

A number of additional tables and figures have been provided in the appendices.

Chapter 12 Conclusion

This dissertation presents the development and characterization of a 2d narrow channel fuel plate hotspot model. The role and importance of research reactors is discussed. Efforts towards converting from HEU to LEU in research reactors, both domestic and international, are described. The HFIR, in particular, is examined including its history and current operating characteristics. The manufacturing process of HFIR fuel is explicated.

12.1 Original Contributions

This work fills out a portion of the hotspot modeling landscape initially developed with the incipience of the HFIR. The consolidation of legacy and modern hotspot modeling work enables the identification of areas for further refinement as well as introduction of new approaches. These areas include the use of thermal contact conductance for non-bonds in place of assuming them to be adiabatic, the modeling of turbulent flow in place of constant convective heat transfer coefficients, verification and validation of the model to estimate model uncertainty, and an analysis of model sensitivity to guide further investigation and develop surrogate models.

The reported assessment of COMOL's thin layer and thermal contact features, Chapter 7, supports the use of thermal contact conductance in non-bond modeling. The application and use of thermal contact conductance in non-bond models, replacing the adiabatic disc used by previous investigators, removes some of the conservatism of earlier models.

Verification, Chapter 9, and validation, Chapter 10, of a fuel plate model in general, and a hotspot model in particular provide new information for uncertainty reduction and increased levels of confidence in the results of simulations. Within code verification, a number of original manufactured solutions are used to evaluate COMSOL. Single physics evaluations are first performed followed by multiphysics evaluations. Verification of the conduction heat transfer using the method of manufacture solutions returned an excellent convergence performance, as presented in section 9.1.1. The observed degradation of convergence performance in heat transfer when coupled with flow physics illustrates the potentially deleterious effect of multiphysics coupling and the need to verify the coupling in addition to the individual physics, as discussed in section 9.1.4. Solution verification, section 9.2, provides a relatively pessimistic view of the numerical uncertainty in the local temperature results as a result of the code convergence behavior. Validation provides an estimate of the model error with uncertainty from a surrogate experiment. This systematic approach to multiphysics V&V provides a framework for future work on plate fuel including LEU program models.

A sensitivity analysis of the hotspot model, Chapter 11, provides insight into the physics controlling the hotspot. Identifying the most significant parameters of the model, section 11.5, provides future researchers with the areas that account for the largest portions of uncertainty. A

grid refinement study on the sensitivity, section 11.5.6, indicates that the largest sources of uncertainty in the hotspot model are independent of mesh density. A process is demonstrated whereby the results from the sensitivity analysis are used to generate simple surrogate models of the high resolution, multiphysics hotspot model, and the quality of the surrogate models are evaluated. Surrogate models may be used in conjunction with the steady state heat transfer code to better represent hot spot influence on operating limits.

12.2 Future Work

While this work advances the state of hotspot modeling, there remains a number of avenues to improve the accuracy of the model. These efforts can be divided into a few broad categories: improving the model, reducing the numerical uncertainty, and reducing the experimental uncertainty.

Improving the model includes expanding from 2d into a 3d curved fuel plate model. This would allow for the 3d power profile that shows variation across the width of a fuel plate as well as the varying thickness of the fuel meat. Incorporating solid mechanics would enable accounting for changes in coolant channel dimensions due to thermal expansion, better estimates of contact stress in the thermal contact model, and distortions due to fluid structure interactions. Moving beyond steady-state and into time-dependent studies would enable examination of the effects of fission gas build-up in non-bonds, allowing conductivity assessment during the addition of interstitial material and likely concomitant lowering of the contact pressure. Additionally, time studies could investigate oxide build up, particularly with temperature dependence as the oxide may more significantly influence the hotspot temperatures. The changes in material properties with irradiation over time, thermal conductivities, mechanical properties, and swelling, for example, may also affect the thermal contact conductance.

Besides including additional physics in the model, including more accurate information in the model would also represent an improvement. Gathering more information about the nature of non-bonds and fuel segregation by dissecting fuel plates that have known defects would help to provide some of this information. Experimentation with non-bonds may enable better selection of thermal contact conductance models. Experimentation with fuel segregations may provide better information about their effect on heat generation.

A number of avenues exist for reducing numerical uncertainty. As mentioned in section 9.1.4, working with COMSOL to improve the observed orders of convergence in grid refinement is likely to yield the greatest decrease in numerical uncertainty. Additionally, further work in code verification remains to be done by including non-constant material properties, more turbulence models, as well as devising more accurate methods to include derivatives of discontinuities in the method of manufactured solutions in COMSOL.

Finally, reducing experimental uncertainty can be accomplished though experiments designed to validate the HFIR fuel plate models in general, and non-bonds and fuel segregations in particular. By performing uncertainty analysis as part of the design of experiment, the experiment can be developed such that it minimizes uncertainty.

List of References

1. World Nuclear Association, "Research Reactors," http://www.world-nuclear.org/info/Non-Power-Nuclear-Applications/Radioisotopes/Research-Reactors/

2. United States Nuclear Regulatory Commission, "Backgrounder on Research and Test Reactors," http://www.nrc.gov/reading-rm/doc-collections/fact-sheets/research-reactors-bg.html

3. IAEA-tecdoc-1715 (2013), "Commercial Products and Services of Research Reactors," Vienna, Austria: International Atomic Energy Agency.

4. Division of Physical and Chemical Sciences (2010), "Research Reactors: Purpose and Future," Vienna, Austria: International Atomic Energy Agency.

5. International Atomic Energy Agency, "Research Reactors Database," https://nucleus.iaea.org/RRDB/RR/ReactorSearch.aspx.

6. "Neutron Scattering," (2015), In Wikipedia, the Free Encyclopedia. https://en.wikipedia.org/wiki/Neutron_scattering

7. Lane, James A. (1958), "Aqueous Homogeneous Reactors," Oak Ridge, TN: Oak Ridge National Laboratory.

8. Nuclear Fuel Cycle and Material Division (2008), "Homogeneous Aqueous Solution Nuclear Reactors for the Production of Mo-99 and other Short Lived Radioisotopes," Vienna, Austria: International Atomic Energy Agency.

9. General Atomics, "Triga®Nuclear Reactors," http://www.ga.com/triga

10 Oak Ridge National Laboratory, "High Flux Isotope Reactor," https://neutrons.ornl.gov/hfir

11. Oak Ridge National Laboratory, "High Flux Isotope Reactor Technical Parameters," http://neutrons.ornl.gov/hfir/parameters

12. Oak Ridge National Laboratory, High Flux Isotope Reactor Core Assembly," http://neutrons.ornl.gov/hfir/core-assembly

13. Xoubi, N., & Primm III, R. T. (2005), "Modeling of the High Flux Isotope Reactor Cycle 400," ORNL/TM-2004/251, Oak Ridge National Laboratory, Oak Ridge, Tennessee.

14. Morris, D. G., & Wendel, M. W. (1993), "High Flux Isotope Reactor System Relap 5 Input Model," ORNL/TM-11647, Oak Ridge National Laboratory, Oak Ridge, Tennessee.

15. Stapleton, D. R., (1992), "A Brief History of the Research Reactors Division of Oak Ridge National Laboratory," ORNL/M-2342, Oak Ridge National Laboratory, Oak Ridge, Tennessee.

16. US Department of Energy, "Neutron Scatter Facilities," http://science.energy.gov/bes/suf/user-facilities/neutron-scattering-facilities/hfir/

17. Phys.org (2014), "High Flux Isotope Reactor named Nuclear Historic Landmark," http://phys.org/news/2014-09-high-flux-isotope-reactor-nuclear.html

18. Selby, D. L. (2007), "Status of the High Flux Isotope Reactor and the reactor scientific upgrades program," Vienna, Austria: International Atomic Energy Agency

19. Hewlett, R. G., & Holl, J. M. (1989), *Atoms for peace and war, 1953-1961.*

20. Loukianova, A., & Hansell, C. (2008), "Leveraging US policy for a global commitment to HEU elimination," *Nonproliferation Review*, *15*(2), 159-183.

21. Travelli, A. (1999), "Progress of the RERTR Program in 1999," In *Proceedings of the XXII International Meeting on Reduced Enrichment for Research and Test Reactors, Budapest, Hungary* (pp. 3-8).

22. Kuperman, A. J., & Leventhal, P. L. (1998), "HEU Core Conversion of Russian Production Reactors: A Major Threat to the International RERTR Regime." In 1*st International Meeting of RERTR, Sao Paulo, Brazil*

23. Glaser, A., & von Hippel, F. (2002), "On the importance of ending the use of heu in the nuclear fuel cycle: An updated assessment," In *2002 International Meeting on Reduced Enrichment for Research and Test Reactors (RERTR), San Carlos de Bariloche, Argentina.*

24. NNSA, (2006)''Research Reactor at University of Florida Has Been Converted,'' October 18, 2006

25. Margarita Jimenez, (2013), "USA and Europe: High-Power Research Reactors," *Nuclear Terrorism and Global Security: The Challenge of Phasing Out Highly Enriched Uranium*, eds. Alan J. Kuperman, Abingdon: Routledge: 2013

26. A. M. Saliba-Silva, E. F. Urano de Carvalho, H. G. Riella and M. Durazzo (2011). "Research Reactor Fuel Fabrication to Produce Radioisotopes," *Radioisotopes - Applications in Physical Sciences*, Prof. Nirmal Singh (Ed.), ISBN: 978-953-307-510-5.

27. Van den Berghe, S., Leenaers, A., Koonen, E., & Sannen, L. (2011, January). "From high to low enriched uranium fuel in research reactors," In *Advances in Science and Technology* (Vol. 73, pp. 78-90).

28. Knight, R. W., & Morin, R. A. (1999), "Fabrication procedures for manufacturing High Flux Isotope Reactor fuel elements-2," No. ORNL-6852, Oak Ridge National Laboratory, Oak Ridge, TN.

29. Primm III, R. T., Moses, D. L., Gehin, J. C., Ellis, R. J., & Binder, J. L. (2005), "Overview of High Flux Isotope Reactor Design Bases Relevant to Possible Conversion to Low-Enriched Uranium," In *2005 International Meeting on Reduced Enrichment for Research and Test Reactors (RERTR), Boston* (pp. 6-10).

30. Rothrock, R. B., Hale, R. E., Knight, R. W., & Cheverton, R. D. (1995), "Enhanced HFIR overpower margin through improvements in fuel plate homogeneity inspection," Oak Ridge National Laboratory, Oak Ridge, TN.

31. Bowden, G. A., Knight, R. W. (1984), "Specifications for High Flux Isotope Reactor Fuel Elements HFlR-FE-3," Oak Ridge National Laboratory, Oak Ridge, TN.

32. Hilvety, N., & Chapman, T. G. (1967), "HFIR Fuel Element Steady State Heat Transfer Analysis," ORNL-TM—1903, Oak Ridge National Laboratory, Oak Ridge, TN.

33. Kirkpatrick, J. R. (1990), "Calculations for HFIR Fuel Plate Non-Bonding and Fuel Segregation Uncertainty Factors," Oak Ridge National Laboratory, Oak Ridge, TN.

34. McLain, H. A. (1967), "HFIR Fuel Element Steady State heat Transfer Analysis Revised Version," ORNL-TM—1904, Oak Ridge National Laboratory, Oak Ridge, TN.

35. Giles Jr, G. E. (1997). "Local analysis technique for the advanced neutron source reactor fuel defect studies," *Nuclear technology*, 117(3), 306-315.

36. Bodey, I. T. (2014). "Thermal Hydraulic Characteristics of Fuel Defects in Plate Type Nuclear Research Reactors," University of Tennessee, Knoxville, TN.

37. Madhusudana, C. V., & Madhusudana, C. V. (1996), *Thermal contact conductance*, New York: Springer-Verlag.

38. Yovanovich, M. M. (2005), "Four decades of research on thermal contact, gap, and joint resistance in microelectronics," *Components and Packaging Technologies, IEEE Transactions on*, 28(2), 182-206.

39. Mantelli, M. B. H., & Yovanovich, M. M. "16 Thermal Contact Resistance," In Gilmore, D. (Ed) *Spacecraft Thermal Control Handbook, Volume I: Fundamental Technologies*, Reston, VA: American Institute of Aeronautics and Astronautics.

40. Jackson, R. L., Ghaednia, H., Elkady, Y., Bhavnani, S. H., & Knight, R. W. (2012), "A closed-form multiscale thermal contact resistance model," *Components, Packaging and Manufacturing Technology, IEEE Transactions on*, 2(7), 1158-1171.

41. Jackson, R. L., Bhavnani, S. H., & Ferguson, T. P. (2008), "A multiscale model of thermal contact resistance between rough surfaces," *Journal of Heat Transfer*, 130(8), 081301.

42. Mikic, B. (1971), "Analytical studies of contact of nominally flat surfaces; effect of previous loading," *Journal of Tribology*, 93(4), 451-456.

43. Lambert, M. A., & Fletcher, L. S. (1997), "Review of models for thermal contact conductance of metals," *Journal of Thermophysics and Heat Transfer*, 11(2), 129-140.

44. Song, S., & Yovanovich, M. (1988), "Relative contact pressure-Dependence on surface roughness and Vickers microhardness," *Journal of thermophysics and heat transfer*, 2(1), 43-47.

45. Bahrami, M., Culham, J. R., & Yovanovich, M. M. (2004), "Modeling thermal contact resistance: a scale analysis approach," *Journal of heat transfer*, 126(6), 896-905.

46. Jackson, R. L., & Streator, J. L. (2006), "A multi-scale model for contact between rough surfaces," *Wear*, 261(11), 1337-1347.

47. Jackson, R. L. (2010), "An analytical solution to an Archard-type fractal rough surface contact model," *Tribology Transactions*, 53(4), 543-553.

48. Nix, W. D., & Gao, H. (1998), "Indentation size effects in crystalline materials: a law for strain gradient plasticity," *Journal of the Mechanics and Physics of Solids*, 46(3), 411-425.

49. Milanez, F. H., Culham, J. R., & Yovanovich, M. M. (2002), "Experimental study on the hysteresis effect of thermal contact conductance at light loads," In *Proceedings of the 40th AIAA Aerospace Science Meeting Exhibit*.

50. Prasher, R. (2005), "Predicting the thermal resistance of nanosized constrictions," *Nano letters*, 5(11), 2155-2159.

51. Li, Y. Z., Madhusudana, C. V., & Leonardi, E. (2000), "On the enhancement of the thermal contact conductance: effect of loading history," *Journal of heat transfer*, 122(1), 46-49.

52. Wahid, S. M., & Madhusudana, C. V. (2003), "Thermal contact conductance: effect of overloading and load cycling," *International journal of heat and mass transfer*, 46(21), 4139-4143.

53. Gopal, V., Whiting, M. J., Chew, J. W., & Mills, S. (2013), "Thermal contact conductance and its dependence on load cycling," *International Journal of Heat and Mass Transfer*, 66, 444-450.

54. Hahn, D. W., & Ozisik, M. N. (2012), *Heat conduction*, John Wiley & Sons.

55. Jiji, L. M., & Jiji, L. M. (2006), *Heat convection,* New York: Springer.

56. Bailly, C., & Comte-Bellot, G. (2015), *Turbulence*, Springer International Publishing

57. Dewan, A. (2010), *Tackling Turbulent Flows in Engineering,* Springer Science & Business Media.

58. Cousteix, T. C. J. (2005), *Modeling and Computation of Boundary-Layer Flows*.

59. van Driest, E.R., (1956), "On Turbulent Flow near a Wall," *J. Aeronautical Sciences*, 23(11), 1007-1011.

60. Spalding, D.B. (1961), "A Single Formula for the Law of the Wall," *J. Appl.Mech.*, 28, 455-457.

61. Reichardt, H. (1951), "Die Grundlagen des Turbulenten Wärmeübergange (Fundamentals of Turbulent Heat Transfer)," *Arch. Gesamte Waermetech*. 2, 129-142.

62. Coles, D. (1956), "The Law of the Wake in the Turbulent Boundary Layer," *J. Fluid Mech.,*1, 191.

63. Whitfield, D.L.(1979), "Analytical Description of the Complete Turbulent Boundary Layer Velocity Profile," *J. AIAA,* 17(10), 1145-1147.

64. Cebeci, T. (2004), *Analysis of Turbulent Flows*, Elsevier, London.

65. Michel, R., Quemard, C, and Durant, R.. (1969), "Application d'un schema de longueur de melange a I'etude des couches limites d'equilibre," *ONERA Note Technique* No. 154.

66. Johnson, D.A. and King, L.S. (1985), "Mathematically Simple Turbulence Closure Model for Attached and Separated Turbulent Boundary Layers," *AIAA J.,* Vol. 23, no. 11, pp. 1684-1692, 1985.

67. Johnson, D.A. and Coakley, T.J. (1990), "Improvement to a Nonequilibrium Algebraic Turbulence Model," *AIAA J.,* 28(11), 2000-2003.

68. Cebeci, T. and Chang, K.C. (1996), "An Improved Cebeci-Smith Turbulence Model for Boundary-Layer and Navier-Stokes Methods," *20th Congress of the International Council of the Aeronautical Sciences,* paper no. ICAS-96-1.7.3, Sorrento, Italy, September 8-13.

69. Baldwin BS, Lomax H. (1978), "Thin-layer approximation and algebraic model for separated flows," *AIAA paper* 78–257, Huntsville.

70. Yakhot, V., Orszag, S.A., Thangam, S., Gatski, T.B., Speziale, C.G. (1992) "Development of turbulence for shear flows by a double expansion technique," *Phys. Fluids* A 4(7), 1510–1520.

71. Shih T-H, Liou WW, Shabbir A, Zhu J. (1995), "A new k-e eddy-viscosity model for high Reynolds number turbulent flows—model development and validation," *Comput Fluids* 24(3), 227–238

72. Kolmogorov, A.N. (1942), "Equations of turbulent motion of an incompressible fluid," *Izvestia Acad. Sci. USSR Phys.* 6(1–2), 56–58

73. Spalding, D.B. (1991), "Kolmogorov's two-equation model of turbulence," *Proc. Roy. Soc. Lond.* A 434, 211–216

74. Menter FR (1994), "Two equation eddy viscosity turbulence models for engineering applications," *AIAA J* 32(8),1598–1605

75. Cho JR, Chung MK (1992), "A k–e–c equation turbulence model," *J Fluid Mech* 237,301–322

76. Dewan A, Arakeri JH (2000), "Use of k–e–c model to predict intermittency in turbulent boundary layers," *ASME J Fluids Eng* 122(3), 542–546

77. Pathak M, Dewan A, Dass AK (2007), "Effect of streamline curvature on flow field of a turbulent plane jet in crossflow," *Mech Res Commun* 34(3), 241–248

78. Smagorinsky J (1963), "General circulation experiments with the primitive equations I. The basic experiment," *Mon Weather Rev* 91, 99–165

79. Germano M, Piomelli U, Moin P, Carbott WH (1991), "A dynamic subgrid scale eddy viscosity model," *Phys Fluids* 3(7), 1760–1765

80. Bardina J, Ferziger JH, Reynolds WC (1980), "Improved subgrid scale models for large eddy simulation," *AIAA J* 80, 1357

81. Dorfman, A. S. (2009), *Conjugate Problems in Convective Heat Transfer,* CRC Press.

82. Dorman, A. S. (2013). *Classical and Modern Engineering Methods in Fluid Flow and Heat Transfer: An Introduction for Engineers and Students*, Momentum Press.

83. Gambill, W. R., & Bundy, R. D. (1961), "HFIR heat-transfer studies of turbulent water flow in thin rectangular channels," ORNL-3079, Oak Ridge National Laboratory, Oak Ridge, TN.

84. Tschaepe, L., Ruggles, A. E., Freels, J. D., & Primm, R. T. (2009), "Evaluation of HFIR LEU Fuel Using the COMSOL Multiphysics Platform," ORNL/TM-2008/188, Oak Ridge National Laboratory, Oak Ridge, TN.

85. *COMSOL Multiphysics Reference Manual*, COMSOL 5.2.

86. *CFD Module User's Guide*, COMSOL 5.2.

87. *Heat Transfer Module User's Guide*, COMSOL 5.2.

88. Freels, J. D., & Jain, P. K. (2011), "Multiphysics Simulations of the Complex 3D Geometry of the High Flux Isotope Reactor Fuel Elements Using COMSOL," In *COMSOL Conference, Boston*.

89. Freels, J. D., Bodey, I. T., Arimilli, R. V., & Lowe, K. T. (2010), "Two-Dimensional Thermal Hydraulic Analysis and Benchmark in Support of HFIR LEU Conversion using COMSOL," ORNL/TM-2010/18, Oak Ridge National Laboratory, Oak Ridge, TN.

90. Roy, C. J., Nelson, C. C., Smith, T. M., & Ober, C. C. (2004), "Verification of Euler/Navier–Stokes codes using the method of manufactured solutions," *International Journal for Numerical Methods in Fluids*, 44(6), 599-620.

91. Eça, L., Hoekstra, M., Hay, A., & Pelletier, D. (2007), "A manufactured solution for a two-dimensional steady wall-bounded incompressible turbulent flow," *International Journal of Computational Fluid Dynamics*, 21(3-4), 175-188.

92. Roache, P. J. (2009), *Fundamentals of verification and validation*. Socorro, New Mexico: Hermosa.

93. Eça, L., & Hoekstra, M. (2014), "A procedure for the estimation of the numerical uncertainty of CFD calculations based on grid refinement studies," *Journal of Computational Physics*, 262, 104-130.

94. Felde, D. K., Farquharson, G., Hardy, J. H., King, J. F., McFee, M. T., Montgomery, B. H., ... & Wood, R. J. (1994). "Advanced neutron source reactor thermal-hydraulic test loop facility description," ORNL/TM—12397, Oak Ridge National Laboratory, Oak Ridge, TN.

95. Seli, Hazman, Awang, Mokhtar, Ismail, Ahmad Izani Md., Rachman, Endri, & Ahmad, Zainal Arifin. (2013), "Evaluation of properties and FEM Model of the Friction welded mild Steel-Al6061-Alumina," *Materials Research*, *16*(2), 453-467. Epub December 18, 2012. Retrieved October 03, 2016, from http://www.scielo.br/scielo.php?script=sci_arttext&pid=S1516-14392013000200022&lng=en&tlng=en

96. Siman-Tov, M., Felde, D. K., McDuffee, J. L., & Yoder, G. L. (1995), "Experimental study of static flow instability in subcooled flow boiling in parallel channels," In *Proceedings of 4th ASME/JSME Thermal Engineers Joint Conference, Maui, HI*.

97. Saltelli, Andrea, Karen Chan, and E. Marian Scott, eds. *Sensitivity analysis*. Vol. 1. New York: Wiley, 2000.

98. Sandia Dakota, "About," https://dakota.sandia.gov/content/about

Appendices

Appendix A: Least Squares GCI

The following MATLAB code was developed using MATLAB version R2014a:

```
clear;
clc;
%Use this to calculate "observed" order of convergence. Based on Eca
%Eca & Hoekstra 2014 "A procedure for the estimation of numerical error
global fi h w n

%Enter Values from Simulation
fi = [321.26
320.49
311.53
315.33
311.94
];

h = [     %Enter the normalized grid sizes
3.693357542
2.248127808
1.360744481
1.200558053
0.853135188
];

w = (1./h)./(sum(1./h)); %weighting factors

n = size(fi,1);    %number of grids used

%Enter initial guesses for variables
alpha = 1;
p = 1;
fi_0 = fi(n-1);

x_0 = [alpha, fi_0, p];
options = optimoptions('fsolve', 'MaxFunEvals',100000, 'MaxIter',100000,
'TolFun', 1.0e-8);

%Solve For RE
func = @S_RE;
[x_0,blank,exitcheck] = fsolve(func,x_0, options);
alpha = x_0(1);
fi_0 = x_0(2);
p = x_0(3);
sigma_RE = sqrt(sum((fi-(fi_0+alpha*h.^p)).^2)/ (n-3));

%Solve For RE_w
func_w = @S_RE_w;
x_0_w = x_0;
[x_0_w, blank, exitcheck_w] = fsolve(func_w,x_0_w, options);
alpha_w = x_0_w(1);
fi_0_w = x_0_w(2);
```

```matlab
p_w = x_0_w(3);
sigma_RE_w = sqrt(sum(n*w.*(fi-(fi_0_w+alpha_w*h.^p_w)).^2)/ (n-3));


%Check convergence level and calculate the error estimate (epsilon)
if (p >=0.5 && p <=2) && (p_w >=0.5 && p_w <=2) %if 0.5<= p & p_w<=2
    if sigma_RE_w < sigma_RE %choose the smaller standard deviation
        epsilon = alpha_w*h.^p_w;
        p = p_w;
        sig = sigma_RE_w;
        fi_0 = fi_0_w;
        p_calc = p;
    else
        epsilon = alpha*h.^p;
        sig = sigma_RE;
        p_calc = p;
    end
elseif p >=0.5 && p <= 2 %if 0.5<= p <=2, but p_w is not
    epsilon = alpha*h.^p;
    sig = sigma_RE;
    p_calc = p;
elseif p_w >=0.5 && p_w <= 2 %if 0.5<= p_w <=2, but p is not
    epsilon = alpha_w*h.^p_w;
    p = p_w;
    sig = sigma_RE_w;
    fi_0 = fi_0_w;
    p_calc = p;
else %p and p_w are too big or too small, so we have to calculate epsilon
     %for an assumed p = 1 and p = 2

    %Solve for S1 (note the need to add in the n's not included in Eca)
    A1 = [n*1 n*sum(h); sum(h) n*sum(h.^2)];
    B1 = [sum(fi); sum(fi.*h)];
    x1 = A1\B1;
    sigma_c(1) = sqrt(sum((fi-x1(1)+x1(2)*h).^2)/(n-2));
    %now with weights
    A1_w = [1 sum(w.*h); sum(w.*h) sum(w.*h.^2)];
    B1_w = [sum(w.*fi); sum(w.*fi.*h)];
    x1_w = A1_w\B1_w;
    sigma_c(2) = sqrt(sum(n*w.*(fi-x1_w(1)+x1_w(2)*h).^2)/(n-2));

    %Solve for S2
    A2 = [n*1 n*sum(h.^2); sum(h.^2) n*sum(h.^4)];
    B2 = [sum(fi); sum(fi.*h.^2)];
    x2 = A2\B2;
    sigma_c(3) = sqrt(sum((fi-x2(1)+x2(2)*h.^2).^2)/(n-2));
    %now with weights
    A2_w = [1 sum(w.*h.^2); sum(w.*h.^2) sum(w.*h.^4)];
    B2_w = [sum(w.*fi); sum(w.*fi.*h.^2)];
    x2_w = A2_w\B2_w;
    sigma_c(4) = sqrt(sum(n*w.*(fi-x2_w(1)+x2_w(2)*h.^2).^2)/(n-2));

    %build comparison (_c) variables
    alpha_c = [x1(2) x1_w(2) x2(2) x2_w(2)];
    fi_c = [x1(1) x1_w(1) x2(1) x2_w(1)];
```

```matlab
    p_c = [1 1 2 2 1 1];

    %calculate epsilon for p too big or too small or unfindable
    if p > 2 &&  or(exitcheck ~= 0, exitcheck_w ~= 0)
        for i =1:4
            if sigma_c(i) == min(sigma_c) %use the smallest std dev
                epsilon = alpha_c(i)*h.^p_c(i);
                sig = sigma_c(i);
                fi_0 = fi_c(i);
                p_calc = p_c(i);
            end
        end
    else
        %Solve for S12
        A12 = [n*1 n*sum(h) n*sum(h.^2); sum(h) n*sum(h.^2) n*sum(h.^3);
sum(h.^2) sum(h.^3) n*sum(h.^4)];
        B12 = [sum(fi); sum(fi.*h); sum(fi.*h.^2)];
        x12 = A12\B12;
        sigma_c(5) = sqrt(sum((fi-x12(1)+x12(2)*h+x12(3)*h.^2).^2)/(n-3));
        %Solve for S12 with weights
        A12_w = [1 sum(w.*h) sum(w.*h.^2); sum(w.*h) sum(w.*h.^2)
sum(w.*h.^3); sum(w.*h.^2) sum(w.*h.^3) sum(w.*h.^4)];
        B12_w = [sum(w.*fi); sum(w.*fi.*h); sum(w.*fi.*h.^2)];
        x12_w = A12_w\B12_w;
        sigma_c(6) = sqrt(sum(n*w.*(fi-
x12_w(1)+x12_w(2)*h+x12_w(3)*h.^2).^2)/(n-3));
        %assign values for for-statement
        alpha_c(5) = x12(2);
        alpha_c(6) = x12_w(2);
        fi_c(5) = x12(1);
        fi_c(6) = x12_w(1);
        alpha_c12 = [0 0 0 0 x12(3) x12_w(3)];
        %compare d1, d2, and d12
        for i =1:6
            if sigma_c(i) == min(sigma_c)
                epsilon = alpha_c(i)*h.^p_c(i)+alpha_c12(i)*h.^2;
                sig = sigma_c(i);
                fi_0 = fi_c(i);
                p_calc = i + 10;
            end
        end
        %calculate epsilon for p too small
    end
end

%Determine data range parameter (delta_fi)
delta_fi = (max(fi)-min(fi))/(n-1);

%Determine the factor of safety (Fs)
if (p >=0.5 && p <=2) && sig < delta_fi
    Fs = 1.25;
else
    Fs = 3;
end
```

```matlab
%Calcualte U95
if sig < delta_fi
    U95 = Fs*epsilon + sig + abs(fi-fi_0);
    U95(n+1) = sig;
    U95(n+2) = p_calc;
else
    U95 = Fs*(sig/delta_fi)*(epsilon + sig + abs(fi-fi_0));
    U95(n+1) = sig;
    U95(n+2) = p_calc;
end


****Functions****

function F = S_RE(x)
global h fi n

F(1) = (n*sum(fi.*h.^x(3)) - sum(fi)*sum(h.^x(3))) / (n*sum(h.^(2*x(3))) -
sum(h.^x(3))^2)- x(1);
F(2) = (sum(fi) - x(1)*sum(h.^x(3)))/n - x(2);
F(3) = sum(fi.*h.^x(3).*log(h)) - x(2)*sum(h.^x(3).*log(h)) -
x(1)*sum(h.^(2*x(3)).*log(h));
end


function F = S_RE_w(x)
global h fi w

F(1) = (sum(w.*fi.*h.^x(3)) - sum(w.*fi)*sum(w.*h.^x(3))) /
(sum(w.*h.^(2*x(3))) - sum(w.*h.^x(3))^2)- x(1);
F(2) = (sum(w.*fi) - x(1)*sum(w.*h.^x(3))) - x(2);
F(3) = sum(w.*fi.*h.^x(3).*log(h)) - x(2)*sum(w.*h.^x(3).*log(h)) -
x(1)*sum(w.*h.^(2*x(3)).*log(h));
end
```

Appendix B: Numerical Uncertainty Plots for THLT k-ω and SST

k-ω quad plots of simulation results with uncertainty

In each of the following quad plots, the same format is used as was used in section 9.2.3.2: showing all 5 grids (top left), without extremely fine grid (top right), without normal grid (bottom left), and the minimum uncertainties from the 3 other combinations (bottom right).
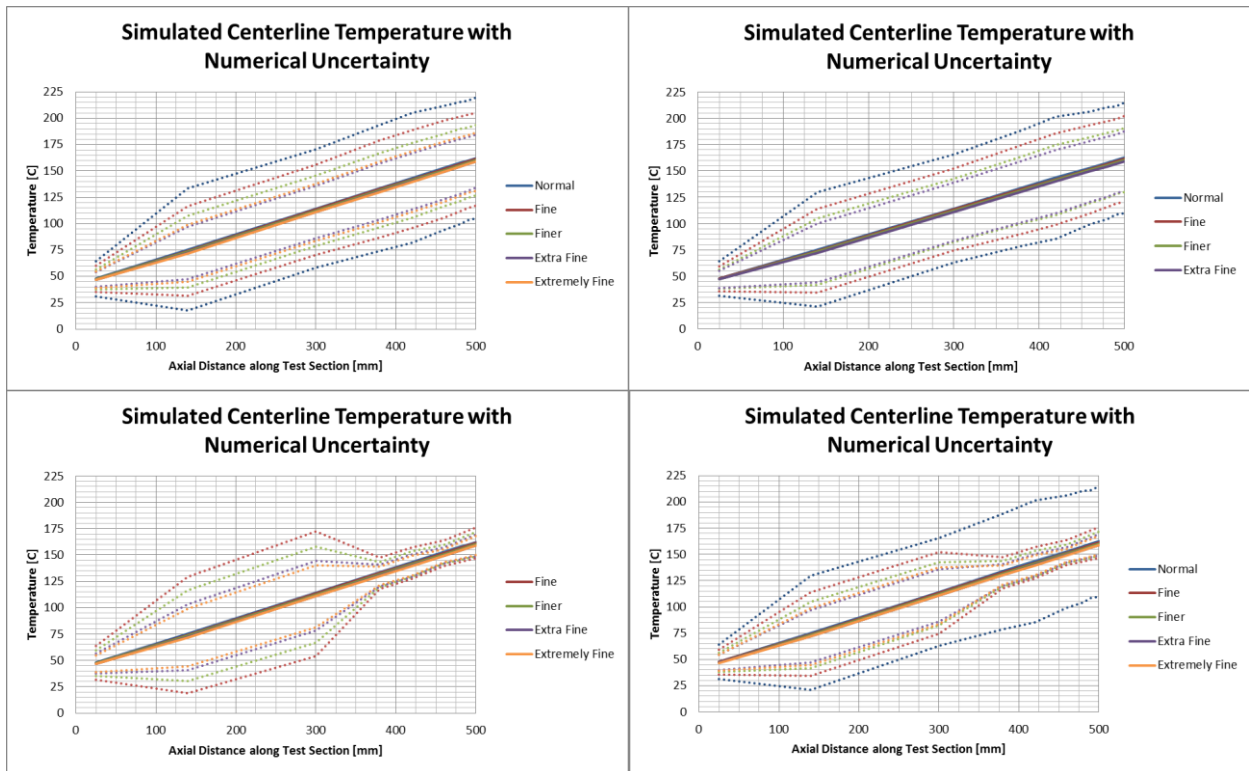
Figure 163 Numerical uncertainty (±U$_{95\%}$) in k-ω centerline temperature for different grids

248
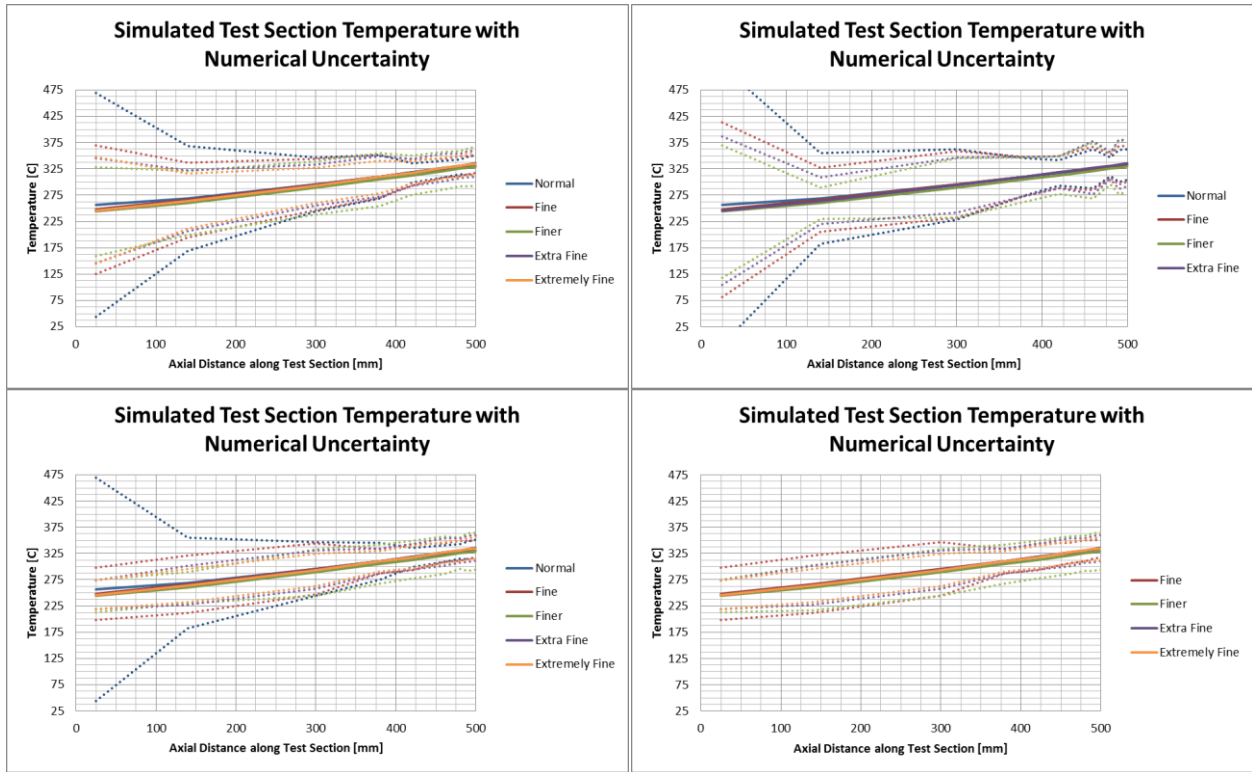
Figure 164 Numerical uncertainty (±U_{95%}) in k-ω test section temperature for different grids
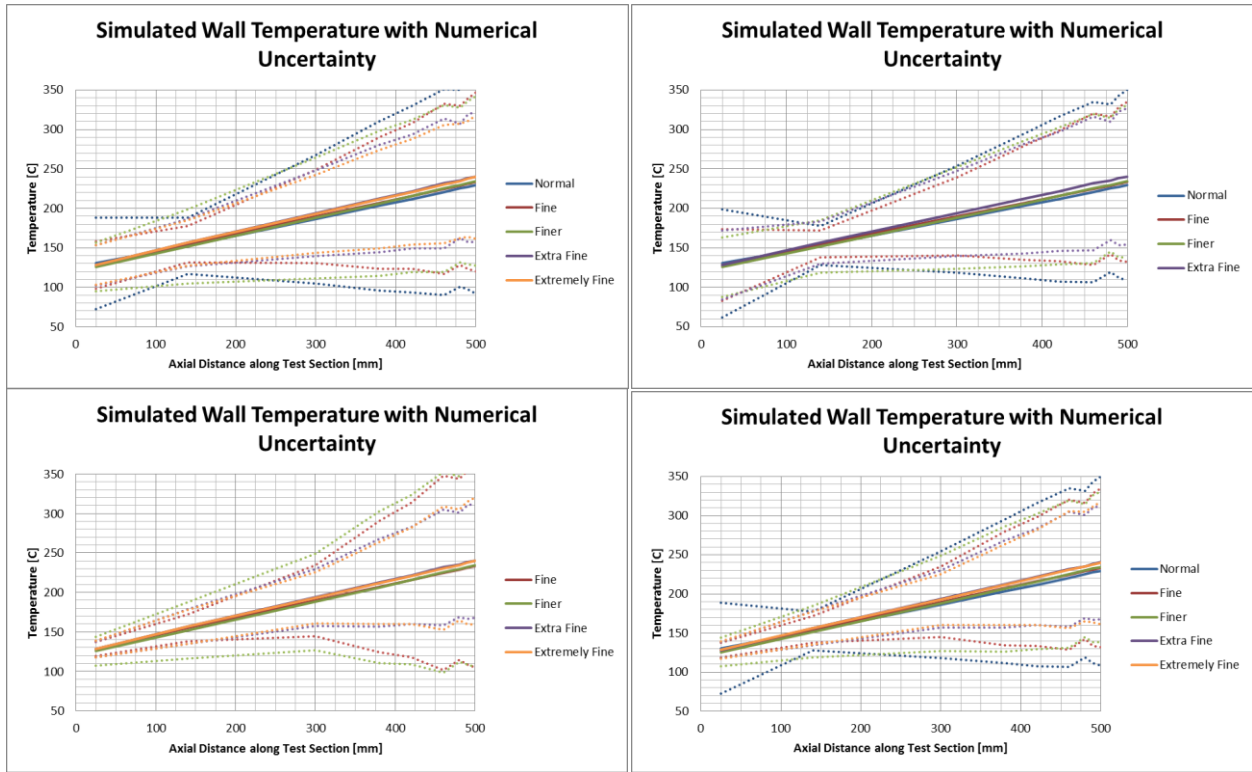
Figure 165 Numerical uncertainty (±U$_{95\%}$) in k-ω wall temperature for different grids

SST quad plots of simulation results with uncertainty
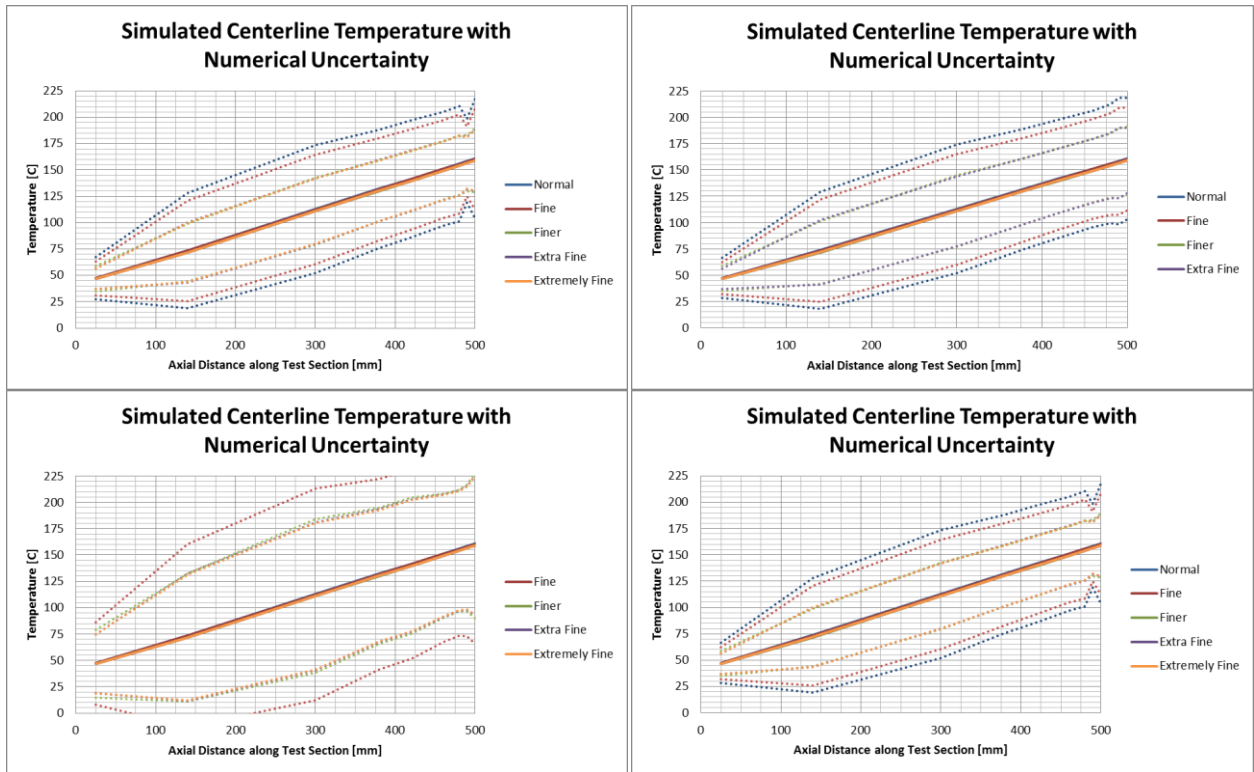
Figure 166 Numerical uncertainty ($\pm U_{95\%}$) in SST centerline temperature for different grids

251
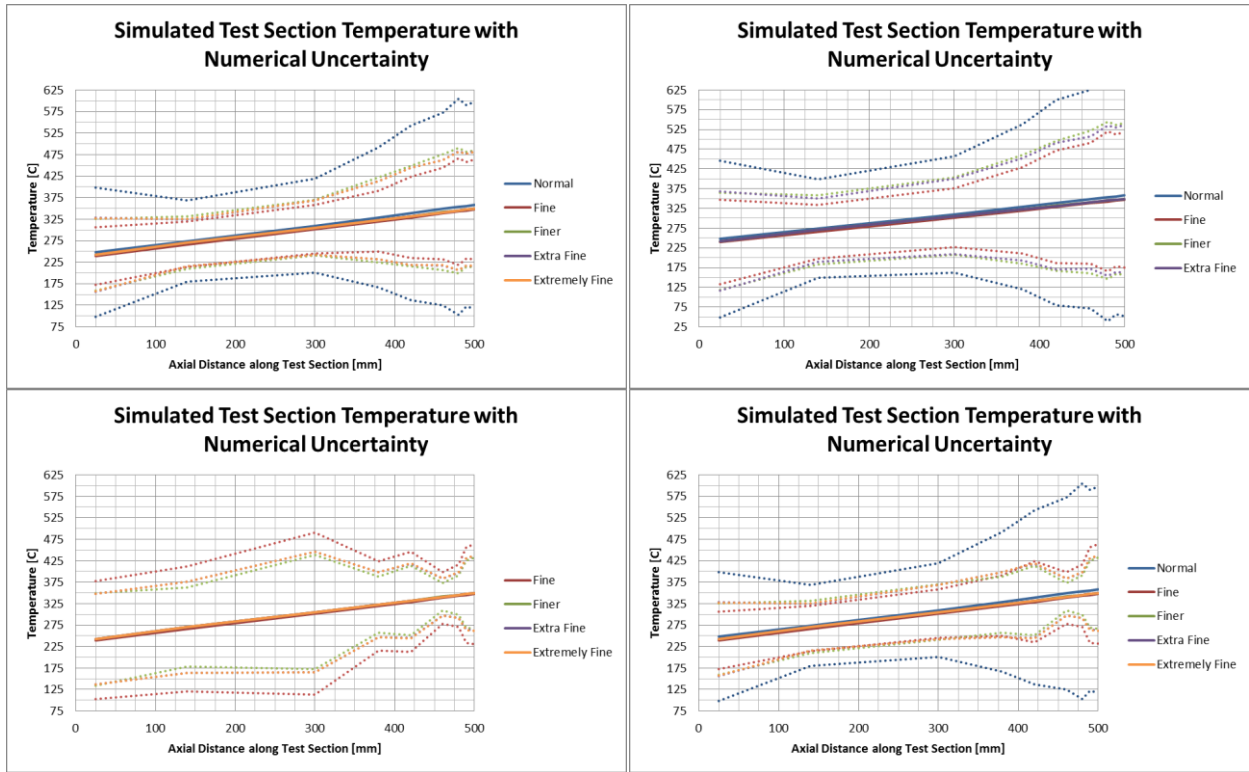
Figure 167 Numerical uncertainty (±$U_{95\%}$) in SST test section temperature for different grids
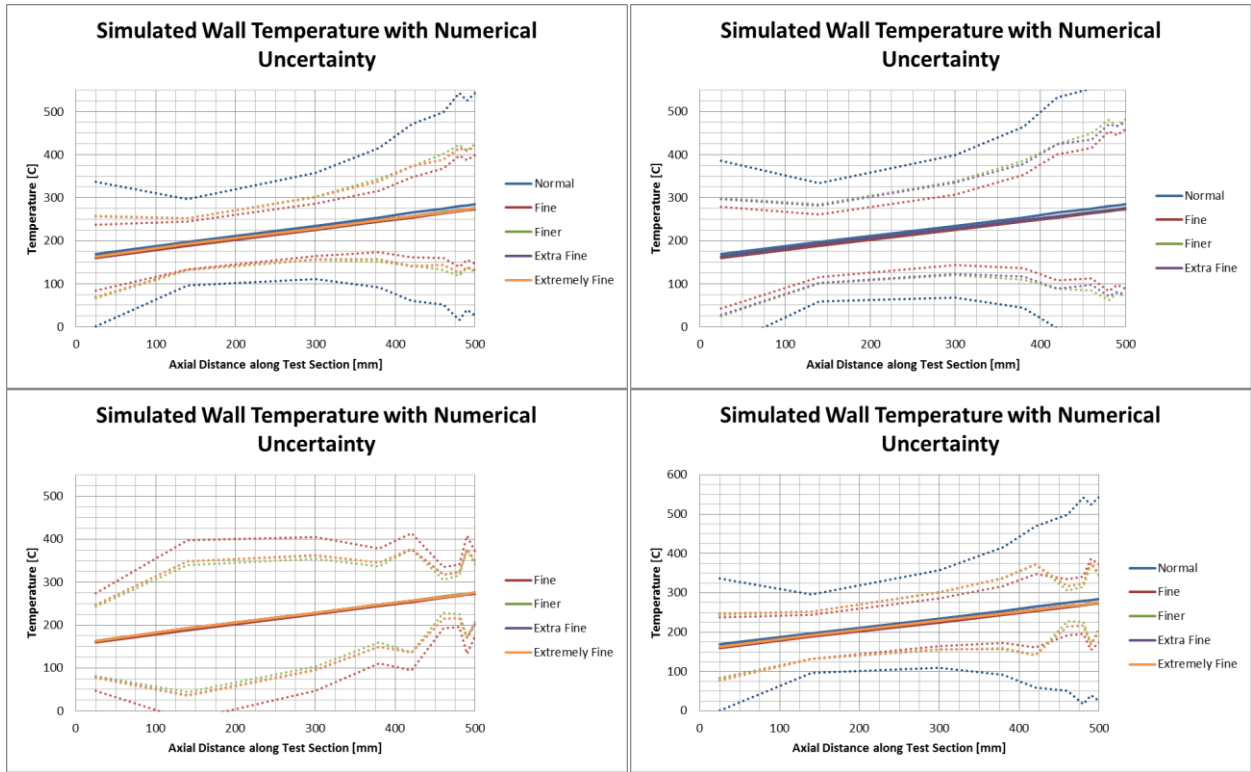
Figure 168 Numerical uncertainty ($\pm U_{95\%}$) in SST wall temperature for different grids

253

Appendix C: Model Error and Uncertainty Plots for THTL

k-ω Quad Plots

The following quad plots use the same format as use previously: showing all 5 grids (top left), without extremely fine grid (top right), without normal grid (bottom left), and the minimum uncertainties from the 3 other combinations (bottom right).
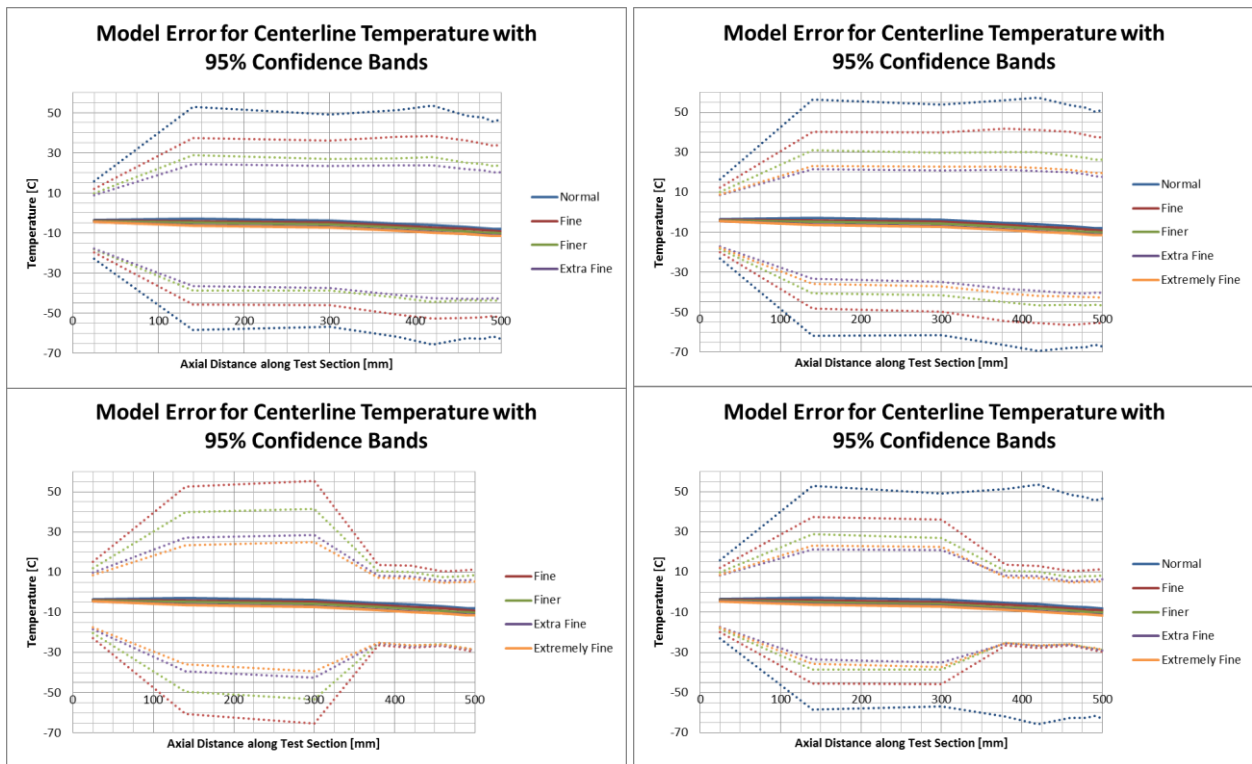
Figure 169 Modeling error with ±U₉₅% confidence intervals for k-ω centerline temperature
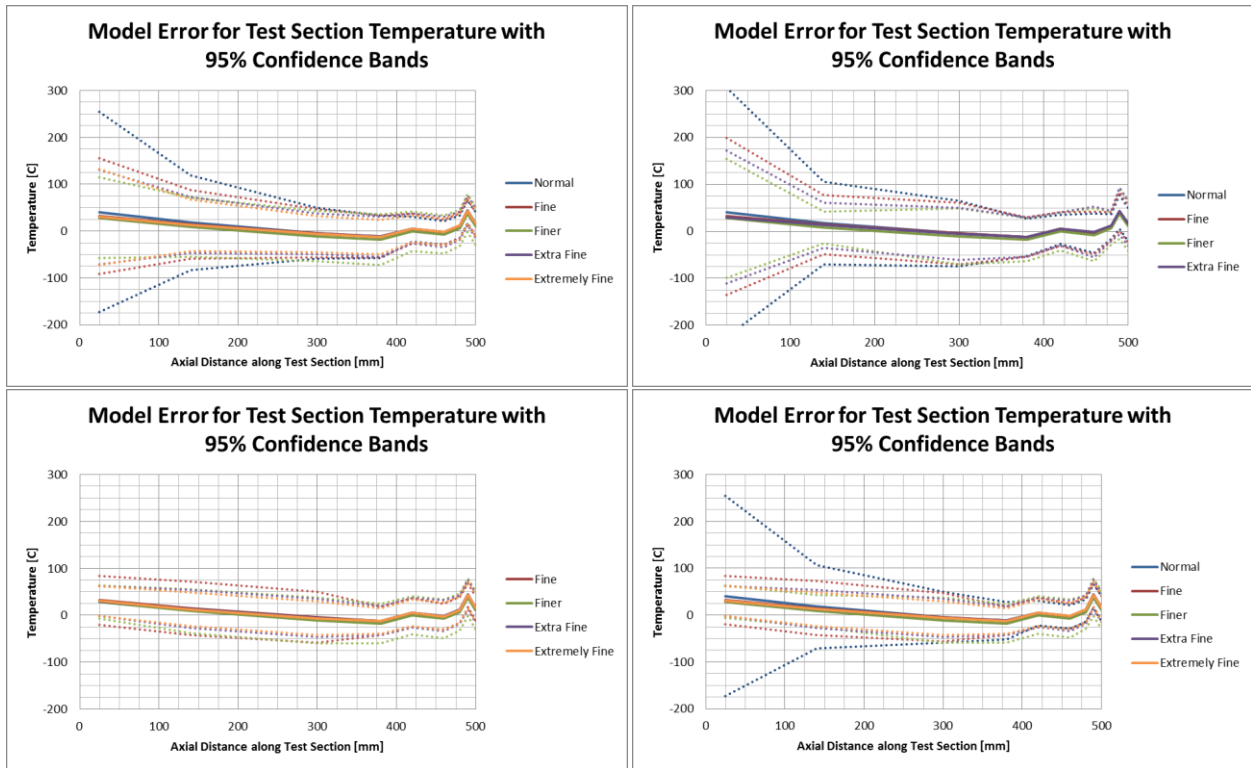
Figure 170 Modeling error with $\pm U_{95\%}$ confidence intervals for k-ω test section temperature
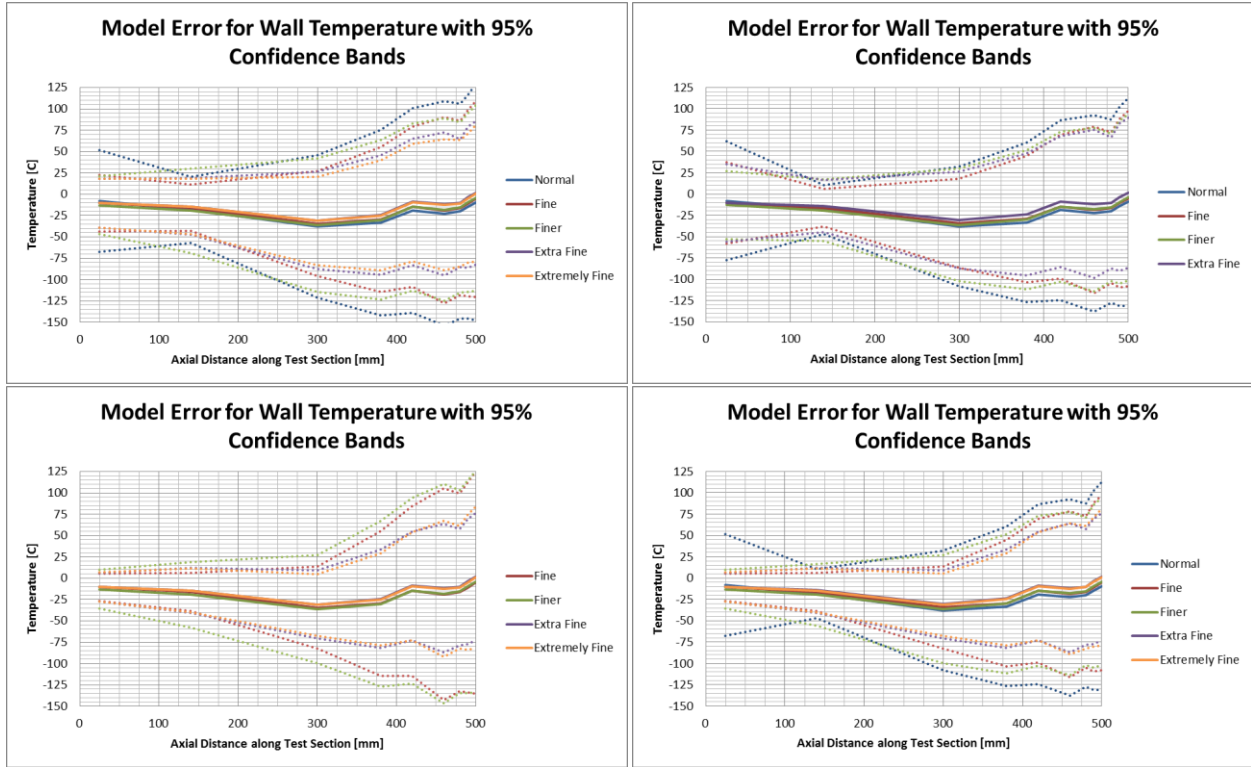
Figure 171 Modeling error with ±U$_{95\%}$ confidence intervals for k-ω wall temperature

SST Quad Plots
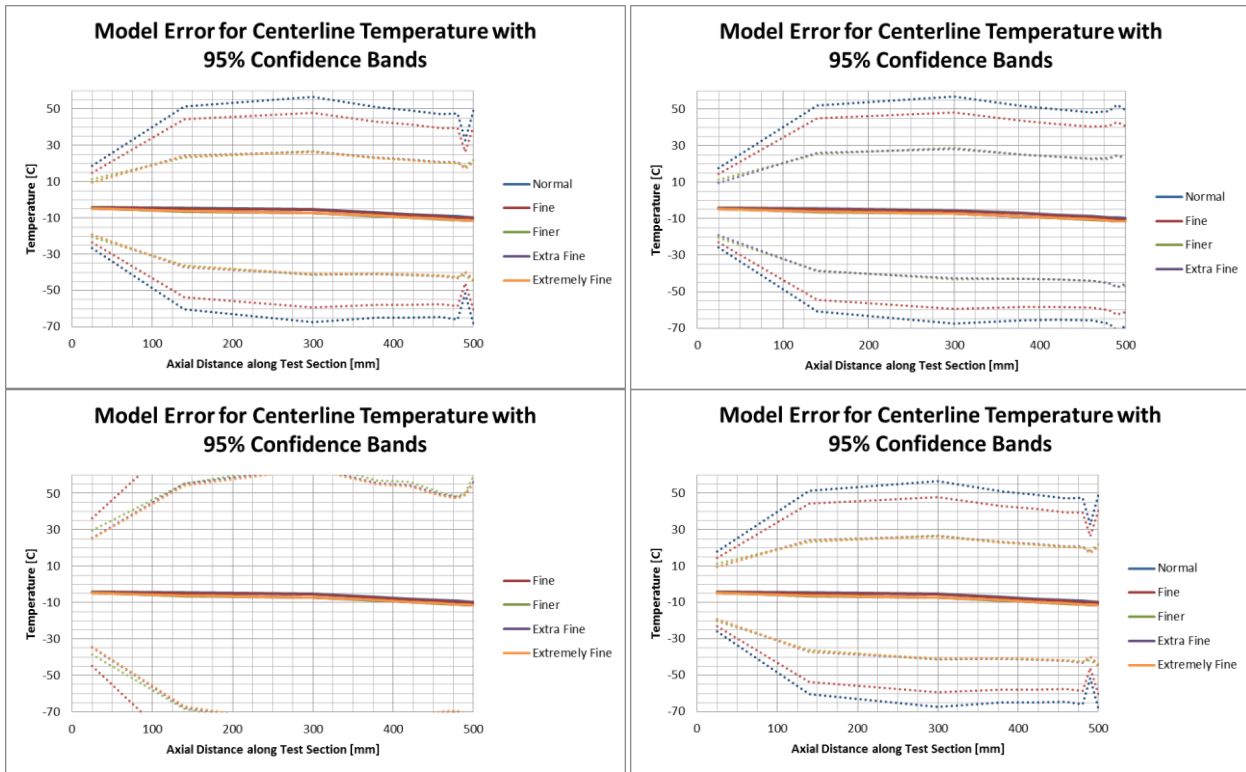
Figure 172 Modeling error with ±U$_{95\%}$ confidence intervals for SST centerline temperature

257
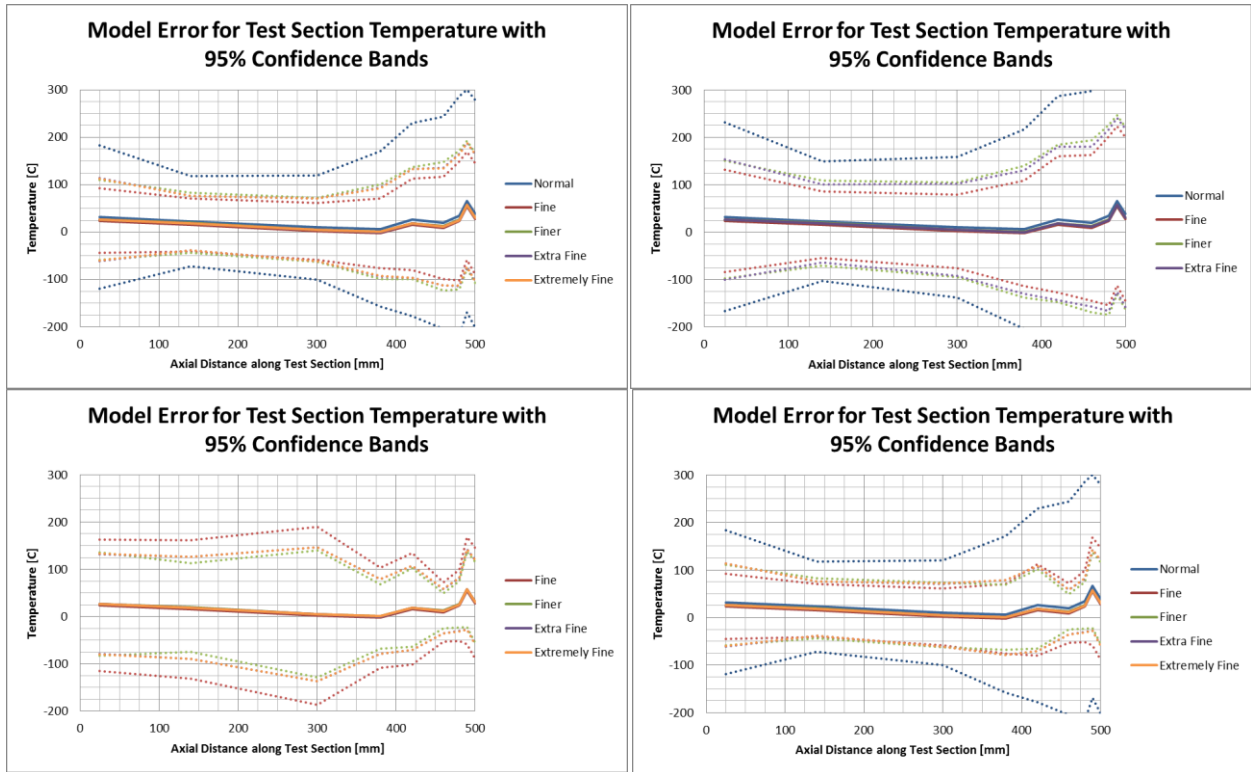
Figure 173 Modeling error with ±U$_{95\%}$ confidence intervals for SST test section temperature
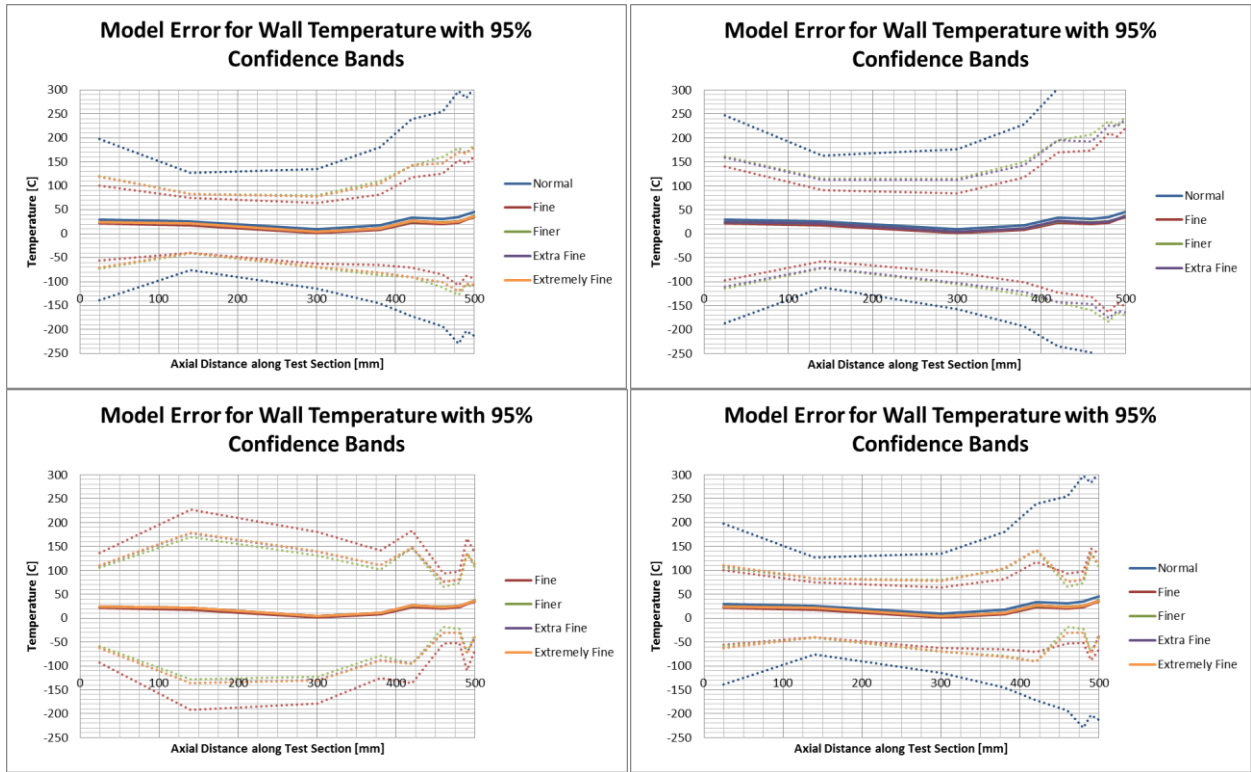
Figure 174 Modeling error with $\pm U_{95\%}$ confidence intervals for SST wall temperature

Appendix D: Parameters for Sensitivity Analysis

Table 37 List of potential parameters for sensitivity analysis

Category			Parameter	Nominal Value	Unit	Brief Description
Geometry	Thicknesses		Th_f	0.03	in	Thickness of the fuel
			Th_p	0.05	in	Thickness of the fuel plate
			Th_w	0.1	in	Thickness of coolant channel
			Th_fs	0.03	in	Thickness of a fuel segregation
			PL	0	%	How the plate is centered within the coolant
			FL_y	0	%	How the fuel is centered within the cladding
	Lengths		L_f	20	in	Length of the fuel
			P_f	24	in	Length of the cladding
			FL_x	0	%	How the fuel is centered within the cladding
			L_fs	0.0082	in	Length (radius) of the fuel segregation
			L_nb	0.0625	in	Length (radius) of the non-bond
			FSL_x	0	%	Location of the fuel segregation
			NBL_x	20	in	Location of the non-bond
Material Properties	Water		k_w	Default	1	Thermal Conductivity of Water
			mu_w	Default	1	Viscosity of Water
			rho_w	Default	1	Density of Water
			cp_w	Default	1	Heat Capacity of Water
	Clad		k_c	Table 18	1	Thermal Conductivity of Cladding
			cp_c		1	Heat Capacity of Cladding
	Fuel		k_f	Table 19	1	Thermal Conductivity of Fuel
			cp_f		1	Heat Capacity of Fuel
	Segregation		k_fs	46.9	W/m-k	Thermal conductivity of Fuel Segregation
Non-bond Properties			m	0.2	rad	Average slope of the surface roughness
			sigma	1	um	Average asperity height (roughness)
			p_nb	480	psi	Contact pressure across the non-bond
			E'	38.66	GPa	Reduced modulus
Power Properties			Q_f	Table 20	1	Heat Generation Rate for the fuel
			Q_fs	10.3	1	Fuel segregation power multiplier
			Q_c	0.00083	1	Clad power multiplier
			Q_w	0	1	Water power multiplier
Flow Properties			v_in	7.944	m/s	Coolant inlet velocity
			p_out	2.606	MPa	Coolant exit pressure
			k_seq	5.63	um	Wall roughness
			Turb_in	Default	1	Turbulent inlet conditions
			T_in	120	F	Coolant inlet temperature

Following is a longer description of those parameters that need further clarification.

Th_p: Total thickness of the fuel plate cladding which encompasses the fuel meat

Th_w: Total thickness of coolant channel which encompasses the fuel plate

PL: How the plate is centered within the coolant channel in the y-direction (along the thickness). 50% is the nominal value and represents the fuel plate centered within the coolant channel. Values greater than 50% move the plate 'up', and essentially reduce the distance to the edge of the coolant channel on the hot side of the hotspot

FL_y: How the fuel is centered within the cladding along the y-direction. 50% is the nominal value and represents the fuel meat centered within the cladding. Values greater than 50% move the fuel meat 'up', and essentially reduce the cladding thickness on the hot side of the hotspot

FL_x: How the fuel is centered within the cladding along the x-direction. 50% is the nominal value and represents the fuel meat centered within the cladding. Values greater than 50% move the fuel 'right' (towards the outlet) within the cladding.

FSL_x: Location of the left (inlet) side of the fuel segregation given as a percent of the length of the fuel meat. 0% represents a fuel segregation at the inlet side of the fuel meat, 100% represents a fuel segregation at the outlet side of the fuel meat.

Q_fs: The fuel segregation power multiplier represents the factor by which the local heat generation rate is increased within the non-bond.

Q_c: The clad power multiplier represents the factor by which the local heat generation rate is multiplied for the heat generated within the clad. (Note: this value was set to 0 for the sensitivity analysis)

Q_w: The water power multiplier is the same as the clad power multiplier, except that it applies to the coolant. (Note: this value was set to 0 for the sensitivity analysis)

Table 38 List of final parameters and lower and upper bounds for SA

Category	Parameter	Nominal Value	Unit	Brief Description	Lower	Upper
Geometry	Th_f	0.03	in	Thickness of the fuel	0.02	0.033
	Th_p	0.05	in	Thickness of the fuel plate	0.049	0.051
	Th_w	0.1	in	Thickness of coolant channel	0.09	0.11
	PL	0.5	%	How the plate is centered within the coolant	0.5	0.75
	FL_y	0.5	%	How the fuel is centered within the cladding	0.5	0.75
	L_f	20	in	Length of the fuel	19.478	20.478
	FL_x	0.5	%	How the fuel is centered within the cladding	0.25	0.75
	L_fs	0.0164	in	Length (diameter) of the fuel segregation	0.004	0.018
	L_nb	0.0625	in	Length (diameter) of the non-bond	0.056	0.0688
Non-bond Properties	FSL_x	0.5	%	Location of FS as a percent of fuel length	0	1
	sigma	1	um	Average asperity height (roughness)	0.1	10
	p_nb	480	psi	Contact pressure across the non-bond	0	1000
Power Properties	Q_f	Table 20		Heat Generation Rate for the fuel	0.88	1.12
	Q_fs	10.3		Fuel segregation power multiplier	5.15	13.081
Flow Properties	v_in	7.944	m/s	Coolant inlet velocity	7.15	8.425
	p_out	2.606	MPa	Coolant exit pressure	2.345	2.8666
	k_sand_eq	5.63	um	Wall roughness in sand equivalent	5.067	6.193
	T_in	120	F	Coolant inlet temperature	120	135

Appendix E: Step-by-step of Sensitivity Analysis

This appendix is to serve as a guide to follow the same procedure for driving COMSOL with Dakota and generating surrogate models in JMP.

Prepare Input Files

Prepare the Dakota input file, analysis driver, MATLAB wrapper, MATLAB call function, COMSOL file as described in section 11.3.1.

Ensure parameters match from (1) Dakota input to (2) wrapper to (3) driver to (4) COMSOL (same number, order, and units)

Place all files in the same directory (ensure functions look in the right directory)

Run Dakota

Start a COMSOL server:

- Windows command prompt: type "comsolmph"

- Linux: type "comsol server", then connect to server from MATLAB (open MATLAB, connect by adding the file path to the comsol MATLAB livelink folder, type command "mphstart" at command line in MATLAB; minimize MATLAB, it does nothing from this point on except keep the comsol server open as Dakota connects and disconnects repeatedly)

Run Dakota:

- Open a terminal, navigate to the folder where all the input files are, at the command prompt:

> Dakota –i <inputfile.in> -o <outputfile.out>

Run JMP

Load simulation_results_tabulated.dat using the "Data with Preview" option. From the Analyze menu, select "Fit Model" for the polynomial surrogates. Select the response that will be modeled (Hot Side Temp, Cold Side, Temp), and click the "Y" button. Select the parameters and, for the linear polynomial, click the "Add" button, for a quadratic polynomial, click the "Macros" button and select "Factorial to degree", in the "Degree" field, enter 2. Press "Run".

For the Gaussian Process, again, select the analyze menu. Highlight the "Specialized Modeling" option and select "Gaussian Process". Again, enter the response that will be modeled, and click "Y". Select the parameters and click "X". Click "OK". To extract the equation, from within the report that is generated, click on the red triangle in the "Gaussian Process Model of …" menu. Click "Publish Prediction Formula". From the Formula Depot report that is generated, click the red triangle on the "Gaussian Process - …" menu. Click "Copy Formula" and then paste it to a text editor.

Appendix F: Additional Results from the Sensitivity Analysis

The following sections provide additional results from the sensitivity analysis. These include the unpresented results for n_op = 50, as well the results for n_op = 32, 16, and 8. The results are presented in order of hot side, cold side, and maximum temperatures, and energy balance. Within each temperature result set is the surrogate predicted vs simulation actual results, residual plot, and parameter estimates for both the linear and quadrilateral surrogates. Because the quadrilateral parameter list is 180 terms long, only those that are statistically significant ($p \leq 0.05$) are included.

The jackknife predicted versus simulation actual results as well as the sensitivity table for the Gaussian Process surrogate model are presented. Within the energy balance section, the distribution of energy balance errors is presented, along with the mean, standard deviation, and maximum and minimum errors. Energy balance errors were evaluated with the Gaussian process and the sensitivities to the various parameters is provided in a table.

n_op 50

Cold Side Temperature Prediction
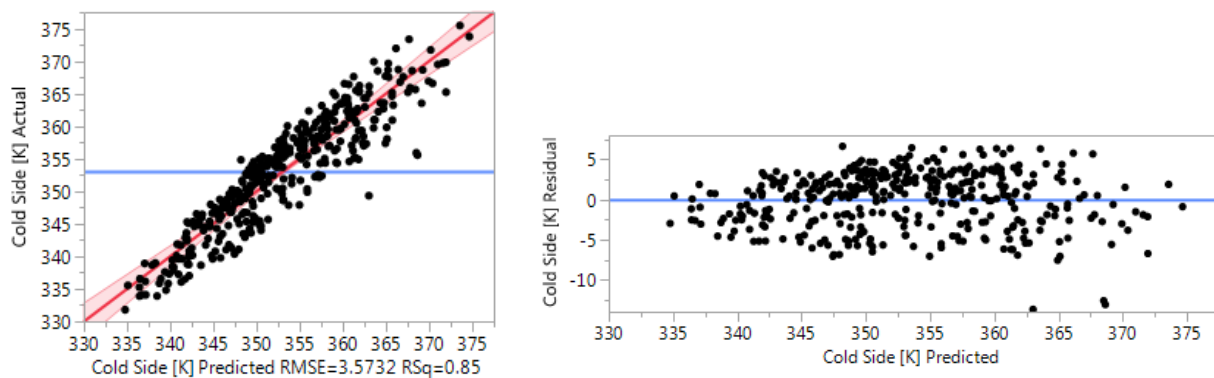
Linear

Figure 175 n_op 50 cold side linear surrogate actual vs predicted and residuals

264

Term	Estimate	Std Error	t Ratio		Prob>|t|
FSL_x	22.954952	0.636071	36.09		<.0001*
Th_f	826.95704	48.97153	16.89		<.0001*
t_in	0.4806362	0.042392	11.34		<.0001*
Q_f	23.545296	2.650738	8.88		<.0001*
L_fs	341.77187	45.43254	7.52		<.0001*
v_in	-3.414641	0.498601	-6.85		<.0001*
Q_fs	0.3638176	0.080174	4.54		<.0001*
Th_w	139.12499	31.8105	4.37		<.0001*
sig	-0.268061	0.064258	-4.17		<.0001*
L_nb	-194.5694	49.68931	-3.92		0.0001*
PL	4.3113148	2.545295	1.69		0.0912
p_nb	0.000723	0.000636	1.14		0.2565
k_sand	0.5510325	0.564446	0.98		0.3296
FL_y	-1.851947	2.542175	-0.73		0.4668
L_f	0.2724171	0.636428	0.43		0.6689
Th_p	-79.50066	317.9335	-0.25		0.8027
p_out	-0.05156	1.219009	-0.04		0.9663
FL_x	0.0159009	1.271146	0.01		0.9900

Figure 176 n_op 50 cold side linear surrogate parameter estimates
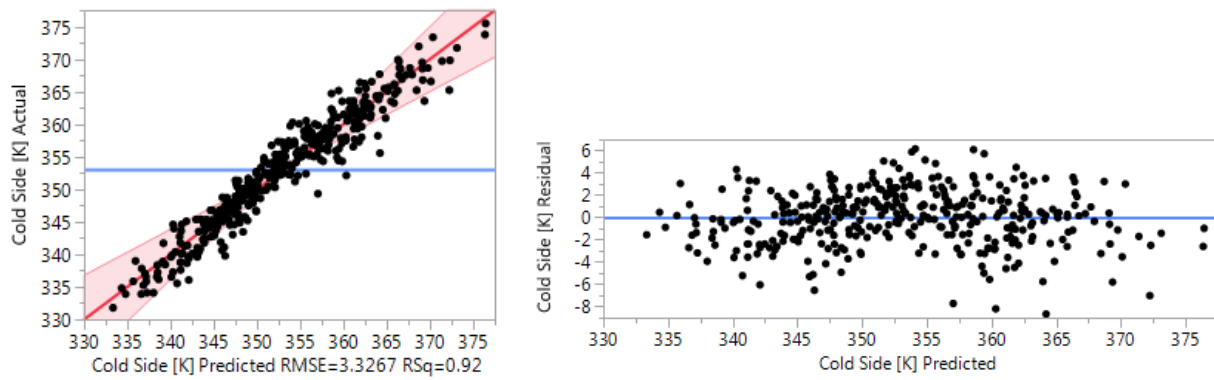
Quadratic

Figure 177 n_op 50 cold side quadratic surrogate actual vs predicted and residuals

265

Term	Estimate	Std Error	t Ratio		Prob>|t|
FSL_x	22.861865	0.332474	68.76		<.0001*
Th_f	872.28519	25.83553	33.76		<.0001*
(FSL_x-0.49987)*(FSL_x-0.49987)	-39.82905	1.315063	-30.29		<.0001*
t_in	0.501517	0.022602	22.19		<.0001*
Q_f	23.656911	1.370672	17.26		<.0001*
L_fs	359.37151	26.57293	13.52		<.0001*
v_in	-3.374704	0.255094	-13.23		<.0001*
Q_fs	0.4745544	0.040463	11.73		<.0001*
sig	-0.295223	0.033004	-8.95		<.0001*
(Th_f-0.0265)*(FSL_x-0.49987)	775.24403	93.94204	8.25		<.0001*
Th_w	101.88308	16.67393	6.11		<.0001*
PL	7.4879235	1.254078	5.97		<.0001*
(PL-0.625)*(PL-0.625)	113.42316	20.86716	5.44		<.0001*
(Th_w-0.1)*(FSL_x-0.49987)	-281.6969	60.54066	-4.65		<.0001*
(sig-5.05072)*(sig-5.05072)	0.0572231	0.013659	4.19		<.0001*
L_nb	-109.8802	26.47151	-4.15		<.0001*
(Th_f-0.0265)*(Q_f-1)	1245.7426	384.2252	3.24		0.0014*
(FSL_x-0.49987)*(v_in-7.78747)	-2.751565	0.851144	-3.23		0.0014*
(L_f-19.978)*(FSL_x-0.49987)	-3.581953	1.120984	-3.20		0.0016*
p_nb	0.0011683	0.000369	3.17		0.0018*
(FL_x-0.50001)*(p_out-2.60582)	-13.62169	4.581534	-2.97		0.0033*
(Q_fs-9.11574)*(v_in-7.78747)	-0.32466	0.117893	-2.75		0.0065*
(Th_f-0.0265)*(v_in-7.78747)	-195.7692	71.83955	-2.73		0.0070*
(FSL_x-0.49987)*(Q_f-1)	13.008228	4.784	2.72		0.0072*
(L_fs-0.011)*(p_nb-500.038)	0.2306806	0.087268	2.64		0.0089*
(FL_x-0.50001)*(p_nb-500.038)	-0.006023	0.0025	-2.41		0.0169*
(L_fs-0.011)*(FSL_x-0.49987)	-206.8864	90.62171	-2.28		0.0235*
(Th_f-0.0265)*(L_fs-0.011)	16020.167	7018.28	2.28		0.0236*
(L_f-19.978)*(L_nb-0.0624)	-205.9513	94.26731	-2.18		0.0301*
(FL_y-0.62501)*(p_nb-500.038)	-0.009868	0.00498	-1.98		0.0489*
(L_fs-0.011)*(Q_fs-9.11574)	19.434363	10.13042	1.92		0.0566

Figure 178 n_op 50 cold side quadratic surrogate parameter estimates

Gaussian Process

Figure 179 n_op 50 cold side Gaussian Process surrogate actual vs jackknife predicted

266

Table 39 n_op 50 cold side Gaussian Process surrogate parameters and sensitivities

Parameter	θ	Total Sensitivity	Main Effect
FSL_x	1.0892	0.6789	0.6571
Th_f	286.4496	0.1441	0.1317
t_in	0.0000	0.0596	0.0593
Q_f	0.3270	0.0375	0.0355
L_fs	178.9249	0.0297	0.0269
v_in	0.0070	0.0211	0.0191
Q_fs	0.0004	0.0191	0.0172
sig	0.0006	0.0118	0.0105
Th_w	54.7000	0.0112	0.0060
PL	0.7320	0.0052	0.0048
L_f	0.0202	0.0030	0.0000
L_nb	4.7855	0.0026	0.0025
p_nb	0.0000	0.0019	0.0016
Th_p	24.6804	0.0003	0.0003
FL_y	0.0010	0.0001	0.0001
k_sand	0.0000	0.0000	0.0000
FL_x	0.0008	0.0000	0.0000
p_out	0.0001	0.0000	0.0000

Maximum Temperature Prediction
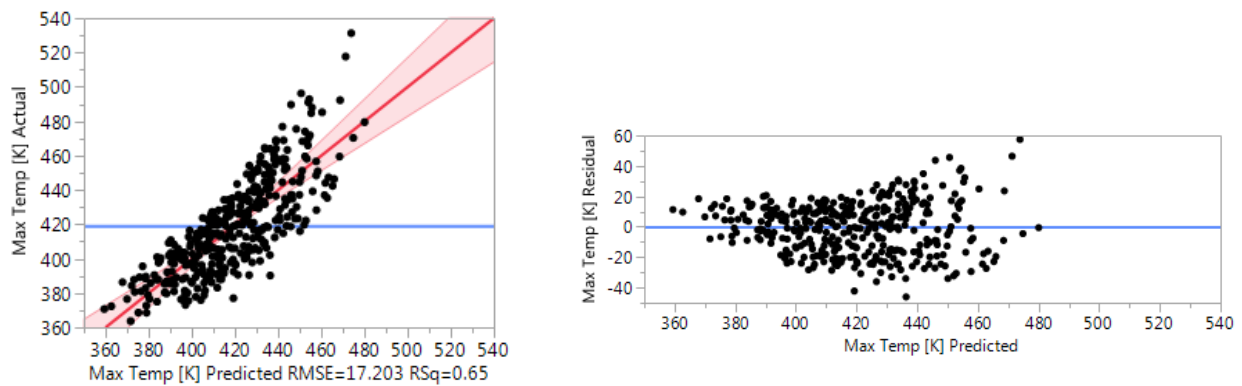
Linear

Figure 180 n_op 50 maximum temperature linear surrogate actual vs predicted and residuals

Term	Estimate	Std Error	t Ratio		Prob>|t|
L_fs	4119.085	218.7415	18.83		<.0001*
Q_fs	4.2754186	0.386008	11.08		<.0001*
Th_f	2287.6506	235.7804	9.70		<.0001*
Q_f	83.152947	12.76236	6.52		<.0001*
FSL_x	14.677797	3.062457	4.79		<.0001*
sig	0.9111171	0.309378	2.95		0.0034*
PL	35.109843	12.25469	2.87		0.0044*
v_in	-5.329602	2.400585	-2.22		0.0270*
Th_w	307.71588	153.1562	2.01		0.0453*
k_sand	4.2212848	2.717608	1.55		0.1212
p_out	8.2626449	5.869093	1.41		0.1600
p_nb	-0.004303	0.003063	-1.41		0.1609
t_in	0.2738468	0.204104	1.34		0.1805
FL_y	-13.55385	12.23967	-1.11		0.2689
L_nb	-142.8218	239.2363	-0.60		0.5509
Th_p	477.53749	1530.736	0.31		0.7552
L_f	0.8401825	3.064171	0.27		0.7841
FL_x	0.386104	6.120112	0.06		0.9497

Figure 181 n_op 50 maximum temperature linear surrogate parameters estimates

Quadratic
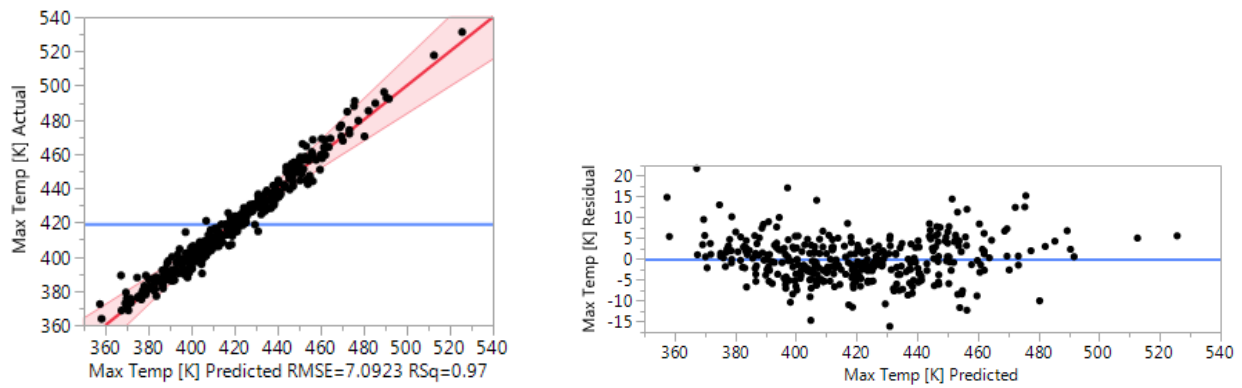
Figure 182 n_op 50 maximum temperature quadratic surrogate actual vs predicted and residuals

268

Term	Estimate	Std Error	t Ratio		Prob>|t|
L_fs	4267.9995	137.0741	31.14		<.0001*
(FSL_x-0.49987)*(FSL_x-0.49987)	-204.3168	6.783634	-30.12		<.0001*
Q_fs	4.8621786	0.208726	23.29		<.0001*
Th_f	2343.7785	133.2703	17.59		<.0001*
Q_f	87.728211	7.070488	12.41		<.0001*
FSL_x	17.18941	1.715036	10.02		<.0001*
PL	56.204907	6.46905	8.69		<.0001*
(L_fs-0.011)*(Q_fs-9.11574)	367.04809	52.25685	7.02		<.0001*
v_in	-6.345218	1.315878	-4.82		<.0001*
t_in	0.4955739	0.116593	4.25		<.0001*
sig	0.6994025	0.170249	4.11		<.0001*
(L_nb-0.0624)*(FSL_x-0.49987)	1716.5188	436.6645	3.93		0.0001*
(sig-5.05072)*(sig-5.05072)	-0.243081	0.070461	-3.45		0.0007*
(Th_p-0.05)*(FL_x-0.50001)	-22905.67	6648.184	-3.45		0.0007*
(L_fs-0.011)*(Q_f-1)	5526.4933	1770.213	3.12		0.0021*
(FL_y-0.62501)*(v_in-7.78747)	58.383518	19.12402	3.05		0.0026*
p_nb	-0.005175	0.001903	-2.72		0.0071*
(FL_x-0.50001)*(p_out-2.60582)	-61.51232	23.63343	-2.60		0.0100*
(L_fs-0.011)*(FSL_x-0.49987)	-1195.233	467.4639	-2.56		0.0113*
(L_fs-0.011)*(L_fs-0.011)	95995.488	37553.07	2.56		0.0114*
p_out	8.5255519	3.336153	2.56		0.0114*
(FL_y-0.62501)*(L_f-19.978)	-64.35994	25.49231	-2.52		0.0124*
(PL-0.625)*(PL-0.625)	241.07328	107.6414	2.24		0.0263*
(FL_y-0.62501)*(p_nb-500.038)	-0.056048	0.025687	-2.18		0.0303*
(L_fs-0.011)*(k_sand-5.62998)	833.67894	382.681	2.18		0.0306*
(FL_x-0.50001)*(p_nb-500.038)	-0.02733	0.012895	-2.12		0.0354*
(FSL_x-0.49987)*(t_in-127.5)	0.8387882	0.408001	2.06		0.0412*
(FL_y-0.62501)*(k_sand-5.62998)	41.360394	20.23787	2.04		0.0424*
(Th_p-0.05)*(sig-5.05072)	587.929	292.1349	2.01		0.0456*
(L_f-19.978)*(p_out-2.60582)	25.119066	12.69889	1.98		0.0494*
Th_w	166.87839	86.01097	1.94		0.0538

Figure 183 n_op 50 maximum temperature quadratic surrogate parameters estimates
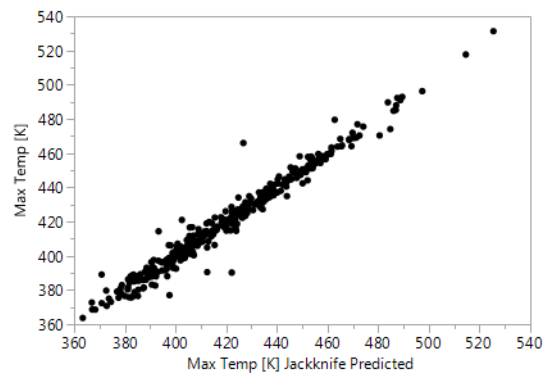
Figure 184 n_op 50 Maximum Temperature Gaussian Process surrogate actual vs jackknife predicted

Table 40 n_op 50 Maximum Temperature Gaussian Process surrogate parameters and

Parameter	θ	Total Sensitivity	Main Effect
Th_f	3717	0.3263	0.3005
Th_w	19293	0.2421	0.2092
v_in	0.6020	0.1630	0.1330
t_in	0.0028	0.0928	0.0814
PL	15.209	0.0791	0.0538
Q_f	6.0048	0.0758	0.0699
Th_p	95309	0.0200	0.0144
FL_x	1.0129	0.0173	0.0115
L_nb	1573.5	0.0096	0.0013
L_f	0.4101	0.0063	0.0017
FSL_x	0.2881	0.0059	0.0005
p_out	0.3989	0.0041	0.0022
p_nb	0.0000	0.0030	0.0004
Q_fs	0.0011	0.0023	0.0002
k_sand	0.0317	0.0010	0.0001
sig	0.0001	0.0005	0.0005
FL_y	0.0515	0.0001	0.0001
L_fs	0.0012	0.0000	0.0000

n_op 32

Hot Side Temperature Prediction

Linear

Hot Side [K] Predicted RMSE=7.1673 RSq=0.76
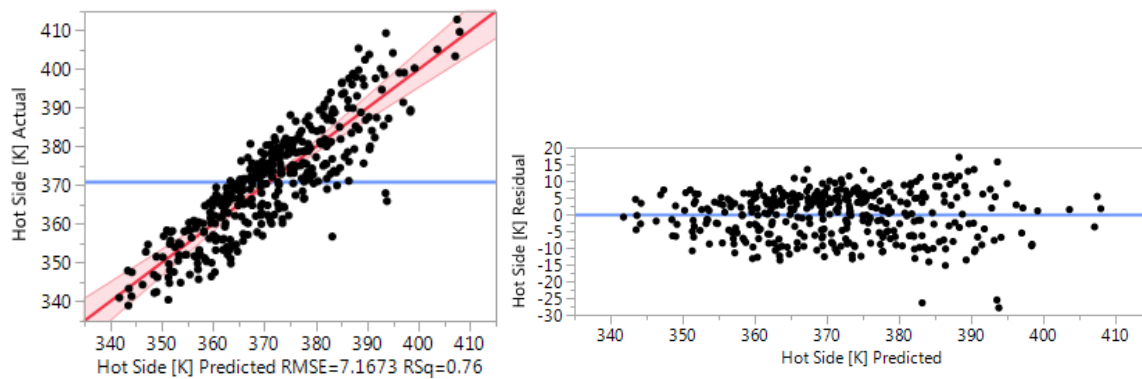
Figure 185 n_op 32 hot side linear surrogate actual vs predicted and residuals

Term	Estimate	Std Error	t Ratio		Prob>|t|
FSL_x	29.730597	1.275883	23.30		<.0001*
Th_f	1433.9831	98.23063	14.60		<.0001*
L_fs	1040.0532	91.13187	11.41		<.0001*
PL	52.763371	5.105538	10.33		<.0001*
Q_f	42.604175	5.317042	8.01		<.0001*
Q_fs	1.1637406	0.160818	7.24		<.0001*
t_in	0.4567295	0.085034	5.37		<.0001*
v_in	-4.206541	1.00013	-4.21		<.0001*
Th_w	145.0919	63.80779	2.27		0.0236*
sig	0.2351443	0.128893	1.82		0.0689
FL_y	7.1903963	5.099279	1.41		0.1594
L_nb	-107.6578	99.67041	-1.08		0.2808
k_sand	1.1837657	1.132208	1.05		0.2965
p_nb	-0.001153	0.001276	-0.90		0.3666
p_out	1.4742873	2.445176	0.60		0.5469
Th_p	269.35332	637.7339	0.42		0.6730
FL_x	0.5771373	2.549756	0.23		0.8211
L_f	0.2460795	1.276592	0.19		0.8473

Figure 186 n_op 32 hot side linear surrogate parameter estimates
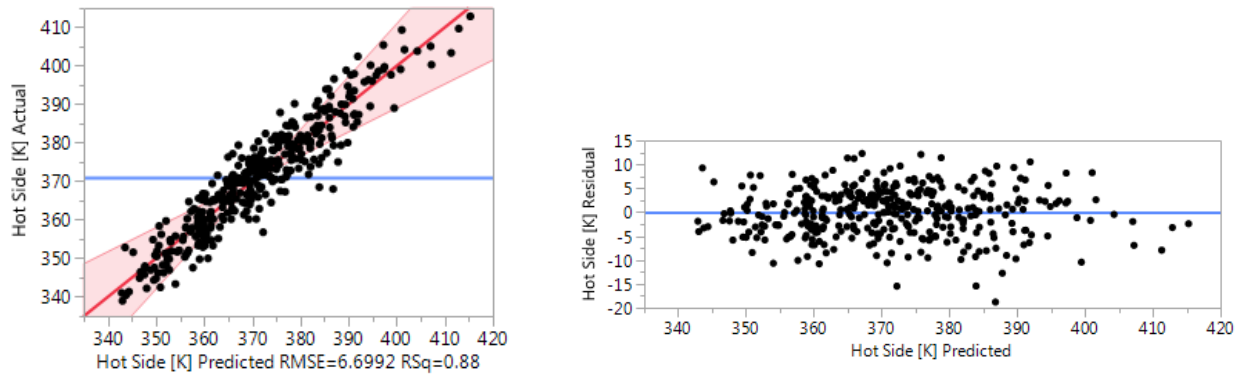
Quadratic

Figure 187 n_op 32 hot side quadratic surrogate actual vs predicted and residuals

272

Term	Estimate	Std Error	t Ratio		Prob>|t|
FSL_x	29.621102	0.664991	44.54		<.0001*
(FSL_x-0.49987)*(FSL_x-0.49987)	-81.06616	2.63032	-30.82		<.0001*
Th_f	1478.342	51.67442	28.61		<.0001*
PL	59.000764	2.508317	23.52		<.0001*
L_fs	1051.3577	53.14919	19.78		<.0001*
Q_fs	1.4136802	0.080932	17.47		<.0001*
Q_f	43.212462	2.741521	15.76		<.0001*
t_in	0.4989392	0.045208	11.04		<.0001*
v_in	-4.282262	0.510221	-8.39		<.0001*
(PL-0.625)*(FSL_x-0.49987)	66.880504	9.307205	7.19		<.0001*
(Th_f-0.0265)*(FSL_x-0.49987)	1032.006	187.8963	5.49		<.0001*
(PL-0.625)*(PL-0.625)	190.64432	41.73697	4.57		<.0001*
FL_y	10.352199	2.722344	3.80		0.0002*
(L_fs-0.011)*(FSL_x-0.49987)	-654.5932	181.2562	-3.61		0.0004*
(L_fs-0.011)*(Q_fs-9.11574)	73.085726	20.26207	3.61		0.0004*
(Th_f-0.0265)*(PL-0.625)	2555.8826	739.2637	3.46		0.0007*
(Th_w-0.1)*(FSL_x-0.49987)	-418.3731	121.0892	-3.46		0.0007*
(v_in-7.78747)*(k_sand-5.62998)	-4.160653	1.491442	-2.79		0.0058*
(FSL_x-0.49987)*(Q_f-1)	24.88003	9.568648	2.60		0.0101*
(Th_p-0.05)*(FL_x-0.50001)	-6558.275	2577.775	-2.54		0.0117*
(FL_x-0.50001)*(k_sand-5.62998)	11.164099	4.395803	2.54		0.0119*
(FL_x-0.50001)*(p_nb-500.038)	-0.012632	0.005	-2.53		0.0123*
(FL_x-0.50001)*(p_out-2.60582)	-21.89003	9.163658	-2.39		0.0179*
(FL_y-0.62501)*(v_in-7.78747)	17.216921	7.415172	2.32		0.0213*
(Th_f-0.0265)*(L_fs-0.011)	32036.644	14037.45	2.28		0.0236*
sig	0.1496114	0.066013	2.27		0.0246*
(L_fs-0.011)*(Q_f-1)	1475.5385	686.3844	2.15		0.0328*
(FL_x-0.50001)*(Q_fs-9.11574)	1.2757027	0.617613	2.07		0.0402*
(Th_p-0.05)*(Th_w-0.1)	121499.41	63518.92	1.91		0.0573

Figure 188 n_op 32 hot side quadratic surrogate parameter estimates
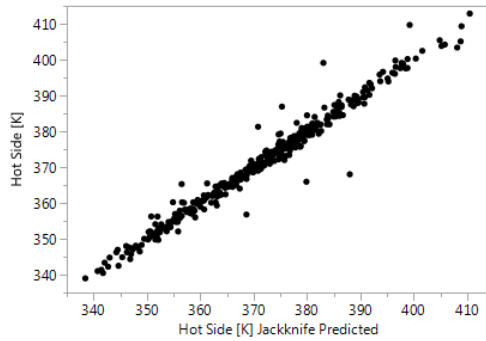
Gaussian Process

Figure 189 n_op 32 hot side Gaussian Process surrogate actual vs jackknife predicted

Table 41 n_op 32 hot side Gaussian Process surrogate parameters and sensitivities

Parameter	θ	Total Sensitivity	Main Effect
FSL_x	2.9206	0.5281	0.4920
Th_f	447.09	0.1541	0.1426
L_fs	496.06	0.0970	0.0872
PL	1.8399	0.0952	0.0815
Q_fs	0.0017	0.0635	0.0556
Q_f	1.0440	0.0458	0.0419
t_in	0.0000	0.0203	0.0198
v_in	0.0177	0.0138	0.0123
L_f	1.5975	0.0116	0.0010
Th_w	162.18	0.0050	0.0013
FL_y	0.0509	0.0031	0.0029
k_sand	0.0127	0.0016	0.0003
sig	0.0000	0.0009	0.0007
L_nb	8.0125	0.0005	0.0004
Th_p	76.590	0.0003	0.0003
FL_x	0.0046	0.0002	0.0000
p_out	0.0058	0.0002	0.0000
p_nb	0.0000	0.0001	0.0000

Cold Side Temperature Prediction
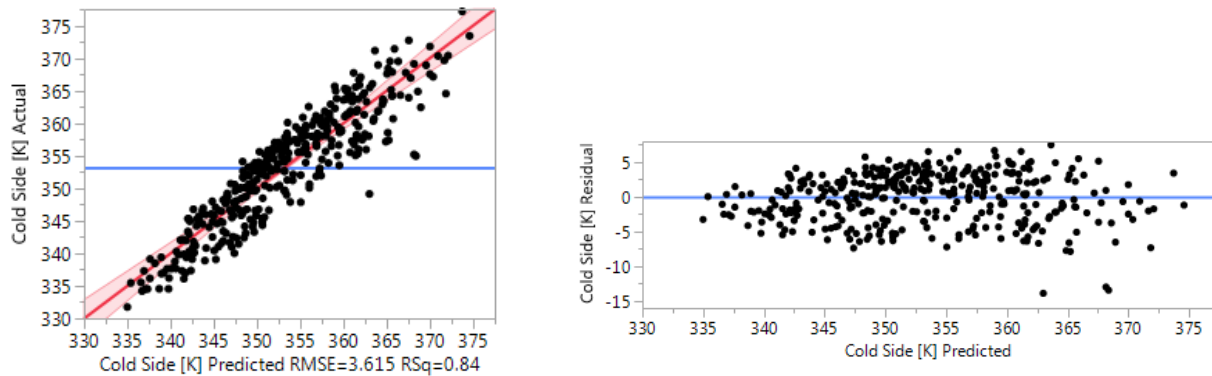
Linear

Figure 190 n_op 32 cold side linear surrogate actual vs predicted and residuals

Term	Estimate	Std Error	t Ratio		Prob>|t|
FSL_x	22.681341	0.643507	35.25		<.0001*
Th_f	807.95596	49.54383	16.31		<.0001*
t_in	0.4889455	0.042888	11.40		<.0001*
Q_f	23.607087	2.681716	8.80		<.0001*
L_fs	348.29832	45.96348	7.58		<.0001*
v_in	-3.347907	0.504428	-6.64		<.0001*
Q_fs	0.3722388	0.081111	4.59		<.0001*
Th_w	131.17622	32.18224	4.08		<.0001*
L_nb	-199.1419	50.26999	-3.96		<.0001*
sig	-0.248446	0.065009	-3.82		0.0002*
PL	4.4793259	2.575041	1.74		0.0828
k_sand	0.6324163	0.571043	1.11		0.2688
p_nb	0.0006019	0.000644	0.94		0.3503
FL_y	-1.976134	2.571884	-0.77		0.4428
Th_p	101.11288	321.6489	0.31		0.7534
L_f	0.1793736	0.643865	0.28		0.7807
FL_x	0.1702022	1.286001	0.13		0.8948
p_out	-0.14802	1.233255	-0.12		0.9045

Figure 191 n_op 32 cold side linear surrogate parameter estimates
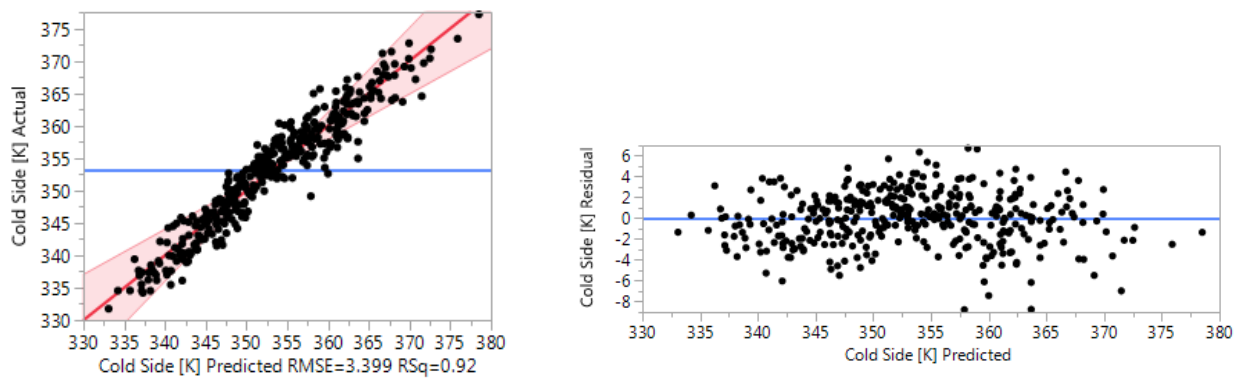
Quadratic

Figure 192 n_op 32 cold side quadratic surrogate actual vs predicted and residuals

275

Term	Estimate	Std Error	t Ratio		Prob>|t|
FSL_x	22.585099	0.349845	64.56		<.0001*
Th_f	852.75184	27.18538	31.37		<.0001*
(FSL_x-0.49987)*(FSL_x-0.49987)	-40.35948	1.383784	-29.17		<.0001*
t_in	0.5099301	0.023783	21.44		<.0001*
Q_f	23.610475	1.442286	16.37		<.0001*
L_fs	359.25091	27.96124	12.85		<.0001*
v_in	-3.396166	0.268422	-12.65		<.0001*
Q_fs	0.510089	0.042577	11.98		<.0001*
sig	-0.275619	0.034729	-7.94		<.0001*
(Th_f-0.0265)*(FSL_x-0.49987)	775.38344	98.8503	7.84		<.0001*
PL	7.226253	1.3196	5.48		<.0001*
Th_w	91.941987	17.54509	5.24		<.0001*
(Th_w-0.1)*(FSL_x-0.49987)	-311.0356	63.7038	-4.88		<.0001*
(PL-0.625)*(PL-0.625)	100.21986	21.95739	4.56		<.0001*
(sig-5.05072)*(sig-5.05072)	0.060267	0.014373	4.19		<.0001*
L_nb	-107.8566	27.85452	-3.87		0.0001*
(Th_f-0.0265)*(Q_f-1)	1370.6289	404.2997	3.39		0.0008*
(Th_f-0.0265)*(v_in-7.78747)	-231.1872	75.5929	-3.06		0.0025*
(FSL_x-0.49987)*(Q_f-1)	15.313447	5.033967	3.04		0.0027*
(L_f-19.978)*(FSL_x-0.49987)	-3.414897	1.179558	-2.90		0.0042*
(L_fs-0.011)*(FSL_x-0.49987)	-272.0051	95.35701	-2.85		0.0048*
(FSL_x-0.49987)*(v_in-7.78747)	-2.416596	0.89563	-2.70		0.0076*
(L_fs-0.011)*(p_nb-500.038)	0.2465421	0.091827	2.68		0.0079*
(FL_x-0.50001)*(p_out-2.60582)	-12.71169	4.820906	-2.64		0.0091*
p_nb	0.0009275	0.000388	2.39		0.0179*
(FSL_x-0.49987)*(t_in-127.5)	0.1965199	0.083227	2.36		0.0192*
(FL_x-0.50001)*(p_nb-500.038)	-0.00568	0.002631	-2.16		0.0321*
(Q_fs-9.11574)*(v_in-7.78747)	-0.259585	0.124052	-2.09		0.0377*
(FL_y-0.62501)*(p_nb-500.038)	-0.010871	0.00524	-2.07		0.0394*
(FL_y-0.62501)*(v_in-7.78747)	8.057797	3.901045	2.07		0.0402*
(L_fs-0.011)*(Q_fs-9.11574)	21.339755	10.65967	2.00		0.0467*
(FL_x-0.50001)*(L_nb-0.0624)	321.51604	177.4182	1.81		0.0715

Figure 193 n_op 32 cold side quadratic surrogate parameter estimates
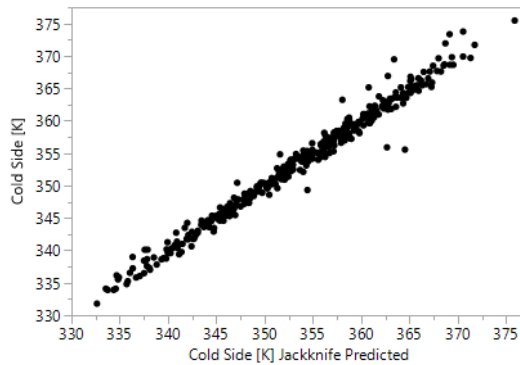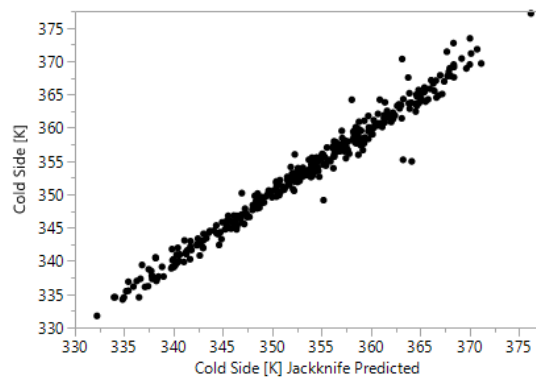
Gaussian Process

Figure 194 n_op 32 cold side Gaussian Process surrogate actual vs jackknife predicted

276

Table 42 n_op 32 cold side Gaussian Process surrogate parameters and sensitivities

Parameter	θ	Total Sensitivity	Main Effect
FSL_x	1.1070	0.6805	0.6587
Th_f	327.03	0.1390	0.1267
t_in	0.0000	0.0627	0.0622
Q_f	0.2940	0.0384	0.0360
L_fs	174.79	0.0314	0.0286
v_in	0.0056	0.0219	0.0200
Q_fs	0.0003	0.0200	0.0180
sig	0.0004	0.0102	0.0093
Th_w	24.500	0.0096	0.0054
PL	0.5482	0.0050	0.0046
L_nb	4.2172	0.0031	0.0030
L_f	0.0058	0.0023	0.0000
p_nb	0.0000	0.0009	0.0009
FL_y	0.0023	0.0001	0.0000
k_sand	0.0000	0.0000	0.0000
Th_p	3.2451	0.0000	0.0000
p_out	0.0003	0.0000	0.0000
FL_x	0.0001	0.0000	0.0000

Maximum Temperature Prediction
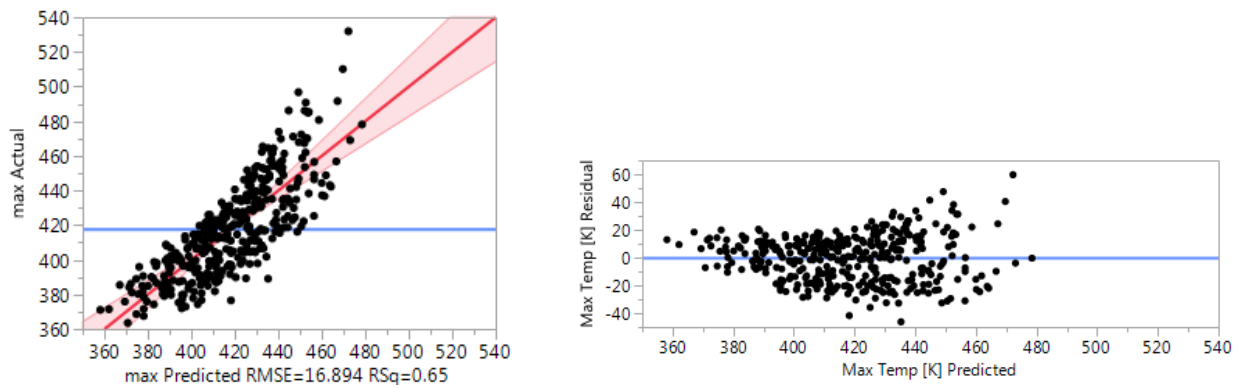
Linear

Figure 195 n_op 32 Maximum temperature linear surrogate actual vs predicted and residuals

Term	Estimate	Std Error	t Ratio		Prob>|t|
L_fs	4097.7051	214.8079	19.08		<.0001*
Q_fs	4.2479422	0.379066	11.21		<.0001*
Th_f	2258.5196	231.5405	9.75		<.0001*
Q_f	82.624235	12.53286	6.59		<.0001*
FSL_x	14.677879	3.007398	4.88		<.0001*
PL	35.134422	12.03432	2.92		0.0037*
sig	0.8746346	0.303814	2.88		0.0042*
Th_w	333.98982	150.402	2.22		0.0270*
v_in	-5.210497	2.357416	-2.21		0.0277*
k_sand	4.1213638	2.668739	1.54		0.1234
p_out	8.0631533	5.763552	1.40		0.1627
p_nb	-0.004007	0.003008	-1.33		0.1836
t_in	0.2586853	0.200434	1.29		0.1977
FL_y	-13.88301	12.01956	-1.16		0.2488
L_nb	-160.9961	234.9342	-0.69		0.4936
L_f	1.0237731	3.009069	0.34		0.7339
Th_p	316.01912	1503.209	0.21		0.8336
FL_x	0.5491561	6.010056	0.09		0.9272

Figure 196 n_op 32 Maximum temperature linear surrogate parameter estimates
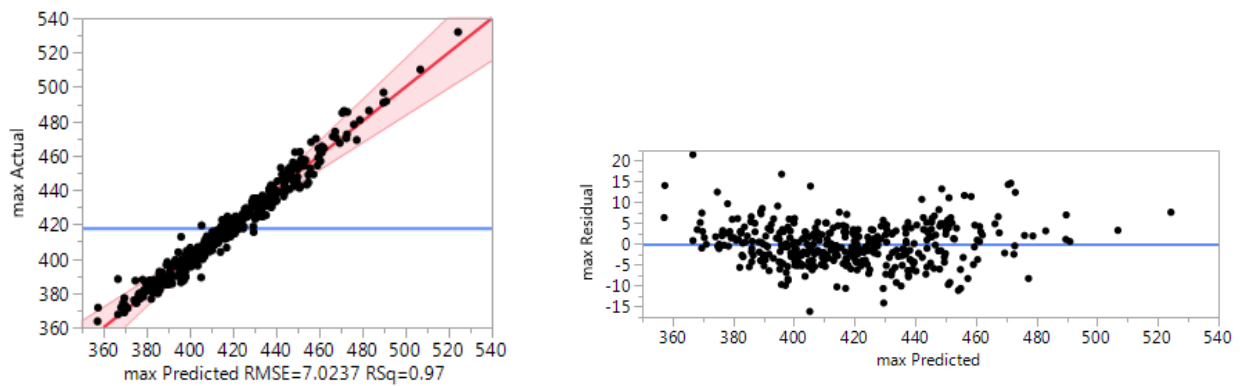
Quadratic

Figure 197 n_op 32 Maximum temperature quadratic surrogate actual vs predicted and residuals

278

Term	Estimate	Std Error	t Ratio		Prob>|t|
L_fs	4262.8627	135.7449	31.40		<.0001*
(FSL_x-0.49987)*(FSL_x-0.49987)	-199.9798	6.71793	-29.77		<.0001*
Q_fs	4.8172827	0.206702	23.31		<.0001*
Th_f	2323.0918	131.9783	17.60		<.0001*
Q_f	86.877609	7.001942	12.41		<.0001*
FSL_x	16.935222	1.69841	9.97		<.0001*
PL	56.024405	6.406331	8.75		<.0001*
(L_fs-0.011)*(Q_fs-9.11574)	370.68211	51.75006	7.16		<.0001*
v_in	-6.063205	1.303122	-4.65		<.0001*
sig	0.7045993	0.168599	4.18		<.0001*
t_in	0.4742514	0.115462	4.11		<.0001*
(L_nb-0.0624)*(FSL_x-0.49987)	1527.5111	432.4312	3.53		0.0005*
(Th_p-0.05)*(FL_x-0.50001)	-22222.56	6583.73	-3.38		0.0009*
(sig-5.05072)*(sig-5.05072)	-0.233349	0.069778	-3.34		0.0010*
(L_fs-0.011)*(L_fs-0.011)	109280.98	37189	2.94		0.0037*
(L_fs-0.011)*(Q_f-1)	5108.9181	1753.05	2.91		0.0040*
(FL_x-0.50001)*(p_out-2.60582)	-63.33739	23.40431	-2.71		0.0074*
(FL_y-0.62501)*(v_in-7.78747)	49.851682	18.93861	2.63		0.0092*
(L_fs-0.011)*(FSL_x-0.49987)	-1173.354	462.9348	-2.53		0.0121*
p_out	8.1532309	3.303808	2.47		0.0145*
p_nb	-0.004368	0.001884	-2.32		0.0215*
(PL-0.625)*(PL-0.625)	244.81594	106.5977	2.30		0.0227*
Th_w	187.59634	85.17709	2.20		0.0288*
(Th_p-0.05)*(sig-5.05072)	625.2705	289.3026	2.16		0.0319*
(FL_y-0.62501)*(L_f-19.978)	-54.2178	25.24514	-2.15		0.0330*
(FL_x-0.50001)*(k_sand-5.62998)	24.089199	11.22704	2.15		0.0332*
(FL_y-0.62501)*(p_nb-500.038)	-0.053346	0.025438	-2.10		0.0373*
(FL_y-0.62501)*(k_sand-5.62998)	40.630283	20.04163	2.03		0.0440*
(FL_x-0.50001)*(L_fs-0.011)	-1705.483	862.5607	-1.98		0.0495*
(L_fs-0.011)*(v_in-7.78747)	-659.9186	335.4938	-1.97		0.0506

Figure 198 n_op 32 Maximum temperature quadratic surrogate parameter estimates
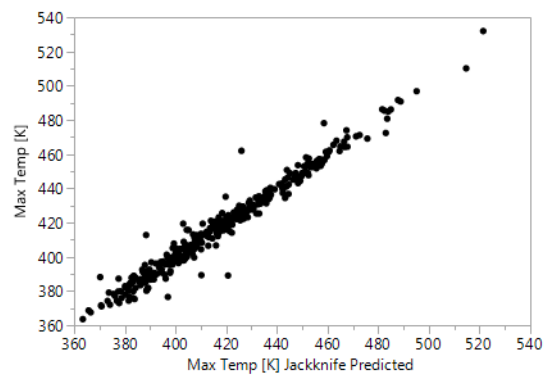
Figure 199 n_op 32 Maximum temperature Gaussian Process surrogate actual vs jackknife predicted

Parameter	θ	Total Sensitivity	Main Effect
L_fs	751.70	0.3882	0.3394
FSL_x	3.6793	0.3096	0.2741
Q_fs	0.0016	0.1862	0.1526
Th_f	103.19	0.0957	0.0915
Q_f	0.8610	0.0477	0.0427
PL	0.0597	0.0135	0.0130
v_in	0.0263	0.0054	0.0042
sig	0.0000	0.0038	0.0034
Th_w	7.8746	0.0038	0.0025
t_in	0.0000	0.0032	0.0031
L_f	0.0022	0.0030	0.0004
L_nb	179.74	0.0016	0.0008
p_nb	0.0000	0.0011	0.0010
Th_p	32.070	0.0001	0.0001
k_sand	0.0002	0.0000	0.0000
FL_y	0.0003	0.0000	0.0000
FL_x	0.0000	0.0000	0.0000
p_out	0.0000	0.0000	0.0000
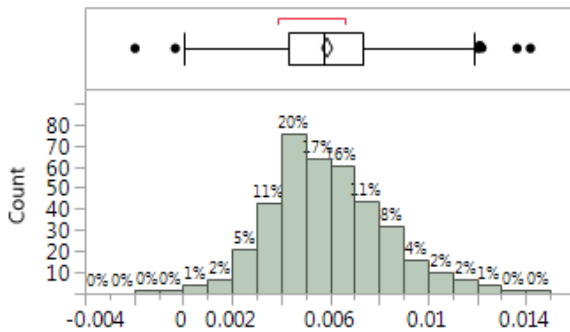
Energy Balance

Figure 200 n_op 32 distribution of energy balance errors

Table 44 Statistics for energy balance errors for n_op 32

n_op 32 Energy Balance Statistics	
Mean	0.005892
Std Dev	0.002339
maximum	0.014199
minimum	-0.00196

281

Parameter	Total Sensitivity	Main Effect
Th_f	0.3307	0.2977
Th_w	0.2278	0.1882
v_in	0.1677	0.1393
t_in	0.1171	0.1053
PL	0.0871	0.0343
Q_f	0.0565	0.0523
FL_x	0.0195	0.0139
FL_y	0.0164	0.0011
L_nb	0.0100	0.0008
Th_p	0.0083	0.0057
p_out	0.0070	0.0031
k_sand	0.0069	0.0039
sig	0.0047	0.0011
p_nb	0.0039	0.0000
L_f	0.0021	0.0001
L_fs	0.0007	0.0003
FSL_x	0.0000	0.0000
Q_fs	0.0000	0.0000

n_op 16

Hot Side Temperature Prediction
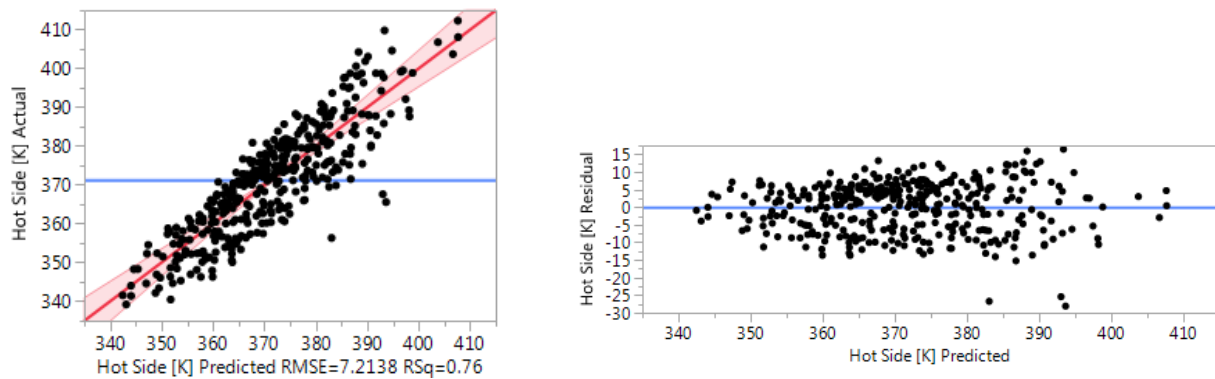
Linear

Figure 201 n_op 16 hot side linear surrogate actual vs predicted and residuals

Term	Estimate	Std Error	t Ratio		Prob>|t|
FSL_x	29.414161	1.284162	22.91		<.0001*
Th_f	1439.8765	98.86638	14.56		<.0001*
L_fs	1044.4947	91.72168	11.39		<.0001*
PL	48.898321	5.138583	9.52		<.0001*
Q_f	42.259522	5.351454	7.90		<.0001*
Q_fs	1.1735555	0.161859	7.25		<.0001*
t_in	0.4620221	0.085584	5.40		<.0001*
v_in	-4.338554	1.006602	-4.31		<.0001*
sig	0.2352481	0.129727	1.81		0.0706
FL_y	7.9238621	5.132281	1.54		0.1235
Th_w	92.355676	64.22076	1.44		0.1513
k_sand	1.1457957	1.139535	1.01		0.3153
p_nb	-0.001209	0.001284	-0.94		0.3469
L_nb	-88.29924	100.3155	-0.88		0.3793
p_out	1.5099854	2.461001	0.61		0.5399
Th_p	374.24892	641.8613	0.58		0.5602
FL_x	0.7008037	2.566258	0.27		0.7849
L_f	0.164297	1.284854	0.13		0.8983

Figure 202 n_op 16 hot side linear surrogate parameter estimates
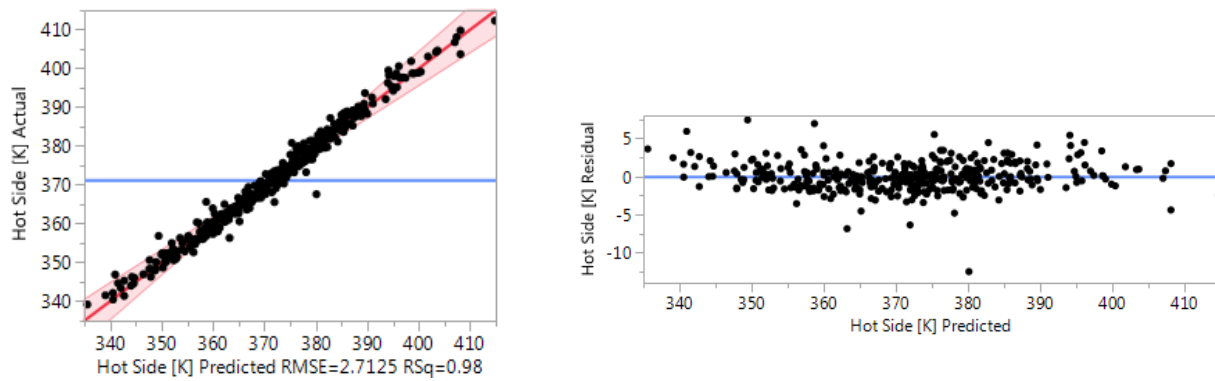
Quadratic

Figure 203 n_op 16 hot side quadratic surrogate actual vs predicted and residuals

283

Figure 204 n_op 16 hot side quadratic surrogate parameter estimates

| Term	Estimate	Std Error	t Ratio		Prob>|t|
FSL_x	29.303872	0.655916	44.68		<.0001*
(FSL_x-0.49987)*(FSL_x-0.49987)	-81.41136	2.594516	-31.38		<.0001*
Th_f	1485.3205	50.96928	29.14		<.0001*
PL	54.978179	2.474078	22.22		<.0001*
L_fs	1065.4986	52.4234	20.32		<.0001*
Q_fs	1.4209543	0.079827	17.80		<.0001*
Q_f	43.387087	2.704105	16.04		<.0001*
t_in	0.5129934	0.044591	11.50		<.0001*
v_in	-4.523992	0.50326	-8.99		<.0001*
(PL-0.625)*(FSL_x-0.49987)	62.680323	9.180427	6.83		<.0001*
(Th_f-0.0265)*(FSL_x-0.49987)	980.80439	185.3324	5.29		<.0001*
FL_y	12.084396	2.685184	4.50		<.0001*
(PL-0.625)*(PL-0.625)	180.1391	41.16721	4.38		<.0001*
(Th_w-0.1)*(FSL_x-0.49987)	-484.5825	119.4372	-4.06		<.0001*
(L_fs-0.011)*(Q_fs-9.11574)	78.866396	19.98527	3.95		0.0001*
(L_fs-0.011)*(FSL_x-0.49987)	-643.0579	178.7867	-3.60		0.0004*
(FL_y-0.62501)*(v_in-7.78747)	21.480931	7.313959	2.94		0.0037*
(Th_f-0.0265)*(PL-0.625)	2052.0379	729.1743	2.81		0.0054*
(FL_x-0.50001)*(p_nb-500.038)	-0.013638	0.004932	-2.77		0.0062*
(Th_p-0.05)*(FL_x-0.50001)	-6925.616	2542.591	-2.72		0.0071*
(L_f-19.978)*(FSL_x-0.49987)	-5.838135	2.211571	-2.64		0.0090*
(v_in-7.78747)*(k_sand-5.62998)	-3.717371	1.471071	-2.53		0.0123*
(FL_x-0.50001)*(p_out-2.60582)	-22.46725	9.038598	-2.49		0.0138*
(L_fs-0.011)*(Q_f-1)	1679.4222	677.0145	2.48		0.0140*
(FL_x-0.50001)*(k_sand-5.62998)	10.671615	4.335755	2.46		0.0147*
(FSL_x-0.49987)*(Q_f-1)	21.783952	9.43818	2.31		0.0221*
(Th_f-0.0265)*(Q_f-1)	1607.0187	758.0103	2.12		0.0353*
sig	0.1368063	0.065112	2.10		0.0370*
(FL_x-0.50001)*(Q_fs-9.11574)	1.2506431	0.609182	2.05		0.0414*
(Th_f-0.0265)*(L_fs-0.011)	27816.467	13845.83	2.01		0.0460*
L_nb	103.09612	52.22336	1.97		0.0498*
(Th_f-0.0265)*(FL_y-0.62501)	-1411.331	718.5312	-1.96		0.0510

Gaussian Process
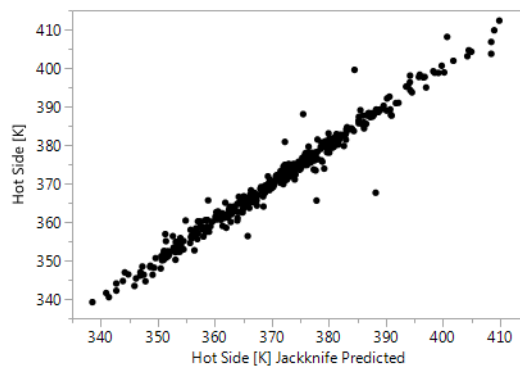
Figure 205 n_op 16 hot side Gaussian Process surrogate actual vs jackknife predicted

Table 46 n_op 16 hot side Gaussian Process surrogate parameters and sensitivities

Parameter	θ	Total Sensitivity	Main Effect
FSL_x	2.1620	0.5384	0.5044
Th_f	345.30	0.1551	0.1444
L_fs	370.28	0.0989	0.0890
PL	1.3200	0.0879	0.0742
Q_fs	0.0014	0.0640	0.0560
Q_f	0.7850	0.0452	0.0416
t_in	0.0000	0.0216	0.0213
v_in	0.0091	0.0129	0.0120
L_f	1.2129	0.0085	0.0009
Th_w	72.845	0.0034	0.0003
FL_y	0.0377	0.0033	0.0030
k_sand	0.0034	0.0009	0.0002
sig	0.0000	0.0007	0.0006
L_nb	2.7770	0.0004	0.0004
Th_p	23.369	0.0001	0.0001
FL_x	0.0001	0.0000	0.0000
p_nb	0.0000	0.0000	0.0000
p_out	0.0005	0.0000	0.0000

Cold Side Temperature Prediction
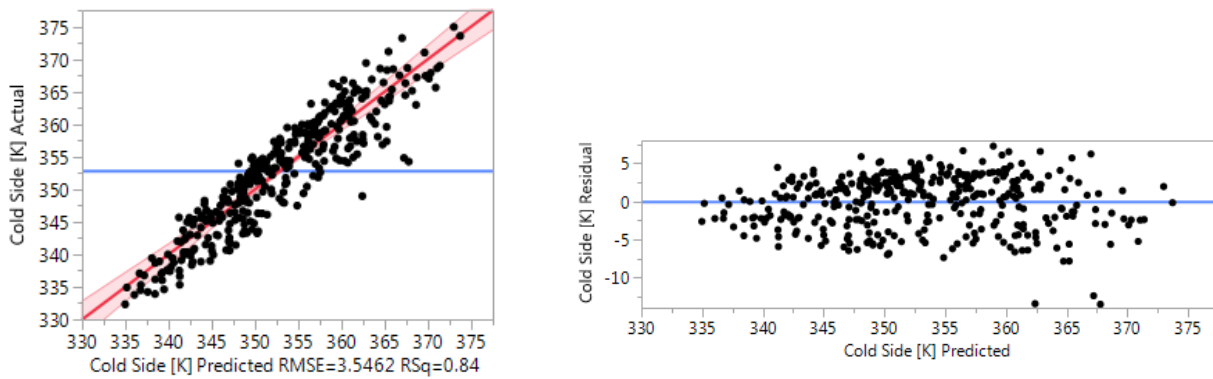
Linear

Figure 206 n_op 16 cold side linear surrogate actual vs predicted and residuals

285

Term	Estimate	Std Error	t Ratio		Prob>|t|
FSL_x	22.615243	0.631261	35.83		<.0001*
Th_f	799.16826	48.60017	16.44		<.0001*
t_in	0.4840175	0.042071	11.50		<.0001*
Q_f	23.671182	2.630637	9.00		<.0001*
L_fs	340.04954	45.08802	7.54		<.0001*
v_in	-3.264595	0.49482	-6.60		<.0001*
Q_fs	0.3721854	0.079566	4.68		<.0001*
sig	-0.255295	0.06377	-4.00		<.0001*
L_nb	-191.6152	49.3125	-3.89		0.0001*
Th_w	88.579414	31.56927	2.81		0.0053*
p_nb	0.0007896	0.000631	1.25		0.2118
k_sand	0.6579589	0.560166	1.17		0.2409
FL_y	-2.831468	2.522897	-1.12		0.2625
PL	0.3772778	2.525995	0.15		0.8814
L_f	0.0691918	0.631601	0.11		0.9128
FL_x	-0.119279	1.261506	-0.09		0.9247
Th_p	21.722059	315.5225	0.07		0.9452
p_out	0.059655	1.209765	0.05		0.9607

Figure 207 n_op 16 cold side linear surrogate parameter estimates

Quadratic

Cold Side [K] Predicted RMSE=1.3458 RSq=0.99
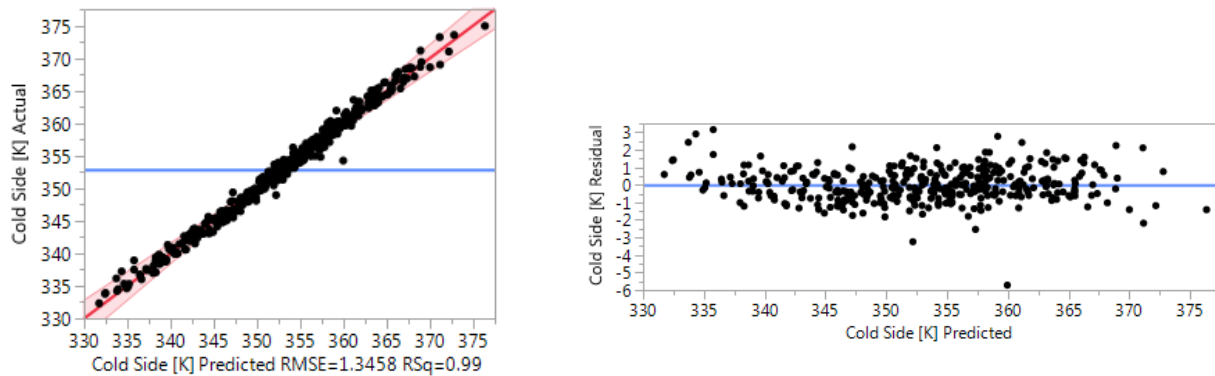
Figure 208 n_op 16 cold side quadratic surrogate actual vs predicted and residuals

Term	Estimate	Std Error	t Ratio		Prob>|t|
FSL_x	22.478258	0.325426	69.07		<.0001*
Th_f	850.11247	25.28788	33.62		<.0001*
(FSL_x-0.49987)*(FSL_x-0.49987)	-39.88033	1.287242	-30.98		<.0001*
t_in	0.4943046	0.022123	22.34		<.0001*
Q_f	23.328979	1.341614	17.39		<.0001*
L_fs	355.16425	26.00933	13.66		<.0001*
Q_fs	0.5007446	0.039605	12.64		<.0001*
v_in	-3.105006	0.249687	-12.44		<.0001*
(Th_f-0.0265)*(FSL_x-0.49987)	785.16044	91.95075	8.54		<.0001*
sig	-0.275684	0.032305	-8.53		<.0001*
(Th_w-0.1)*(FSL_x-0.49987)	-323.0333	59.25751	-5.45		<.0001*
(sig-5.05072)*(sig-5.05072)	0.0662856	0.01337	4.96		<.0001*
(PL-0.625)*(PL-0.625)	83.387796	20.42469	4.08		<.0001*
L_nb	-101.1244	25.91008	-3.90		0.0001*
p_nb	0.0011887	0.000361	3.29		0.0012*
(FSL_x-0.49987)*(Q_f-1)	14.507512	4.682656	3.10		0.0022*
Th_w	50.17391	16.32041	3.07		0.0024*
(L_f-19.978)*(FSL_x-0.49987)	-3.349166	1.097248	-3.05		0.0026*
PL	3.7459195	1.227488	3.05		0.0026*
(FSL_x-0.49987)*(v_in-7.78747)	-2.527818	0.833178	-3.03		0.0028*
(Th_f-0.0265)*(Q_f-1)	1041.4982	376.079	2.77		0.0062*
(Th_f-0.0265)*(v_in-7.78747)	-186.3488	70.31626	-2.65		0.0087*
(Q_fs-9.11574)*(v_in-7.78747)	-0.295574	0.115393	-2.56		0.0112*
(L_fs-0.011)*(sig-5.05072)	-20.87565	8.281117	-2.52		0.0125*
(FL_x-0.50001)*(p_out-2.60582)	-10.97293	4.484407	-2.45		0.0153*
(L_fs-0.011)*(FSL_x-0.49987)	-197.4271	88.7032	-2.23		0.0272*
(L_fs-0.011)*(Q_fs-9.11574)	19.742995	9.915484	1.99		0.0479*
(L_fs-0.011)*(L_nb-0.0624)	12175.783	6269.586	1.94		0.0536

Figure 209 n_op 16 cold side quadratic surrogate parameter estimates
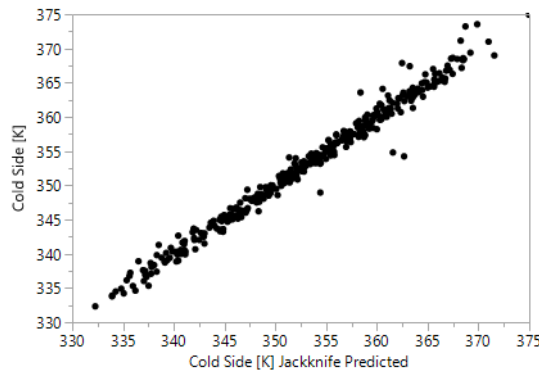
Gaussian Process

Figure 210 n_op 16 cold side Gaussian Process surrogate actual vs jackknife predicted

287

Table 47 n_op 16 cold side Gaussian Process surrogate parameters and sensitivities

Parameter	θ	Total Sensitivity	Main Effect
FSL_x	1.1328	0.6861	0.6635
Th_f	346.81	0.1426	0.1298
t_in	0.0000	0.0614	0.0610
Q_f	0.1970	0.0390	0.0368
L_fs	278.65	0.0309	0.0282
Q_fs	0.0002	0.0196	0.0181
v_in	0.0046	0.0191	0.0178
sig	0.0006	0.0109	0.0099
Th_w	48.678	0.0070	0.0018
L_nb	7.0429	0.0029	0.0027
L_f	0.0127	0.0026	0.0001
PL	0.5456	0.0018	0.0014
p_nb	0.0000	0.0016	0.0015
Th_p	19.149	0.0001	0.0001
FL_x	0.0037	0.0001	0.0000
k_sand	0.0000	0.0000	0.0000
p_out	0.0004	0.0000	0.0000
FL_y	0.0004	0.0000	0.0000

Maximum Temperature Prediction
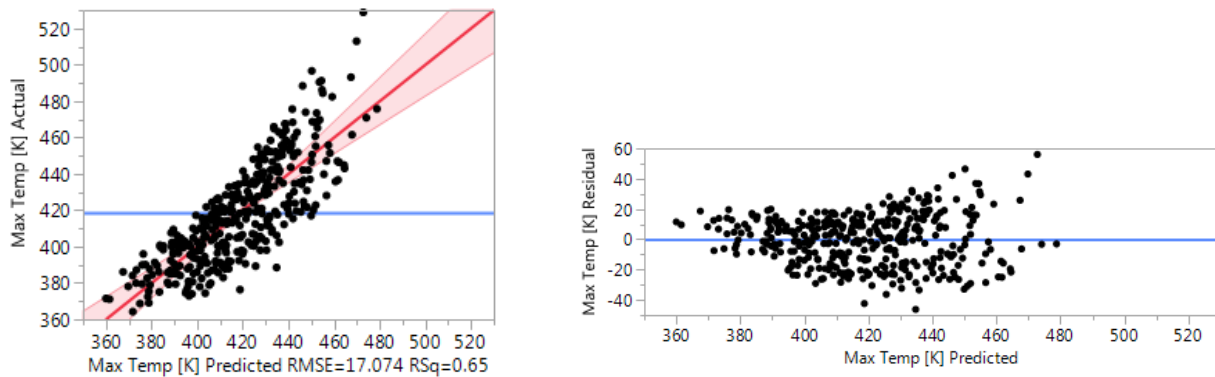
Linear

Figure 211 n_op 16 Maximum temperature linear surrogate actual vs predicted and residuals

Term	Estimate	Std Error	t Ratio		Prob>|t|
L_fs	4126.2777	217.0951	19.01		<.0001*
Q_fs	4.2679718	0.383103	11.14		<.0001*
Th_f	2272.0277	234.0059	9.71		<.0001*
Q_f	82.26707	12.6663	6.49		<.0001*
FSL_x	14.523536	3.03947	4.78		<.0001*
sig	0.8831678	0.307049	2.88		0.0043*
PL	30.535078	12.16246	2.51		0.0125*
v_in	-5.554075	2.382517	-2.33		0.0203*
Th_w	259.08005	152.0035	1.70		0.0892
k_sand	3.995531	2.697155	1.48		0.1394
p_nb	-0.004263	0.00304	-1.40		0.1616
p_out	8.1658876	5.82492	1.40		0.1618
t_in	0.2681865	0.202568	1.32		0.1864
FL_y	-11.79253	12.14754	-0.97		0.3323
L_nb	-142.3714	237.4357	-0.60		0.5491
Th_p	575.27745	1519.215	0.38		0.7052
L_f	0.9175154	3.041109	0.30		0.7631
FL_x	0.9752205	6.074051	0.16		0.8725

Figure 212 n_op 16 Maximum temperature linear surrogate parameter estimates
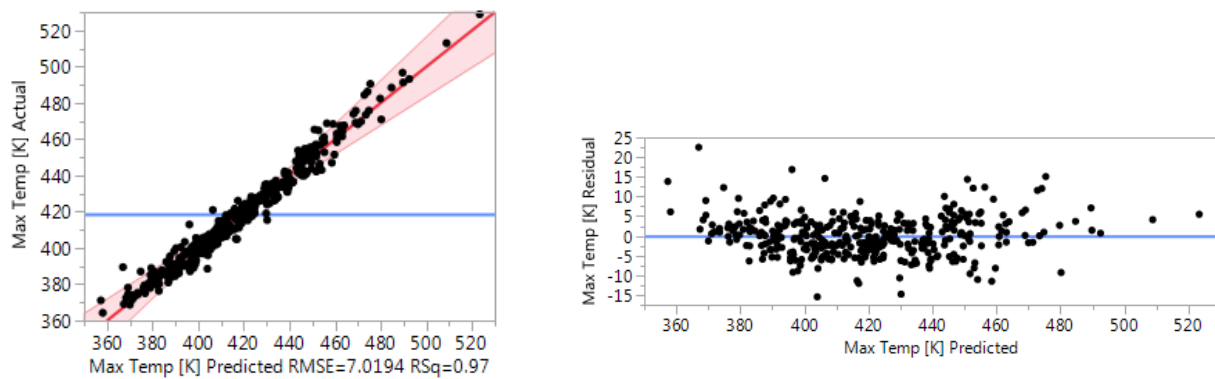
Quadratic

Figure 213 n_op 16 Maximum temperature quadratic surrogate actual vs predicted and residuals

289

Term	Estimate	Std Error	t Ratio		Prob>|t|
L_fs	4295.7604	135.6692	31.66		<.0001*
(FSL_x-0.49987)*(FSL_x-0.49987)	-201.2364	6.714481	-29.97		<.0001*
Q_fs	4.8327322	0.206588	23.39		<.0001*
Th_f	2325.8396	131.906	17.63		<.0001*
Q_f	87.212602	6.998093	12.46		<.0001*
FSL_x	16.924769	1.697479	9.97		<.0001*
PL	50.762353	6.402793	7.93		<.0001*
(L_fs-0.011)*(Q_fs-9.11574)	375.50861	51.7209	7.26		<.0001*
v_in	-6.710649	1.302413	-5.15		<.0001*
t_in	0.5004592	0.115399	4.34		<.0001*
sig	0.6806289	0.168506	4.04		<.0001*
(L_nb-0.0624)*(FSL_x-0.49987)	1647.7063	432.1934	3.81		0.0002*
(sig-5.05072)*(sig-5.05072)	-0.252672	0.069739	-3.62		0.0004*
(Th_p-0.05)*(FL_x-0.50001)	-23387.4	6580.102	-3.55		0.0005*
(L_fs-0.011)*(Q_f-1)	5546.8091	1752.08	3.17		0.0018*
(FL_y-0.62501)*(v_in-7.78747)	58.887782	18.92817	3.11		0.0022*
(L_fs-0.011)*(L_fs-0.011)	107499.98	37168.5	2.89		0.0043*
(FL_x-0.50001)*(p_out-2.60582)	-66.21959	23.39145	-2.83		0.0051*
(L_fs-0.011)*(FSL_x-0.49987)	-1253.66	462.6914	-2.71		0.0074*
p_nb	-0.005034	0.001883	-2.67		0.0082*
(FL_y-0.62501)*(L_f-19.978)	-62.43676	25.23114	-2.47		0.0142*
(L_fs-0.011)*(k_sand-5.62998)	915.59628	378.7583	2.42		0.0166*
(FL_y-0.62501)*(p_nb-500.038)	-0.060794	0.025424	-2.39		0.0178*
p_out	7.7980952	3.301984	2.36		0.0192*
(FL_x-0.50001)*(p_nb-500.038)	-0.02801	0.012763	-2.19		0.0294*
(PL-0.625)*(PL-0.625)	233.134	106.5387	2.19		0.0299*
(Th_p-0.05)*(sig-5.05072)	631.91927	289.1426	2.19		0.0301*
(FSL_x-0.49987)*(t_in-127.5)	0.873018	0.403828	2.16		0.0319*
(FL_x-0.50001)*(k_sand-5.62998)	23.481143	11.22072	2.09		0.0377*
(FL_y-0.62501)*(k_sand-5.62998)	40.595362	20.03046	2.03		0.0441*
(sig-5.05072)*(t_in-127.5)	0.0794093	0.040815	1.95		0.0532

Figure 214 n_op 16 Maximum temperature quadratic surrogate parameter estimates
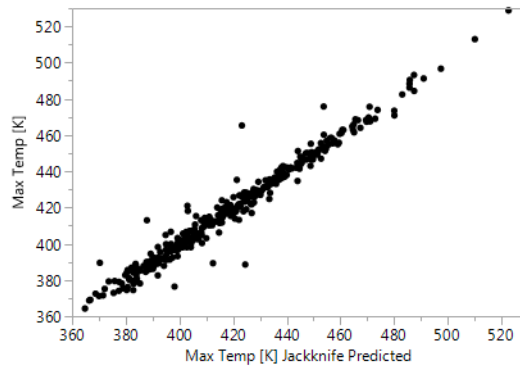
Gaussian Process

Figure 215 n_op 16 Maximum temperature Gaussian Process surrogate actual vs jackknife predicted

Table 48 n_op 16 Maximum temperature Gaussian Process surrogate parameters and sensitivities

Parameter	θ	Total Sensitivity	Main Effect
L_fs	591.46	0.3969	0.3500
FSL_x	3.7246	0.3093	0.2750
Q_fs	0.0016	0.1844	0.1510
Th_f	172.21	0.0953	0.0906
Q_f	0.3668	0.0461	0.0416
PL	0.0246	0.0103	0.0099
v_in	0.0021	0.0051	0.0047
t_in	0.0000	0.0046	0.0042
sig	0.0000	0.0035	0.0033
L_f	0.0034	0.0032	0.0005
Th_w	2.4255	0.0019	0.0011
p_nb	0.0000	0.0013	0.0012
L_nb	0.6871	0.0004	0.0004
k_sand	0.0002	0.0002	0.0000
Th_p	58.885	0.0000	0.0000
FL_y	0.0014	0.0000	0.0000
FL_x	0.0001	0.0000	0.0000
p_out	0.0001	0.0000	0.0000

Energy Error

Sample 132 had an anomalous energy balance error of 2.247. There is no clear indication how this error was generated. It was removed from these statistics.
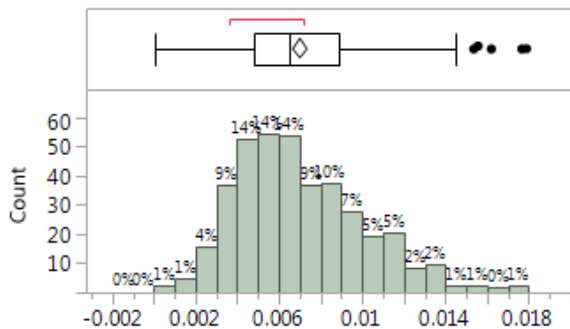
Figure 216 n_op 16 distribution of energy

Table 49 Statistics for energy balance errors for

n_op 16 Energy Balance Statistics	
Mean	0.007016
Std Dev	0.003016
maximum	0.017888
minimum	4.51E-05

Parameter	Total Sensitivity	Main Effect
Th_f	0.3527	0.2919
Th_w	0.2025	0.1303
v_in	0.1272	0.1019
t_in	0.0949	0.0849
Q_f	0.0851	0.0633
PL	0.0813	0.0088
p_out	0.0246	0.0065
L_nb	0.0241	0.0084
Th_p	0.0176	0.0129
FL_x	0.0174	0.0144
k_sand	0.0168	0.0000
sig	0.0131	0.0010
L_f	0.0070	0.0005
p_nb	0.0021	0.0016
FL_y	0.0018	0.0010
FSL_x	0.0000	0.0000
Q_fs	0.0000	0.0000
L_fs	0.0000	0.0000

n_op 8

Hot Side Temperature Prediction
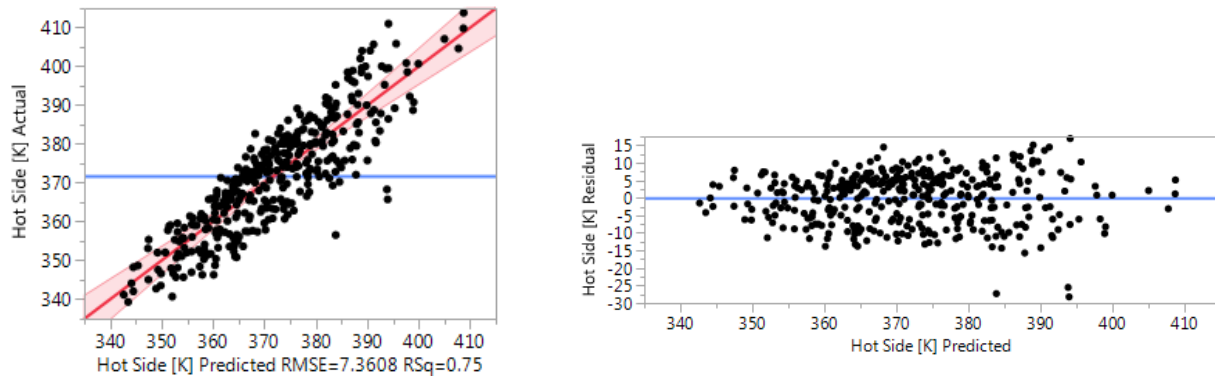
Linear

Figure 217 n_op 8 hot side linear surrogate actual vs predicted and residuals

Term	Estimate	Std Error	t Ratio		Prob>|t|
FSL_x	29.753763	1.310415	22.71		<.0001*
Th_f	1449.7339	100.8834	14.37		<.0001*
L_fs	1076.6256	93.59298	11.50		<.0001*
PL	50.571007	5.243426	9.64		<.0001*
Q_f	43.649809	5.460636	7.99		<.0001*
Q_fs	1.1864577	0.165161	7.18		<.0001*
t_in	0.4631164	0.08733	5.30		<.0001*
v_in	-4.307459	1.027139	-4.19		<.0001*
sig	0.2217966	0.132374	1.68		0.0947
FL_y	7.6934154	5.236988	1.47		0.1427
Th_w	95.557897	65.53101	1.46		0.1457
L_nb	-124.314	102.3621	-1.21		0.2254
k_sand	1.1430764	1.162785	0.98		0.3262
p_nb	-0.001174	0.00131	-0.90		0.3711
p_out	1.4266221	2.511211	0.57		0.5703
Th_p	339.19114	654.9565	0.52		0.6049
FL_x	0.8821297	2.618616	0.34		0.7364
L_f	0.0879274	1.311067	0.07		0.9466

Figure 218 n_op 8 hot side linear surrogate parameter estimates
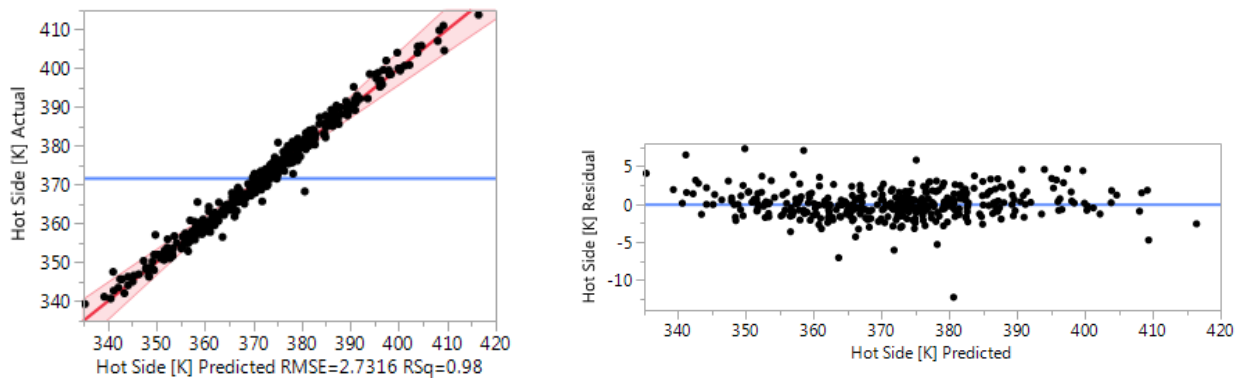
Quadratic

Figure 219 n_op 8 hot side quadratic surrogate actual vs predicted and residuals

293

Term	Estimate	Std Error	t Ratio		Prob>|t|
FSL_x	29.749342	0.660555	45.04		<.0001*
(FSL_x-0.49987)*(FSL_x-0.49987)	-83.03264	2.61311	-31.78		<.0001*
Th_f	1492.0878	51.32843	29.07		<.0001*
PL	56.775878	2.491502	22.79		<.0001*
L_fs	1083.532	52.7921	20.52		<.0001*
Q_fs	1.4432919	0.080389	17.95		<.0001*
Q_f	44.239666	2.723164	16.25		<.0001*
t_in	0.5132879	0.044905	11.43		<.0001*
v_in	-4.316598	0.506807	-8.52		<.0001*
(PL-0.625)*(FSL_x-0.49987)	66.762919	9.245429	7.22		<.0001*
(Th_f-0.0265)*(FSL_x-0.49987)	987.82988	186.6422	5.29		<.0001*
(PL-0.625)*(PL-0.625)	201.35234	41.45668	4.86		<.0001*
FL_y	12.06048	2.704082	4.46		<.0001*
(Th_w-0.1)*(FSL_x-0.49987)	-467.0132	120.2788	-3.88		0.0001*
(L_fs-0.011)*(Q_fs-9.11574)	77.656662	20.12557	3.86		0.0002*
(L_fs-0.011)*(FSL_x-0.49987)	-661.2545	180.0601	-3.67		0.0003*
(Th_f-0.0265)*(PL-0.625)	2296.451	734.3073	3.13		0.0020*
(FL_y-0.62501)*(v_in-7.78747)	21.5422	7.365443	2.92		0.0039*
(Th_p-0.05)*(FSL_x-0.50001)	-7401.933	2560.497	-2.89		0.0043*
(FL_x-0.50001)*(p_nb-500.038)	-0.013111	0.004967	-2.64		0.0090*
(L_f-19.978)*(FSL_x-0.49987)	-5.713635	2.227291	-2.57		0.0111*
(FL_x-0.50001)*(p_out-2.60582)	-22.39518	9.102161	-2.46		0.0148*
(v_in-7.78747)*(k_sand-5.62998)	-3.644537	1.481403	-2.46		0.0148*
(L_fs-0.011)*(Q_f-1)	1622.8629	681.777	2.38		0.0183*
(FSL_x-0.49987)*(Q_f-1)	22.420381	9.504882	2.36		0.0193*
(FL_x-0.50001)*(k_sand-5.62998)	9.8829083	4.36626	2.26		0.0247*
(L_fs-0.011)*(v_in-7.78747)	-283.6262	130.477	-2.17		0.0310*
(Th_f-0.0265)*(FL_y-0.62501)	-1530.827	723.5838	-2.12		0.0357*
(Th_w-0.1)*(PL-0.625)	-957.6188	454.5503	-2.11		0.0365*
(FL_y-0.62501)*(L_f-19.978)	-20.68357	9.818018	-2.11		0.0365*
(Th_f-0.0265)*(Q_f-1)	1575.0303	763.3451	2.06		0.0404*
(FL_x-0.50001)*(Q_fs-9.11574)	1.2106443	0.613465	1.97		0.0499*
(Th_f-0.0265)*(L_fs-0.011)	26616.721	13943.25	1.91		0.0578
(FSL_x-0.49987)*(v_in-5.05072)	0.4167275	0.222911	1.87		0.0620

Figure 220 n_op 8 hot side quadratic surrogate parameter estimates

Gaussian Process

Figure 221 n_op 8 hot side Gaussian Process surrogate actual vs jackknife predicted

Table 51 n_op 8 hot side Gaussian Process surrogate parameters and sensitivities

Parameter	θ	Total Sensitivity	Main Effect
FSL_x	1.5100	0.5416	0.5101
Th_f	283.06	0.1564	0.1446
L_fs	398.86	0.1032	0.0924
PL	1.0124	0.0885	0.0743
Q_fs	0.0008	0.0602	0.0518
Q_f	0.4838	0.0470	0.0431
t_in	0.0000	0.0227	0.0225
v_in	0.0038	0.0115	0.0106
L_f	0.0282	0.0038	0.0004
Th_w	23.052	0.0037	0.0003
FL_y	0.0233	0.0037	0.0034
sig	0.0000	0.0002	0.0002
Th_p	36.805	0.0002	0.0002
p_nb	0.0000	0.0000	0.0000
k_sand	0.0000	0.0000	0.0000
L_nb	0.0278	0.0000	0.0000
p_out	0.0002	0.0000	0.0000
FL_x	0.0000	0.0000	0.0000

Cold Side Temperature Prediction
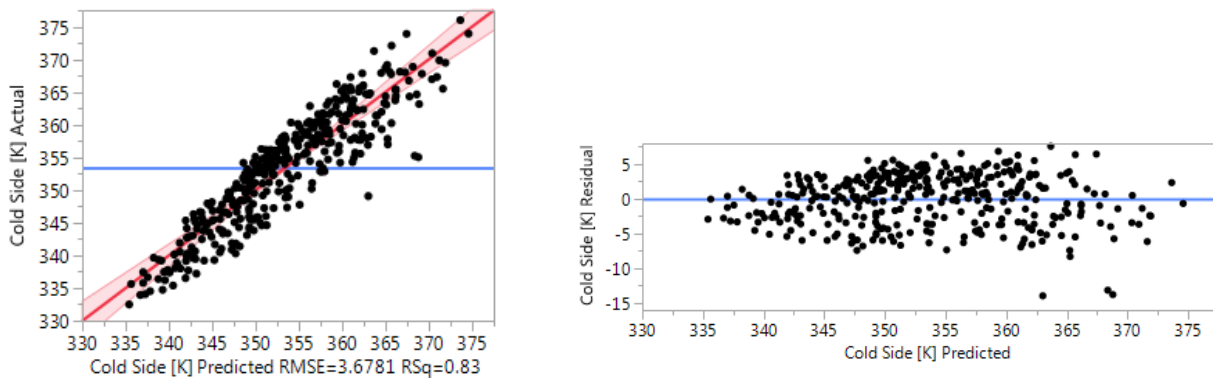
Linear

Figure 222 n_op 8 cold side linear surrogate actual vs predicted and residuals

Term	Estimate	Std Error	t Ratio		Prob>|t|
FSL_x	22.734284	0.654803	34.72		<.0001*
Th_f	822.98537	50.4106	16.33		<.0001*
t_in	0.4851216	0.043638	11.12		<.0001*
Q_f	23.9939	2.728633	8.79		<.0001*
L_fs	306.55098	46.76762	6.55		<.0001*
v_in	-3.202603	0.513252	-6.24		<.0001*
Q_fs	0.3661736	0.08253	4.44		<.0001*
sig	-0.239474	0.066146	-3.62		0.0003*
Th_w	104.58718	32.74529	3.19		0.0015*
L_nb	-157.9966	51.14947	-3.09		0.0022*
FL_y	-3.003366	2.616879	-1.15		0.2519
k_sand	0.658099	0.581034	1.13		0.2581
p_nb	0.0006884	0.000655	1.05		0.2938
PL	2.0558924	2.620095	0.78		0.4332
L_f	0.1256236	0.655129	0.19		0.8480
p_out	0.1704469	1.254831	0.14		0.8920
Th_p	34.484833	327.2762	0.11		0.9161
FL_x	-0.023567	1.3085	-0.02		0.9856

Figure 223 n_op 8 cold side linear surrogate parameter estimates
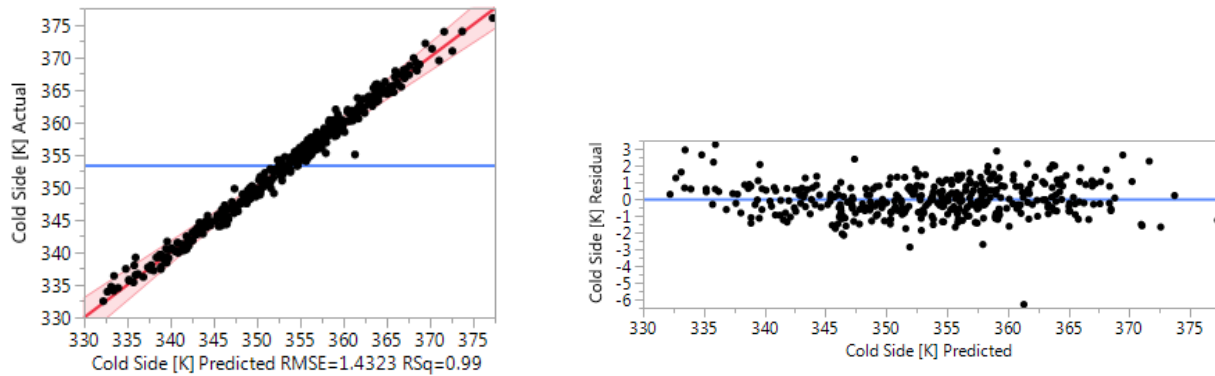
Quadratic

Figure 224 n_op 8 cold side quadratic surrogate actual vs predicted and residuals

Term	Estimate	Std Error	t Ratio		Prob>|t|
FSL_x	22.648036	0.346353	65.39		<.0001*
Th_f	879.60623	26.91333	32.68		<.0001*
(FSL_x-0.49987)*(FSL_x-0.49987)	-41.06697	1.370147	-29.97		<.0001*
t_in	0.5028476	0.023545	21.36		<.0001*
Q_f	24.286631	1.427852	17.01		<.0001*
L_fs	333.38161	27.68079	12.04		<.0001*
Q_fs	0.4948797	0.042151	11.74		<.0001*
v_in	-3.064542	0.265737	-11.53		<.0001*
(Th_f-0.0265)*(FSL_x-0.49987)	869.19113	97.8632	8.88		<.0001*
sig	-0.272551	0.034381	-7.93		<.0001*
(Th_w-0.1)*(FSL_x-0.49987)	-314.2908	63.06646	-4.98		<.0001*
(PL-0.625)*(PL-0.625)	103.50157	21.73722	4.76		<.0001*
(sig-5.05072)*(sig-5.05072)	0.0667477	0.014229	4.69		<.0001*
PL	5.3767609	1.306384	4.12		<.0001*
Th_w	63.523298	17.36934	3.66		0.0003*
(FL_x-0.50001)*(p_out-2.60582)	-14.05459	4.772589	-2.94		0.0036*
(Th_f-0.0265)*(Q_f-1)	1171.0863	400.2492	2.93		0.0039*
(L_f-19.978)*(FSL_x-0.49987)	-3.389643	1.167849	-2.90		0.0041*
p_nb	0.0011127	0.000384	2.90		0.0042*
(FSL_x-0.49987)*(Q_f-1)	14.189004	4.98375	2.85		0.0049*
(Th_f-0.0265)*(v_in-7.78747)	-210.7884	74.83523	-2.82		0.0054*
(FSL_x-0.49987)*(v_in-7.78747)	-2.490404	0.886827	-2.81		0.0055*
(Q_fs-9.11574)*(v_in-7.78747)	-0.338307	0.122809	-2.75		0.0064*
(L_fs-0.011)*(Q_fs-9.11574)	28.406555	10.55256	2.69		0.0077*
L_nb	-71.19397	27.57494	-2.58		0.0106*
(L_fs-0.011)*(FSL_x-0.49987)	-230.1735	94.41194	-2.44		0.0157*
(FL_x-0.50001)*(L_nb-0.0624)	390.51137	175.6385	2.22		0.0274*
(Th_p-0.05)*(Th_w-0.1)	69497.448	33082.06	2.10		0.0370*
(L_fs-0.011)*(p_nb-500.038)	0.1827945	0.090907	2.01		0.0458*
(L_f-19.978)*(L_f-19.978)	-2.742683	1.381723	-1.98		0.0486*
(FSL_x-0.49987)*(sig-5.05072)	0.2239337	0.116828	1.92		0.0568

Figure 225 n_op 8 cold side quadratic surrogate parameter estimates
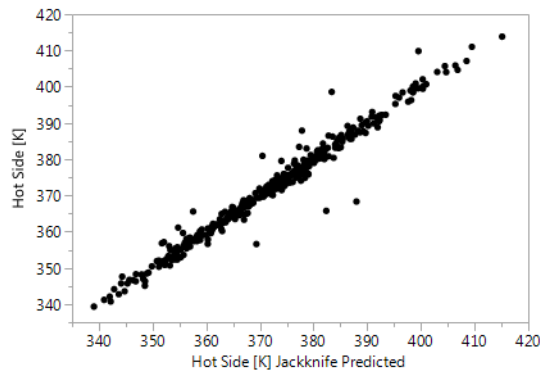
12.2.1.1.1 Gaussian Process
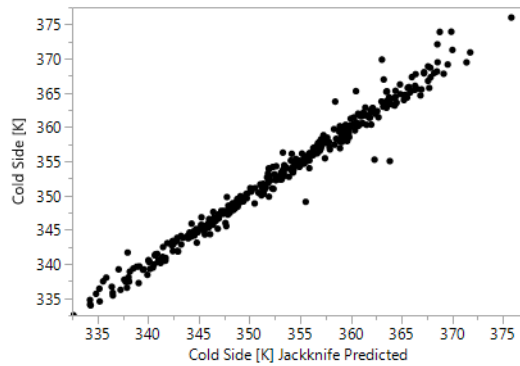
Figure 226 n_op 8 cold side Gaussian Process surrogate actual vs jackknife predicted

Table 52 n_op 8 cold side Gaussian Process surrogate parameters and sensitivities

Parameter	θ	Total Sensitivity	Main Effect
FSL_x	1.1685	0.6874	0.6653
Th_f	274.51	0.1458	0.1330
t_in	0.0000	0.0609	0.0605
Q_f	0.2080	0.0383	0.0363
L_fs	228.22	0.0266	0.0233
Q_fs	0.0004	0.0214	0.0187
v_in	0.0047	0.0183	0.0169
sig	0.0006	0.0103	0.0094
Th_w	62.922	0.0077	0.0028
PL	0.6573	0.0037	0.0030
L_f	0.0128	0.0025	0.0000
p_nb	0.0000	0.0014	0.0014
L_nb	3.3968	0.0014	0.0014
k_sand	0.0001	0.0001	0.0001
Th_p	15.120	0.0001	0.0001
FL_x	0.0060	0.0001	0.0000
p_out	0.0043	0.0001	0.0000
FL_y	0.0072	0.0000	0.0000

Maximum Temperature Prediction
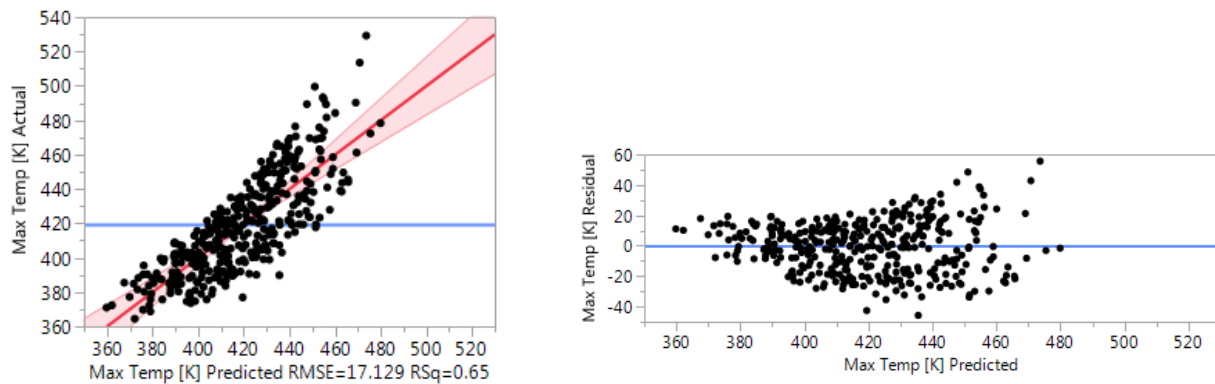
Linear

Figure 227 n_op 8 Maximum temperature linear surrogate actual vs predicted and residuals

298

Term	Estimate	Std Error	t Ratio		Prob>|t|
L_fs	4186.473	217.7911	19.22		<.0001*
Q_fs	4.2969471	0.384331	11.18		<.0001*
Th_f	2285.9854	234.756	9.74		<.0001*
Q_f	84.193958	12.70691	6.63		<.0001*
FSL_x	14.581619	3.04934	4.78		<.0001*
sig	0.8460273	0.308034	2.75		0.0063*
PL	31.796608	12.20147	2.61		0.0095*
v_in	-5.556797	2.390154	-2.32		0.0206*
Th_w	266.5778	152.4908	1.75		0.0813
k_sand	4.0791366	2.705803	1.51		0.1325
p_nb	-0.004112	0.003049	-1.35		0.1784
p_out	7.8272139	5.843594	1.34		0.1813
t_in	0.2705132	0.203217	1.33		0.1840
FL_y	-11.90336	12.18649	-0.98		0.3293
L_nb	-220.7485	238.1969	-0.93		0.3547
Th_p	504.61797	1524.086	0.33		0.7408
L_f	0.783611	3.050857	0.26		0.7974
FL_x	1.1181093	6.093526	0.18		0.8545

Figure 228 n_op 8 Maximum temperature linear surrogate parameter estimates
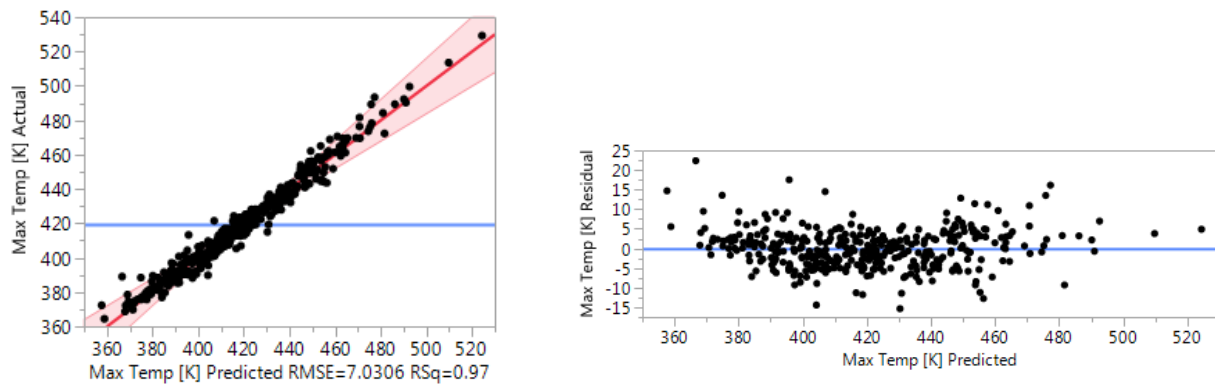
Quadratic

Figure 229 n_op 8 Maximum temperature quadratic surrogate actual vs predicted and residuals

299

Term	Estimate	Std Error	t Ratio		Prob>|t|
L_fs	4332.4215	135.8766	31.88		<.0001*
(FSL_x-0.49987)*(FSL_x-0.49987)	-202.8358	6.725636	-30.16		<.0001*
Q_fs	4.8765766	0.206905	23.57		<.0001*
Th_f	2335.6302	132.1094	17.68		<.0001*
Q_f	88.101631	7.008893	12.57		<.0001*
FSL_x	17.089689	1.700141	10.05		<.0001*
PL	52.455302	6.412641	8.18		<.0001*
(L_fs-0.011)*(Q_fs-9.11574)	368.90975	51.79929	7.12		<.0001*
v_in	-6.432465	1.304423	-4.93		<.0001*
t_in	0.496494	0.115576	4.30		<.0001*
(L_nb-0.0624)*(FSL_x-0.49987)	1706.6436	432.8563	3.94		0.0001*
sig	0.650522	0.168764	3.85		0.0002*
(sig-5.05072)*(sig-5.05072)	-0.252822	0.069845	-3.62		0.0004*
(Th_p-0.05)*(FL_x-0.50001)	-23356.11	6590.219	-3.54		0.0005*
(L_fs-0.011)*(Q_f-1)	5645.7121	1754.761	3.22		0.0015*
(FL_y-0.62501)*(v_in-7.78747)	57.883054	18.95721	3.05		0.0026*
(FL_x-0.50001)*(p_out-2.60582)	-65.16918	23.42719	-2.78		0.0060*
(FL_y-0.62501)*(L_f-19.978)	-66.11609	25.26966	-2.62		0.0096*
(L_fs-0.011)*(FSL_x-0.49987)	-1198.863	463.4395	-2.59		0.0104*
p_out	8.4360677	3.307041	2.55		0.0115*
p_nb	-0.00477	0.001886	-2.53		0.0123*
(FL_y-0.62501)*(p_nb-500.038)	-0.062888	0.025462	-2.47		0.0144*
(L_fs-0.011)*(L_fs-0.011)	91426.465	37225.58	2.46		0.0149*
(PL-0.625)*(PL-0.625)	258.33301	106.7014	2.42		0.0164*
(L_fs-0.011)*(v_in-7.78747)	-765.9299	335.8222	-2.28		0.0237*
(Th_p-0.05)*(sig-5.05072)	654.04148	289.5852	2.26		0.0250*
(L_fs-0.011)*(k_sand-5.62998)	835.06562	379.3353	2.20		0.0289*
(FSL_x-0.49987)*(t_in-127.5)	0.8870858	0.404453	2.19		0.0295*
(FL_y-0.62501)*(k_sand-5.62998)	43.603984	20.061	2.17		0.0310*
(sig-5.05072)*(t_in-127.5)	0.0887891	0.040877	2.17		0.0311*
(FL_x-0.50001)*(p_nb-500.038)	-0.027388	0.012783	-2.14		0.0334*
(FL_x-0.50001)*(k_sand-5.62998)	22.588999	11.2379	2.01		0.0458*
(L_f-19.978)*(p_out-2.60582)	24.940554	12.58793	1.98		0.0490*
(L_f-19.978)*(Q_f-1)	45.074337	24.03232	1.88		0.0622

Figure 230 n_op 8 Maximum temperature quadratic surrogate parameter estimates
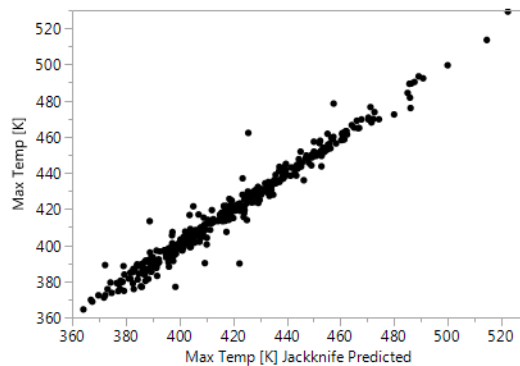
Gaussian Process

Figure 231 n_op 8 Maximum temperature Gaussian Process surrogate actual vs jackknife predicted

Table 53 n_op 8 Maximum temperature Gaussian Process surrogate parameters and sensitivities

Parameter	θ	Total Sensitivity	Main Effect
L_fs	877.59	0.3965	0.3471
FSL_x	4.0228	0.3081	0.2729
Q_fs	0.0016	0.1850	0.1520
Th_f	127.58	0.0937	0.0898
Q_f	0.8790	0.0487	0.0432
PL	0.0495	0.0111	0.0107
v_in	0.0170	0.0056	0.0046
t_in	0.0000	0.0040	0.0036
L_f	0.0028	0.0035	0.0006
sig	0.0000	0.0031	0.0028
Th_w	4.6494	0.0023	0.0014
p_nb	0.0000	0.0012	0.0010
L_nb	81.020	0.0010	0.0003
Th_p	44.485	0.0000	0.0000
k_sand	0.0001	0.0000	0.0000
FL_x	0.0004	0.0000	0.0000
FL_y	0.0005	0.0000	0.0000
p_out	0.0000	0.0000	0.0000
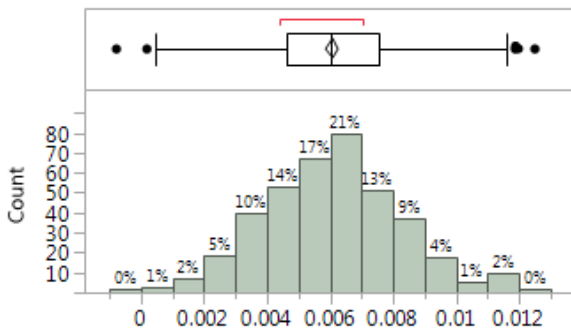
Energy Error

Figure 232 n_op 8 distribution of energy balance errors

Table 54 Statistics for energy balance errors for n_op 8

n_op 8 Energy Balance Statistics	
Mean	0.006059
Std Dev	0.002147
maximum	0.012494
minimum	-0.00077

Table 55 Total Sensitivity and Main Effects of the parameters on the energy balance error for n_op 8

Parameter	Total Sensitivity	Main Effect
Th_w	0.36489	0.32074
Th_f	0.22785	0.20974
v_in	0.18685	0.15684
Q_f	0.06619	0.05446
PL	0.07537	0.02960
t_in	0.03024	0.02698
FL_x	0.03073	0.01714
L_fs	0.00533	0.00353
L_f	0.00346	0.00183
p_nb	0.00559	0.00145
p_out	0.00586	0.00103
Th_p	0.01857	0.00054
k_sand	0.00505	0.00039
FSL_x	0.00185	0.00037
L_nb	0.00431	0.00010
Q_fs	0.00000	0.00000
sig	0.00000	0.00000
FL_y	0.00000	0.00000

Grid Convergence

Table 56 LogWorth for each of the parameters at each of the grid refinement levels for the linear, cold side temperature

Parameter	n_op 50	32	16	8
FSL_x	121.08	118.20	120.19	116.37
Th_f	46.837	44.463	45.019	44.535
t_in	24.968	25.198	25.581	24.163
Q_f	16.505	16.250	16.877	16.220
L_fs	12.366	12.524	12.421	9.7150
v_in	10.491	9.9300	9.8270	8.9110
Q_fs	5.1110	5.2110	5.3860	4.9160
Th_w	4.7950	4.2490	2.2770	2.8160
sig	4.4210	3.8070	4.1200	3.4730
L_nb	3.9680	4.0470	3.9160	2.6650
PL	1.0400	1.0820	0.0550	0.3630
p_nb	0.5910	0.4560	0.6740	0.5320
k_sand	0.4820	0.5710	0.6180	0.5880
FL_y	0.3310	0.3540	0.5810	0.5990
L_f	0.1750	0.1080	0.0400	0.0720
Th_p	0.0950	0.1230	0.0240	0.0380
p_out	0.0150	0.0440	0.0170	0.0500
FL_x	0.0040	0.0480	0.0340	0.0060

Table 57 LogWorth for each of the parameters at each of the grid refinement levels for the linear, Maximum temperature

Parameter	n_op			
	50	32	16	8
L_fs	54.864	55.879	55.592	56.484
Q_fs	24.015	24.488	24.249	24.393
Th_f	19.204	19.380	19.227	19.323
Q_f	9.6130	9.8140	9.5600	9.9010
FSL_x	5.6190	5.7980	5.5890	5.5960
sig	2.4640	2.3740	2.3700	2.1990
PL	2.3550	2.4290	1.9030	2.0200
v_in	1.5680	1.5570	1.6930	1.6850
Th_w	1.3440	1.5690	1.0500	1.0900
k_sand	0.9160	0.9090	0.8560	0.8780
p_out	0.7960	0.7890	0.7910	0.7420
p_nb	0.7940	0.7360	0.7910	0.7490
t_in	0.7430	0.7040	0.7300	0.7350
FL_y	0.5700	0.6040	0.4780	0.4820
L_nb	0.2590	0.3070	0.2600	0.4500
Th_p	0.1220	0.0790	0.1520	0.1300
L_f	0.1060	0.1340	0.1170	0.0980
FL_x	0.0220	0.0330	0.0590	0.0680

Table 58 LogWorth for the significant (p ≤ 0.05) parameters at each of the grid refinement levels for the quadratic, cold side temperature.

n_op			
50	32	16	8
FSL_x 135.47	FSL_x 130.48	FSL_x 135.83	FSL_x 131.49
Th_f 81.487	Th_f 76.335	Th_f 81.182	Th_f 79.197
FSL_x*FSL_x 73.921	FSL_x*FSL_x 71.357	FSL_x*FSL_x 75.478	FSL_x*FSL_x 73.209
t_in 53.916	t_in 51.890	t_in 54.331	t_in 51.661
Q_f 40.041	Q_f 37.422	Q_f 40.420	Q_f 39.307
L_fs 28.905	L_fs 26.873	L_fs 29.300	L_fs 24.463
v_in 28.019	v_in 26.285	Q_fs 26.258	Q_fs 23.560
Q_fs 23.522	Q_fs 24.274	v_in 25.635	v_in 22.940
sig 15.479	sig 12.755	Th_f*FSL_x 14.366	Th_f*FSL_x 15.304
Th_f*FSL_x 13.593	Th_f*FSL_x 12.513	sig 14.352	sig 12.732
Th_w 8.2580	PL 6.8650	Th_w*FSL_x 6.8120	Th_w*FSL_x 5.8540
PL 7.9440	Th_w 6.3730	sig*sig 5.8030	PL*PL 5.4200
PL*PL 6.7790	Th_w*FSL_x 5.6550	PL*PL 4.1840	sig*sig 5.2850
Th_w*FSL_x 5.2130	PL*PL 5.0470	L_nb 3.8800	PL 4.2410
sig*sig 4.3680	sig*sig 4.3750	p_nb 2.9260	Th_w 3.4810
L_nb 4.3010	L_nb 3.8290	FSL_x*Q_f 2.6490	FL_x*p_out 2.4400
Th_f*Q_f 2.8540	Th_f*Q_f 3.0710	Th_w 2.6160	Th_f*Q_f 2.4140
FSL_x*v_in 2.8400	Th_f*v_in 2.5940	L_f*FSL_x 2.5860	L_f*FSL_x 2.3830
L_f*FSL_x 2.7860	FSL_x*Q_f 2.5720	PL 2.5850	p_nb 2.3740
p_nb 2.7460	L_f*FSL_x 2.3730	FSL_x*v_in 2.5600	FSL_x*Q_f 2.3100
FL_x*p_out 2.4780	L_fs*FSL_x 2.3170	Th_f*Q_f 2.2090	Th_f*v_in 2.2700
Q_fs*v_in 2.1900	FSL_x*v_in 2.1190	Th_f*v_in 2.0590	FSL_x*v_in 2.2590
Th_f*v_in 2.1530	L_fs*p_nb 2.1020	Q_fs*v_in 1.9510	Q_fs*v_in 2.1910
FSL_x*Q_f 2.1460	FL_x*p_out 2.0430	L_fs*sig 1.9020	L_fs*Q_fs 2.1110
L_fs*p_nb 2.0510	p_nb 1.7480	FL_x*p_out 1.8150	L_nb 1.9750

Table 59 LogWorth for the significant (p ≤ 0.05) parameters at each of the grid refinement levels for the quadratic, Maximum temperature.

	n_op						
50		**32**		**16**		**8**	
L_fs	75.823	L_fs	76.414	L_fs	76.985	L_fs	77.470
FSL_x*FSL_x	73.541	FSL_x*FSL_x	72.742	FSL_x*FSL_x	73.204	FSL_x*FSL_x	73.631
Q_fs	56.857	Q_fs	56.885	Q_fs	57.115	Q_fs	57.576
Th_f	40.997	Th_f	41.042	Th_f	41.131	Th_f	41.268
Q_f	25.552	Q_f	25.552	Q_f	25.715	Q_f	26.038
FSL_x	18.523	FSL_x	18.375	FSL_x	18.373	FSL_x	18.607
PL	14.773	PL	14.929	PL	12.734	PL	13.400
L_fs*Q_fs	10.427	L_fs*Q_fs	10.772	L_fs*Q_fs	11.016	L_fs*Q_fs	10.670
v_in	5.5370	v_in	5.2130	v_in	6.1930	v_in	5.7500
t_in	4.4760	sig	4.3510	t_in	4.6300	t_in	4.5570
sig	4.2270	t_in	4.2260	sig	4.1090	L_nb*FSL_x	3.9460
L_nb*FSL_x	3.9270	L_nb*FSL_x	3.2870	L_nb*FSL_x	3.7310	sig	3.8000
sig*sig	3.1610	Th_p*FL_x	3.0490	sig*sig	3.4280	sig*sig	3.4220
Th_p*FL_x	3.1540	sig*sig	3.0030	Th_p*FL_x	3.3200	Th_p*FL_x	3.3050
L_fs*Q_f	2.6820	L_fs*L_fs	2.4310	L_fs*Q_f	2.7440	L_fs*Q_f	2.8180
FL_y*v_in	2.5860	L_fs*Q_f	2.3990	FL_y*v_in	2.6670	FL_y*v_in	2.5870
p_nb	2.1460	FL_x*p_out	2.1290	L_fs*L_fs	2.3690	FL_x*p_out	2.2250
FL_x*p_out	2.0010	FL_y*v_in	2.0370	FL_x*p_out	2.2890	FL_y*L_f	2.0180

Parameter	n_op			
	50	32	16	8
FSL_x	0.6789	0.6805	0.6861	0.6874
Th_f	0.1441	0.1390	0.1426	0.1458
t_in	0.0596	0.0627	0.0614	0.0609
Q_f	0.0375	0.0384	0.0390	0.0383
L_fs	0.0297	0.0314	0.0309	0.0266
v_in	0.0211	0.0219	0.0191	0.0183
Q_fs	0.0191	0.0200	0.0196	0.0214
sig	0.0118	0.0102	0.0109	0.0103
Th_w	0.0112	0.0096	0.0070	0.0077
PL	0.0052	0.0050	0.0018	0.0037
L_f	0.0030	0.0023	0.0026	0.0025
L_nb	0.0026	0.0031	0.0029	0.0014
p_nb	0.0019	0.0009	0.0016	0.0014
Th_p	0.0003	0.0000	0.0001	0.0001
FL_y	0.0001	0.0001	0.0000	0.0000
k_sand	0.0000	0.0000	0.0000	0.0001
FL_x	0.0000	0.0000	0.0001	0.0001
p_out	0.0000	0.0000	0.0000	0.0001

Table 61 Total sensitivity for each parameter at each of the grid refinement levels for the Gaussian Process, maximum temperature

Parameter	n_op			
	50	32	16	8
L_fs	0.3848	0.3882	0.3969	0.3965
FSL_x	0.3109	0.3096	0.3093	0.3081
Q_fs	0.1900	0.1862	0.1844	0.1850
Th_f	0.0927	0.0957	0.0953	0.0937
Q_f	0.0471	0.0477	0.0461	0.0487
PL	0.0144	0.0135	0.0103	0.0111
v_in	0.0062	0.0054	0.0051	0.0056
sig	0.0050	0.0038	0.0035	0.0031
t_in	0.0036	0.0032	0.0046	0.0040
L_f	0.0034	0.0030	0.0032	0.0035
L_nb	0.0021	0.0016	0.0004	0.0010
Th_w	0.0020	0.0038	0.0019	0.0023
p_nb	0.0012	0.0011	0.0013	0.0012
k_sand	0.0002	0.0000	0.0002	0.0000
Th_p	0.0000	0.0001	0.0000	0.0000
FL_y	0.0000	0.0000	0.0000	0.0000
FL_x	0.0000	0.0000	0.0000	0.0000
p_out	0.0000	0.0000	0.0000	0.0000

**Appendix G: Sensitivity Analysis Model and Mesh Description**

In order to reduce the computation time and to examine the effect of mesh density on the results of the SA, the meshing strategy for the narrow channel model was changed from using the COMSOL built-in "Physics Controlled" to "User Controlled". Boundary Layer meshing was used for the coolant channel. Mapped meshes were used for the fuel segregation, the fuel meat, and the cladding. Mapped meshing only works for domains that have at least 4 edges and no interior voids. Because the fuel is an interior void within the cladding, the cladding was broken up into multiple domains. Figure 233 shows how the clad was divided into sections upstream and downstream of the fuel, above and below the fuel, as well as upstream, downstream, above and below the fuel segregation, for a total of 13 domains. The 12 rectangular domains used mapped meshing and the tip used free triangles. The mesh was constructed using the n_op parameter. Figure 234 shows how the mesh density changes at the tip of the fuel plate with increasing n_op. Figure 235 shows how the mesh density around the fuel segregation changes with increasing n_op, and Figure 236 and Figure 237 show progressively enlarged views of the same fuel segregation shown in Figure 235.
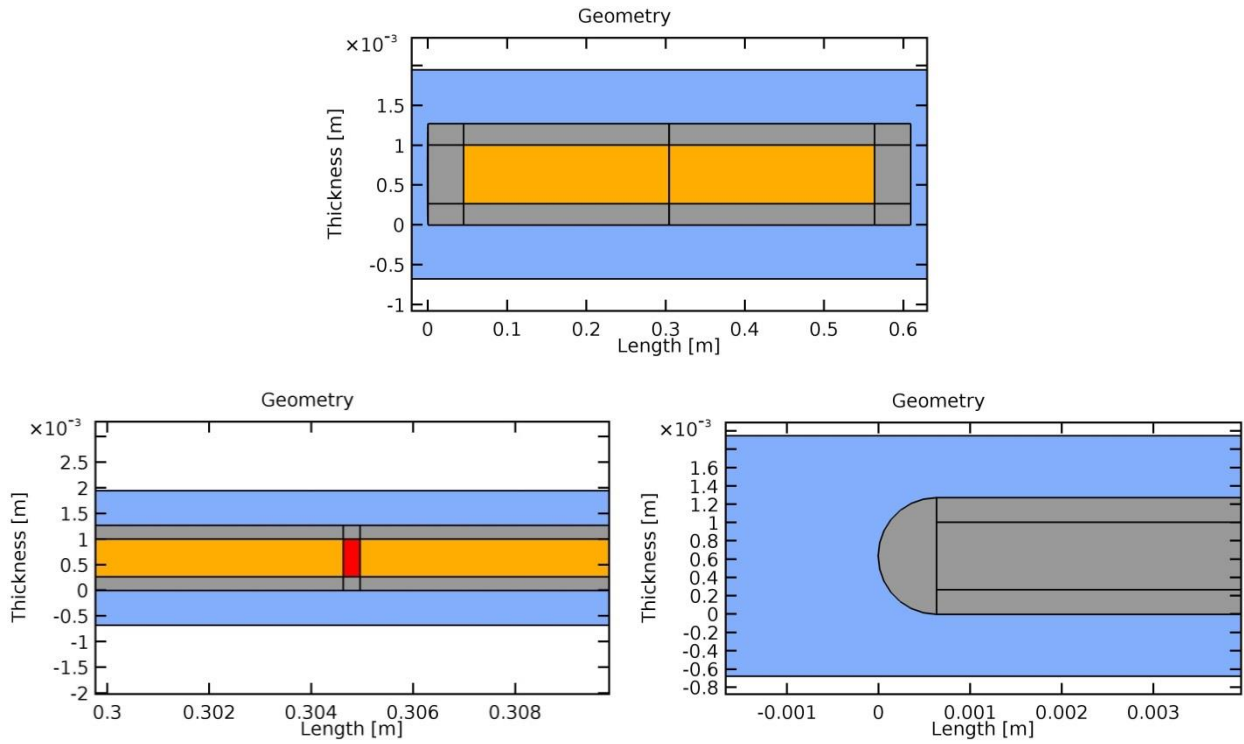
Figure 233 Geometry of the narrow channel model with the cladding broken up into multiple domains. Note that the top image has an enlarged y-axis. The coolant channel is in blue, the cladding in gray, the fuel meat in orange, and the fuel segregation in red.
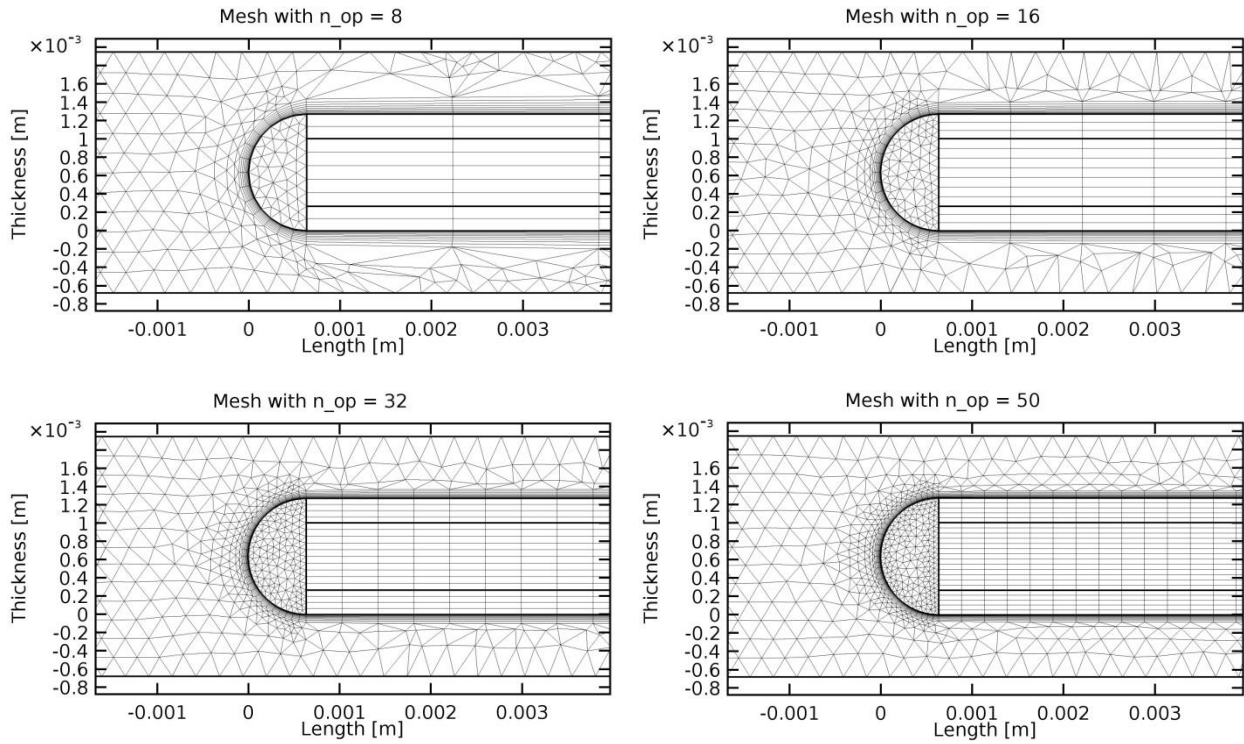
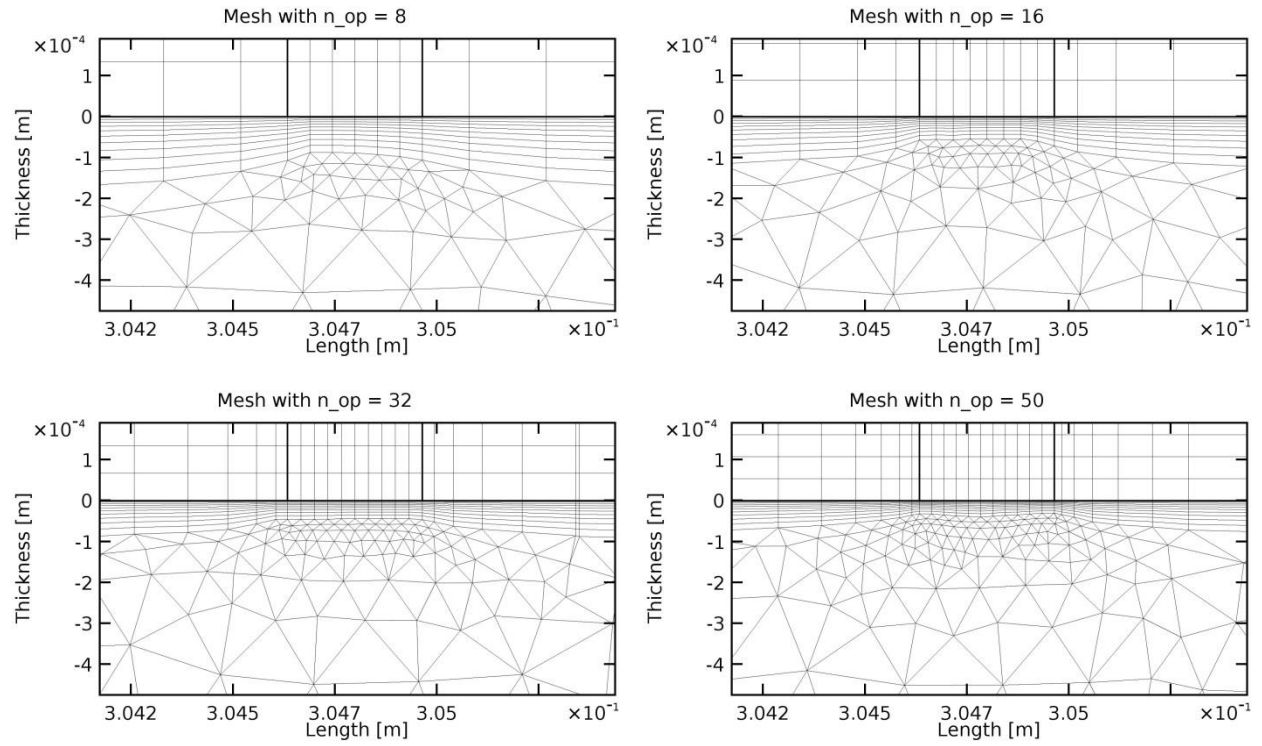**Figure 234 Meshing of the tip of the fuel plate at each of the different grid refinement levels**
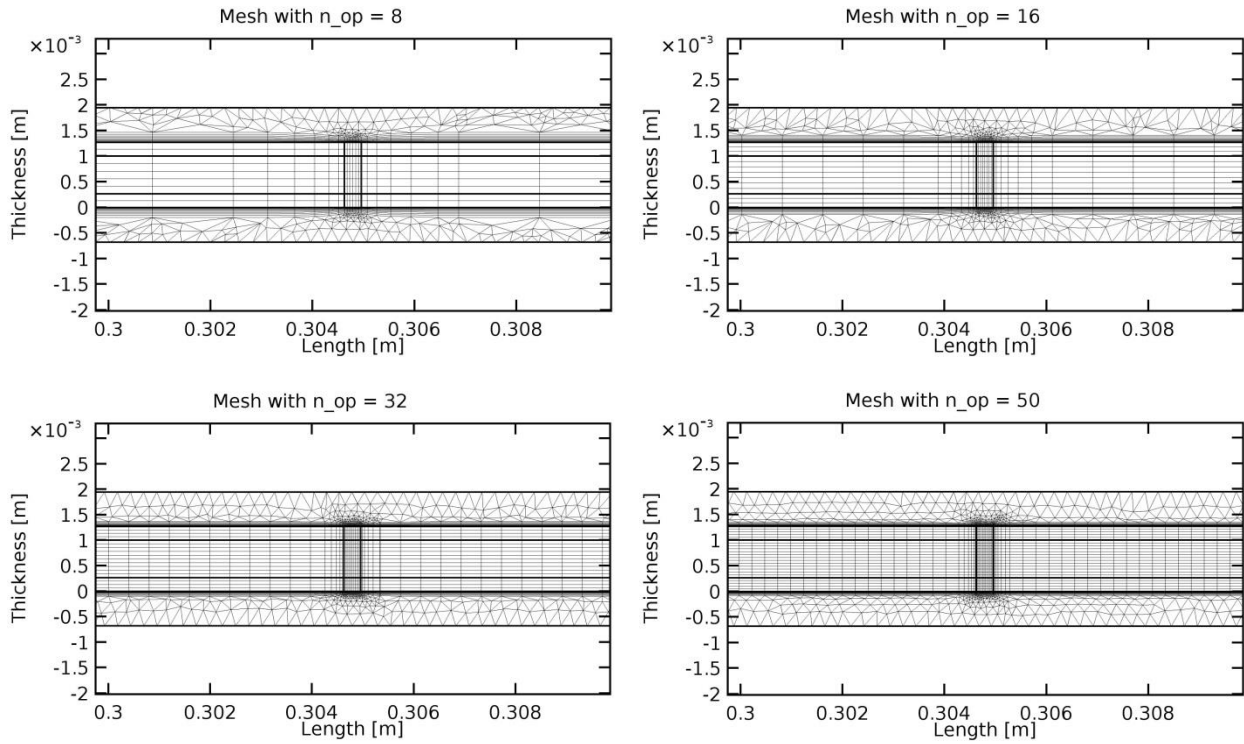
Figure 235 Meshing of the fuel segregation at each of the different grid refinement levels from a distance
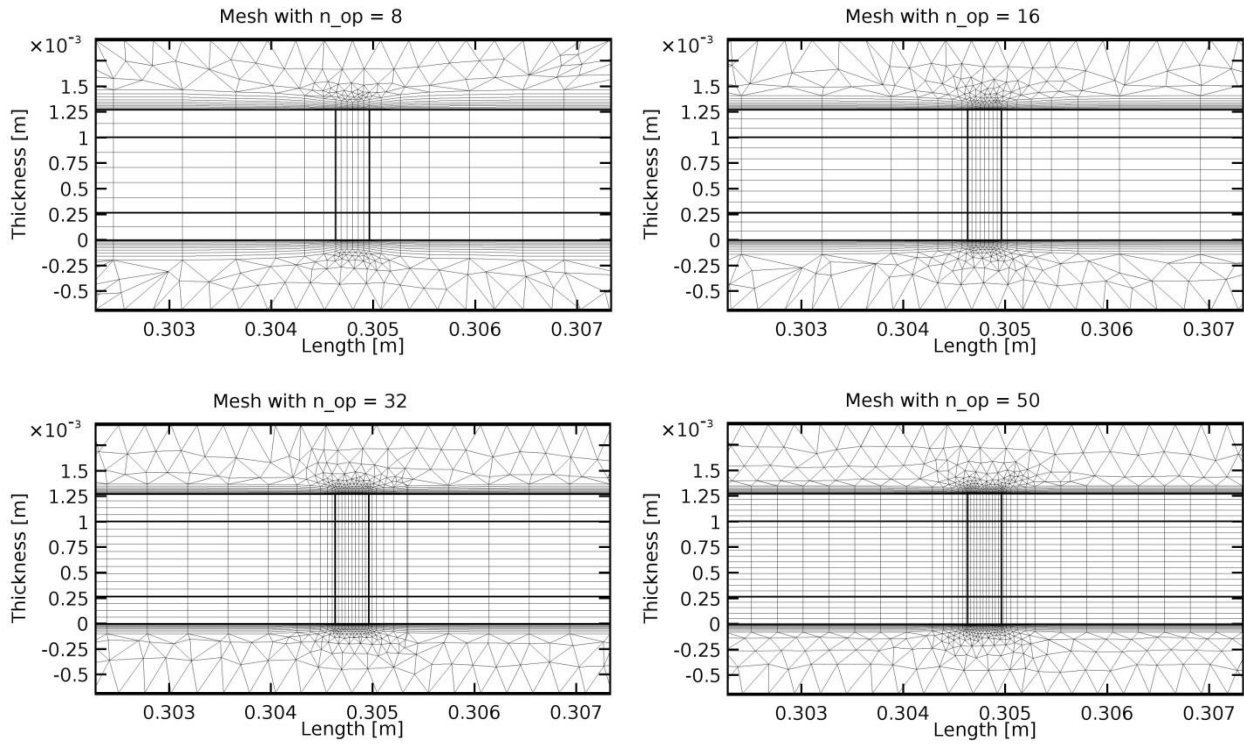
Figure 236 Meshing of the fuel segregation at each of the different grid refinement levels, magnified

Figure 237 Meshing of the bottom of the fuel segregation at each of the different grid refinement levels, very magnified

Appendix H: Graphical Display of Parameter Interactions

The next three pages, Figure 238, presents the hot side quadratic response curve at n_op=50 in a graphical format. Each index is a plot of the Hot Side Temperature vs one of the parameters. There are 2 curves in each plot that show the minimum and maximum values of a second parameter. An example may help to understand the information being presented:

The first plot at the top on the left, which is outlined by a blue box, shows the Hot Side Temperature vs Th_p (the thickness of the plate). On that plot are 2 curves: one is drawn with Th_f (the thickness of the fuel meat) at its minimum (the red curve at 0.02 inches) and the other at its maximum (the blue curve at 0.033 inches). It can be seen from this plot that the temperature does not change greatly with the thickness of the plate (because both curves are close to horizontal), that it does change with the thickness of the fuel meat (because the two curves are separated from each other), and that there is a small degree of interaction between these two parameters (because the curves are not parallel). The plots on this row show all of the other parameters plotted with minimum and maximum fuel thickness. The column shows the changes to the temperature across the range of fuel thicknesses for the minimum and maximum of each of the other parameters.

Figure 238 Graphical presentation of the hot side temperature quadratic surrogate model
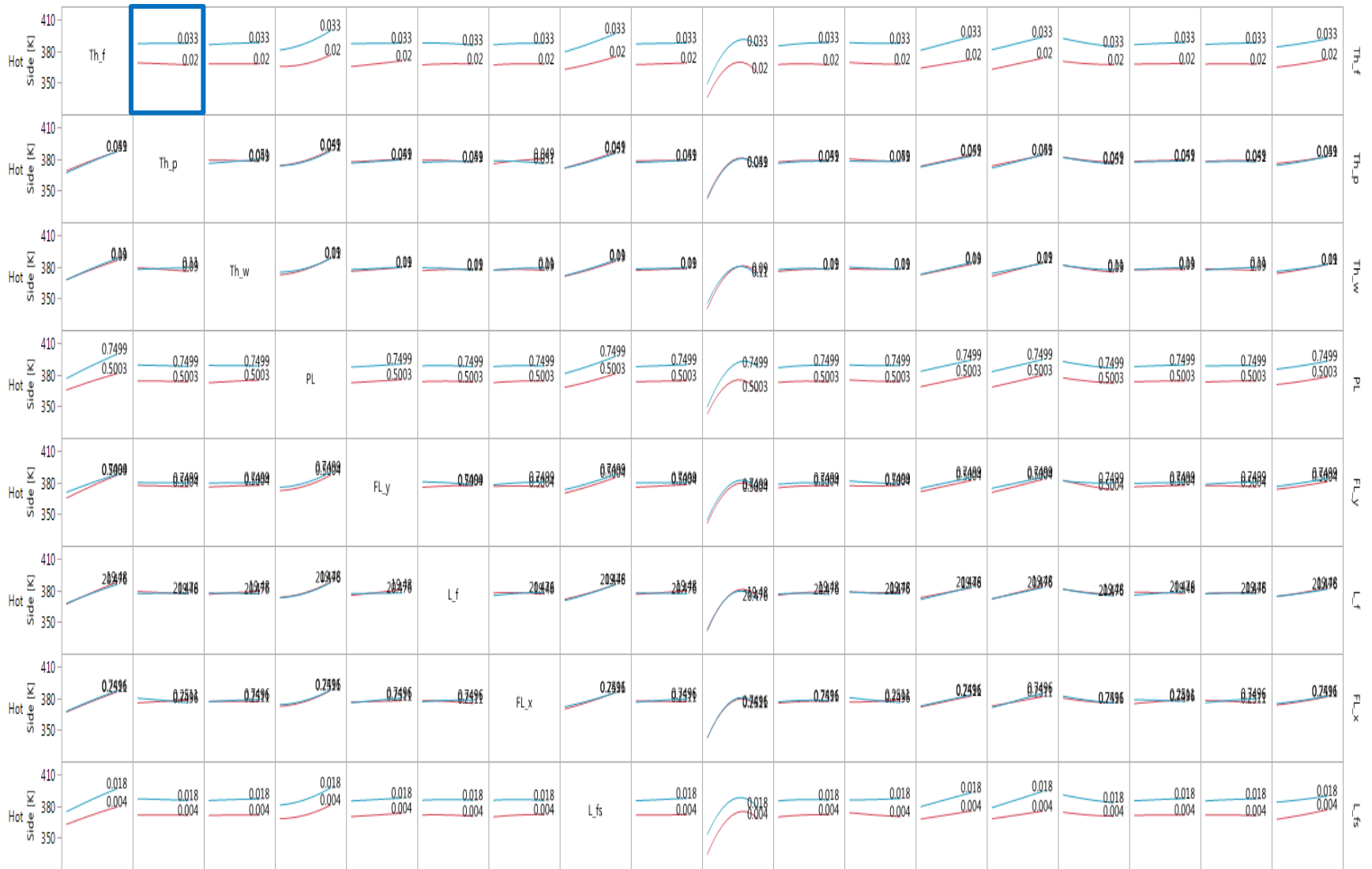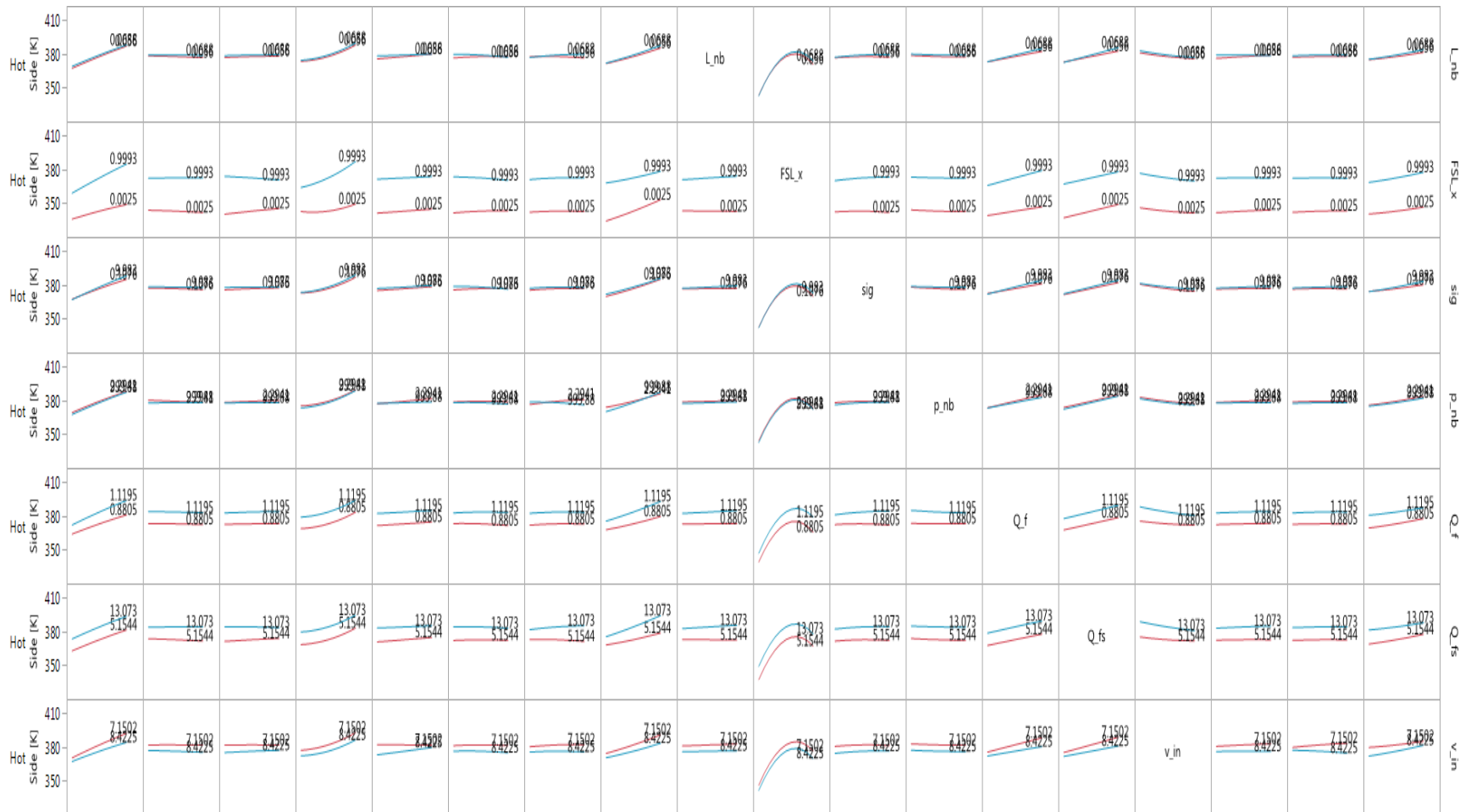
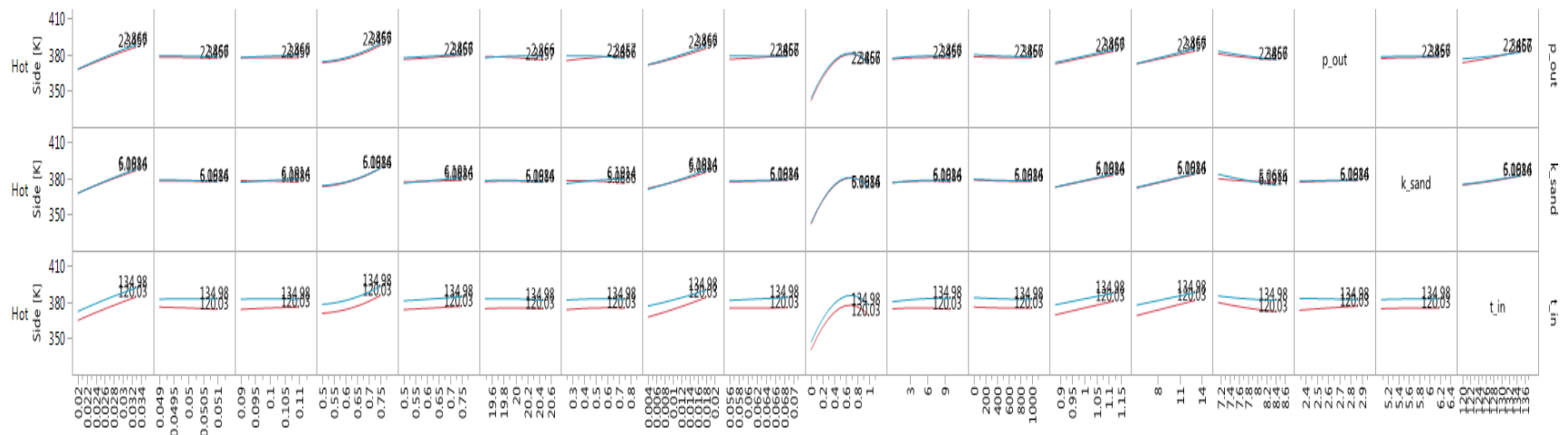**Figure 238 Continued**

317

Figure 238 Continued

318

Figure 238 Continued

Vita

Michael Richards was born in San Antonio, Texas, the 4th of 5 children. He moved frequently throughout his childhood and no longer recalls the names of the elementary or middle schools he attended. He graduated from Fallston High School in Harford County, Maryland. He attended 1 semester at Brigham Young University before leaving on a proselyting mission for his church. He taught the gospel for 2 years in Norway. He returned to Brigham Young University where he was married, joined the Air Force, and completed a BS in mechanical engineering in 2005. He served at Tinker Air Force Base for 3 ½ years as a deputy flight chief, an aircraft battle damage repair engineer, and a responsible engineer for the B-2 bomber. He attended the Air Force Institute of Technology and graduated with an MS in Nuclear Engineering in 2011. He was then assigned to the Air Force Academy where he taught courses in engineering mechanics. While there he attained the rank of assistant professor. In 2014 he entered the Energy Science and Engineering program at the University of Tennessee.